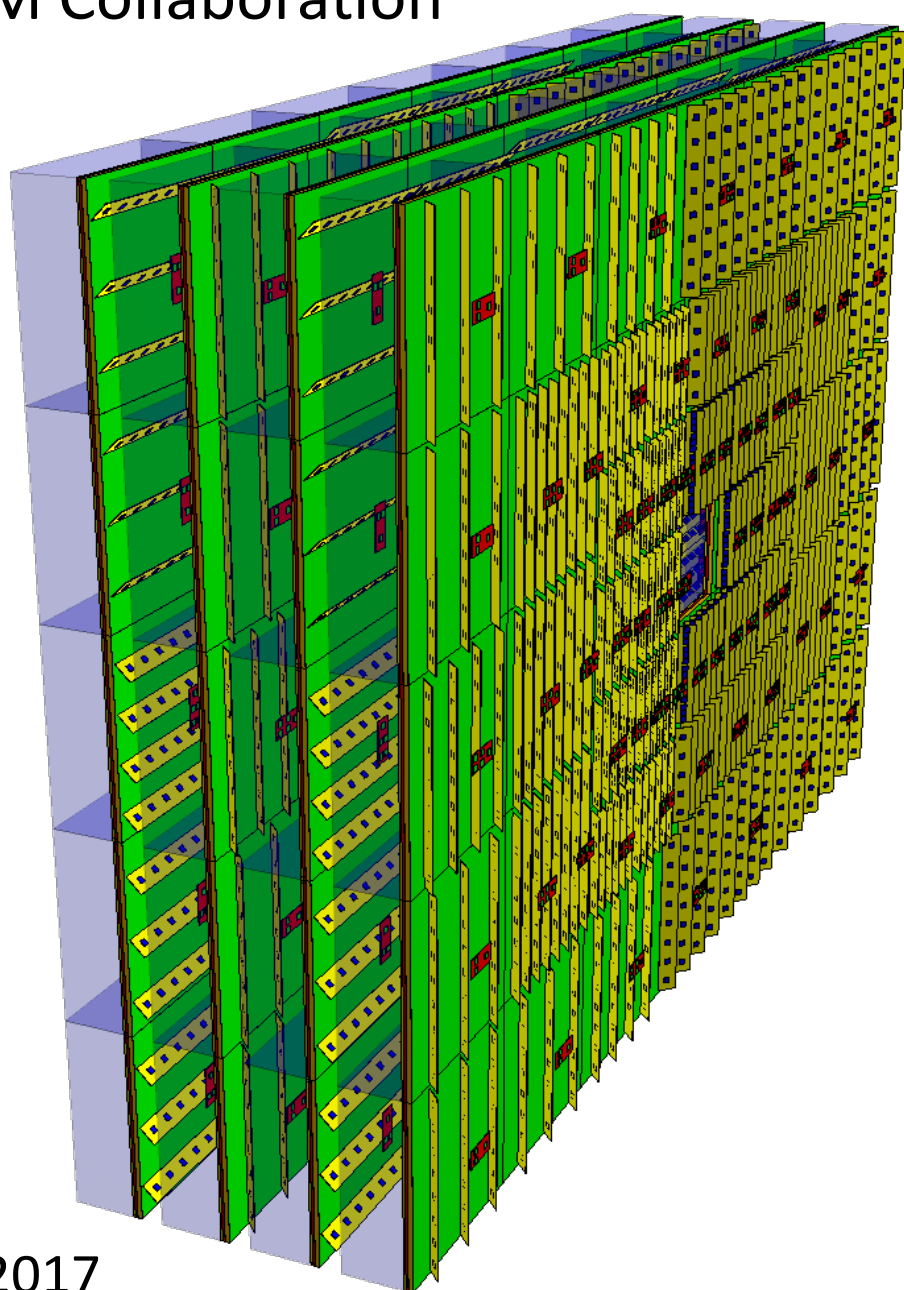


Compressed Baryonic Matter Experiment

# Technical Design Report for the CBM

## Transition Radiation Detector (TRD)

The CBM Collaboration



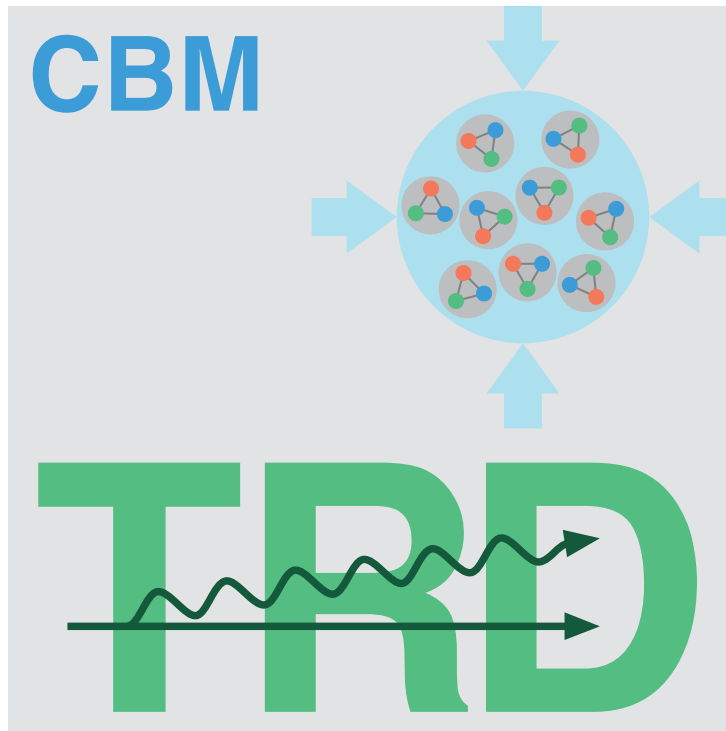
January 2017



The  
Transition Radiation Detector  
of the  
CBM Experiment at FAIR

The TRD Working Group

**Draft – January 25, 2017**



# The TRD Working Group and the CBM Collaboration<sup>1</sup>

The TRD working group comprises participants from the CBM Collaboration and cooperating institutes:

**Horia Hulubei National Institute of Physics and Nuclear Engineering (IFIN-HH), Bucharest, Romania**

A. Bercuci, D. Bartoş, G. Caragheorgheopol, V. Cătănescu, F. Constantin, M. Petcu, M. Petriş, M. Petrovici, A. Radu, L. Radulescu, M.G. Tarzila.

**GSI Helmholtz Center for Heavy-Ion Research GmbH (GSI), Darmstadt, Germany**

D. Emschermann<sup>2</sup>, W. Niebur, A. Lebedev.

**Institut für Kernphysik Frankfurt (IKF), Goethe-Universität Frankfurt, Frankfurt am Main, Germany**

W. Amend, H. Appelshäuser, E. Bechtel, C. Blume<sup>2</sup>, J. Book, P. Dillenseger, S. Gläfel, F. Roether, M. Tanha.

**Institut für Infrastruktur und Rechnersysteme in der Informationsverarbeitung (IRI), Goethe-Universität Frankfurt, Frankfurt am Main, Germany**

J. Gebelein, T. Janson, C. de Jesus Garcia Chavez, I. Keschull, C. Lüdde.

**Institut für technische Informatik (ZITI), Ruprecht-Karls-Universität Heidelberg, Germany**

P. Fischer, M. Krieger.

**Institut für Kernphysik (IKP), Westfälische Wilhelms Universität Münster, Münster, Germany**

R. Berendes, C. Bergmann<sup>2</sup>, N. Heine, P. Kähler, C. Klein-Bösing, M. Kohn, W. Verhoeven, J.P. Wessels.

---

<sup>1</sup>The current list of CBM members is provided in Appendix A

<sup>2</sup>Corresponding authors

## Summary

This document describes the technical design and the performance of the Transition Radiation Detector (TRD) of the Compressed Baryonic Matter (CBM) experiment at FAIR. The main task of the TRD is to identify electrons above momenta of  $1 \text{ GeV}/c$  and thus to extend the electron identification capabilities of the Ring Image CHerenkov (RICH) detector above momenta of  $p \sim 5 \text{ GeV}/c$ . This identification has to be achieved with a pion suppression factor in the range  $10 - 20$ , in order to allow for a measurement of dielectrons in the mass range from below the  $\rho$  and  $\omega$  masses to beyond the  $J/\psi$  mass with a good signal-to-background ratio. Due its capability to identify charged particles via their specific energy loss, the TRD in addition will provide valuable information for the measurement of nuclear fragments. This is in particular important for the separation of, e.g, deuterons and  ${}^4\text{He}$ , which cannot be achieved using a time-of-flight measurement alone.

These requirements can be fulfilled with  $\text{Xe}/\text{CO}_2$  based Multi-Wire Proportional Chambers (MWPC) detector in combination with an adequate radiator. The default MWPC for the CBM-TRD is composed of a symmetric amplification area of  $3.5 + 3.5 \text{ mm}$  thickness, followed by a  $5 \text{ mm}$  drift region to enhance the TR-photon absorption probability in the active gas volume. This geometry provides also efficient and fast signal creation, as well as readout, with timescales below  $200 \mu\text{s}$  per charged particle track. The performance of the detector is optimized by reducing the material budget between radiator and gas volume to a minimum.

The baseline design of the TRD foresees one station composed of four detector layers. It will be positioned between the RICH and the Time-Of-Flight (TOF) detector and thus allows to reduce the background in the TOF resulting from track mismatches by providing additional position information for high precision tracking between Silicon Tracking System (STS) and TOF. The TRD will also be used as tracking station behind the last absorber of the MUCH detector in the muon configuration of CBM.

In this technical design report the design and performance of the TRD, as planned for the SIS100 accelerator, is described in detail. The TRD project is currently being realized in cooperation of institutes from Germany and Romania. The detector system is foreseen to be constructed and installed into the CBM experiment for the Modularized Start Version (MSV) of FAIR.



# Contents

<b>1</b>	<b>The Compressed Baryonic Matter Experiment</b>	<b>7</b>
1.1	Exploring the phase diagram of nuclear matter . . . . .	7
1.2	Diagnostic probes of the high-density fireball . . . . .	8
1.3	CBM physics cases and observables . . . . .	10
1.4	The Facility for Antiproton and Ion Research (FAIR) . . . . .	12
1.5	The Compressed Baryonic Matter (CBM) experiment . . . . .	13
<b>2</b>	<b>Physics Objectives and Design Parameters</b>	<b>16</b>
2.1	Physics objectives . . . . .	16
2.2	Design considerations . . . . .	17
2.3	Summary of TRD design parameters . . . . .	19
<b>3</b>	<b>Physics Performance at SIS100</b>	<b>20</b>
3.1	Simulation setup . . . . .	20
3.1.1	Geometries . . . . .	20
3.1.2	Input to the simulations . . . . .	21
3.1.3	Reconstruction . . . . .	21
3.2	Intermediate mass dileptons . . . . .	22
3.2.1	Pion suppression in the IMR . . . . .	23
3.2.2	Dielectron reconstruction in the IMR . . . . .	24
3.3	$J/\psi$ mesons in proton-nucleus collisions . . . . .	29
3.3.1	Reconstructed $J/\psi$ signal . . . . .	29
3.4	Fragments . . . . .	30
3.4.1	Fragment identification via TRD- $dE/dx$ . . . . .	31
<b>4</b>	<b>The Transition Radiation Detector</b>	<b>34</b>
4.1	Working principle . . . . .	34
4.2	Design optimization . . . . .	35
4.3	TRD station layout . . . . .	36
4.4	General system layout . . . . .	38
4.4.1	TRD in the CBM electron setup . . . . .	39
4.4.2	TRD in the CBM muon setup . . . . .	39
4.4.3	TRD in the CBM hadron setup . . . . .	41
4.5	Occupancy and trigger rates . . . . .	41
4.5.1	Occupancy simulation . . . . .	41
4.5.2	Trigger and data rate estimations . . . . .	42
4.5.3	Test beam results . . . . .	42
4.5.3.1	Results from a high rate and high multiplicity test . . . . .	42
4.5.3.2	Position resolution at low rates but realistic material budget environment . . . . .	43

4.6	Radiation environment . . . . .	45
4.7	Material Budget . . . . .	47
4.7.1	Radiator . . . . .	47
4.7.2	Frontpanel and gas window . . . . .	47
4.7.3	Gas volume . . . . .	48
4.7.4	Backpanel and pad plane . . . . .	48
4.7.5	Front end electronics . . . . .	48
4.7.6	Total material budget . . . . .	49
<b>5</b>	<b>Readout Chamber</b>	<b>51</b>
5.1	Gas mixture . . . . .	51
5.2	ROC design . . . . .	53
5.2.1	MWPC description . . . . .	53
5.2.2	ROC production . . . . .	58
5.2.2.1	Entrance window stress test . . . . .	61
5.2.3	Electrostatic calculations . . . . .	62
5.3	Pad planes and front end boards . . . . .	64
5.3.1	Pad plane layout . . . . .	64
5.3.2	Front end board arrangement . . . . .	66
<b>6</b>	<b>Radiator</b>	<b>69</b>
6.1	Theoretical description of radiators . . . . .	69
6.1.1	Regular radiators . . . . .	69
6.1.2	Irregular radiators . . . . .	71
6.2	Optimization procedure . . . . .	73
6.3	Three best radiator options . . . . .	74
6.3.1	Test beam results on radiator performance . . . . .	75
6.3.2	Mechanical layout of the radiators . . . . .	76
<b>7</b>	<b>Front End Electronics and Readout Chain</b>	<b>77</b>
7.1	The SPADIC front-end ASIC . . . . .	77
7.1.1	Overview . . . . .	77
7.1.2	Chip versions and history . . . . .	78
7.1.3	Charge Sensitive Amplifier (CSA) and ADC . . . . .	79
7.1.4	Digital signal processing . . . . .	82
7.2	Data transport . . . . .	85
7.3	The readout chain . . . . .	85
7.3.1	The TRD readout concept . . . . .	85
7.3.2	TRD readout proposal . . . . .	86
7.3.3	TRD readout prototype . . . . .	87
7.3.4	Feature extraction . . . . .	87
7.3.4.1	Baseline correction . . . . .	87
7.3.4.2	Signal preprocessing . . . . .	88
7.3.4.3	Cluster finder . . . . .	88
<b>8</b>	<b>System Integration and Services</b>	<b>89</b>
8.1	CBM-TRD commissioning and installation . . . . .	89
8.2	Mechanical structure . . . . .	90
8.2.1	ROC mounting . . . . .	90
8.2.2	Radiator mounting . . . . .	91
8.2.3	FEB mounting . . . . .	91

8.3	Gas system . . . . .	92
8.3.1	Gas choice . . . . .	92
8.3.2	Layout . . . . .	92
8.3.2.1	Mixing unit . . . . .	94
8.3.2.2	Circulation and purification system . . . . .	94
8.3.2.3	Backup system . . . . .	96
8.3.2.4	Recovery station . . . . .	96
8.4	High voltage and low voltage . . . . .	97
8.4.1	Low voltage power distribution . . . . .	97
8.4.2	High voltage power distribution . . . . .	101
8.5	Cooling . . . . .	102
8.5.1	Cooling distribution . . . . .	102
8.6	Monitoring and detector control . . . . .	102
8.7	Safety aspects . . . . .	102
<b>9</b>	<b>Simulation and Reconstruction</b>	<b>104</b>
9.1	Simulation framework . . . . .	104
9.2	Detector simulation . . . . .	105
9.2.1	Energy loss in the detector gas . . . . .	105
9.2.2	Transition radiation . . . . .	106
9.2.3	Signal generation . . . . .	107
9.2.3.1	Digitization . . . . .	107
9.2.3.2	Clustering and hit reconstruction . . . . .	108
9.3	Reconstruction routines . . . . .	109
9.3.1	Track reconstruction . . . . .	109
9.3.1.1	Track propagation . . . . .	110
9.3.1.2	Track finding . . . . .	110
9.3.1.3	Track selection . . . . .	111
9.3.2	Electron identification . . . . .	111
9.3.2.1	Artificial neural network . . . . .	112
9.3.2.2	Likelihood function ratio . . . . .	113
9.3.2.3	Ordered statistics (median) . . . . .	114
9.3.2.4	Boosted decision tree . . . . .	114
9.3.3	Performance of the tracking and electron identification. . . . .	114
9.3.3.1	Reconstruction efficiency and resolution in the TRD . . . . .	114
9.3.3.2	Matching efficiency between TRD and TOF . . . . .	116
9.3.3.3	Electron identification efficiency . . . . .	117
9.3.4	Reconstruction efficiency of the TRD in the muon setup . . . . .	118
9.4	Calibration and alignment . . . . .	118
9.4.1	Gain calibration procedures . . . . .	119
9.4.1.1	Krypton calibration . . . . .	119
9.4.1.2	Online gain monitoring . . . . .	120
9.4.1.3	Calibration with data . . . . .	120
9.4.2	Alignment procedure . . . . .	121
<b>10</b>	<b>Mass Production</b>	<b>122</b>
10.1	Production equipment . . . . .	122
10.1.1	Existing laboratory infrastructure . . . . .	123
10.1.1.1	Bucharest laboratory . . . . .	123
10.1.1.2	Frankfurt laboratory . . . . .	123

10.1.1.3	Münster laboratory . . . . .	123
10.2	Production timeline . . . . .	124
10.2.1	Human resources . . . . .	124
10.2.2	Time consumption . . . . .	124
10.2.2.1	Entrance window . . . . .	124
10.2.2.2	Backpanel . . . . .	125
10.2.2.3	Wiring and glueing to ledges . . . . .	125
10.2.2.4	Total production time . . . . .	125
<b>11</b>	<b>Project Organization</b>	<b>126</b>
11.1	Responsibilities . . . . .	127
11.1.1	Participating institutes . . . . .	127
11.1.2	Sharing of tasks . . . . .	127
11.1.3	TRD task force . . . . .	127
11.1.4	TRD TDR editorial committee . . . . .	128
11.2	Costs . . . . .	128
11.2.1	Single readout chamber and FEE . . . . .	128
11.2.2	Total TRD setup . . . . .	129
11.3	Schedule . . . . .	130
11.3.0.1	Milestones . . . . .	130
<b>12</b>	<b>Alternative Design Options</b>	<b>132</b>
12.1	Overview on alternative TRD design options . . . . .	132
12.2	Readout chamber design for optimum performance PID and tracking . . . . .	134
12.2.1	Single MWPC prototype . . . . .	134
12.2.2	Double-sided MWPC prototype . . . . .	134
12.2.3	Single-sided MWPC prototype with drift section . . . . .	136
12.2.4	ROC simulations . . . . .	138
12.2.5	PID performance comparison . . . . .	138
12.2.6	Real size TRD prototype . . . . .	139
12.3	TRD pad plane design for optimum position information . . . . .	141
12.3.1	Triangular pad readout . . . . .	142
12.3.1.1	Laboratory tests using $^{55}\text{Fe}$ X-rays . . . . .	143
12.3.1.2	Low-rate tests at the CERN-PS . . . . .	143
12.3.1.3	Tests in realistic CBM conditions at CERN-SPS . . . . .	145
12.3.2	Two-ways paired pads readout . . . . .	148
12.3.2.1	Laboratory tests using $^{55}\text{Fe}$ X-rays . . . . .	148
12.3.3	Simulation of the detector response . . . . .	149
12.3.3.1	Cross talk effects . . . . .	150
12.3.3.2	Systematic effects of position reconstruction across pads . . . . .	151
12.4	Electronic readout based on the FASP ASIC . . . . .	153
12.4.1	Features of the FASP-0.1 ASIC . . . . .	154
12.4.2	Features of the FASP-0.2 ASIC . . . . .	155
12.4.3	Simulations of the FEE . . . . .	157
12.4.3.1	Analog channel response to GARFIELD input . . . . .	157
12.4.4	FEE integration . . . . .	159
12.4.4.1	FASP FEB . . . . .	159
12.4.4.2	Free running DAQ . . . . .	160
12.5	Fast ROC design . . . . .	164
12.5.1	Conceptional chamber design . . . . .	164

12.5.2	Layout of the fast TRD prototype . . . . .	165
12.5.3	Electrostatic simulations . . . . .	166
12.5.4	Simulations and measurements of the gain stability . . . . .	166
12.5.5	Fast prototype with alternating high voltage configuration . . . . .	168
12.5.6	Test beam performance . . . . .	170
12.5.7	Conclusion on the fast MWPC prototype . . . . .	171
<b>A</b>	<b>The CBM Collaboration</b>	<b>173</b>
<b>B</b>	<b>List of Acronyms</b>	<b>177</b>
<b>C</b>	<b>Additional Figures</b>	<b>181</b>



## Chapter 1

# The Compressed Baryonic Matter Experiment

### 1.1 Exploring the phase diagram of nuclear matter

Substantial experimental and theoretical efforts worldwide are devoted to the exploration of the phase diagram of nuclear matter. Figure 1.1 illustrates the possible phases of nuclear matter and their boundaries in a diagram of temperature versus the baryon chemical potential. Cold nuclear matter - as found in normal nuclei with a net-baryon density equal to one - consists of protons and neutrons (i.e. nucleons) only. At moderate temperatures and densities, nucleons are excited to short-lived states (baryonic resonances) which decay by the emission of mesons. At higher temperatures, also baryon-antibaryon pairs are created. This mixture of baryons, anti-baryons and mesons, all strongly interacting particles, is generally called hadronic matter, or baryonic matter if baryons prevail. At very high temperatures or densities the hadrons melt, and the constituents, the quarks and gluons, form a new phase: the Quark-Gluon-Plasma (QGP). For very low net-baryon densities where the numbers of particles and anti-particles are approximately equal, Quantum Chromo-Dynamics (QCD) on the lattice predicts that hadrons dissolve into quarks and gluons above a temperature of about 160 MeV [B<sup>+</sup>10, B<sup>+</sup>12]. The inverse process happened in the universe during the first few microseconds after the big bang: the quarks and gluons were confined into hadrons. In this region of the phase diagram the transition is expected to be a smooth crossover from partonic to hadronic matter [A<sup>+</sup>06]. Calculations suggest a critical endpoint at relatively large values of the baryon chemical potential [FK04]. Beyond this critical endpoint, for larger values of net-baryon densities (and for lower temperatures), one expects a phase transition from hadronic to partonic matter with a phase coexistence region in between. A new phase of so called quarkyonic matter has been proposed to exist beyond the first order phase transition at large baryon chemical potentials and moderate temperatures [A<sup>+</sup>10b]. High-density but cold nuclear matter is expected to exist in the core of neutron stars, and at very high densities correlated quark-quark pairs are predicted to form a color superconductor.

As illustrated in Fig. 1.1, it is expected that the QCD phase diagram exhibits a rich structure at finite values of baryon chemical potentials, such as the critical point, the predicted first order phase transition between hadronic and partonic or quarkyonic matter, and the chiral phase transition. The experimental discovery of these prominent landmarks of the QCD phase diagram would be a major breakthrough in our understanding of the properties of nuclear matter. Equally important is quantitative experimental information on the properties of hadrons in dense matter which may shed light on chiral symmetry restoration and the origin of hadron masses.

In the laboratory hot and dense nuclear matter is generated in a wide range of temperatures and densities by colliding atomic nuclei at high energies. The goal of the experiments at RHIC

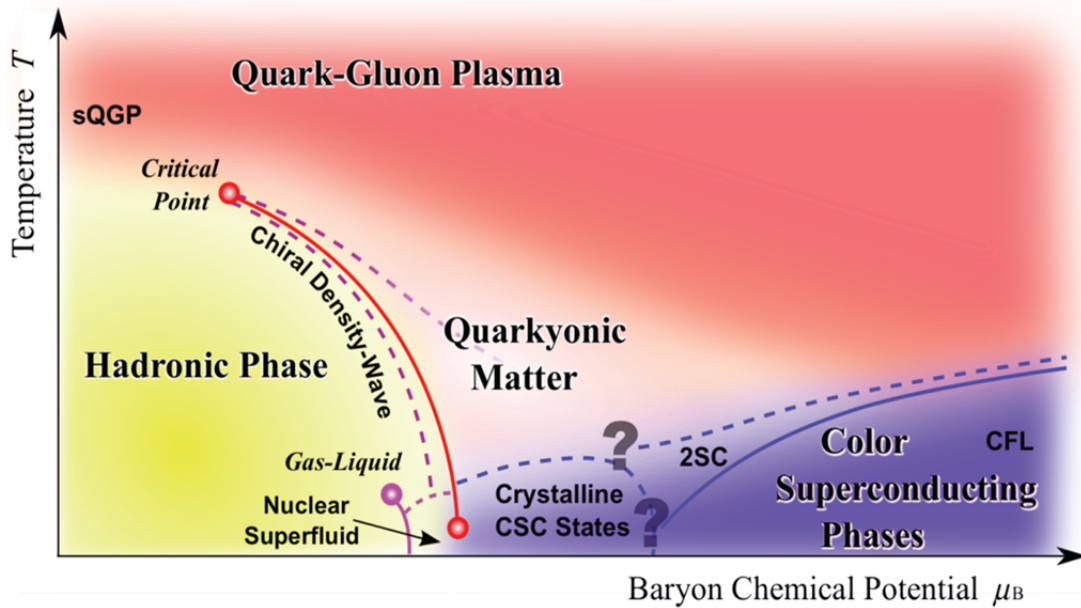


Figure 1.1: Sketch of the phase diagram for strongly-interacting matter (taken from [FH11]).

and LHC is to investigate the properties of deconfined QCD matter at very high temperatures and almost zero net-baryon densities. Several experimental programs are devoted to the exploration of the QCD phase diagram at high net-baryon densities. The STAR collaboration at RHIC scanned the beam energies in order to search for the QCD critical endpoint [S<sup>+</sup>12]. For the same reason, measurements are performed at the CERN-SPS with the upgraded NA49 detector (NA61) using light and medium size ion beams [A<sup>+</sup>12]. At the Joint Institute for Nuclear Research (JINR) in Dubna, a heavy-ion collider project (NICA) is planned with the goal to search for the coexistence phase of nuclear matter [B<sup>+</sup>16c]. However, due to luminosity or detector limitations these experiments are constrained to the investigation of particles which are abundantly produced. In contrast, the Compressed Baryonic Matter (CBM) experiment at the Facility for Antiproton and Ion Research (FAIR) in Darmstadt is designed for precision measurements of multidimensional observables including particles with very low production cross sections using the high-intensity heavy-ion beams provided by the FAIR accelerators.

The SIS100/300 accelerators at FAIR are very well suited to create high net-baryon densities. This is illustrated in Fig. 1.2 which depicts results of transport code calculations for central Au + Au collisions. According to these calculations, densities of up to seven times saturation density can be produced already at beam energies of 10 AGeV. Under these conditions the nucleons overlap, and theory predicts a transition to a mixed phase of baryons and quarks.

## 1.2 Diagnostic probes of the high-density fireball

Figure 1.3 depicts three snapshots of the evolution of a heavy-ion collision at FAIR energies as calculated with the UrQMD transport code [B<sup>+</sup>98], and illustrates the time of production and eventual emission of various particle species. Particles containing charm quarks are expected to be created in the very first stage of the reaction. Then, D mesons and  $J/\psi$  mesons may serve as probes for the dense fireball and its degrees of freedom. Vector mesons like  $\omega$ ,  $\rho$  and  $\phi$  mesons are produced continuously via  $\pi\pi$  annihilation during the course of the reaction, and decay either

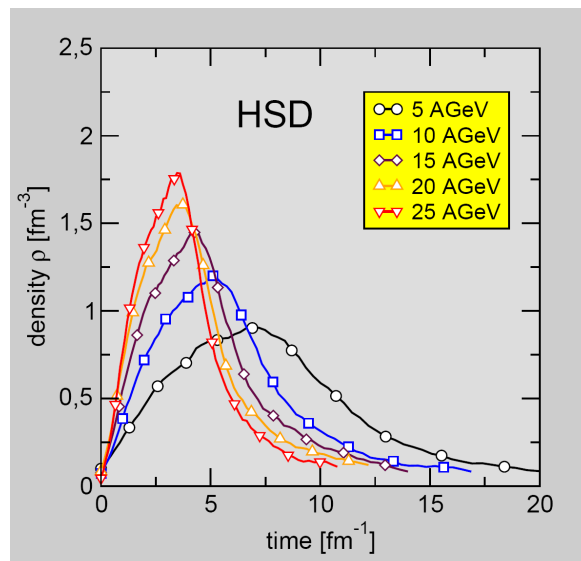


Figure 1.2: Baryon density as function of elapsed time for central Au + Au collisions at different energies as calculated with the HSD transport code [EC96].

again into mesons or into a pair of leptons. However, as leptons are not affected by final-state interactions, the dileptonic decay offers the possibility to look into the fireball. In particular, the short-lived  $\rho$  meson is a promising diagnostic probe of hot and dense nuclear matter. Due to their small hadronic cross sections, also multi-strange hyperons and  $\phi$  mesons carry information on the dense phase of the collision, in particular via their collective flow. Finally, the bulk of the particles freezes out at densities below saturation density. Up to date, essentially only these bulk particles have been measured in heavy-ion collisions at beam energies between 2 and 40 AGeV (on stationary target). Diagnostic probes of the dense stage of the fireball such as multi-strange baryons, dilepton pairs and charmed particles will be measured for the first time by the CBM experiment in this beam energy range. Therefore, the CBM experiment has a unique discovery potential both at SIS100 and SIS300 energies.

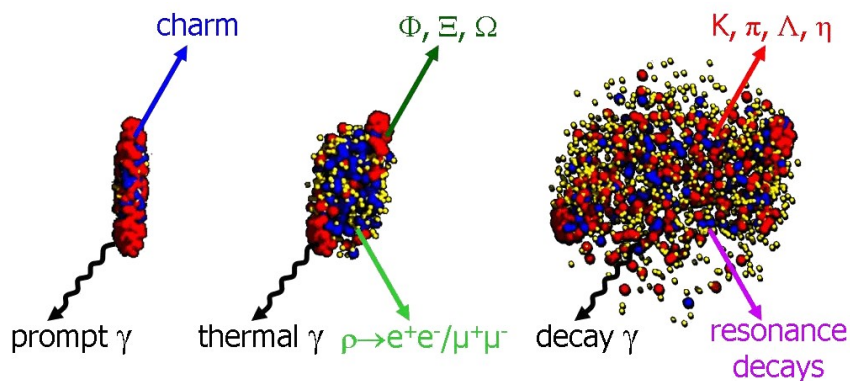


Figure 1.3: Three stages of a U + U collision at a laboratory beam energy of 23 AGeV as calculated with the UrQMD model [B<sup>+</sup>98]: The initial stage where the two Lorentz-contracted nuclei overlap (left), the high density phase (middle), and the final stage (“freeze-out”) when all hadrons have been formed (right). Different particles are created in different stages of the collisions or escape from the interaction region at different times (see text). Almost 1000 charged particles are created in such a collision, most of them are pions.

The experimental challenge is to measure multi-differential observables and particles with very low production cross sections such as multi-strange (anti-)hyperons, particles with charm and lepton pairs with unprecedented precision. The situation is illustrated in the left panel of Fig. 1.4 which depicts the multiplicities for various particle species produced in central Au + Au collisions at 4 AGeV. The data points are calculated using the thermal model based on the corresponding temperature and baryon-chemical potential [ABMS06]. The dilepton decay of vector mesons, here illustrated for the  $\phi$  meson, is suppressed by the square of the electromagnetic coupling constant  $(1/137)^2$ , resulting in a dilepton yield which is about six orders of magnitude below the pion yield, similar to the multiplicity of multi-strange anti-hyperons.

In order to produce high-statistics data even for the particles with the lowest production cross sections, the CBM experiment is designed to run at reaction rates of 100 kHz up to 1 MHz. For charmonium measurements - where a trigger on high-energy lepton pairs can be generated - reaction rates up to 10 MHz are envisaged. This exceeds the rate capabilities of other existing and planned heavy-ion experiments by orders of magnitude, as illustrated in the right panel of Fig. 1.4.

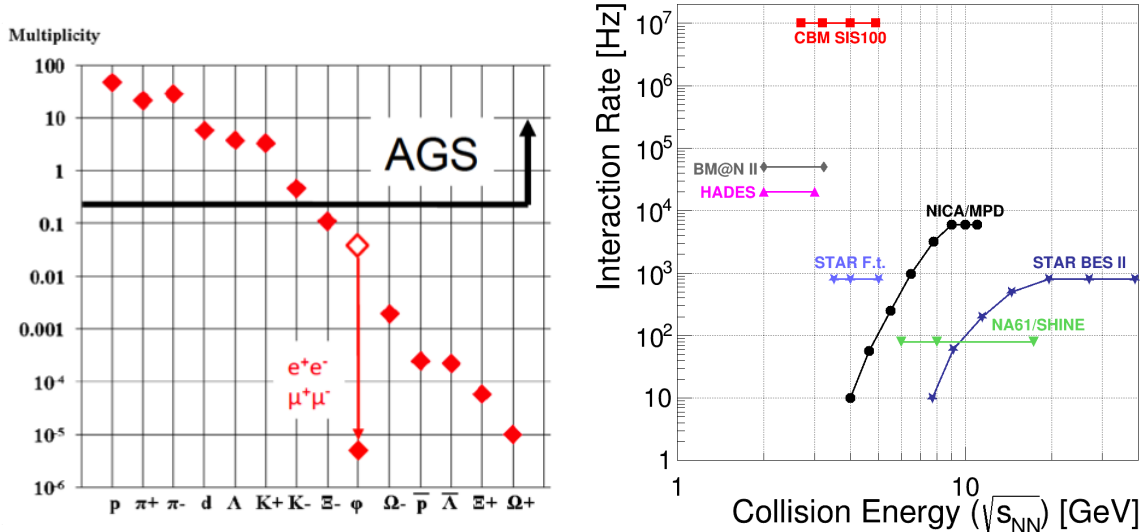


Figure 1.4: Left: Particle multiplicities for central Au + Au collisions at 4 AGeV as calculated with a statistical model [ABMS06]. For the  $\phi$  meson also the branching fraction for the decay into lepton pairs is included (open symbol). The black line roughly indicates the multiplicities that were available to the AGS heavy-ion program at BNL at this energy. Right: Interaction rates achieved by existing and planned heavy-ion experiments as a function of center-of-mass energy [C<sup>+</sup>16]. “STAR F.t.” denotes the fixed-target operation of STAR.

### 1.3 CBM physics cases and observables

The CBM research program is focused on the following physics cases:

#### The equation-of-state of baryonic matter at neutron star densities.

The relevant measurements are:

- The excitation function of the collective flow of hadrons which is driven by the pressure created in the early fireball (SIS100).

- The excitation functions of multi-strange hyperon yields in Au + Au and C + C collisions at energies from 2 to 11 AGeV (SIS100). At sub-threshold energies,  $\Xi$  and  $\Omega$  hyperons are produced in sequential collisions involving kaons and  $\Lambda$ , and are therefore sensitive to the density in the fireball.

#### **In-medium properties of hadrons.**

The restoration of chiral symmetry in dense baryonic matter will modify the properties of hadrons. The relevant measurements are:

- The in-medium mass distribution of vector mesons decaying in lepton pairs in heavy-ion collisions at different energies (2 – 45 AGeV), and for different collision systems. Leptons are penetrating probes carrying the information out of the dense fireball (SIS100/300).
- Yields and transverse mass distributions of charmed mesons in heavy-ion collision as a function of collision energy (SIS100/300).

#### **Phase transitions from hadronic matter to quarkyonic or partonic matter at high net-baryon densities.**

Already at SIS100 energies densities of up to seven times of the normal nuclear density are reached in central collisions between heavy-ions. A discontinuity or sudden variation in the excitation functions of sensitive observables would be indicative of a transition. The relevant measurements are:

- The excitation function of yields, spectra and collective flow of strange particles in heavy-ion collisions from 6 – 45 AGeV (SIS100/300).
- The excitation function of yields, spectra and collective flow of charmed particles in heavy-ion collisions from 6 – 45 AGeV (SIS100/300).
- The excitation function of yields and spectra of lepton pairs in the intermediate mass region in heavy-ion collisions from 6 – 45 AGeV (SIS100/300).
- Event-by-event fluctuations of conserved quantities like baryons, strangeness, net-charge etc. in heavy-ion collisions with high precision as function of beam energy from 6 – 45 AGeV (SIS100/300).

#### **Hypernuclei, strange dibaryons and massive strange objects.**

Theoretical models predict that single and double hypernuclei, strange dibaryons and heavy multi-strange short-lived objects are produced via coalescence in heavy-ion collisions with the maximum yield in the region of SIS100 energies. The planned measurements include:

- The decay chains of single and double hypernuclei in heavy-ion collisions at SIS100 energies.
- Search for strange matter in the form of strange dibaryons and heavy multi-strange short-lived objects. If these multi-strange particles decay into charged hadrons including hyperons they can be identified via their decay products.

#### **Charm production mechanisms, charm propagation and in-medium properties of charmed particles in (dense) nuclear matter.**

The relevant measurements are:

- Cross sections and momentum spectra of open charm (D-mesons) in proton-nucleus collisions at SIS100/300 energies. In-medium properties of D-mesons can be derived from the transparency ratio  $T_A = (\sigma_{pA} \rightarrow DX) / (A \times \sigma_{pN} \rightarrow DX)$  measured for different size target nuclei.

- Cross sections, momentum spectra and collective flow of open charm (D-mesons) in nucleus-nucleus collisions at SIS300 energies.
- Cross sections, momentum spectra and collective flow of charmonium ( $J/\psi$ ) in proton-nucleus and nucleus-nucleus collisions at SIS100/300 energies.

As discussed above, a substantial part of the CBM physics cases can be addressed already with beams from the SIS100 synchrotron [C<sup>+</sup>16]. The intended measurements at SIS100 including the results of simulations and count rate estimates are described in [Col11]. A general review of the physics of compressed baryonic matter, the theoretical concepts, the available experimental results and predictions for relevant observables in future heavy-ion collision experiments can be found in the CBM Physics Book [F<sup>+</sup>11].

## 1.4 The Facility for Antiproton and Ion Research (FAIR)

The international Facility for Antiproton and Ion Research (FAIR) in Darmstadt will provide unique research opportunities in the fields of nuclear, hadron, atomic and plasma physics [G<sup>+</sup>06]. The research program devoted to the exploration of compressed baryonic matter will start with primary beams from the SIS100 synchrotron (protons up to 29 GeV, Au up to 11 AGeV, nuclei with  $Z/A = 0.5$  up to 14 AGeV), and will be continued with beams from the SIS300 synchrotron (protons up to 90 GeV, Au up to 35 AGeV, nuclei with  $Z/A = 0.5$  up to 45 AGeV). The layout of FAIR is presented in Fig. 1.5. The beam extracted to the CBM cave reaches intensities up to  $10^9$  Au ions per second.

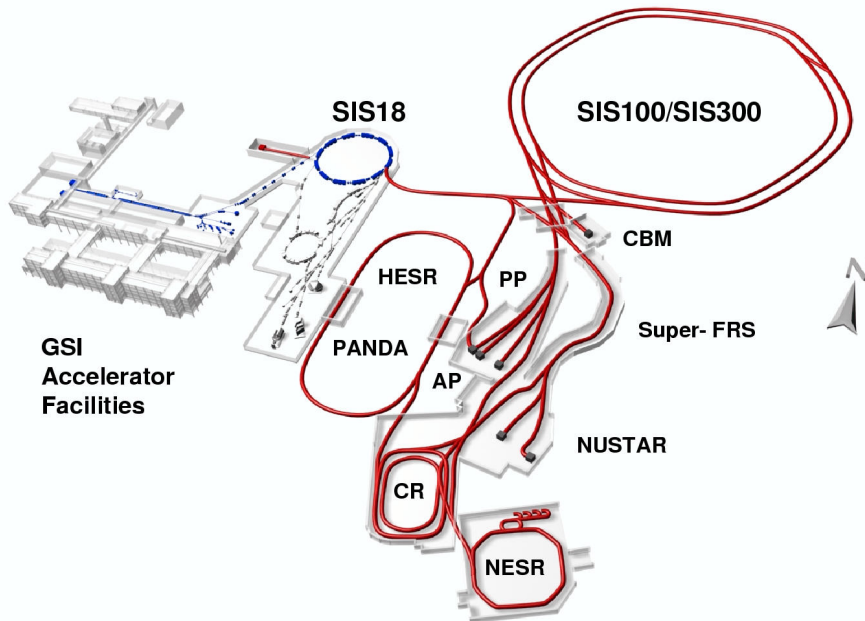


Figure 1.5: Layout of the Facility for Antiproton and Ion Research (FAIR) [G<sup>+</sup>06].

## 1.5 The Compressed Baryonic Matter (CBM) experiment

The CBM experimental strategy is to perform systematic both integral and differential measurements of almost all the particles produced in nuclear collisions (i.e. yields, phase-space distributions, correlations and fluctuations) with unprecedented precision and statistics. These measurements will be performed in nucleus-nucleus, proton-nucleus, and - for baseline determination - proton-proton collisions at different beam energies. The identification of multi-strange hyperons, hypernuclei, particles with charm quarks and vector mesons decaying into lepton pairs requires efficient background suppression and very high interaction rates. In order to select events containing those rare observables, the tracks of each collision have to be reconstructed and filtered online with respect to physical signatures. This concept represents a paradigm shift for data taking in high-energy physics experiments: CBM will run without hierarchical trigger system. Self-triggered readout electronics, a high-speed data processing and acquisition system, fast algorithms, and, last but not least, radiation hard detectors are indispensable prerequisites for a successful operation of the experiment. Figure 1.6 and depict the CBM experimental setup for SIS100. The CBM experiment comprises the following components:

### Dipole magnet

The dipole magnet will be superconducting in order to reduce the operation costs. It has a large aperture of  $\pm 25^\circ$  polar angle, and provides a magnetic field integral of 1 Tm.

### Micro-Vertex Detector (MVD)

The MVD will provide excellent position resolution and low material budget as required for the identification of open charm particles by the measurement of their displaced decay vertex. It consist of four layers of Monolithic Active Pixel Sensor (MAPS) detectors located from 5 cm to 20 cm downstream of the target in vacuum. The detector arrangement provides a resolution of secondary vertices of about 50 – 100  $\mu\text{m}$  along the beam axis.

### Silicon Tracking System (STS)

The task of the STS is to provide track reconstruction and momentum determination of charged particles. The system consists of eight tracking layers of silicon strip detectors, located downstream of the target at distances between 30 cm and 100 cm inside the magnetic dipole field, and provides a momentum resolution of about  $\Delta p/p = 1.5\%$ .

### Ring Imaging Cherenkov Detector (RICH)

The RICH detector will provide the identification of electrons via the measurement of their Cherenkov radiation. This will be achieved using a gaseous RICH detector build in a standard projective geometry with focusing mirror elements and a photon detector. The detector will be positioned behind the dipole magnet about 1.6 m downstream of the target. It will consist of a 1.7 m long gas radiator (overall length approximately 2 m) and two arrays of mirrors and photon detector planes. The design of the photon detector plane is based on MAPMTs in order to provide high granularity, high geometrical acceptance, high detection efficiency of photons also in the near UV region and a reliable operation.

### Muon Chamber System (MUCH)

The concept of the muon detection system is to track the particles through a hadron absorber and thus perform a momentum dependent muon identification. The absorber/detector system is placed downstream of the STS, which determines the particle momentum. In order to reduce meson decays into muons the absorber/detector system is designed as compact as possible. It consists of six hadron absorber layers made of iron plates and 18 gaseous tracking chambers

located in triplets behind each iron slab (SIS300 setup). The trigger concept is based on the measurement of short track segments in the last tracking station triplet, and extrapolation of these tracks to the target. For  $J/\psi$  measurements at SIS100 a MUCH start version with three chamber triplets is sufficient.

### Transition Radiation Detector (TRD)

The Transition Radiation Detector, consisting of four detector layers grouped into one station in the SIS100 configuration (ten layers in three stations for SIS300), will serve for particle tracking and for the identification of electrons and positrons with  $p > 1.0 \text{ GeV}/c$  ( $\gamma \geq 1000$ ). The detector layers are located at approximately 4.1 m to 5.9 m downstream of the target, the total active detector area amounts to about  $114 \text{ m}^2$  (SIS100). The TRD readout will be realized in rectangular pads giving a resolution of  $\sim 300 \mu\text{m}$  across and  $3 - 30 \text{ mm}$  along the pad. Every second TRD layer is rotated by  $90^\circ$ .

### Time-Of-Flight System (TOF)

An array of Multi-gap Resistive Plate Chambers (MRPC) will be used for hadron identification via TOF measurements. The TOF wall covers an active area of about  $120 \text{ m}^2$  and is located about 6 m downstream of the target for measurements at SIS100, and at 10 m at SIS300. The required time resolution is on the order of 80 ps. At small deflection angles the pad size is about  $5 \text{ cm}^2$  corresponding to an occupancy of below 5% for central Au + Au collisions at 25 AGeV.

### Electromagnetic Calorimeter (ECAL)

A “shashlik” type calorimeter as installed in the HERA-B, PHENIX and LHCb experiments will be used to measure direct photons and neutral mesons ( $\pi^0, \eta$ ) decaying into photons. The ECAL will be composed of modules which consist of 140 layers of lead and scintillator sheets. The shashlik modules can be arranged either as a wall or in a tower geometry with variable distance from the target.

### Projectile Spectator Detector (PSD)

The PSD will be used to determine the collision centrality and the orientation of the reaction plane. The detector is designed to measure the number of non-interacting nucleons from a projectile nucleus in nucleus-nucleus collisions. The PSD is a fully compensating modular lead-scintillator calorimeter which provides very good and uniform energy resolution. The calorimeter comprises 44 individual modules, each consisting of 60 lead/scintillator layers.

### Online event selection and data acquisition

High-statistics measurements of particles with very small production cross sections require high reaction rates. The CBM detectors, the online event selection systems and the data acquisition will be designed for event rates of 10 MHz, corresponding to a beam intensity of  $10^9$  ions/s and a 1% interaction target, for example. Assuming an archiving rate of 1 GByte/s and an event volume of about 10 kByte for minimum bias Au + Au collisions, an event rate of 100 kHz can be accepted by the data acquisition. Therefore, measurements with event rates of 10 MHz require online event selection algorithms (and hardware) which reject the background events (which contain no signal) by a factor of 100 or more. The event selection system will be based on a fast online event reconstruction running on a high-performance computer farm equipped with many-core CPUs and graphics cards (GSI GreenIT cube). Track reconstruction, which is the most time consuming combinatorial stage of the event reconstruction, will be based on parallel track finding and fitting algorithms, implementing the Cellular Automaton and Kalman Filter methods. For open charm production the trigger will be based on an online search for secondary vertices, which requires high speed tracking and event reconstruction in the STS and MVD. The

highest suppression factor has to be achieved for  $J/\psi$  mesons where a high-energetic pair of electrons or muons is required in the TRD or in the MUCH. For low-mass electron pairs no online selection is possible due to the large number of rings/event in the RICH caused by the material budget of the STS. In the case of low-mass muon pairs some background rejection might be feasible.

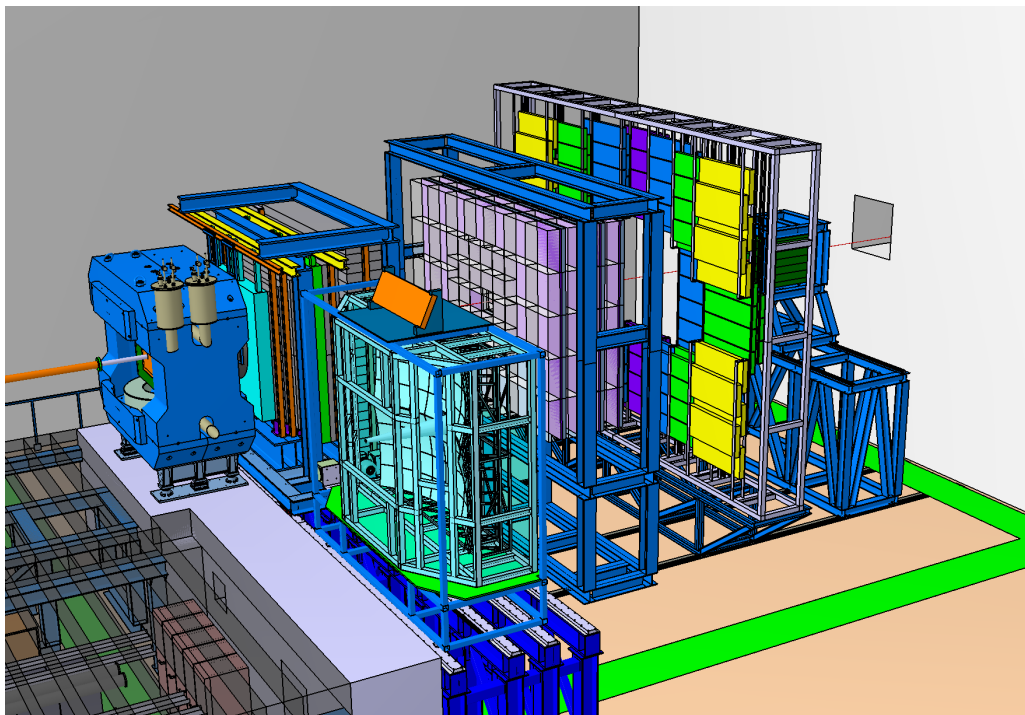


Figure 1.6: Drawing of the experimental setup of CBM for the SIS100.

## Chapter 2

# Physics Objectives and Design Parameters

Here we give a brief overview on the physics observables which mainly define the requirements on the CBM-TRD. Based on these considerations, the design parameters of the TRD have been defined and are also summarized here.

### 2.1 Physics objectives

The capability to measure dielectrons with high precision and low background is of essential relevance for the CBM physics program at the SIS100 accelerator, since crucial observables in heavy-ion physics, such as low mass vector mesons and quarkonia, are addressed via this decay channel.

Within CBM electron identification is the task of two detector systems, the RICH detector and the TRD, which in conjunction will provide the necessary hadron suppression. Since the electron identification capabilities of the RICH are limited to the lower momentum region ( $p < 5 \text{ GeV}/c$ ), the TRD will be mandatory as an additional device to supplement and extend the electron PID towards higher momenta. The TRD configuration envisaged for the CBM setup at the SIS100 will therefore be able to identify electrons above a momentum threshold of  $p > 1 \text{ GeV}/c$  with a 90% efficiency, while simultaneously suppressing the hadronic background by a factor of 10 – 20. This additional pion rejection capabilities will on one side augment the measurement of low mass vector mesons ( $m_{ee} < m(\phi)$ ), but on the other side will be essential for the study of dielectrons in the intermediate mass region ( $m(\phi) < m_{ee} < m(J/\psi)$ ). This mass region is of particular interest, since it allows to access thermal radiation from the hot and dense medium created in heavy-ion collisions. A systematic study of the thermal dilepton component as a function of centre-of-mass energy will thus provide very important information relevant for the characterization of the strongly interacting medium, especially since this observable covers the whole time evolution of the system. Without the addition of a TRD to the CBM setup this physics will not be accessible and therefore this observable defines the main physics case for the TRD. Due to its capability to identify electrons at high momenta, the TRD will also allow for a clean measurement of the  $J/\psi$  in proton-nucleus, and potentially also in nucleus-nucleus collisions at the SIS100. Finally, photons can be detected via their conversion into  $e^+e^-$ -pairs in the detector material. This measurement will also significantly benefit from the additional electron identification provided by the TRD.

Another important contribution of the TRD to the CBM physics program arises from the possibility to support the identification of nuclear fragments via the measurement of their specific energy loss inside the TRD detector gas. This provides essential informations in addition

to what is accessible with the TOF detector system and will be important for the detection of hyper- and anti-nuclei. In particular, the TRD will allow to differentiate between  $Z = 1$  and  $Z = 2$  fragments (e.g.  $d$  and  ${}^4\text{He}$ ), which cannot be separated via a time-of-flight measurement alone.

In summary, the TRD is therefore being designed for the following main physics observables:

- **Intermediate mass dileptons:** dileptons in the mass range between the  $\phi$  and the  $J/\psi$  meson can provide access to thermal radiation from the hot and dense fireball and thus convey unique information on its properties and time evolution.
- **Fragments:** the measurement of nuclear fragments is essential for the study of hyper- and anti-nuclei.
- **Quarkonia:** quarkonia states, such as the  $J/\psi$  meson, are probes for the presence of deconfined matter, since free color charges can screen the  $c\bar{c}$ -potential and thus reduce the production rates of these particles (“ $J/\psi$ -suppression”).
- **Low mass vector mesons:** the measurement of these mesons provides informations on medium induced modification of the hadron spectral functions and is thus essential for understanding of the chiral phase transition and the origin of hadron masses.
- **Photons:** direct photons can provide information on the temperatures of the early stages in a heavy-ion collision. They can be measured via their conversion into dielectron pairs in the detector material.

A detailed discussion of the performance of CBM with a TRD for the first three physics observables (intermediate mass dileptons, fragments and quarkonia) and collisions systems at the SIS100 can be found in the Chap. 3.

## 2.2 Design considerations

To fulfil the above listed physics objectives the design of the TRD for an operation at the SIS100 has to take the following considerations into account:

- **Pion rejection capability:** the required pion rejection dictates the number of detector layers needed in the TRD setup, as well as the thickness of the gas volume of the readout chambers and the choice of the radiator. For the physics program envisaged with the TRD, a pion suppression factor of 10 – 20 will be necessary.
- **Charged particle identification:** in order to be able to separate fragments with masses higher than the proton mass, a resolution in the energy loss measurement in the  $1/\beta^2$  region of better than 30% will be needed.
- **Tracking capabilities:** the TRD is supposed to ensure an efficient track matching between the STS and the TOF, since track mismatches would significantly deteriorate the particle identification capabilities, both of TRD and TOF. Also, the charge measurement by the TRD will be essential for a correct momentum determination of heavier fragments. In order to achieve a sufficient spatial space point resolution (around 300  $\mu\text{m}$ ), a correspondingly high pad granularity is required. This also minimizes the occupancy in the TRD. Furthermore, the material budget of the TRD should be kept minimal to keep the number of secondary particles produced in the TRD on an acceptable level.

- **Interaction rates:** in order to be able to cope with the high interaction rates and particle multiplicities, the signal collection in the TRD readout chambers should be sufficiently fast (signal collection times below  $0.3 \mu(\text{s})$ ). Therefore, the thickness of the gas volume is kept as low as possible without compromising the pion rejection capabilities. Furthermore, the pad granularity has to be adjusted such that the produced data rate is low enough for the front-end electronics to handle. The current design is optimized for interaction rates up to 10 MHz, as foreseen for observables as the  $J/\psi$ , and the corresponding charged particle multiplicities at the highest beam energy of the SIS100.
- **Tracking of muons:** it is foreseen to use the TRD as a tracking device together with the MUCH detector. In this setup no particle identification is needed. However, it needs to be ensured that the TRD acceptance matches the one of the MUCH in an optimal way.

To guarantee the required performance for the bulk of the measured tracks, we foresee for the SIS100 a baseline detector layout of four TRD layers. In combination with the RICH pion suppression factors of more than  $5 \cdot 10^3$  can be achieved, which is mandatory for the measurement of dileptons in the intermediate mass region and will in addition allow for an observation of  $J/\psi$  mesons in proton-nucleus reactions at SIS100 beam energies. The TRD will be composed of modules with only two different sizes (small:  $57 \times 57 \text{ cm}^2$ , large:  $95 \times 95 \text{ cm}^2$ ), which facilitates the readout chamber production. Also, the number of pad planes with different granularities has been optimized in a way that limits on one side the construction complexity, while on the other side it keeps the recorded hit rates per pad on a tolerable level. Simulations with a realistic overall material budget indicate that this can be achieved with six different pad plane configurations. The corresponding pad areas range between  $1 \text{ cm}^2$  and  $11 \text{ cm}^2$ . The readout chain will provide, in addition to the data transfer, an efficient online data reduction and feature extraction (e.g. digital filtering and online clustering). The TRD setup will also be movable along the beam direction so that its position can be adjusted to the MUCH detector, when the TRD is used as tracking station for the muon measurements.

It is foreseen that this TRD setup can easily be extended for an operation at the SIS300, where even higher pion suppression factors will be required. In the ultimate configuration the TRD will therefore consist of maximally ten layers, grouped into three stations (station 1: layers 1 – 4 as in the SIS100 setup, station 2: layers 5 – 8, station 3: layers 9 – 10). Therefore, the upgrade to the full setup will imply the addition of the stations 2 and 3 without modifications on the already available station 1.

## 2.3 Summary of TRD design parameters

The physics objectives, together with the design considerations detailed in this report, lead to a baseline design concept for the TRD. The following table summarizes its main parameters for the TRD setup at the SIS100:

Table 2.1: Synopsis of TRD design parameters (SIS100 setup)

Pseudo-rapidity coverage	$0.89 < \eta < 3.74$
Azimuthal coverage	$2\pi$
$z$ position	$4.1 \text{ m} < z < 5.9 \text{ m}$
Maximal height (station 1)	4.75 m
Maximal width (station 1)	6.65 m
Gas volume	$1.37 \text{ m}^3$
Total thickness of one layer	0.45 m
Number of stations	1
Number of layers	4
Total number of modules	200
Number of readout channels	287744
Dimension of large module	$95 \times 95 \text{ cm}^2$
Dimension of small module	$57 \times 57 \text{ cm}^2$
Average pad size	$3.97 \text{ cm}^2$
Detector active area	$114 \text{ m}^2$
Radiator thickness	30 cm per layer
Detector radiation length	$< 4.2\% X_0$ per layer
Detector gas	Xe (85%), CO <sub>2</sub> (15%) Ar (80%), CO <sub>2</sub> (20%)
Depth of amplification region	7 mm
Depth of drift region	5 mm
Drift field	100 V/mm
Max. signal collection time	0.3 $\mu\text{s}$
Typical space point resolution at $p = 1 \text{ GeV}/c$	$\sim 300 \mu\text{m}$
Pion suppression at 90% electron efficiency and $p \geq 1.5 \text{ GeV}/c$	10 – 20
$dE/dx$ resolution above $p = 1 \text{ GeV}/c$	$\sim 25\%$

## Chapter 3

# Physics Performance at SIS100

In the following we discuss the performance of CBM at the SIS100 for several physics observables which require the addition of the TRD to the experimental setup. The main focus of these studies lies on the measurement of dielectrons in the Intermediate Mass Range (IMR) in Au + Au collisions, which can only be accessed with the electron identification capabilities of the TRD. Also, the performance for measuring  $J/\psi$  mesons in proton-nucleus collisions is presented. Finally, the contribution of the TRD to the identification of fragments by exploiting their measured energy loss is discussed.

### 3.1 Simulation setup

The simulations presented in the following were performed within the CBMROOT framework, which is based on the object-oriented C++ ROOT software environment [BR97]. CBMROOT supports several external particle generators and transport algorithms, such as GEANT3 [B<sup>+</sup>87], GEANT4 [A<sup>+</sup>03] or FLUKA [B<sup>+</sup>07], without the need for a change in the user code. It features detailed descriptions of the geometries and responses of the CBM sub-detectors and therefore allows for a realistic study of the CBM performance for different physics observables. The overall CBM detector setup used here includes, apart from the TRD, also MVD, STS, RICH, and TOF, as well as the beam pipe and the magnet. In the following studies the particles are propagated through the CBM detector model using the transport code GEANT3.

#### 3.1.1 Geometries

For the TRD the four layer SIS100 geometry, arranged in one detector station, is used, as described in Chap. 4 and as implemented in the simulation software (see e.g. Fig. 4.4). The details of the simulation of the TRD response are given in Chap. 9. For the following studies the full simulation chain, including digitization and clustering, was used (see Sect. 9.2). The artificial neural network (ANN) was employed for the electron identification (see Sect. 9.3.2).

The STS detector is composed of eight tracking stations equidistantly positioned between 30 cm and 100 cm downstream of the target. Each station comprises double-sided silicon strip sensors of 300  $\mu\text{m}$  thickness with a 58  $\mu\text{m}$  pitch of the strips. The detector simulation includes the complete chain of physical processes caused by a charged particle traversing the detector, from charge creation in the silicon to the digital output signals. Signal sharing between strips together with charge collection inefficiency, Lorentz shift due to the presence of the magnetic field, channel dead time, and single-channel inefficiency are taken into account.

For the RICH detector a setup is used which includes a mirror with a tilt of  $10^\circ$ , mounted on a carbon support structure combined with a grid of aluminum tubes. The multi-anode photomultipliers (MAPT) are mounted inside two steel boxes that shield them from the magnetic

stray field. The simulated detector response describes MAPT photon detectors of the type Hamamatsu H8500-03 with a UV window. Their quantum efficiency, the effect of cross talk between neighboring pixels and noise pixels are taken into account here. A realistic description of the mirror reflectivity and inhomogeneity is implemented as detailed in [H<sup>+</sup>13].

The TOF geometry used in these simulations is describing the setup intended for dielectron measurements at SIS100, which is positioned at a distance to the target of  $z = 10$  m. The simulations include a detailed modeling of the detector response.

An Au-target with a thickness of 25  $\mu\text{m}$  was chosen for these studies in order to keep the amount of conversions inside the target minimal.

### 3.1.2 Input to the simulations

As input to the simulation studies Au + Au events (10% most central, i.e. impact parameter  $b < 4.65$  fm) at a beam energy of 8 AGeV or minimum bias p + Au events at 30 GeV, both generated with the UrQMD model [B<sup>+</sup>98], were used. These UrQMD events provide the hadronic background events with a realistic multiplicity of particles into which the considered signals are embedded.

To study the CBM performance with respect to intermediate mass dileptons, a corresponding signal has been added to the UrQMD background events described above. This signal is composed of a cocktail of low mass vector mesons ( $\rho^0$ ,  $\omega$ ,  $\omega$ -Dalitz, and  $\phi$ ), the  $J/\psi$  and thermal radiation from the hadronic and partonic medium and is generated with the PLUTO event generator [F<sup>+</sup>07]. The decay of the  $J/\psi$  is performed with the EVTGEN package [Lan01], using the PHOTOS model [EZ94], to include the effect of final state radiation. This introduces, together with bremsstrahlung in the detector material, a tail towards lower masses in the reconstructed  $J/\psi$  signal distribution.

In order to accumulate sufficient statistics the dielectron signals were generated with a yield of one pair per event for each dielectron source. After reconstruction the dielectron pairs were rescaled according to the yields expected from their corresponding source (see Tab. 3.1). In case of the low mass vector mesons and of the  $J/\psi$  the yields were adjusted following the predictions of the HSD model [CB99]. The yields of the thermal components are chosen as predicted by the MC approach described in [Sec15, G<sup>+</sup>16]. This model, which also calculates the mass dependence of the thermal dielectron components, is based on a coarse grained transport model calculation to extract the space-time evolution of the local temperatures and baryo-chemical potentials and uses the parametrized spectral functions provided by [RWvH10].

The simulations performed to investigate the TRD performance in terms of fragment identification are also based on the 10% most central Au + Au events at 8 AGeV generated with UrQMD. To this background events fragments of the type d, t,  $^3\text{He}$ , and  $^4\text{He}$  have been added. These were generated with a flat  $p_t$  distribution between  $0 < p_t < 3$  GeV/ $c$  and a rate of one particle per event to obtain sufficient statistics.

### 3.1.3 Reconstruction

The simulated events were reconstructed with the standard reconstruction algorithms as described in detail in Sect. 9.3.

In the analysis of the simulated events the following selection criteria were applied to the reconstructed tracks: they should be inside the geometrical acceptance of the RICH detector, have an associated MC hit in the TRD ( $N_{\text{MCHit}}^{\text{TRD}} > 0$ ) and a transverse momentum of  $p_t > 200$  MeV/ $c$ . To guarantee a sufficient reconstruction quality the track was in addition required to have at least one hit in the MVD, more than three hits in MVD and STS combined, and a primary vertex fit with  $\chi^2/\text{ndf} < 3$ .

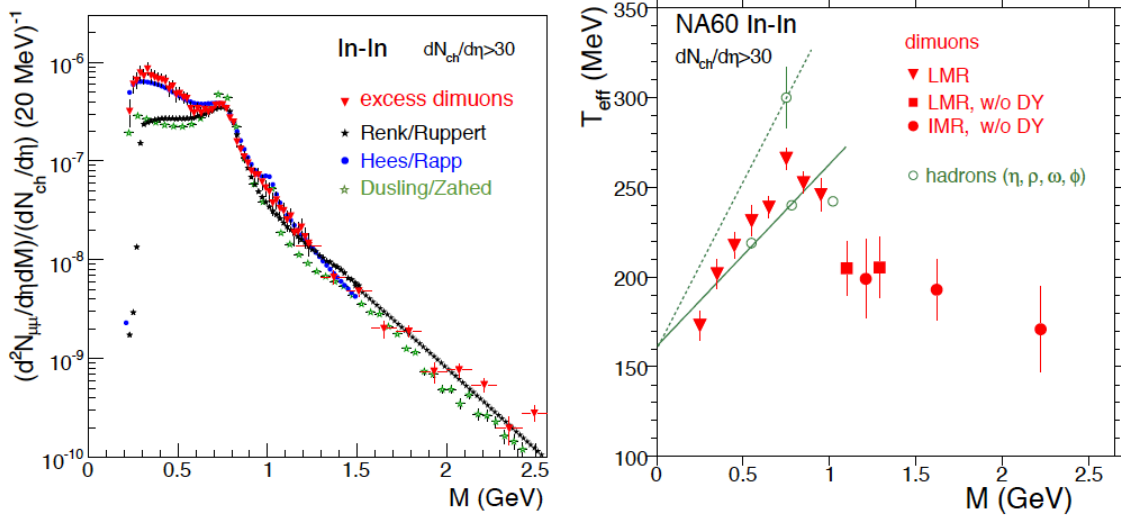


Figure 3.1: Left panel:  $p_t$  integrated invariant mass spectrum of excess dimuons as measured by NA60 for In+In collisions at 158 AGeV. The data are compared to several thermal model calculations. Right panel: The inverse slope parameter  $T_{\text{eff}}$  of the dimuon  $m_t$  spectra as a function of their invariant mass. The figures are taken from [Spe10].

Source	$BR_{e^+e^-}$	Total multiplicities	
		p + Au	Au + Au
$\rho^0$	$4.72 \cdot 10^{-5}$	$3.4 \cdot 10^{-3}$	9.0
$\omega$	$7.28 \cdot 10^{-4}$	$5.7 \cdot 10^{-3}$	19.0
$\phi$	$2.97 \cdot 10^{-4}$	$1.7 \cdot 10^{-4}$	0.12
$J/\psi(1S)$	$5.97 \cdot 10^{-2}$	$5.1 \cdot 10^{-8}$	—
$\psi(2S)$	$7.89 \cdot 10^{-3}$	$1.3 \cdot 10^{-9}$	—
In-medium radiation	—	—	$2.2 \cdot 10^{-2}$
QGP radiation	—	—	$5.8 \cdot 10^{-3}$

Table 3.1: Input multiplicities ( $4\pi$ ) and the corresponding branching ratios for the dielectron decay as used in the p + Au and Au + Au simulations (see text for details).

Electron identification is performed by requiring a 90% efficiency on the output of the ANN applied to the RICH data, with an additional cut on the number of reconstructed hits in the RICH of  $N_{\text{hit}}^{\text{RICH}} \geq 6$ . The same condition on the electron efficiency is applied to the TRD-ANN output, while here for the minimum number of reconstructed hits the criterion  $N_{\text{hit}}^{\text{TRD}} \geq 3$  is used.

## 3.2 Intermediate mass dileptons

The intermediate mass range between the masses of the  $\phi$  and the  $J/\psi$  meson is of particular interest in heavy-ion physics. At lower centre-of-mass energies, where charm production is not dominant, this range provides a direct access to dileptons originating from thermal sources. At SPS energies this kind of measurement has been performed already by the NA60 collaboration, which has extracted the inverse slope parameter  $T_{\text{eff}}$  from dimuon pairs in the mass range above 1 GeV/ $c^2$  in In+In collisions at 158 AGeV [A<sup>+</sup>09].  $T_{\text{eff}}$  was found to be in the range 170 – 200 MeV

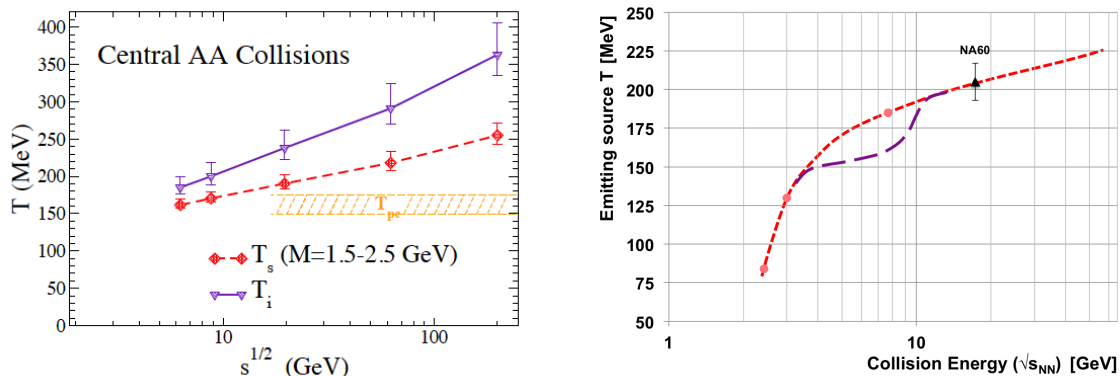


Figure 3.2: Left panel: excitation function of the inverse slope parameter for IMR dileptons (here denoted as  $T_s$ ) in the mass range  $1.5 < m_{ee} < 2.5 \text{ GeV}/c^2$  (diamond symbols) as calculated by [RvH16]. This is compared to the initial temperature  $T_i$  of the system (triangles) and the pseudo-critical temperature  $T_{pc}$  (hatched band). Right panel: excitation function of  $T_{\text{eff}}$  as calculated with a coarse-graining approach (dotted red curve) [G<sup>+</sup>16]. The dashed violet line corresponds to a hypothetical energy dependence in the presence of a first order phase transition. Also shown is the value by NA60 [Spe10]. The figure is taken from [C<sup>+</sup>16].

and thus indicated a non-hadronic origin, since other components such as Drell-Yan and semi-leptonic decays of open charm mesons are negligible at these energies (see right panel of Fig. 3.1). The corresponding invariant mass distribution of excess dimuons is shown in the left panel of Fig. 3.1, together with several thermal model calculations [Spe10].

This kind of measurement is unique, since it allows to study the thermal properties of the early stages of the produced medium and is also sensitive to the thermal radiation from a QGP phase. A systematic study of the energy dependence of  $T_{\text{eff}}$  in the IMR towards lower energies can therefore provide information on the onset of partonic thermal radiation and might allow to locate the phase boundary. This is illustrated in the left panel of Fig. 3.2, which shows the energy dependence of the inverse slope parameter of IMR dileptons as calculated by [RvH16] for  $\sqrt{s_{NN}} > 6 \text{ GeV}$ . While at these higher energies a clear signature of thermal QGP radiation is expected, with temperatures above the pseudo-critical ( $T_{pc}$ ) and relatively close to initial temperature ( $T_i$ ), at lower energies the situation is still quite open. As pointed out in [C<sup>+</sup>16, Gal14, RvH16] this energy range is therefore of particular interest, since it allows to map out the transition regime between partonic and hadronic matter. The presence of a first order phase transition might reveal itself as a flattening in the energy dependence of  $T_{\text{eff}}$  extracted from IMR dileptons as a consequence of a latent heat at the phase boundary. This is illustrated in the right panel of Fig. 3.2, where the dashed violet curve depicts the possible energy dependence in the presence of a first order phase transition.

### 3.2.1 Pion suppression in the IMR

Following from the above, it is obviously essential for the CBM physics program to be able to address dilepton measurements in the IMR. The dielectron channel will be important in this context, since it allows to measure also the low  $p_t$  region with high accuracy. In addition, it will enable the correlation of a dielectron measurement with other hadronic observables measured for the same event. However, for a dielectron study in the IMR it will be mandatory to achieve a sufficient pion suppression also at electron momenta higher than those accessible with the RICH

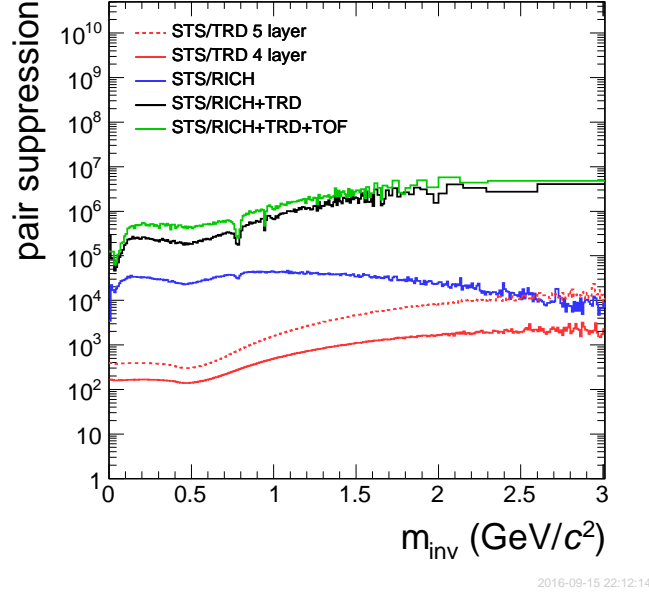


Figure 3.3: The suppression factor obtained for opposite-sign pairs as a function of the invariant mass of opposite-sign pairs measured with different detector combinations (red: TRD alone, blue: RICH alone, black: RICH and TRD, green: RICH, TRD and TOF). In addition, also the values for a TRD configuration with an additional fifth layer is shown (dashed red line). All curves are obtained for the dielectron cocktail (see text for details) in central Au + Au collisions at 8 AGeV.

alone. As illustrated in the right panel of Fig. 9.13, the RICH is effective for momenta only up to 5 – 6 GeV/c. To identify electrons at higher momenta the TRD will have to supply additional information. In fact, the electron identification for  $p \geq 7$  GeV/c is effectively only provided by the TRD. As can be seen from Fig. 3.3, this additional pion suppression is particularly important for pair combinations in the higher mass region above  $m_{ee} > 2$  GeV/c<sup>2</sup>, where it approaches the one obtainable by the RICH detector alone. The TRD will of course also enhance the electron identification capabilities of CBM in the low mass region as well and will thus augment the RICH measurement of low mass vector mesons by providing an important safety margin in the case of detector inefficiencies.

For the TRD two alternative scenarios have been evaluated. In addition to the standard configuration, which is composed of four detector layers, a second geometry has been evaluated that includes an additional fifth layer, identical to the four others. A five layer TRD naturally provides a higher pion suppression factor (see Fig. 9.13 and Tab. 9.1) and would in case of the simulation cocktail analyzed here even exceed suppression achieved by the RICH detector alone for masses above 2.5 GeV/c<sup>2</sup>. However, since the addition of an additional detector layer would substantially increase the overall cost of the project (roughly by 25%), it is important to assess whether it is really mandatory to achieve the main physics goals (i.e. the measurement of dielectrons in the IMR and the extraction of their inverse slope parameter).

### 3.2.2 Dielectron reconstruction in the IMR

The reconstruction of dielectrons proceeds by combining unlike-sign pairs of electron candidates, as identified with the TRD, RICH and TOF. In the case of the TRD, track with  $N_{\text{hits}}^{\text{TRD}} \geq 3$  are accepted and a momentum independent electron efficiency of 80% was applied, corresponding to a pion suppression factor of  $\sim 50$  for  $p > 8$  GeV/c (see also Fig. 9.13 and Tab. 9.13). Since

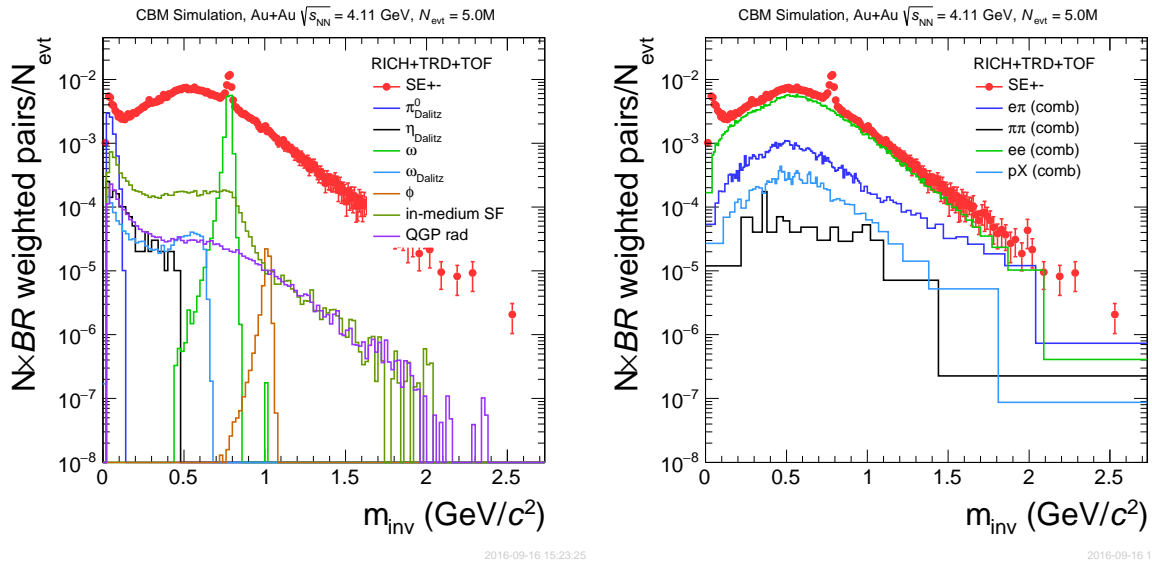


Figure 3.4: The total reconstructed invariant mass distribution of unlike-sign electron pairs as identified by the combination of RICH, TRD (standard configuration with four layers) and TOF for  $5 \times 10^6$  most central (10%) Au + Au collisions at 8 AGeV. The different direct dielectron sources ( $\pi^0$ -Dalitz,  $\eta$ -Dalitz,  $\omega$ ,  $\omega$ -Dalitz,  $\phi$ , and thermal radiation) are shown on the left panel together with the total invariant mass spectrum including the combinatorial background (red dots). The right panel shows different components of the combinatorial background ( $e\pi$ ,  $\pi\pi$ ,  $ee$  and  $pX$ ). All contributions are weighted according to their expected yield and the corresponding branching ratios (see Tab. 3.1).

a large fraction of electrons and positrons originate from the conversion of photons inside the target and the following material, algorithms aiming at a suppression of this contribution need to be applied. For this purpose all electron candidates were combined into unlike-sign pairs and rejected, if any of these pairs resulted in an invariant mass below  $25 \text{ MeV}/c^2$ . In order include as many potential candidates as possible in the procedure, the identification of these electron candidates is using criteria that are more relaxed than the ones applied to the electron candidates for the final invariant mass spectra. Here, the identification is always using RICH, while the TRD is only applied for tracks with  $N_{\text{hits}}^{\text{TRD}} \geq 3$  (i.e. tracks with  $N_{\text{hits}}^{\text{TRD}} < 3$  are accepted without additional TRD identification) and the TOF is not used at all.

The reconstructed final invariant mass distributions of the various components of unlike-sign electron pairs are shown in Fig. 3.4. They are weighted according to the expected yields as described above (see Tab. 3.1) and multiplied by the corresponding branching ratios. Apart from the direct contributions ( $\pi^0$ -Dalitz,  $\eta$ -Dalitz,  $\omega$ ,  $\omega$ -Dalitz,  $\phi$  and thermal radiation, left panel) also the background resulting from combinations between real electrons and misidentified pions ( $e\pi$ ,  $\pi\pi$ ,  $ee$  and  $pX$ , right panel) is shown.

Mass range	$S/B$ 4 layers	$S/B$ 5 layers
$> 1 \text{ GeV}/c^2$	$(1.4 \pm 0.3) \cdot 10^{-2}$	$(1.6 \pm 0.2) \cdot 10^{-2}$
$1.0 - 1.1 \text{ GeV}/c^2$	$(1.8 \pm 0.5) \cdot 10^{-2}$	$(1.9 \pm 0.4) \cdot 10^{-2}$
$1.2 - 2.0 \text{ GeV}/c^2$	$(1.2 \pm 0.4) \cdot 10^{-2}$	$(1.4 \pm 0.3) \cdot 10^{-2}$

Table 3.2: The signal-to-background ratios  $S/B$  for a dielectron measurement in the IMR in central Au + Au collisions at 8 AGeV for a four and five layer configuration.

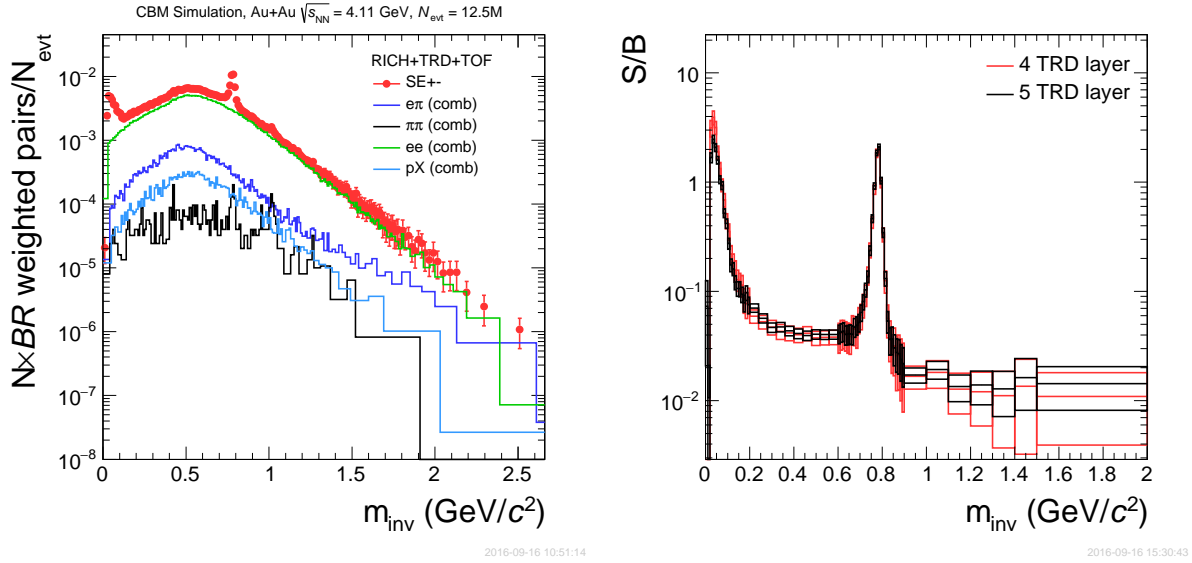


Figure 3.5: Left panel: the total reconstructed invariant mass distribution of unlike-sign electron pairs as identified by the combination of RICH, TRD (modified configuration with five layers) and TOF for  $12.5 \times 10^6$  most central (10%) Au + Au collisions at 8 AGeV, together with the different components of the combinatorial background ( $e\pi$ ,  $\pi\pi$ ,  $ee$  and  $pX$ ). Right panel: the signal-to-background ratio as a function of the invariant mass of the unlike-sign dielectron pairs calculated for two TRD configurations (four and five detector layers) for  $5 \times 10^6$ , resp.  $12.5 \times 10^6$ , central (10%) Au + Au events at 8 AGeV.

The default TRD setup (i.e. four detector layers) results in a pion suppression that is sufficient to reduce the  $\pi\pi$ -component (i.e. remaining pions misidentified as electrons) in the combinatorial background to the same level as the thermal component in the signal above  $m_{\text{inv}} = 1 \text{ GeV}/c^2$ , but is still clearly below the remaining  $e\pi$  combinatorics. The overall signal-to-background ratio for  $5 \times 10^6$  central Au + Au events at 8 AGeV is shown in the right panel Fig. 3.5 and summarized in Tab. 3.2 for the two different TRD configurations. The standard TRD setup with four detector layers will result in a  $S/B$ -ratio which varies between  $\sim 1.8 \cdot 10^{-2}$  in the mass range  $1.0 - 1.1 \text{ GeV}/c^2$  and  $\sim 1.2 \cdot 10^{-2}$  for  $1.2 - 2.0 \text{ GeV}/c^2$ . With a five layer TRD setup and the correspondingly higher pion suppression factors (see Tab. 9.13) the  $S/B$ -ratio is slightly larger in the higher mass regions, while around  $m_{\text{inv}} = 1 \text{ GeV}/c^2$  no significant difference is seen. The difference between four and five layers in the high mass region is mainly due to the fact that the  $e\pi$  component is somewhat reduced. While for the four layer TRD it is above  $m_{\text{inv}} > 1.8 \text{ GeV}/c^2$  on the same level than the irreducible  $ee$  component (see right panel of Fig. 3.4), a five layer TRD is able to reduce the  $e\pi$ -part by roughly a factor two (see left panel of Fig. 3.5). However, since the  $ee$  component is independent on the electron identification performance and always the dominating background contribution in the IMR, the  $S/B$  ratio changes only slightly when adding another TRD layer. Thus we conclude that a setup with four TRD layers will be sufficient to address a measurement of IMR dielectrons at these energies. This configuration is therefore chosen as the baseline design for the TRD at SIS100.

Before extracting the signal in the mass range of the thermal component, the combinatorial background has to be carefully determined with a mixed event technique and subtracted. In the case of a small signal-to-background ratio this procedure will introduce a systematic uncertainty. This uncertainty on the combinatorial background will be the dominant systematic effect and propagates into the systematic uncertainty of the extracted signal as  $\delta_{\text{sys}}(S)/S = \delta_{\text{sys}}(B)/B/(S/B)$ . A conservative assumption on the background assumption is  $\delta_{\text{sys}}(B)/B \approx$

0.25 % [ $A^+10a$ ], however, it was demonstrated that a description of the combinatorial background in dielectron distributions on the level of  $\sim 0.1\%$  is achievable without problems [Boo14]. In the latter case a  $S/B$ -ratio of  $10^{-2}$  ( $2 \cdot 10^{-2}$ ) would correspond to a systematic error of 10 % (5 %). It should therefore be possible to extract the thermal dielectron component with good significance.

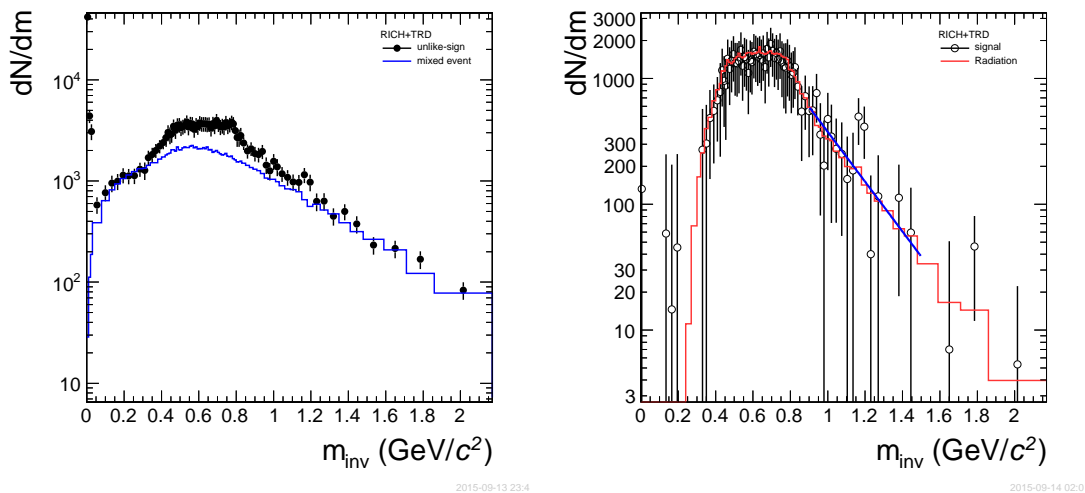


Figure 3.6: Left panel: The invariant mass distribution of unlike-sign electron pairs (symbols) as identified by the combination of RICH and TRD (four layers) for minimum bias Au + Au collisions at 8 AGeV, together with the combinatorial background evaluated with the mixed event technique (solid line). In this simulation the  $S/B$  ratio has been increased to values around  $\sim 0.2$ . Right panel: The remaining signal distribution after subtraction of the combinatorial background (symbols). The simulated thermal component is shown in comparison (red solid line). The result of an exponential fit to the IMR ( $0.9 < m_{\text{inv}} < 1.5 \text{ GeV}/c^2$ ) is displayed as the blue solid line.

The huge number of events, which is required to perform a full analysis of the thermal dielectron spectrum at the expected  $S/B$  ratio, and the corresponding requirements in terms of CPU time and storage space make such a study on MC events in the full simulation framework impossible. In order to determine the needed significance of the signal component, and thus be able to estimate the required event statistics, a simulation with an artificially enhanced  $S/B$  ratio was performed, see Fig. 3.6. In this case minimum bias Au + Au events at 8 AGeV from UrQMD were used as background, while the yield of the dielectron signal components was increased such that a  $S/B$  ratio of  $\sim 0.2$  for  $m_{\text{inv}} > 1 \text{ GeV}/c^2$  results, i.e. higher by a factor of  $\sim 10$  compared to the realistic values given in Tab. 3.2. A data set of  $2.5 \cdot 10^6$  events in this scenario corresponds to a significance of  $S/\sqrt{S+B} \approx 3.5$ . The left panel of Fig. 3.6 shows the resulting invariant mass distribution of all unlike-sign electron pairs. Also included is the corresponding combinatorial background (shown as a solid line), as estimated with the mixed event technique. By subtracting the background the signal distribution, displayed in the right panel of Fig. 3.6, is obtained. This reconstructed signal distribution agrees very well with the distribution of thermal dielectrons that was used as input to the simulation procedure. The signal is fitted with an exponential function  $\propto \exp(-m_{\text{inv}}/T_{\text{eff}})$  in the IMR  $0.9 < m_{\text{inv}} < 1.5 \text{ GeV}/c^2$  in order to extract the inverse slope parameter  $T_{\text{eff}}$ . It is found to be  $T_{\text{eff}} = 216 \pm 64(\text{stat.}) \text{ MeV}$ , which agrees well with the inverse slope parameter of the MC input distribution of  $T_{\text{eff}}^{\text{MC}} = 230 \text{ MeV}$ . This demonstrates that the proposed analysis is feasible, if a corresponding significance in the region of  $\geq 10$  is achieved.

In the case of a realistic scenario, corresponding to the numbers given in Tab. 3.1 and as shown in Figs. 3.4 and 3.5, i.e. a  $S/B$  ratio of around  $10^{-2}$  and a signal per event of  $S/\text{evt.} \approx 6 \cdot 10^{-6}$ , about  $10^{10}$  central (10 %) Au + Au events at 8 AGeV will be needed to reach a significance of

$\geq 10$ , respectively  $10^{11}$  minimum bias events. Assuming an interaction rate of 1 MHz, this would translate into a measurement time of only  $\sim 30$  h.

### 3.3 $J/\psi$ mesons in proton-nucleus collisions

The measurement of  $J/\psi$  mesons is of prime importance in the field of heavy-ion physics, since their production rate is supposed to be modified by the presence of a deconfined state of matter [MS86]. While at high center-of-mass energies (SPS, RHIC, and LHC) a significant suppression of  $J/\psi$  in nucleus-nucleus collisions has been observed relative to the corresponding yield in pp-collisions, scaled by the number of binary nucleon-nucleon collisions [ $A^+05$ ,  $A^+11$ ,  $A^+14$ ], with a stronger suppression at SPS and RHIC than at the LHC, the evolution of this modification towards even lower energies is still unclear. In order to extend these measurements into these so far unexplored energy range via the dielectron channel with a sufficiently high signal-to-background ratio a good electron identification is required. Due to its high mass the  $J/\psi$  mesons decay into dielectrons of predominantly high momenta, so that the TRD will be necessary to suppress hadronic background in this region of phase space sufficiently well, where the RICH is no longer efficient.

The p+A collision system will provide an indispensable baseline for the interpretation of the heavy-ion data. It allows the investigation of cold nuclear matter effects which whose measurement is needed to quantify any non-trivial  $J/\psi$  suppression. It is therefore important to also be able to measure the  $J/\psi$  production in these more elementary reactions at all the relevant center-of-mass energies. This is especially true for very low energies just above threshold, where currently no precision data are existing. The SIS100 will make available proton beams up to 30 GeV beam energy, which can be exploited to perform these measurements.

#### 3.3.1 Reconstructed $J/\psi$ signal

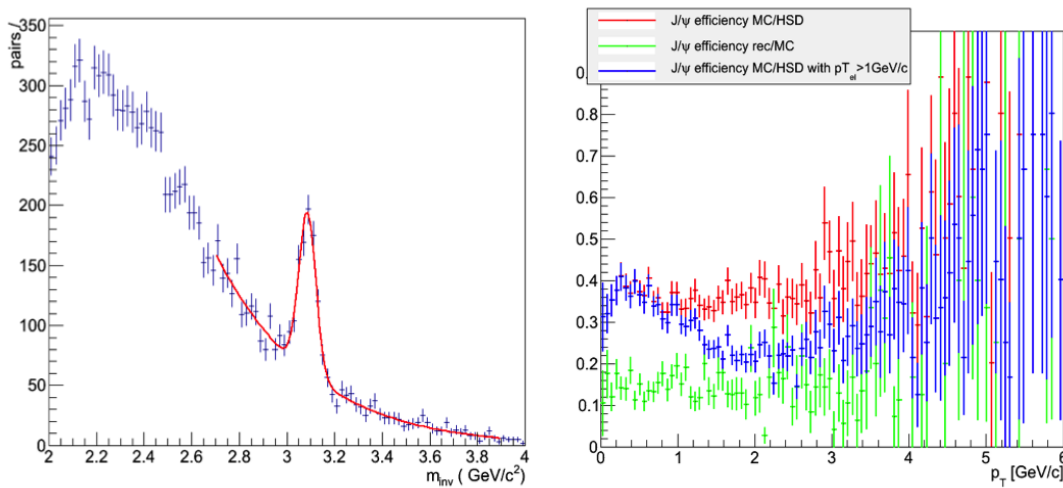


Figure 3.7: The invariant mass distribution of  $e^+e^-$  pairs in the  $J/\psi$  mass region in p + Au collisions at 30 GeV beam energy (left panel) measured with a four layer TRD. The right panel shows the corresponding total efficiency and acceptance as a function of the  $J/\psi$  transverse momentum.

Figure 3.7 shows in the left panel a simulated invariant mass distribution of electron-positron pairs for p + Au collisions at 30 GeV beam energy. As a generator for the signal distribution of  $J/\psi$  the HSD model has been used [CBS01], providing an input multiplicity per event of  $1.0 \cdot 10^{-8}$ . In this analysis all tracks were required to have at least five hits in the STS and three in the TRD and a minimum momentum of  $p_t > 1$  GeV/c. Electrons were identified using RICH and TRD information. The resulting distribution corresponds to  $2.5 \cdot 10^{13}$  collected events,

equivalent to about 30 days of data taking at an interaction rate of 10 MHz. A clean  $J/\psi$  signal over a moderate background can be observed with a  $S/B$  ratio around 1.25. Around 600  $J/\psi$  are reconstructed after background subtraction.

The right panel of Fig. 3.7 shows the acceptance and reconstruction efficiency for  $J/\psi$  mesons at 30 GeV. The red symbols represent the pure acceptance and is found to be around 35%. The introduction of the  $p_t$  cut on the electron tracks at 1 GeV/ $c$  lowers it to  $\sim 20\%$  above a  $J/\psi$   $p_t$  of 1.5 GeV/ $c$  (blue symbols). The inefficiencies of the reconstruction procedure cause a further reduction towards a value for the product of acceptance and efficiency of about 15% (green symbols), independent on the  $J/\psi$  transverse momentum.

### 3.4 Fragments

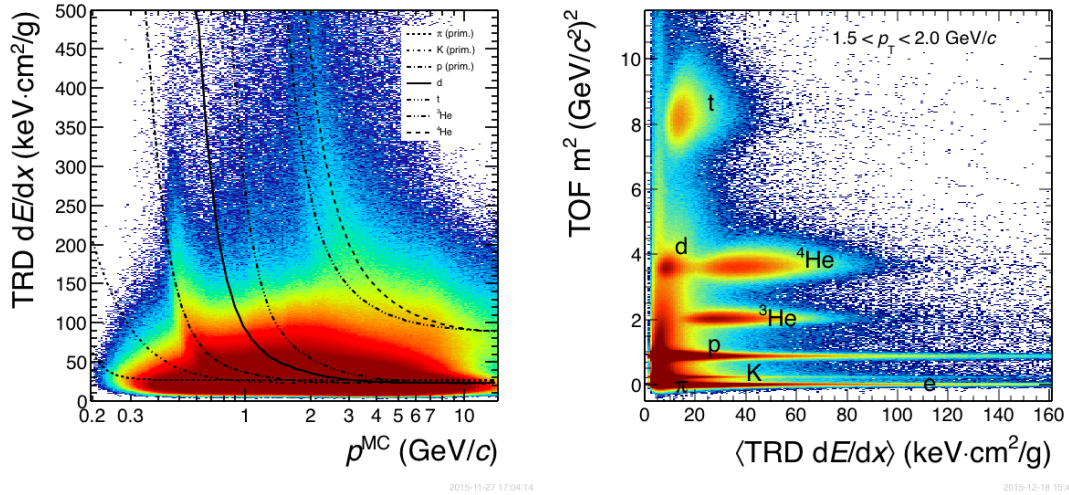


Figure 3.8: Left: The averaged  $\langle dE/dx \rangle$  signal as reconstructed with the TRD as a function of the true momentum  $p^{\text{MC}}$ . The lines depict the expectations for the different particle species. Right: Comparison of the TRD signal to the mass squared as measured by the TOF in central Au + Au collisions at 8 AGeV. Shown is the momentum interval  $1.5 < p < 2.0 \text{ GeV}/c$ , where  $p$  in this case is the reconstructed momentum.

In addition to its electron identification capabilities, the TRD will also be able to separate hadrons on the basis of a measurement of their specific energy loss  $dE/dx$ . This will extend the possibilities of the CBM experiment beyond what is accessible with a time-of-flight measurement alone. A general disadvantage of a hadron identification with the TOF detector alone is that it is not able to distinguish different charge states. E.g. the TOF detector will not be able to separate  $Z = 1$  and  $Z = 2$  fragments. Since the  $dE/dx$  measured in the TRD depends on  $Z^2$ , this additional information will allow for a separation of these states.

This is in particular crucial for the identification of double- $\Lambda$  hypernuclei, such as  ${}^6_{\Lambda\Lambda}\text{He}$ , whose decay chain  ${}^6_{\Lambda\Lambda}\text{He} \rightarrow {}^5_{\Lambda}\text{He} + p + \pi^-$ ,  ${}^5_{\Lambda}\text{He} \rightarrow {}^4\text{He} + p + \pi^-$  would be indistinguishable from the decay  ${}^3_{\Lambda}\text{He} \rightarrow d + p + \pi^-$  without the additional TRD information that allows the separation of  ${}^4\text{He}$  and deuterons. Therefore, the TRD will help to significantly extend the number of hypernuclei states accessible within the CBM physics program. As discussed in [C<sup>+</sup>16], a high statistics measurement of double- $\Lambda$  hypernuclei would represent a breakthrough in this field of physics, since up to now only very few double- $\Lambda$  hypernuclei events have been identified. The capability of identifying a substantial number of these exotic nuclei (e.g. around 60  ${}^6_{\Lambda\Lambda}\text{He}$  per week data taking are expected according to a statistical model prediction [ABMSS11]) will

open up new possibilities in studying the hyperon-nucleon and hyperon-hyperon interaction with unprecedented precision and thus will provide essential ingredients for the understanding of the structure of neutron stars.

### 3.4.1 Fragment identification via TRD- $dE/dx$

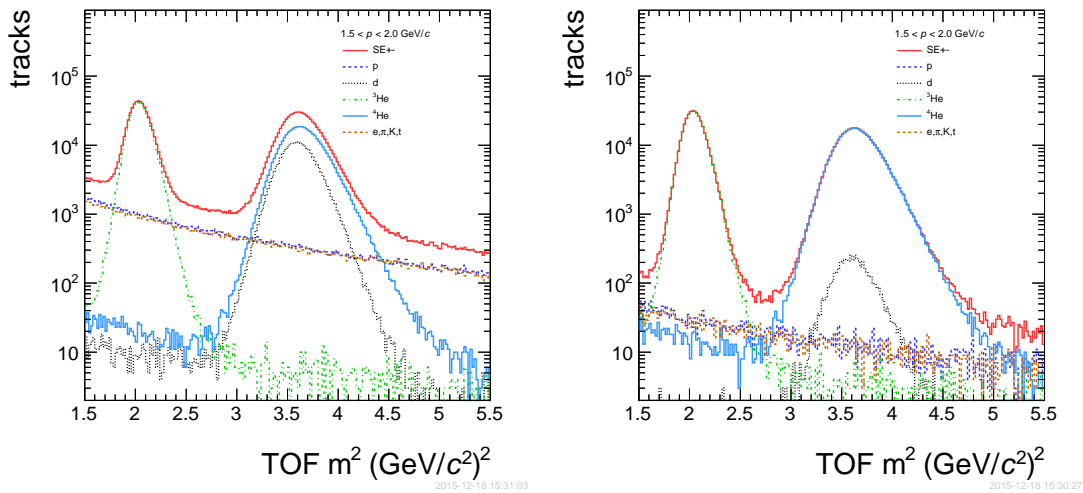


Figure 3.9: The  $m^2$  measurement provided by the TOF in the momentum interval  $1.5 < p < 2 \text{ GeV}/c$  and the mass region of heavy fragments without (left) and with TRD PID selection on  ${}^4\text{He}$  (right).

The TRD is able to provide up to four independent measurements of the specific energy loss of a charged particle in the four layers of Xe/CO<sub>2</sub> gas mixture<sup>1</sup>, as planned in the setup for the SIS100. The achievable  $dE/dx$  resolution will be sufficient to separate fragments in the  $1/\beta^2$  region of the Bethe-Bloch curve. Since  ${}^4\text{He}$  reach their minimum ionizing momentum only at  $p \sim 14 \text{ GeV}/c$ , this allows their identification over a large momentum range. The charge information obtained by the TRD- $dE/dx$  measurement can also be exploited in the tracking in order to determine the correct momentum for  $Z = 2$  particles.

The averaged  $\langle dE/dx \rangle$  signal measurable with a four layer TRD, requiring at least four reconstructed hits, is shown as a function of the true particle momentum in the left panel of Fig. 3.8. The different branches for protons, deuterons, tritons,  ${}^3\text{He}$  and  ${}^4\text{He}$  are clearly distinguishable above a minimum  $\langle dE/dx \rangle$ -value of around  $100 \text{ keV}\cdot\text{cm}^2/\text{g}$ . Figure 3.8 shows exemplary for the momentum interval  $1.5 < p < 2.0 \text{ GeV}/c$  how a unique identification of d and  ${}^4\text{He}$  can be performed by combining TOF and TRD information. Please note that here the reconstructed momentum is used, which in this case does not take into account the different fragment charges, such that the  $\langle dE/dx \rangle$  branches for, e.g., deuterons and  ${}^4\text{He}$  are moved closer in momentum. While the  $m^2$  measurement alone, as provided by TOF, does not allow to separate these two fragments, the addition of the TRD- $dE/dx$  signal results in a clear separation of the two. The energy loss measurement with the TRD also helps to reduce the background in the identification of other fragments, e.g. of  ${}^3\text{He}$ . As can be seen in the lower part of Fig. 3.8, the TOF signal alone is still affected by a background, resulting from wrong track matches, which can be separated by combining it with the TRD- $dE/dx$  information. This background rejection is illustrated in Fig. 3.9 in the TOF  $m^2$  spectrum by requiring a TRD- $dE/dx > 25 \text{ keV}\cdot\text{cm}^2/\text{g}$ .

<sup>1</sup>Alternatively, the TRD can be operated with a less expensive Ar/CO<sub>2</sub> gas mixture, if no electron identification is required in a special running scenario.

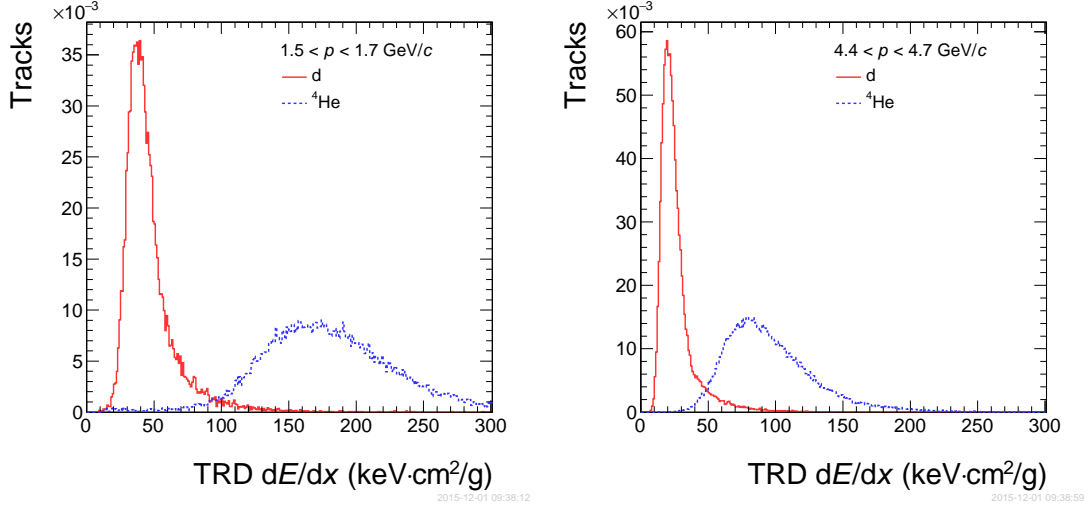


Figure 3.10: The averaged  $\langle dE/dx \rangle$  distributions for the fragments d and  ${}^4\text{He}$  as reconstructed with the TRD in central Au + Au collisions at 8 AGeV, requiring at least four measured hits. Shown are the reconstructed momentum intervals  $1.5 < p < 1.7 \text{ GeV}/c$  (left panel) and  $4.4 < p < 4.7 \text{ GeV}/c$  (right panel).

A suppression factor  $\sim 20$  can be achieved for deuterons in the region above  $p > 1.5 \text{ GeV}/c$ . TRD- $dE/dx$  might even be used to clean up the particle identification of lighter hadrons, such as protons and kaons.

The distributions of the averaged energy loss signal  $\langle dE/dx \rangle$  of deuterons and  ${}^4\text{He}$ , as reconstructed in the TRD for Au + Au collisions at 8 AGeV, is displayed in Fig. 3.10 for two different reconstructed momentum intervals. A clear separation of d and  ${}^4\text{He}$  is visible at both momentum ranges. By fitting these  $\langle dE/dx \rangle$  distributions with Gaussians the momentum dependence of the corresponding energy loss resolution  $\sigma(p)/(\langle dE/dx(p) \rangle)$  can be obtained, as shown in the left panel of Fig. 3.11. The typical  $dE/dx$  resolution achievable with a four layer TRD when requiring a measured hit in each of them, is around 25% above  $p = 1 \text{ GeV}/c$  and constant up to  $p = 15 \text{ GeV}/c$ . This can be translated into a separation power, defined for the particle species  $i$  and  $j$  as

$$S_{ij}(p) = \frac{\langle dE/dx \rangle_i(p) - \langle dE/dx \rangle_j(p)}{\sigma_i(p)}, \quad (3.1)$$

which is shown for deuterons and  ${}^4\text{He}$  in the right panel of Fig. 3.11. A separation of deuterons and  ${}^4\text{He}$  on a level of  $\sigma \gtrsim 2.5$  should therefore be possible in the whole accessible momentum range. The separation power can be improved even further in the lower momentum region, if the charge information can be taken into account in the momentum determination (blue diamonds in the right panel of Fig. 3.11). In this case a separation around  $\sigma \sim 4$  can be reached for a true momentum of  $p^{\text{MC}} = 2 \text{ GeV}/c$ .

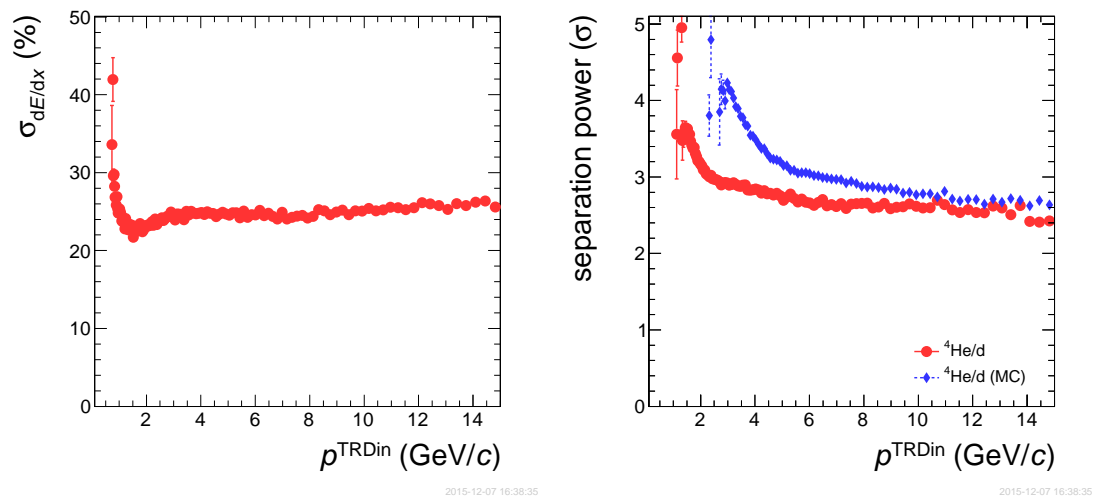


Figure 3.11: Left: The resolution of the averaged  $\langle dE/dx \rangle$  as a function of the particle momentum reconstructed with the TRD for the fragments d and  ${}^4\text{He}$  in central Au + Au collisions at 8 AGeV, requiring at least four measured hits. Right: The corresponding separation power for deuterons and  ${}^4\text{He}$  as a function of the reconstructed (red dots) and the true MC (blue diamonds) momentum.

## Chapter 4

# The Transition Radiation Detector

In the following we outline the design for the CBM-TRD as it is foreseen for the various experimental setups of CBM at the SIS100. The configuration described here is based on a well established and robust readout chamber design (see Chap. 5), which fulfills the performance parameters outlined in Sect. 2.2. In the course of the R&D program for the CBM-TRD also other design options have been thoroughly investigated (see Chap. 12). These can therefore provide alternative solutions, if it still turns out that not all design criteria can be met with the setup described in this chapter.

Another important aspect of the current design is its modularity and the reduction of the number of different components to a minimum. This facilitates mass production and allows for a flexible configuration of the detector geometry.

### 4.1 Working principle

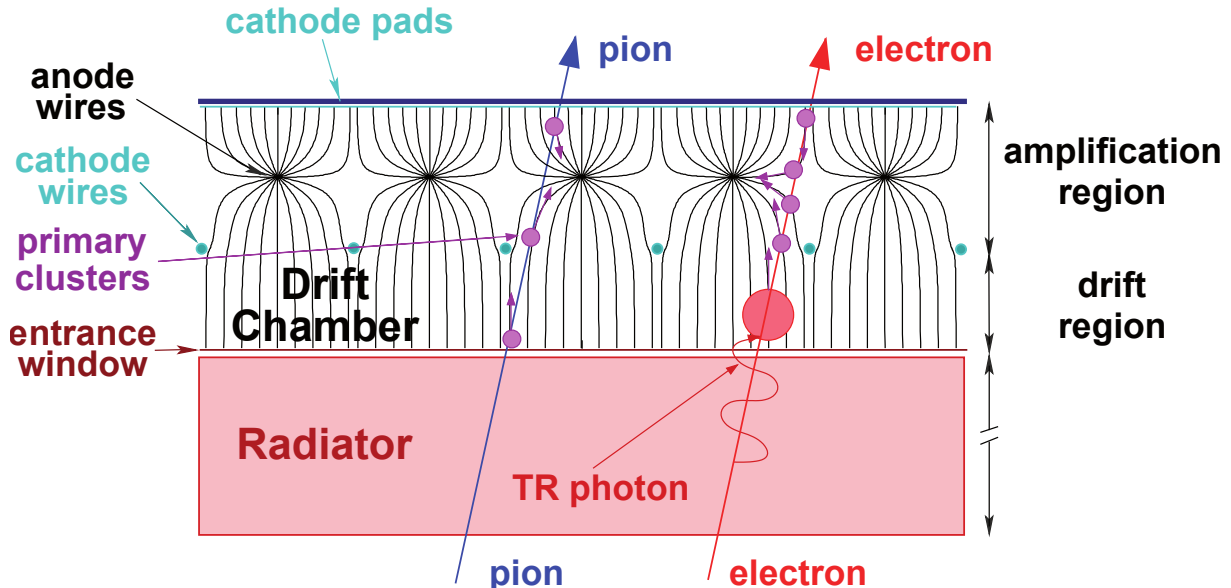


Figure 4.1: A schematic illustration of the working principle of the CBM-TRD.

The basic working principle of the CBM-TRD is illustrated in Fig. 4.1. The detector is essentially composed of two parts, the Read-Out Chamber (ROC) and the radiator. Transition Radiation (TR) photons are generated in the radiator by electrons with a given probability, while the heavier pions, being too slow, pass through without producing any TR. In order to efficiently

absorb the TR-photons in the gas volume of the ROC, a xenon gas mixture, having a high absorption cross section for photons in the TR spectral range, is used as a counting gas. Thus, the TR-photon is predominantly absorbed in the region directly behind the entrance window. On top of the TR-signal, the ROCs also collect the charge released via the specific energy loss ( $dE/dx$ ) due to the primary ionization processes in the gas. Differences in the  $dE/dx$  between electrons and pions additionally enhance the separation power between the two and also extend the electron identification towards lower  $p_t$  where no TR-photons are produced. Furthermore, the  $dE/dx$  measurement can be used to support the identification of nuclear fragments.

## 4.2 Design optimization

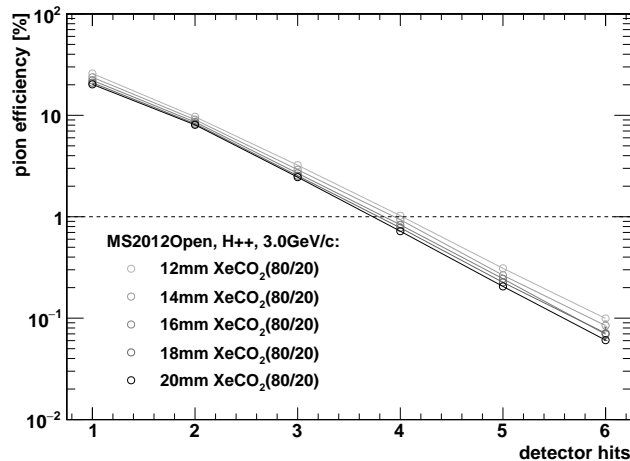


Figure 4.2: Pion efficiency at 90 % electron efficiency as a function of the gas gap thickness, filled with Xe/CO<sub>2</sub>(80/20), for different number of TRD layers.

The layout of the CBM-TRD has been optimized based on results from test beam measurements in 2012. The measured electron and pion energy loss spectra have been used to estimate the full system performance as a function of the number of detector layers and the total thickness of the Xe/CO<sub>2</sub> gas volume as presented in Fig. 4.2 for an extended version of the default radiator solution H, labelled H++ (see also Sect. 6). The simulated  $dE/dx$  spectra have been tuned to in-beam test results measured in 2012 with a TRD prototype comprising a 12 mm thick gas gap. Increasing the thickness further by additional 10 mm leads to a very moderate improvement of the pion suppression. However, regarding the fact that this also causes a significant increase in signal collection time (see Fig. 4.3) this is not a viable option in a high counting rate environment. The values presented here have been estimated using GARFIELD simulations [Vee98].

By building additional two detector layers the pion suppression factor could be increased by one order of magnitude. To keep the projectivity of the TRD geometry, the additional layers have to be larger compared to the four planned ones. This would increase the required finance budget by roughly a factor of two. Also, the increase in the material budget would enlarge the background from secondary particles seen by the TOF. Therefore, a four layer TRD detector with a gas thicknesses of 12 mm, subdivided into 7 mm amplification and 5 mm drift regions, has been identified as the best compromise with respect to material budget, costs and detector performance and is described in the following

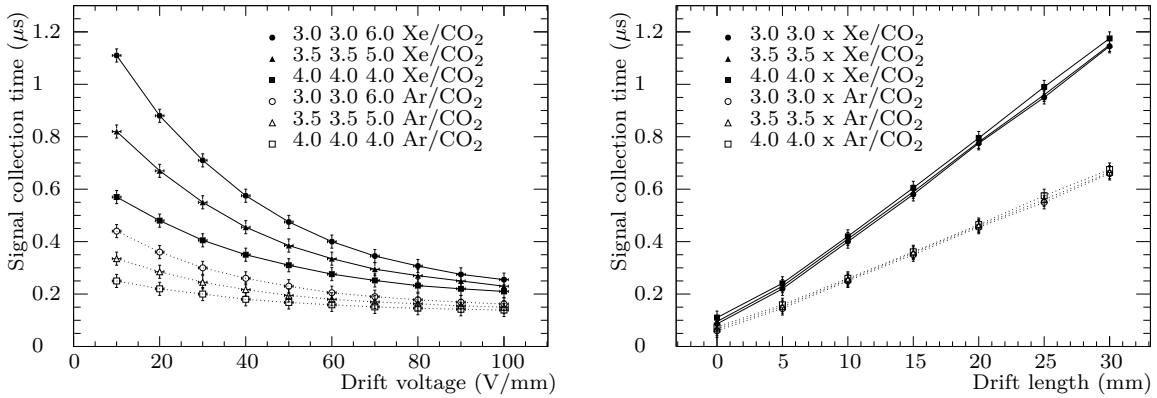


Figure 4.3: Signal collection time for a simulated electron signal as calculated with GARFIELD. Data for Xe/CO<sub>2</sub> (80/20) are represented by filled symbols and for Ar/CO<sub>2</sub> (80/20) by open symbols. An anode voltage of 1675 V is applied for 3.0 3.0  $x$  geometries, 1800 V for 3.5 3.5  $x$  geometries, and 1925 V for 4.0 4.0  $x$  geometries. The drift voltage scan is shown on the left and the drift length scan at 100 V/mm on the right hand side.

### 4.3 TRD station layout

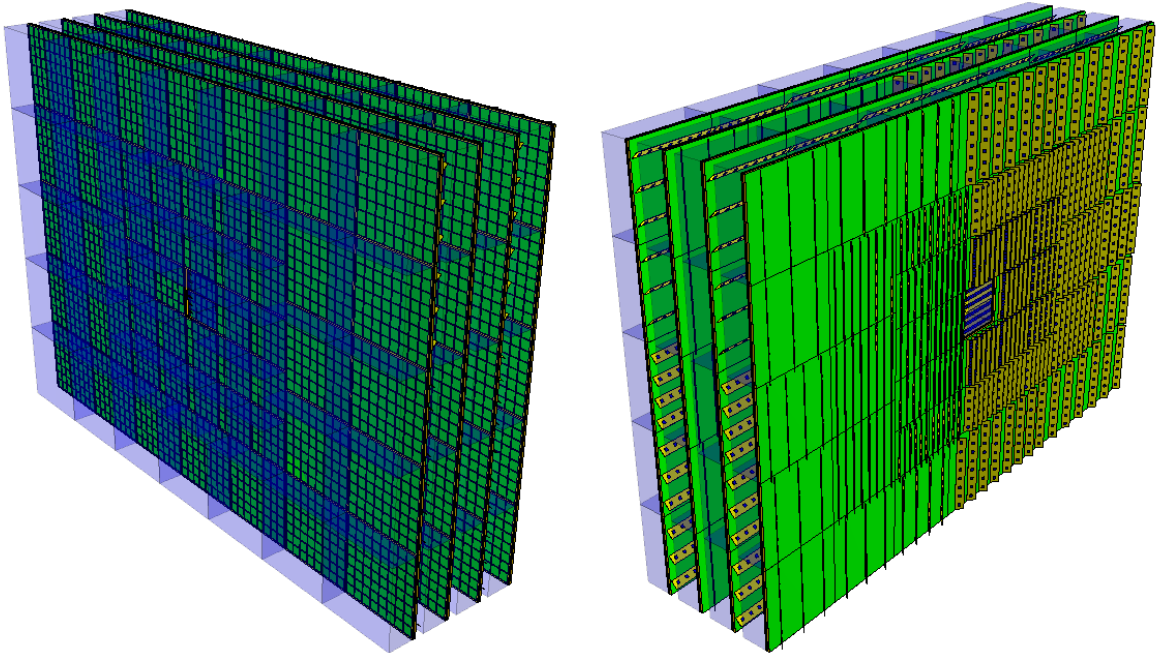


Figure 4.4: CBM-TRD geometry for SIS100, consisting of one station with four layers of detectors. Shown here is the implementation of the TRD geometry in the CBMROOT simulation framework. Visible are the ROCs with the radiator boxes in the front view (left), while the rear view (right) shows the backpanels of the ROCs together with the front-end electronics.

The required performance parameter for the SIS100, as summarized in Sect. 2.2, can be achieved by a TRD consisting of four layers of radiators and ROCs as demonstrated in Chap. 3. For a possible use of the TRD at a future SIS300, this setup can easily be adapted by extending it to up to ten detector layers.

Module type	# Modules/plane	# Pads	Pad area (cm <sup>2</sup> )
1	8	23,040	1.01
2	6	9,600	1.69 / 1.86
3	10	9,600	3.04
6	6	12,288	4.13
7	8	8,192	8.27
8	12	9,216	11.14 / 10.96
Total for one TRD layer	50	71,936	

Table 4.1: The number of different TRD module types per detector layer, together with the corresponding number of readout channels (pads).

The TRD is designed in a way that the entire system can be built with modules of only two different sizes, see Fig. 5.4. TRD modules are square-cut, the small modules have outer dimensions of  $57 \times 57 \text{ cm}^2$  and the large modules are  $95 \times 95 \text{ cm}^2$  in size. Given the CBM fixed target geometry we expect large hit rates at forward angles dropping over few orders of magnitude towards larger angles. The spatial distribution of the hit rates, as common for all fixed target experiments falls exponentially with increasing distance to the beam axis, as discussed in Sect. 4.5. This requires a high detector granularity in the inner part, equipped with the small modules, whereas the outer areas are covered with large modules. To deal with the high hit rate, a high granularity is realized by a small pad size in the inner part. Towards the outer regions the pad area is scaled up by one order of magnitude. The size of the largest commercially available single piece of Printed Circuit Board (PCB), which can be used for the the pad plane, defines the maximum size of the small, innermost modules. The large modules will have to be equipped with pad planes assembled from several PCBs and special precautions in order to achieve gas tightness will have to be implemented in this case. The maximal size of the modules is further constrained by possible gain instabilities which can occur at the highest count rates, if the anode wires were too long and thus have to collect too much charge. The scaling of the pad size is implemented on pad planes with different layouts. All required pad sizes can be accommodated by six different pad plane types, three for the small and three for the large module types as described in Sect. 5.3.

A given module of the CBM-TRD consists of three different components: the ROC, the radiator, and the Front-End Electronics (FEE). The construction details of the ROCs are summarized in Chap. 5, the choice and the design of the radiator is described in Chap. 6, and details on the FEE implementation are given in Chap. 7.

The modules will be arranged in four layers which together form a single TRD station with a common support structure (see Fig. 4.4). Figure 5.22 displays the arrangement of the ROCs and Front-End Boards (FEB) on two different TRD layers. Their orientation changes by  $90^\circ$  in each alternating layer, i.e. the long sides of the readout pads point vertical in layers one and three, and horizontal in layers two and four. The orientation of the FEBs follows the one of the readout pads. This way an optimal tracking resolution in both dimensions can be achieved. Table 4.1 summarizes the numbers of the the different TRD module types needed to build one detector layer (see also Fig. 5.19) and the corresponding number of readout channels (pads). In total this results in 200 modules with 287744 readout channels for a complete TRD station with four detector layers.

The module arrangement allows for a vertical segmentation of a TRD layer in three parts, two outer ones, consisting each of two columns of large module types, and a central one, containing the small module types surrounding the hole for the beam pipe and six large ones on the top and

bottom (see also Fig. 8.2). This segmentation will be useful during installation and maintenance, since it they can be moved and hoisted to the ground level separately.

The TRD modules will be mounted in a supporting structure that holds all four layers of the TRD station. It will comprise an outer frame to which the ledges that support the ROCs and the radiators will be attached and which will also allow the movement of the TRD with a crane. It also supports the gas supply, LV and HV services, as well as the cooling. A detailed description of the layout of the supporting system and its mechanical structure and components can be found in Sect. 8.2.

#### 4.4 General system layout

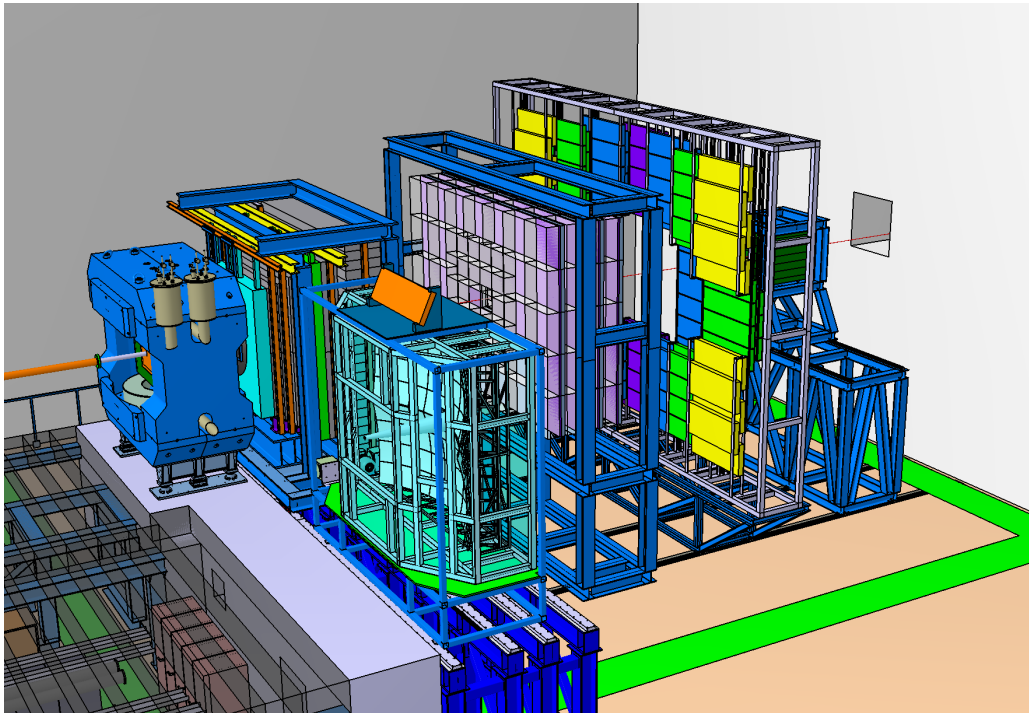


Figure 4.5: Drawing of the experimental setup of CBM for the SIS100. The four layer TRD station is shown as gray boxes positioned in beam direction behind the magnet and MUCH, respectively RICH, followed by the TOF wall and the PSD.

The complete setup of CBM as planned for SIS100 is displayed in Fig. 4.5. Shown are the following components from left to right:

- The magnet, surrounding the tracking detectors MVD and STS.
- The muon spectrometer MUCH, situated directly behind the magnet, and the RICH detector in its parking position next to it.
- The TRD with four layers of ROCs (gray boxes), together with its support frame.
- The TOF wall with different type of Resistive Plate Chamber (RPC) detectors (yellow, green, blue and violet boxes).
- The Participant Spectator Detector (PSD) for centrality and event plane determination.

Due to the modular structure of the CBM setup, the experiment can easily be configured in various ways by moving in and out different detector components, such that the setup can be

optimized for different physics cases. The TRD will play an important role in three of these configurations. In the electron setup the TRD station will directly follow the RICH detector and bridge the region between RICH and TOF. In the muon configuration the RICH will be replaced by the muon arm MUCH, consisting of absorbers and tracking chambers, and the TRD will serve here as the last tracking device for muons. Finally, the TRD can also be used in a setup dedicated to hadron measurements only, where neither RICH nor MUCH are part of the setup.

#### 4.4.1 TRD in the CBM electron setup

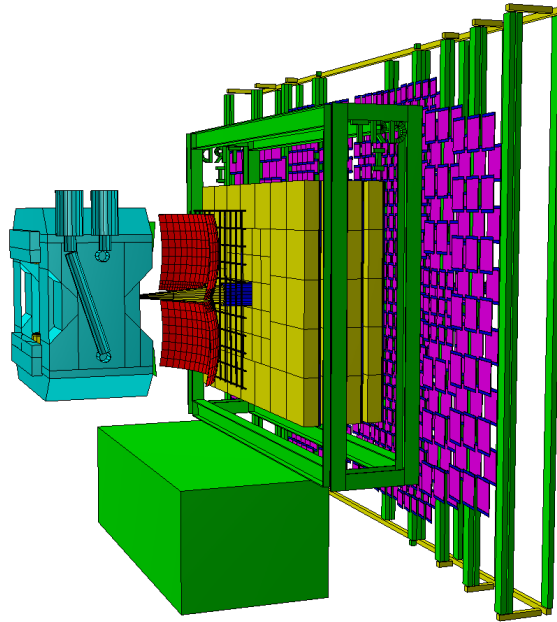


Figure 4.6: Sketch of the CBM electron setup for SIS100 with the TRD (yellow) as electron identification device.

Figure 4.6 shows the CBM electron setup, consisting of MVD, STS, RICH, TRD and TOF. In this configuration the RICH and TRD together will provide the electron identification necessary for the measurement of low and intermediate dielectrons (see Sect. 3.2). The tracking will be performed by the STS, while the MVD will be essential to reject conversion electrons.

#### 4.4.2 TRD in the CBM muon setup

It is foreseen to employ the TRD as last tracking station in the configuration SIS100-C of the MUCH [C<sup>+</sup>15], as shown in Fig. 4.7. This configuration will therefore consist of two layers of GEM detectors, two layers of straw tubes, and the four layer TRD station. This setup will be complemented by a 60 cm carbon absorber in front of the first GEM layer, and four iron absorbers between the consecutive tracking devices with a total thickness of 170 cm (see Tab. 2.1 in [C<sup>+</sup>15]). Tracking before the first absorber will be done with the STS. As the TRD station will be placed behind the last absorber, essentially only muons will pass through it and thus create only a very low hit rate in the TRD. The main physics case for this setup is the measurement of  $J/\psi$  mesons via their dimuon decay in  $p + \text{Au}$  collisions at 30 GeV beam energy.

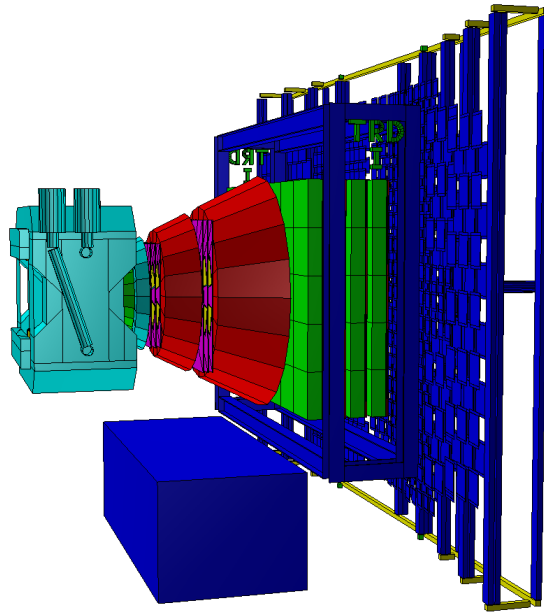


Figure 4.7: Sketch of the CBM muon setup SIS100-C with the TRD (green) as last tracking device of the MUCH.

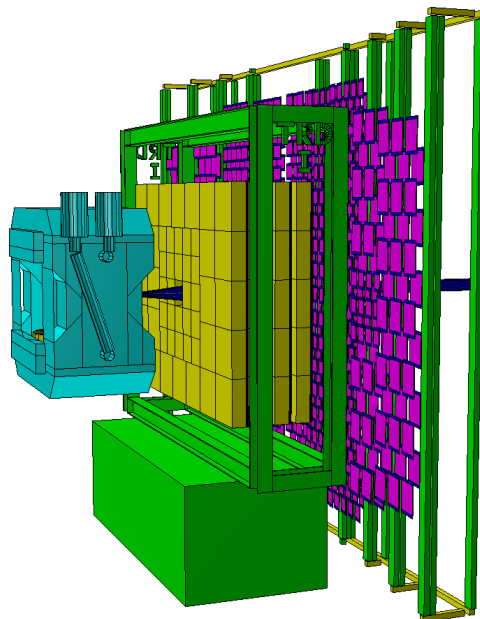


Figure 4.8: Sketch of the CBM hadron setup for SIS100 including the TRD (yellow).

### 4.4.3 TRD in the CBM hadron setup

Another possible scenario in which the TRD can be included is the CBM setup for hadrons only. In this case, neither RICH nor MUCH is part of the experimental setup, but only MVD, STS, TRD and TOF (see Fig. 4.8). Tracking and secondary vertex reconstruction will be done by STS and MVD, while the hadron identification will be performed by TRD and TOF. Here the TRD will augment the time-of-flight measurement by its additional  $dE/dx$  information, as discussed in Sect. 3.4. In this configuration TRD and TOF can be moved closer to the target in order to improve the time-of-flight resolution for protons and heavier fragments. To reduce the running costs, the TRD can in this scenario also be operated with an Ar/CO<sub>2</sub> mixture, instead of the much more expensive Xe/CO<sub>2</sub>, because no TR-photon detection is needed in this case.

## 4.5 Occupancy and trigger rates

The TRD will be operated in the high multiplicity environment generated by Au + Au collisions at interaction rates up to 10 MHz. In the following the corresponding detector occupancy and trigger rates are estimated for Au + Au collisions at 10 AGeV, as simulated with the UrQMD event generator. These values serve as a basis for a determination of the data rate produced by the CBM-TRD at the SIS100.

### 4.5.1 Occupancy simulation

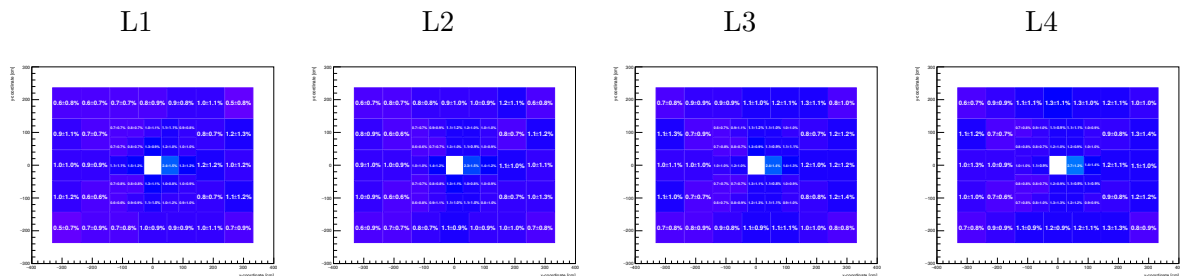


Figure 4.9: Averaged occupancy for 787 k minimum bias Au + Au events at 10 AGeV. The order is, from left to right, layer (L) 1, 2, 3 and 4. The coordinate system covers a range of  $\pm 6$  m in  $x$ - and  $\pm 5$  m in  $y$ -direction. The color scale represents the mean occupancy and is:

purple < 5 %, blue < 10 %, cyan < 15 %, green < 20 %, and yellow < 25 %.

The averaged occupancy seen by the TRD ROCs in the different detector layers is shown in Fig. 4.9 for minimum bias Au + Au collisions at 10 AGeV. The granularity of the different ROCs corresponds to the pad sizes as described in Sect. 5.3 (see Tab. 5.3 and Fig. 5.19). Since the pad sizes are adjusted to the local track density, the resulting occupancy has very similar values in the different regions of the detector layers. For most ROCs it ranges between 0.6 % and 1.4 %, while for the innermost small ROC in the bending plane next to the beam hole it can reach values up to 2.7 %. Generally, for the environment at the SIS100 the occupancy is relatively moderate and should not pose any problem for the tracking and particle identification algorithms described in Sect. 9.3.

## 4.5.2 Trigger and data rate estimations

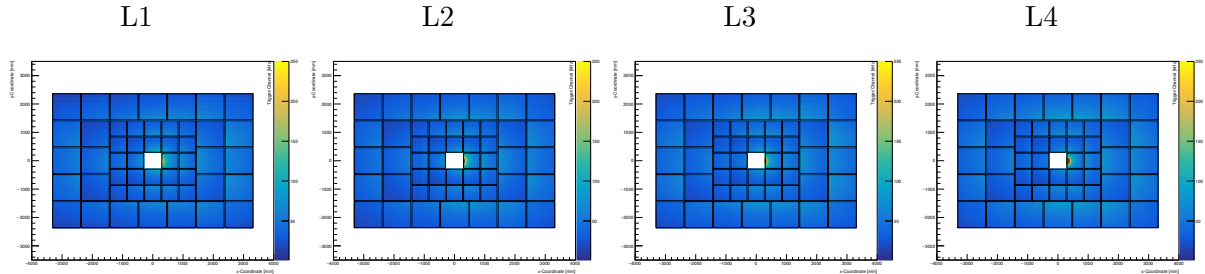


Figure 4.10: Average trigger rate for 787 k minimum bias Au + Au events at 10 AGeV, scaled to an interaction rate of 10 MHz. The order is, from left to right, layer (L) 1, 2, 3 and 4. The coordinate system covers a range of  $\pm 6$  m in  $x$ - and  $\pm 5$  m in  $y$ -direction. Forced neighbor readout is included. The color scale represents the mean trigger rate and is:

royal blue: 0 – 25 kHz,      ultramarine: 25 – 75 kHz,      turquoise: 75 – 125 kHz,  
 green: 125 – 175 kHz,      ocher: 175 – 225 kHz,      yellow: 225 – 250 kHz,      and  
 gray: > 250 kHz.

The averaged trigger rates in the TRD ROCs of the different detector layers is shown in Fig. 4.10 for minimum bias Au + Au collisions at 10 AGeV, scaled to an interaction rate of 10 MHz. In this calculated the forced neighbor readout is assumed, as implemented in the SPADIC chip and described in Sect. 7.1. The granularity of the different ROCs corresponds to the pad sizes as described in Sect. 5.3 (see Tab. 5.3 and Fig. 5.19). Similar to the averaged occupancy, only small variations of the trigger rate over a given detector layer are visible. It is found to be around 50 kHz in most positions and never exceeds values of 150 kHz.

Based on this results, a maximal data rate of 5 Gbit/s for minimum bias Au + Au collisions at 10 AGeV is expected for the full TRD with four layers.

## 4.5.3 Test beam results

In the following we summarize some results from the test beam campaigns performed at the CERN-PS in 2012 and at the CERN-SPS in 2015. They illustrate the performance of the TRD prototypes in terms of position resolution (CERN-PS) and in a high multiplicity environment (CERN-SPS).

### 4.5.3.1 Results from a high rate and high multiplicity test

During the CERN SPS/T2-H4 high rate test beam, using Pb + Pb collisions at 30 AGeV, a setup combining two full scale ROC prototypes was operated. The DAQ consisted of a SPADICv1.0 ASIC connected via HDMI-cable to the SysCore FPGA board sending the data via optical fiber to the FLIB-FPGA board in the FLES-PC. A set of 32 channels grouped in 16 channels within two adjacent rows with an active area of  $1 \text{ cm}^2$  each have been read out per detector. The recorded trigger frequency per channel is presented in Fig. 4.11. Its distribution has a maximum around  $5 \cdot 10^4$  Hz (left panel), such that the test beam environment roughly corresponds to the expected running scenario for Au + Au collisions at 10 AGeV at an interaction rate of 10 MHz

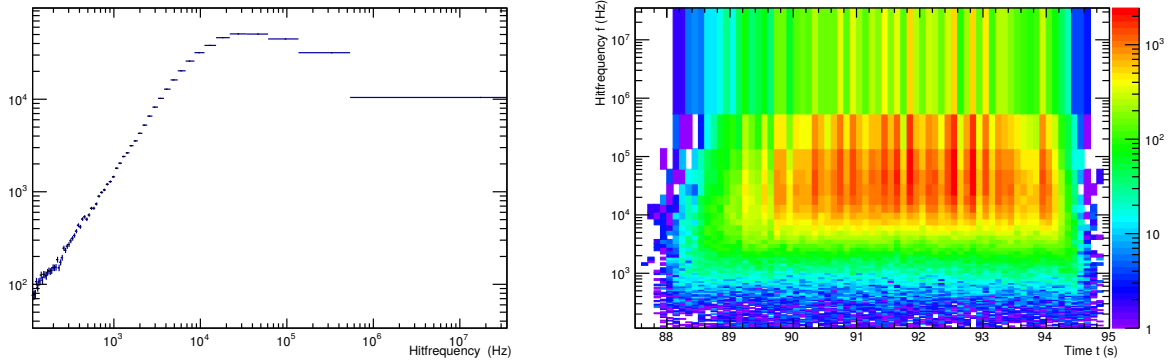


Figure 4.11: Trigger rate per channel and  $\text{cm}^2$  recorded during the CBM high rate test at the CERN-SPS in 2015. The normalized frequency spectrum is presented on the left hand side. The recorded hit frequency distributions as a function of time during one SPS spill is shown on the right hand side.

(see Fig. 4.10). No significant variation of the trigger rate over the spill duration was observed (right panel).

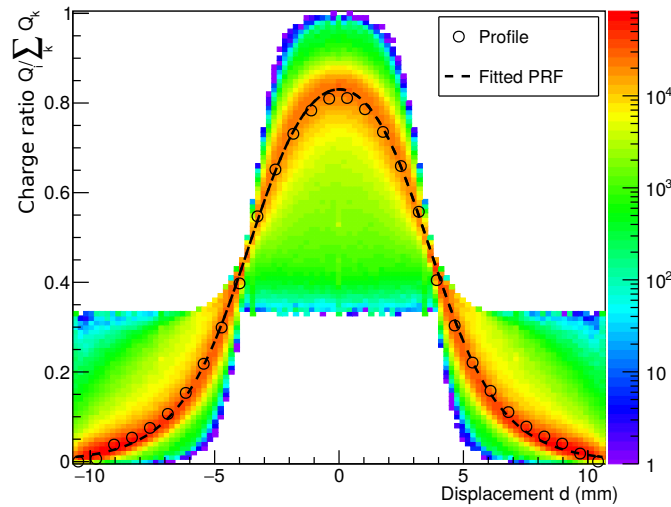


Figure 4.12: A measured PRF at the CBM high rate in beam test at CERN-SPS 2015 is presented. The one-dimensional projection of the distribution (black circles) is fitted using the Mathieson formula (Eq. 9.1). The extracted  $K_3$  value is  $0.388 \pm 0.008$ .

The data quality under these conditions has been assessed e.g. by comparing the measured Pad Response Function (PRF) to the theoretical prediction by Mathieson (Eq. 9.1). As shown in Fig. 4.12, a very good correspondance between the measurement and the theoretical expectation is observed. Generally, no deterioration of the data quality has been seen under the conditions present at the CERN-SPS.

#### 4.5.3.2 Position resolution at low rates but realistic material budget environment

The position resolution performance of the small detector prototypes has been investigated during an in-beam test at CERN-PS/T9 in 2012 in a setup that included several other detector

prototypes (RICH, TRD and TOF), and was thus quite similar in terms of material budget to the final the CBM SIS100 electron setup. The full setup was composed of the following detectors (in this order looking downstream): two fiber hodoscopes (position reference), two air Cherenkov detectors, one CO<sub>2</sub> RICH prototype, six TRD and two TOF RPC prototypes, as well as one Pb-glass calorimeter (PID reference).

The position resolution has been estimated using an one-dimensional linear tracking algorithm based on the information from the two fiber hodoscopes and two TRD prototypes with the same pad plane orientation. The results are presented in Fig. 4.13 as function of the beam momentum for a beam composed of electrons, muons and pions. A rough estimation of a homogeneous radiation length equivalent to the material present in the setup between the two hodoscopes was calculated using the modified Highland-Lynch-Dahl approximation:

$$\Theta_{\text{proj}}^{\text{rms}} = \frac{13.6 \text{ MeV}}{p \beta c} z \sqrt{\frac{X}{X_0}} \left[ 1 + 0.038 \ln \left( \frac{X}{X_0} \right) \right] \quad (4.1)$$

Here  $\Theta_{\text{proj}}^{\text{rms}}$  is the width of the projected angle distribution (which has an approximately Gaussian distribution for small scattering angles),  $p$ ,  $\beta c$  and  $z$  are the momentum, velocity and charge number of the incident particle, and  $X/X_0$  is the true path length in units of radiation length.

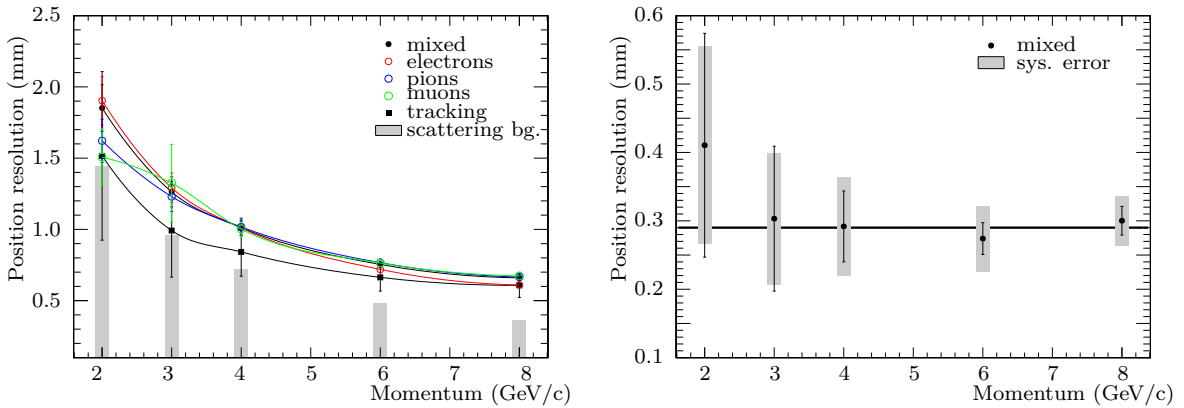


Figure 4.13: Left: Position resolution as function of particle momentum at an anode voltage of 1775 V and a drift voltage of 500 V determined via a PRF fit. The position resolution represented by circles is estimated after a misalignment compensation. This is based on the residuals seen in the first two identical prototypes, whose position resolution, represented by the squares, is estimated with a linear track fit using an iterative misalignment compensation which includes data from the two fiber hodoscopes as external position reference. The gray boxes correspond to the simulated mean track displacement,  $\Delta x_{\text{scat}}$ , occurring between TRD1 and TRD2, as caused by beam scattering in the detector material.

Right: Position resolution using a PRF fit for the mixed particle beam at an anode voltage of 1775 V, including a misalignment correction based on the point residuals in TRD1 and TRD2 after scattering compensation. The resulting position resolution is  $(290 \pm 15) \mu\text{m}$ , estimated by fitting a constant. The systematic uncertainties (10% of  $\Delta x_{\text{scat}}$ ) of the simulation are visualized by gray boxes. The errors of the data points include fitting errors and statistical uncertainties. The distribution was fitted according to the Highland-Lynch-Dahl formula (Eq. 4.1) to estimate the material budget and distribution in front of the detectors.

A detailed simulation has been performed to estimate the broadening of the residual distribution measured in the detectors under test. The residuals have been calculated assuming

a linear particle tracking. The material budget of the individual detector modules has been calculated as input for the simulation. There are three main contributions to the material budget within the RICH in front of the first two TRD prototypes: two gas windows made from 2 mm PMMA ( $X/X_0 = 2 \times 0.58\%$ ) and the 6 mm SIMAX glass mirror ( $X/X_0 = 5.1\%$ ), 168.45 cm behind the entrance window. Also, the two scintillators ( $X/X_0 = 2 \times 3.0\%$ ) as well as the first fiber hodoscope ( $X/X_0 = 2.0\%$ ) and the first TRD prototype ( $X/X_0 = 1.54\%$ ) with radiator N25 ( $X/X_0 = 1.5\%$ ) and K++ ( $X/X_0 = 3.09\%$ ) are taken into account. The resulting position resolution is in good agreement with  $300\ \mu\text{m}$  within the uncertainties over the full momentum range (see right panel of Fig. 4.13). This result agrees with the expectation from the full detector simulation as shown in Fig. 9.11, see Sect. 9.3.3.1.

## 4.6 Radiation environment

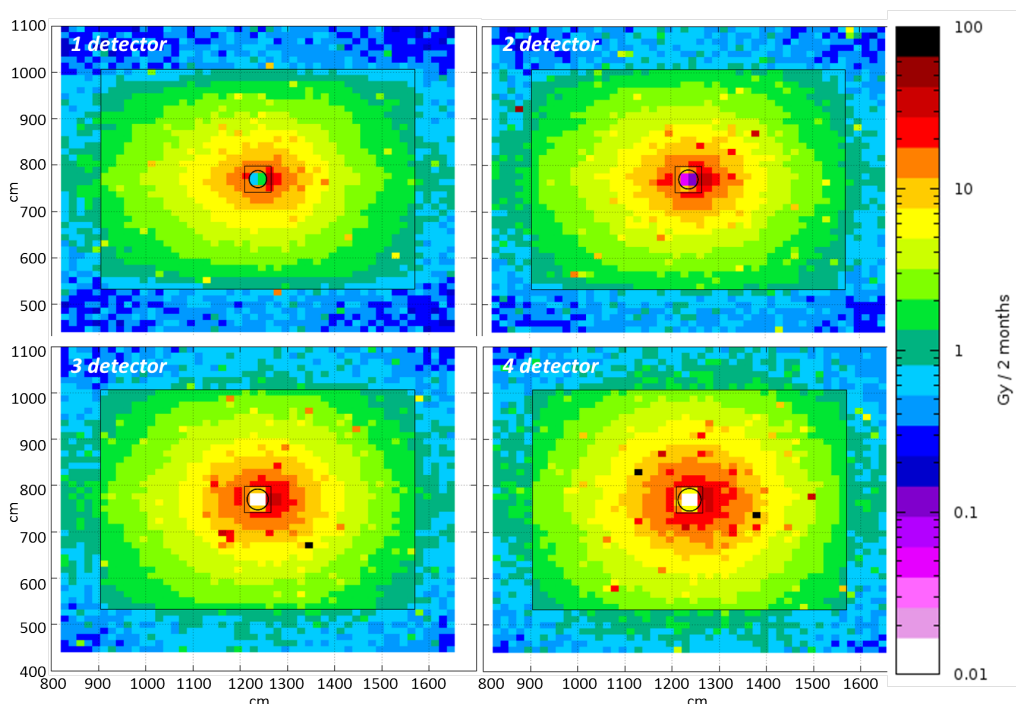


Figure 4.14: The total ionizing radiation dose expected in the four TRD layers. The calculation was performed with FLUKA [B<sup>+</sup>07] and corresponds to two months of Au + Au collisions at 10 AGeV with an interaction rate of 5 MHz.

The TRD will cover a region of polar angles between  $\sim 3^\circ - 45^\circ$  over which the anticipated particle rates, and correspondingly also the radiation environment, changes drastically. In order to assess the radiation background in which the TRD will have to be operated, simulations using the FLUKA package [B<sup>+</sup>07] have been performed. The results corresponding to two months of Au + Au collisions at 10 AGeV with an interaction rate of 5 MHz are summarized in Figs. 4.14 – 4.16.

The total ionizing radiation dose is found to be below 10 Gy / (2 months) for the largest part of the detector area (see Fig. 4.14). In the innermost chambers close to the beam pipe a dose of about 20 – 40 Gy/(2 months) might be expected. The total non-ionizing radiation dose should remain below  $5 \times 10^{11}$  NIEL/cm<sup>2</sup>/(2 months) for the entire detector area (see Fig. 4.15), while the expected neutron density is not expected to exceed  $2 \times 10^{12}$  n/cm<sup>2</sup>/(2 months) anywhere in the acceptance of the TRD (see Fig. 4.16).

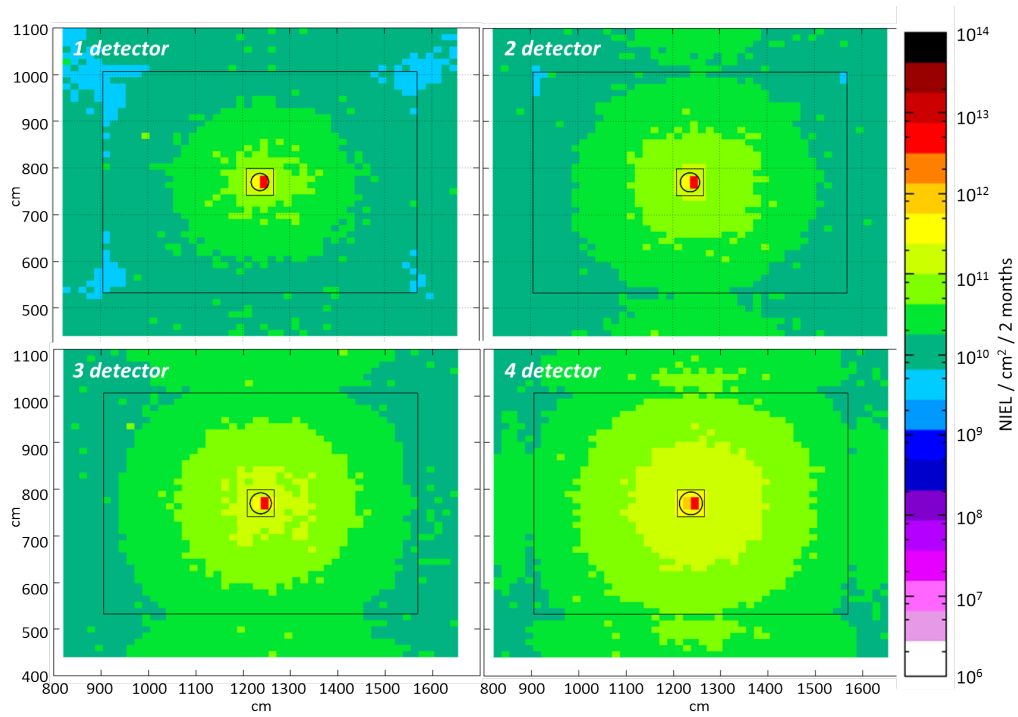


Figure 4.15: The total non-ionizing radiation dose expected in the four TRD layers. The calculation was performed with FLUKA [B<sup>+</sup>07] and corresponds to two months of Au + Au collisions at 10 AGeV with an interaction rate of 5 MHz.

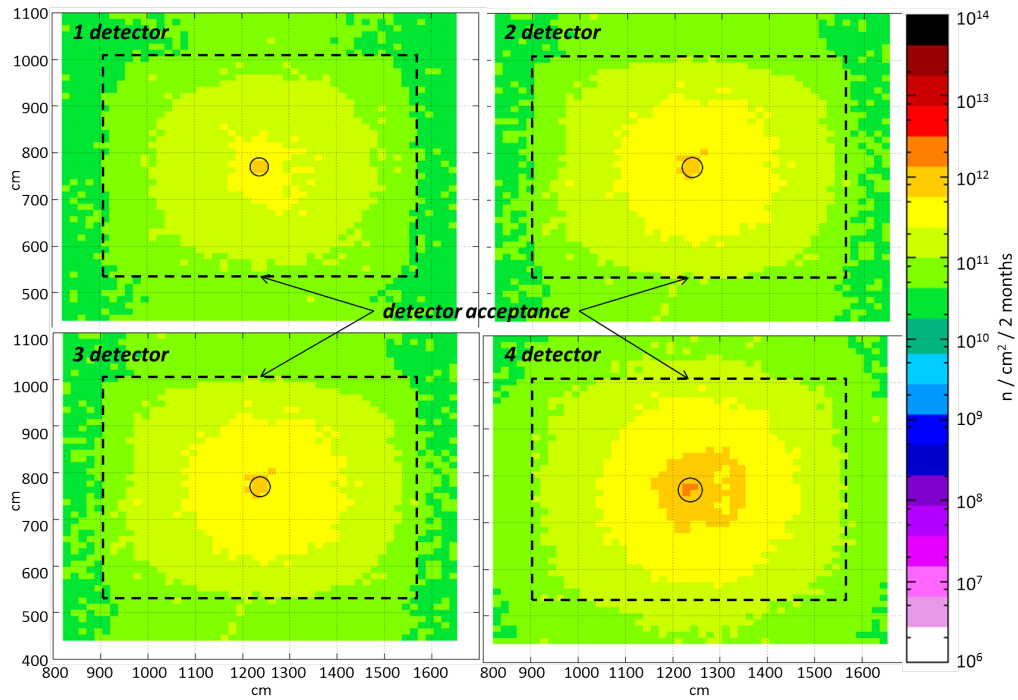


Figure 4.16: The total neutron density expected directly behind the four TRD layers. The calculation was performed with FLUKA [B<sup>+</sup>07] and corresponds to two months of Au + Au collisions at 10 AGeV with an interaction rate of 5 MHz.

Based on the presented simulated radiation doses, we prefer to keep the number of active electronic components as low as possible which supports our choice for the LV-system in Chap. 8.4. The ASIC foreseen for the FEE, the SPADIC 2.x, is based on the UMC 180 nm technology (see Sect. 7.1) and is expected to work in the above described environment without problems.

## 4.7 Material Budget

The CBM-TRD is generally designed such to minimize the material inside the active area of the detector to limit multiple scattering and the production of secondary particles. This is in particular important for the matching of tracks from the TRD to the TOF, but also a prerequisite for a good performance of the TRD itself. The goal of a minimal material budget is achieved by using thin, lightweight MWPC as described above. In the following the contributions from the different detector components are described.

### 4.7.1 Radiator

Table 4.2 summarizes the material budget in terms of radiation length for three different radiator materials, G30, H and K++, which are under consideration. The baseline TRD design will employ the H radiator type. A detailed discussion on the various radiator types can be found in Sect. 6.3. Depending on the material and thickness of the radiator the material budget varies between  $X/X_0 = 1.44 - 3.09\%$ .

Table 4.2: The material budget of the different radiator options.

Prototype	Material	Density (g/cm <sup>3</sup> )	Thickness (cm)	$X/X_0$ (%)
G30	PP fibers	0.064 – 0.074	12	1.70 – 1.96
H	PE foam	0.026	30	1.39 – 1.75
K++	POKALON		25	3.09

### 4.7.2 Frontpanel and gas window

A minimal amount of material between radiator and active gas volume can be achieved by using a single Kapton foil, stabilized by a CF support grid, as shown in Fig. 5.10. The resulting radiation lengths are presented in Tab. 4.3.

Table 4.3: The material budget of the frontpanel and gas window components.

Material	Thickness (μm)	$X/X_0$ (%)
Aluminum	3	0.003
Kapton	25	0.009
CF	10000	(4.215)
CF	15000	(6.323)
<b>Sum</b>		<b>0.012</b>
CF support grid		+ (4.215 – 6.323)

The material budget seen by a particle passing perpendicularly through the full thickness of the CF support grid is naturally higher. However, only a very small fraction of the active area will be affected (see Fig. 5.7).

### 4.7.3 Gas volume

The second important component affecting the PID performance is the thickness of the active gas volume and the used gas mixture. The two noble gas mixtures which are under consideration are xenon and argon based as discussed in Sect. 5.1. The transmission probability of these mixtures (85 % noble gas and 15 %  $\text{CO}_2$ ) at different thicknesses are presented in Fig. 4.17. The default counting gas mixture which will be used in the CBM-TRD is  $\text{Xe}/\text{CO}_2$  (85/15), due to its higher TR-photon absorption cross section, whereas a (80/20) mixture is used for the test beams to reduce the costs. A total gas mixture thickness of 12 mm under operating conditions contributes with a radiation length of  $X/X_0 = 0.065\%$ .

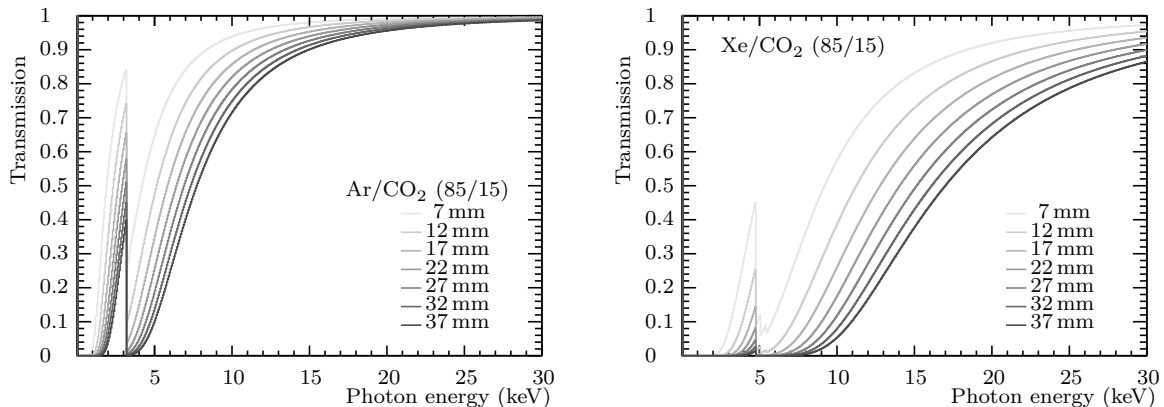


Figure 4.17: Transmission probability for argon (left) and xenon (right) based mixtures (85 % noble gas and 15 %  $\text{CO}_2$ ) of different gas thicknesses: 7, 12, 17, 22, 27, 32, and 37 mm.

### 4.7.4 Backpanel and pad plane

Table 4.4: Radiation lengths of the backpanel and pad plane components.

Material	Thickness ( $\mu\text{m}$ )	$X/X_0$ (%)
Honeycomb	22000	0.170
Air	22000	0.007
Epoxy	100	0.028
CF sheet	$2 \times 300$	0.253
FR4	360	0.226
Cu	25	0.174
Aluminum frame	27000	(30.045)
<b>Sum</b>		<b>0.858</b>
Aluminum frame		+ 30.045

The radiation length for each subcomponent as well as the total radiation length in different regions of the backpanel (with and without aluminum frame) are listed in Tab. 4.4. The backpanel thus contributes the highest amount of material to the budget of a ROC (without radiator), while the gas window and the gas itself can be rather neglected.

### 4.7.5 Front end electronics

The FEBs can be installed at the backpanel with different tilting angle  $\alpha$ , which will depend on the available space on a given module. Therefore, the amount of material introduced by

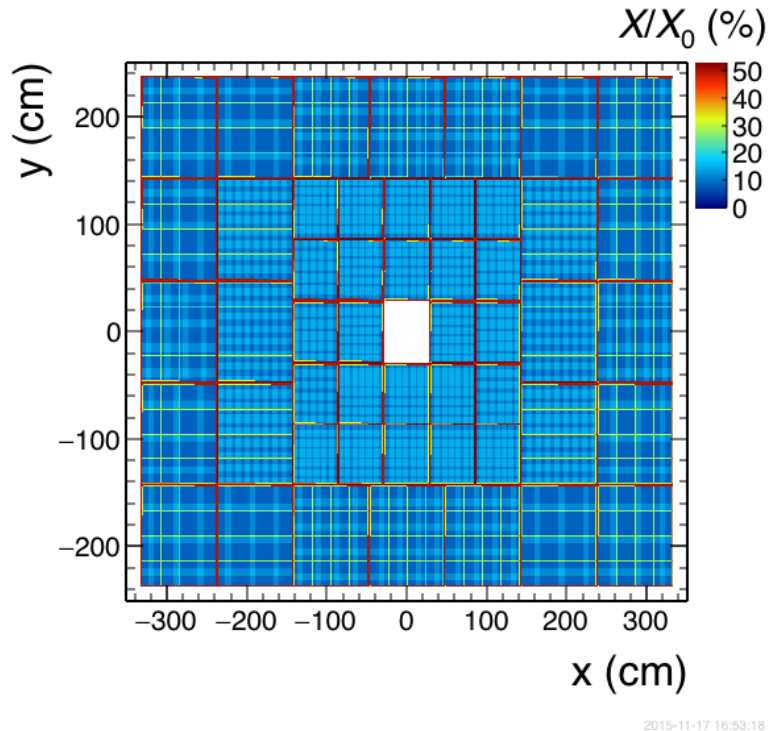


Figure 4.18: The material budget distribution for four layers of TRD-ROCs. Shown are the percentages of radiation length  $X/X_0$  calculated by following straight trajectories from the target through the TRD geometry as implemented in GEANT3.

the FEBs, as seen by a particle passing through a TRD module with perpendicular incidence angle, will depend on  $\alpha$  and is listed in Tab. 4.5. The minimal and most uniform material distribution will be achieved when the FEBs are installed flat on the backpanel (i.e.  $\alpha = 0$ ) with  $X/X_0 < 1.1\%$ . Due to the requirements for cable routing and cooling tilting angles  $\alpha > 0$  might be necessary. If the angle can be limited to  $\alpha \leq 45^\circ$ , this would imply only a moderate increase in radiation lengths to  $X/X_0 \leq 1.51\%$ . Larger angles, however, should be avoided since this would result in localized areas with relatively large material budget. The extreme case is  $\alpha = 90^\circ$ , which corresponds to  $X/X_0 = 52.13\%$  at the FEB mounting positions but no material in the largest fraction of the active area.

#### 4.7.6 Total material budget

The total material budget of one detector layer inside its active region, including the default radiator H, varies therefore between a minimum of 2.33 – 2.69% (empty regions between the CF grid) and 6.54% (small module CF grid), respectively 8.65% (large module CF grid) for particles passing perpendicularly through the full grid thickness. To this the material of the FEBs has to be added which amounts to  $X/X_0 = 1.51\%$  for a default mounting angle of  $\alpha = 45^\circ$ . The size of the active area covered by the FEBs in this configuration varies between  $\sim 18\%$  (module type 8) and  $\sim 62\%$  (module types 1 and 3) (see Fig. 5.21). The chamber frame adds 43.58% per detector layer in localized outer areas of the modules. A parallel projection of the material budget including the FEB material is presented in Fig. 4.18. In the largest fraction of the TRD area the budget is relatively moderate ( $X/X_0 < 10 - 20\%$ ). Due to the non-projective arrangement of the modules in the different TRD layers, the material of the module frames and of the CF support grids is not seen under the same angles and thus more evenly distributed.

Table 4.5: Radiation lengths of the FEBs as function of their installation tilting angle  $\alpha$  estimated for perpendicular tracks.

Material	$\alpha$ (deg)	Thickness (cm)	$X/X_0$ (%)
FR4	0	0.170	1.068
	5	0.171	1.072
	10	0.173	1.084
	15	0.176	1.105
	20	0.181	1.136
	25	0.188	1.178
	30	0.196	1.233
	35	0.208	1.303
	40	0.222	1.394
	45	0.240	1.510
	50	0.264	1.661
	55	0.296	1.861
	60	0.340	2.135
	65	0.402	2.526
	70	0.497	3.122
	75	0.657	4.125
	80	0.979	6.148
	85	1.951	12.250
90	8.300	52.127	

## Chapter 5

# Readout Chamber

This chapter summarizes the design of the ROCs. It will be based on a Multi-Wire Proportional Chamber (MWPC) with an amplification region of 3.5+3.5 mm thickness, combined with a thin drift region (5 mm thickness) separated by a cathode wire plane. The entrance window to the drift region is defined by a aluminized foil, which also serves as cathode for the drift field. On the backpanel of the ROC a pad plane will be mounted, where the charge induced by the gas amplification around the anode wires is collected. Via the segmented pads a precise reconstruction of the position of the ionization processes is possible.

### 5.1 Gas mixture

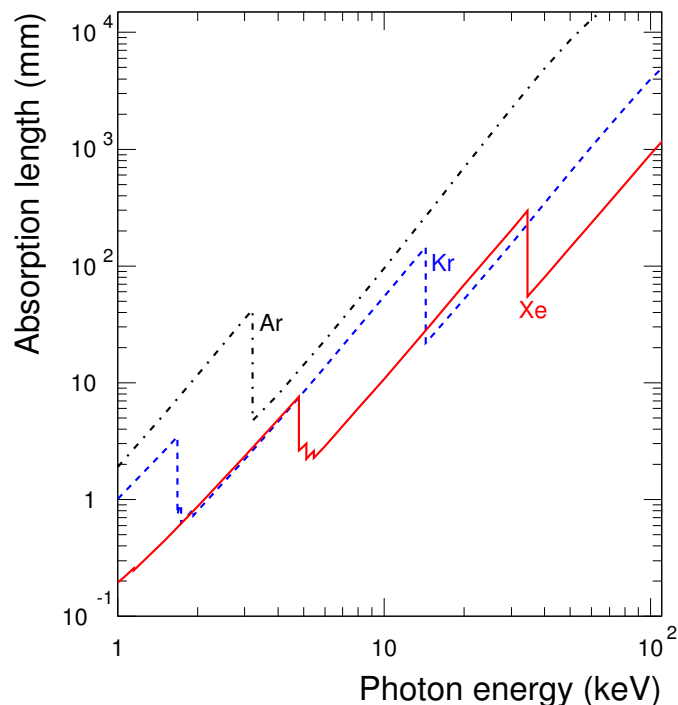


Figure 5.1: The X-ray absorption length in different noble gases [C<sup>+</sup>01].

In the standard operation scenario of the CBM-TRD a mixture of 85 % xenon and 15 % CO<sub>2</sub> is foreseen as counting gas. A sufficiently short absorption length for the TR-photons produced in the radiator is mandatory in order to achieve an efficient electron identification with gas detectors

of limited thickness. From the comparison of X-ray absorption lengths of different noble gases, shown in Fig. 5.1, it is obvious that this goal can only be achieved with xenon as the main gas component. For a typical TR-photon energy of 10 keV xenon has an absorption length of 10 mm.

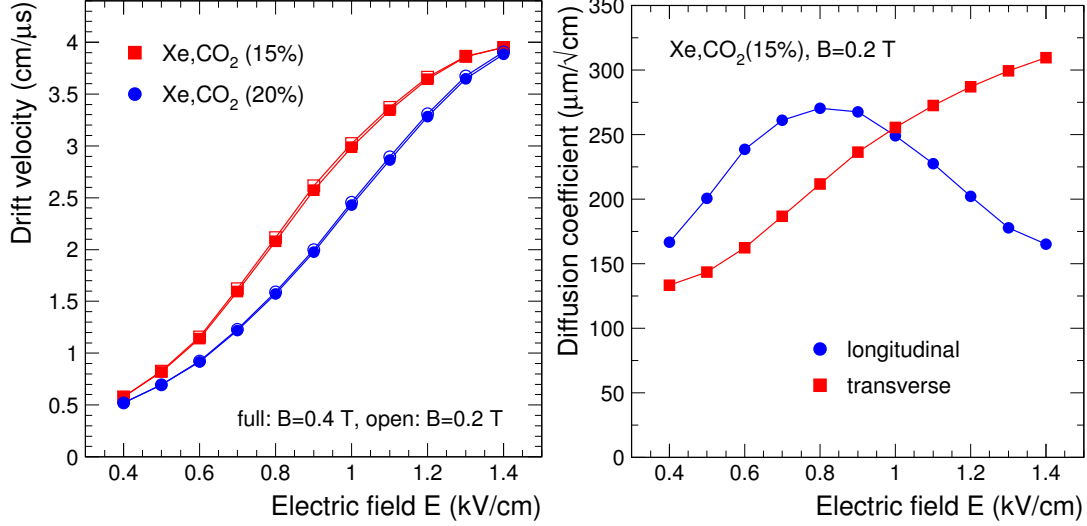


Figure 5.2: The drift velocity (left) and the diffusion coefficient (right) for Xe/CO<sub>2</sub> mixtures as calculated with GARFIELD for different electric drift fields [C<sup>+</sup>01].

The technical properties of the Xe/CO<sub>2</sub> gas mixture are discussed in Sect. 8.3.1. Two other important aspects are illustrated in Fig. 5.2: the drift velocity and the diffusion coefficients. It should be pointed out, that in [C<sup>+</sup>01] no significant dependence of neither the drift velocity, nor of the diffusion coefficients on the magnetic field was observed up to  $B = 0.6$  T. Therefore, the simulations shown in Fig. 5.2 can also be applied to the CBM-TRD which is operated outside of the magnetic field.

For a default drift field of 1 kV/cm a drift velocity  $v_D$  of about 3 cm/μm can be expected for Xe/CO<sub>2</sub> (85/15). A high drift velocity is advantageous for the CBM-TRD, since the high interaction rates require short signal collection times. Since the TRD is not going to be operated as a real drift chamber, i.e. the drift time information is not being used in the space point reconstruction, a precise knowledge of  $v_D$  is not required which facilitates the operation and calibration of the TRD.

At the default drift field of 1 kV/cm the diffusion coefficients are expected to be about  $250 \mu\text{m}/\sqrt{\text{cm}}$ , both in longitudinal and in transverse direction, see right panel of Fig. 5.2. For the foreseen drift length of 0.5 cm this corresponds to maximum spread of an initially point-like electron cloud of  $\sim 180 \mu\text{m}$ , which is small enough to not affect the position resolution and the signal shape.

The electrons produced in the ionization processes can be absorbed by gas impurities during their drift to the amplification region. In particular oxygen is of relevance here due to its electronegativity. The resulting signal loss follows an exponential behavior as function of drift time  $t_D$  and depends on the total gas pressure  $p$ , as well as the oxygen partial pressure  $p(\text{O}_2)$ :

$$N(t_{\text{drift}}) = N(0) \cdot \exp(-p \cdot p(\text{O}_2) \cdot C_{\text{att}} \cdot t_D) \quad (5.1)$$

Figure 5.3 summarizes the electron attachment coefficients  $C_{\text{att}}$  measured for different gas mixtures [C<sup>+</sup>01]. It is relative large for CO<sub>2</sub> mixtures due to its large number of low lying excitation levels. However, since the drift times in the CBM-TRD are short ( $t_D < 0.2 \mu\text{s}$ ), the resulting effect on the signal height will be only 1% or less (for  $C_{\text{att}} = 400 \text{ atm}^{-2} \mu\text{s}^{-1}$  and assuming  $p(\text{O}_2) = 100 \text{ ppm}$ ).

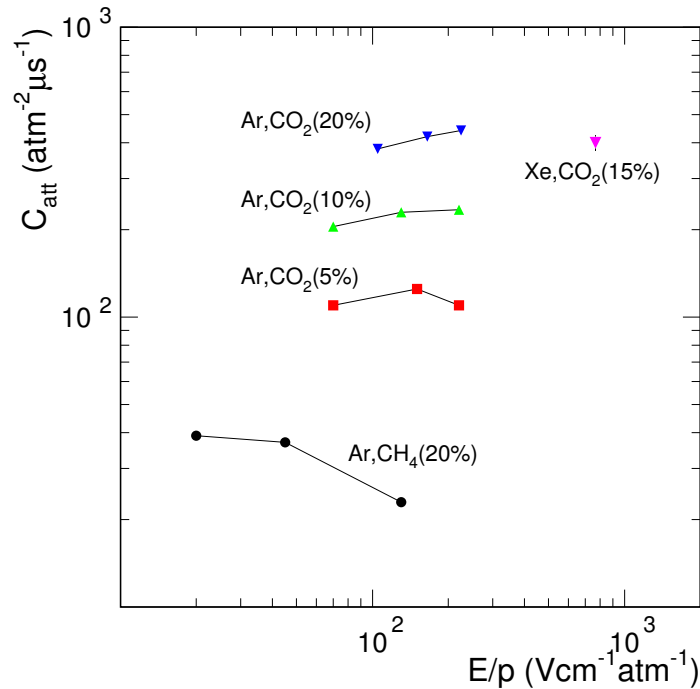


Figure 5.3: The electron attachment coefficient as a function of the reduced drift field for different gas mixtures [C<sup>+</sup>01].

## 5.2 ROC design

The layout of the pad plane foresees rectangular pads, whose widths along a pad row (direction along the wires) are determined by the fixed distance between the pad plane and the anode wire grid. This way the pad response function can be adjusted such that an optimal charge distribution on adjacent pads (10%/80%/10%), and thus a good energy and position resolution, is ensured. In addition, the fixed pad width minimizes the numbers of different layouts of the FEBs. The various pad sizes have therefore to be realized by scaling the long edge of the pads (i.e. orthogonal to the wires) accordingly. In this direction the position resolution will thus effectively be limited to the pad dimension, since the charge sharing between pad rows is marginal, at least for the larger pad sizes implemented in the outer detector regions. Therefore, it is foreseen to rotate the modules by 90° between each detector layer in order to achieve a good position resolution in  $x$  and  $y$  direction. However, this requires a quadratic shape of the TRD modules, if the number of different module types is supposed to be kept minimal.

### 5.2.1 MWPC description

A MWPC design with additional drift region is chosen as the default solution for the ROCs of the CBM-TRD (a symmetric, fast MWPC without drift region as a possible alternative is described in Sect. 12.5). The additional drift region ensures a high TR absorption probability, which in general is proportional to the total gas volume thickness and depends on the chosen gas mixture, and it provides a higher gain stability of the ROC under external pressure variations. At the same time it allows to keep the size of the induced charge clusters small, which is determined by the distance between the anode wire plane and the readout electrode. A small cluster size is of special importance in the high occupancy environment of CBM. A potential drawback of a drift detector is a reduced signal collection speed (for electrons it is 0.1 μs for a symmetric 3.5+3.5 mm MWPC and additional 0.125 μs in a 5 mm drift region with 100 V/mm field, see Fig. 5.14) and

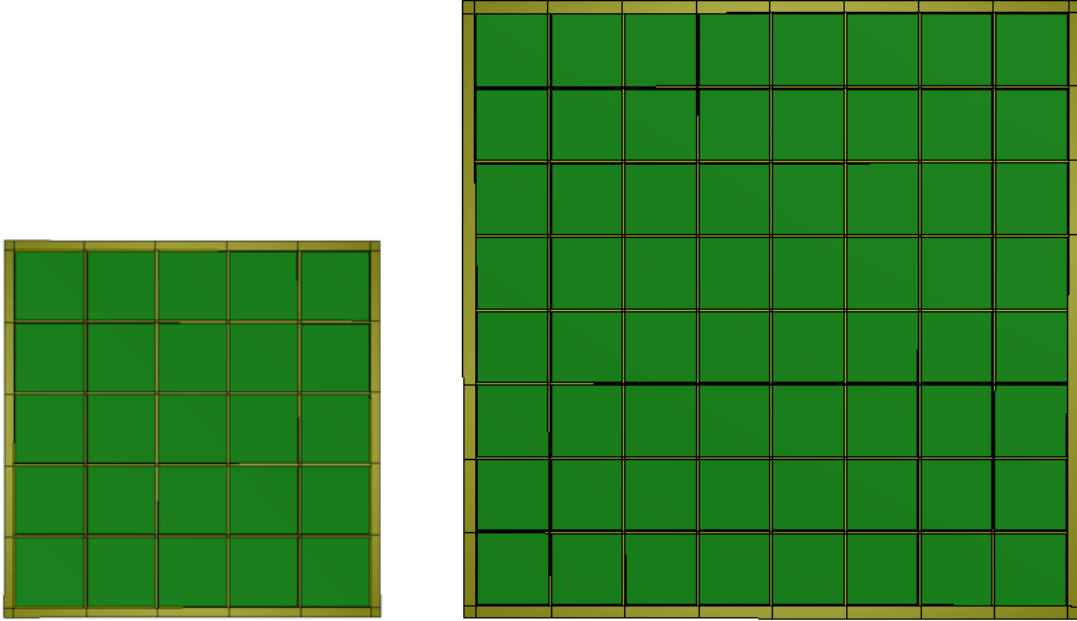


Figure 5.4: Sketch of a small (left panel) and large (right panel) CBM-TRD module type (front view). The outer dimensions are  $57 \times 57 \text{ cm}^2$  for small and  $95 \times 95 \text{ cm}^2$  for large types. Shown here is the implementation of the module geometry in the simulation framework.

a possibly increased accumulation of space charge compared to a MWPC without drift region. Nevertheless, a signal collection time of below  $0.3 \mu\text{s}$  should in any case be sufficient even at a trigger rate of  $100 \text{ kHz}$  (as expected at the SIS300) in the most inner part of the detector with a readout pad area of  $1 \text{ cm}^2$ , corresponding to an average trigger separation in time of  $10 \mu\text{s}$ . For the running scenarios at the SIS100 only maximal trigger rates well below  $50 \text{ kHz}$  are expected, as summarized in Sect. 4.5. Therefore, the proposed ROC design should fulfil the requirements in terms of readout speed in all possible cases.

Figure 5.5 presents a cross section of the outer region of one ROC together with the corresponding dimensions and positions. Shown are the different components, such as the honeycomb structure, the pad plane and the aluminum frame, which together form the backpanel, the different wire distance ledges together with the cathode and anode wire planes, and the entrance window with the carbon fibre support structure. The full chamber layout for a large module type is illustrated in Fig. 5.6 and the dimensions and basic parameters are summarized in Tab. 5.1.

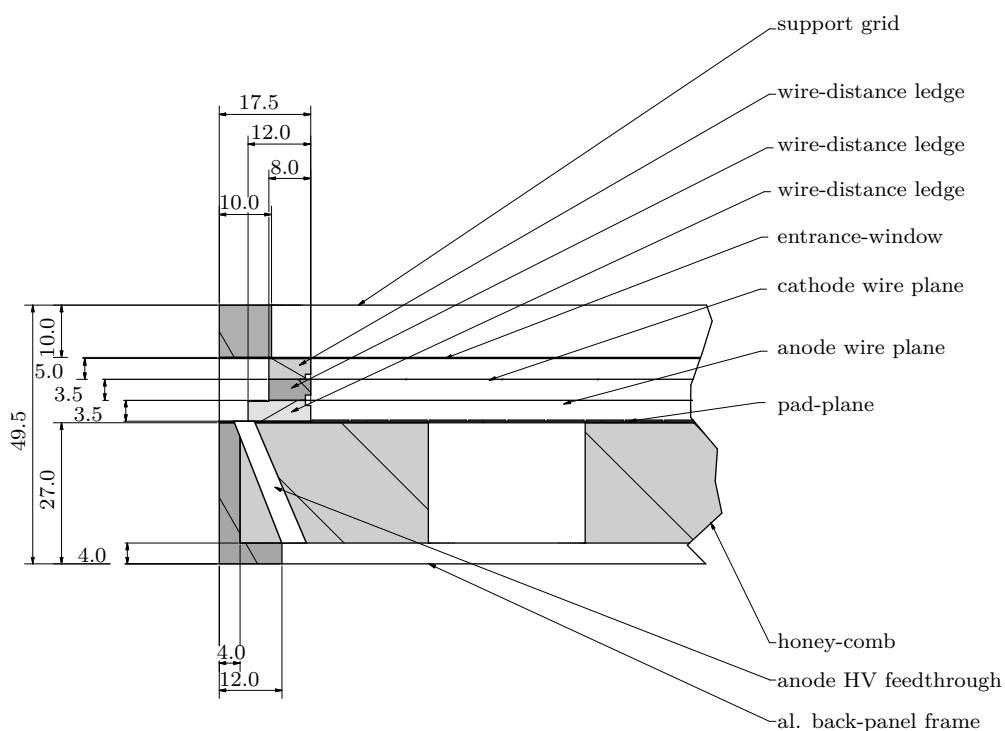


Figure 5.5: Cross section of the outer part of a CBM-TRD ROC. All presented lengths are given in millimeter. The parts shown are from top to bottom: support grid, entrance window, wire distance ledge, cathode wire plane, wire distance ledge, anode wire plane, wire distance ledge, pad plane, honeycomb, and aluminum backpanel frame.

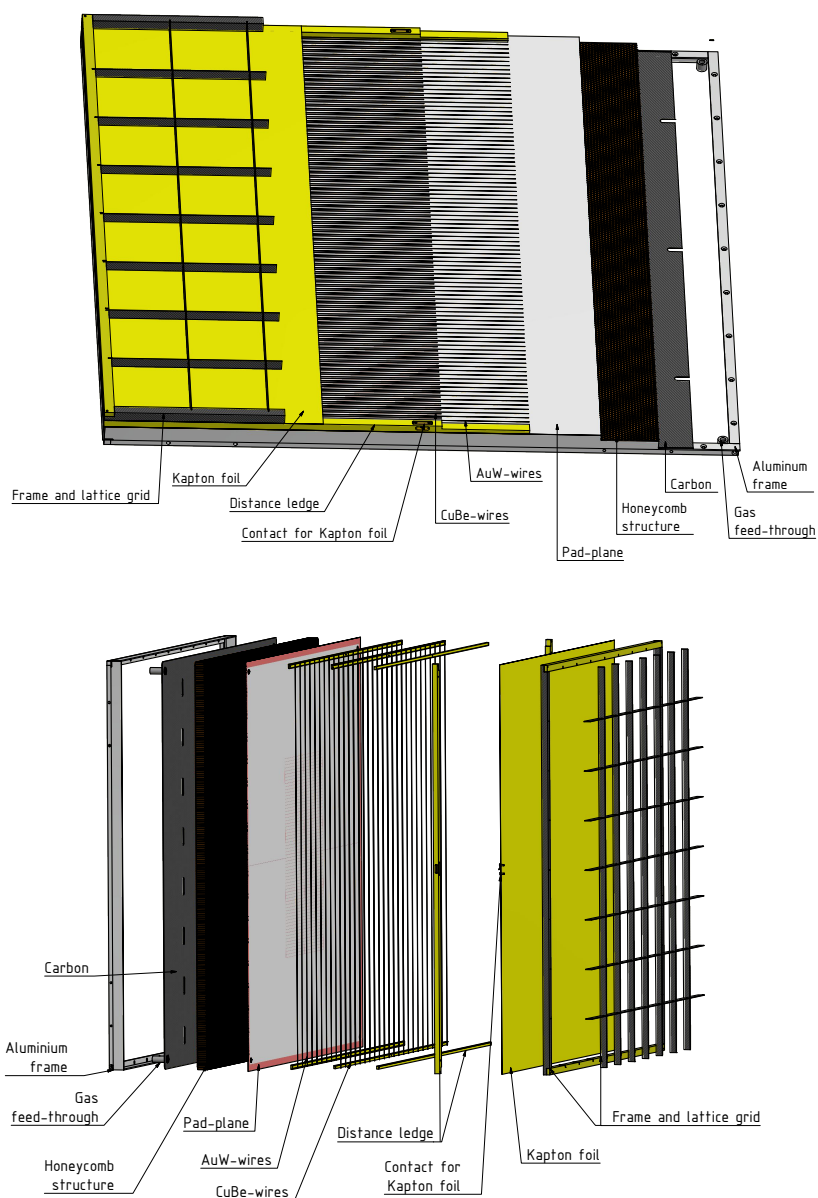


Figure 5.6: Upper panel: drawing of a full CBM-TRD ROC of the large module type. Visible are the different layers from left to right: frame and carbon support lattice, Kapton foil as entrance window, distance ledge with electrical contact for the foil, wire planes, pad plane, honeycomb structure, carbon layer, and outer aluminum frame. Also shown are the gas feedthroughs in the backpanel. Lower panel: Explosion view of the same ROC module.

ROC type	small	large
Module type	1, 2, 3	6, 7, 8
Outer dimensions	$57 \times 57 \text{ cm}^2$	$95 \times 95 \text{ cm}^2$
Active area	$2862.25 \text{ cm}^2$	$8372.25 \text{ cm}^2$
Total height	49.5 mm	
Height amplification region	3.5+3.5 mm	
Height drift region	5.0 mm	

Table 5.1: Summary of the dimensions of the two ROC layouts.

The first detector component is the entrance window made from a  $25 \mu\text{m}$  thick Kapton foil, aluminized on a single side. This foil can be stretched using a thermally expanding frame and is glued to a carbon lattice window support structure (a prototype is presented in Fig. 5.10). The production procedure is described in Sect. 5.2.2. The entrance window ensures gas tightness and acts at the same time as drift potential plane. The mechanical deformation has therefore to be limited to keep gain variations caused by pressure changes within a reasonable range. The maximally acceptable foil deflection due to an over- or under-pressure in the detector volume of 1 mbar has been estimated to be 1 mm based on GARFIELD simulations (see Sect. 5.2.3). The goal to limit the foil deflections to  $\pm 1$  mm can not be reached with a single foil with a surface of up to  $1 \text{ m}^2$  without additional mechanical support. This motivates the addition of a support grid in order to subdivide the surface into smaller areas inside which the mechanical properties of the stretched foil are sufficient to limit the deflection below 1 mm, including a safety margin for the deflection of the support structure itself. This critical size was determined in lab tests to be  $10 \times 10 \text{ cm}^2$ . Another important constraint for the lattice structure is that cross braces above readout pads should be avoided. For these reasons a rectangular grid design was chosen. The inhomogeneous lattice influences the PID performance in a negative way, since the parts of the active gas volume which are shadowed by it have a lower probability to be reached by TR-photons. The covered surface fraction can be reduced by using a lattice rip width as thin as 0.8 mm. The mechanical stability of the entrance window is not affected, since the stiffness perpendicular to the foil surface scales with rip height, which is 10 mm (15 mm) for the small (large) module type. The resulting surface coverage would in this case be of the order of 1%, but depends on the impact angle as shown in Fig. 5.7. It is the lowest for particles with an impact angle of  $0^\circ$ , where the shadowed fraction of the total surface is around 1%, and reaches a maximum value of approximately 9% for an angle of  $35^\circ$  in the case of a large module type. Figure 5.8 shows a drawing of the currently foreseen implementation of the grid, to be manufactured from carbon fibre material.

The active gas volume is enclosed on the four sides by two end strips made from G11 and a stack of three wire distance ledges (5.0 mm, 3.5 mm and 3.5 mm thick). The wire distance ledges define the distance between the two wire planes, whose geometrical arrangement is depicted in Fig. 5.9. A summary of the parameters of wire planes is given in Tab. 5.2. The gas volume is closed on the bottom side by the readout electrode, the pad plane. This PCB layer is glued to a honeycomb carbon fiber sandwich [C<sup>+</sup>01], which is carried by an outer aluminum frame. The last two components define the mechanical stability of the detector and compensate the wire tension. The design of the detector is optimized to maximize the acceptance of each detector plane. Therefore all supplies are routed and connected from the backside of the detector, including high voltage, gas, and LV supply of the readout electronics. E.g. the gas feedthroughs are inserted into the backpanel as shown in Fig. 5.6.

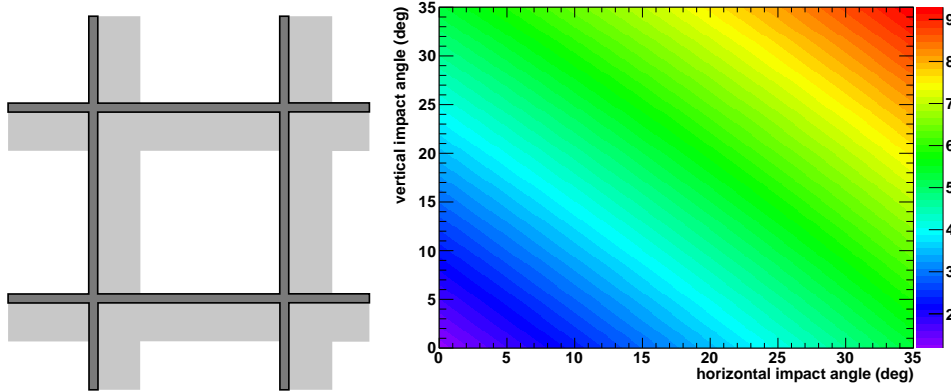


Figure 5.7: On the left side a schematic drawing of part of a support grid is shown. The dark gray area is covered by the lattice itself where the light gray area is the additional shadowed area seen by particles coming from the upper left side. The light gray area varies as a function of the horizontal and vertical impact angle of the particle relative to the chamber surface. The shadowed active area fraction in percent calculated for one TRD module of  $57 \times 57 \text{ cm}^2$  with  $4 \times 4$  lattice ribs of 0.8 mm width and a rib height of 10 mm as function of the horizontal and vertical impact angle is presented on the right side. The covered area is 1 % where the additional shadowed area fraction at maximum impact angles is 9 %.

	Anode wires	Cathode wires
Material	Cu-Be	W (Au-plated)
Diameter	75 $\mu\text{m}$	20 $\mu\text{m}$
Tension	100 cN	50 – 55 cN
Pitch	2.5 mm	2.5 mm
Nominal voltage	+1850 V	0 V

Table 5.2: Summary of the dimensions and parameters of the wire planes.

### 5.2.2 ROC production

The following description of the production procedure for TRD ROCs is based on the extensive experiences with the ALICE-TRD production and on the special requirements for the construction of the prototypes for the CBM-TRD (see Fig. 5.5). The detector assembly starts with the aluminum backpanel support frame. A 23 mm thick honeycomb carbon fiber sandwich [C<sup>+</sup>01] is glued to this frame using Araldite AW 106 and the remaining gap between them is filled with AW 116. This combination will ensure the mechanical stability of the chamber and compensate the wire tension from the anode as well as the cathode wires. After hardening of the backpanel pad plane sandwich the missing reamed holes for the wire distance ledges and the eight anode HV cable feedthroughs are drilled next to the wire distance ledge position in regular spacing through the pad plane backpanel. The pad side of the pad plane backpanel sandwich is finally cleaned with isopropanol. The wire distance ledges are prepared with a 2.5 mm copper adhesive tape glued to the 0.2 mm deep groove on the top side. The ledges are connected to the backpanel using AW 106 and Nylon aligning pins parallel to the long pad size direction to adjust a precise distance of 3.5 mm between the pad plane and the anode wires. The anode wires (20  $\mu\text{m}$  Au-plated W-wire) are wound to a wire transfer frame with a pitch of 2.5 mm and a tension of 50 – 55 cN. Technicoll is used to fix wires in position on the frame before dividing the frame in half. The wire grid is positioned and lowered to the wire ledges until the wires rest on top of the ledges. A schematic

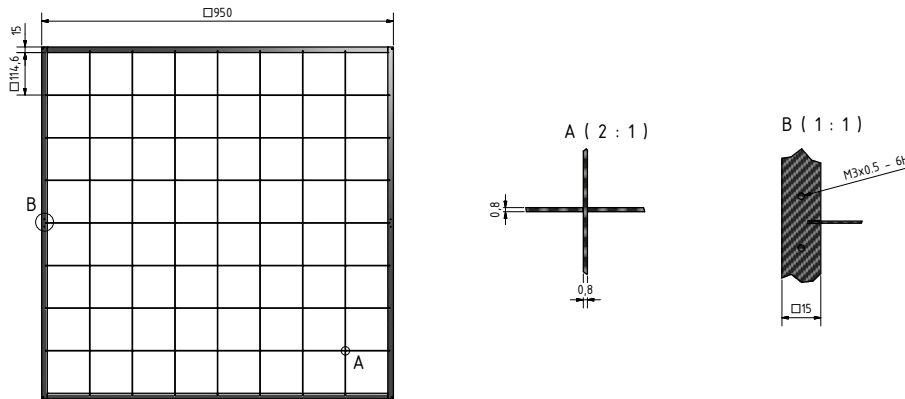


Figure 5.8: Drawing of the planned carbon support grid with a lattice rip of 0.8 mm and a height of 15 mm, as foreseen for a large module type.

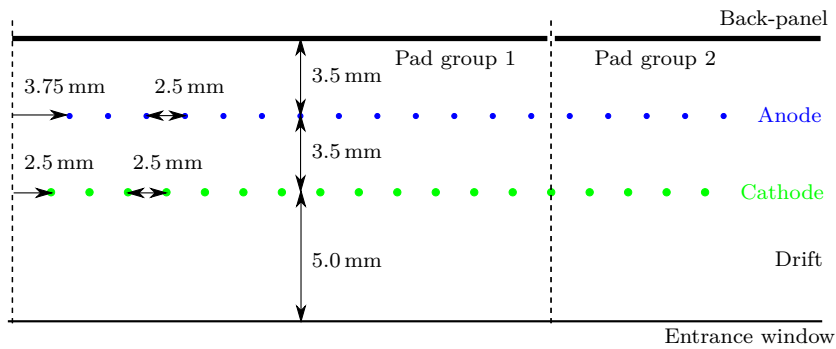


Figure 5.9: Schematic drawing of the anode and cathode wire grid positions relative to the pad plane and the entrance window.

drawing of the anode and cathode wire grid position relative to the pad plane is presented in Fig. 5.9. The anode wire copper strip is subdivided into eight equal anode sectors. A thin film of AW 106 is applied on top of the wire ledges and a second wire ledge of 3.5 mm thickness is put on top of this film to keep the wires in position. The second distance ledge on the opposite side of the anode wire copper strip is prepared with another copper strip to connect the cathode wires later. After hardening of the glue the wires are soldered to the copper strip and cut off the transfer frame. The anode HV cables are coated with a thin Technicoll film and pitched through the backpanel feedthroughs. The glue film ensures gas tightness and mechanical load removal from the soldering point on the copper strip, to which the anode HV cables are soldered. The cathode wires (75  $\mu$ m Cu-Be) are winded with the same spacing and a tension of 100 cN. The second wire plane is positioned staggered relative to the anode wire grid. The glueing procedure is analog to the anode procedure. A last wire distance ledge of 5.0 mm thickness is put on top of the glue film. The cathode wires are cut away from the transfer frame after hardening of the glue and soldered to the copper strip on the opposite side of the wire ledge, to which the anode wires have been soldered previously. The cathode cable is soldered to the copper strip. The open sides are completed by the end strip which is adjusted by another set of Nylon aligning pins.



Figure 5.10: Gas foil window supported with the carbon lattice window support structure.

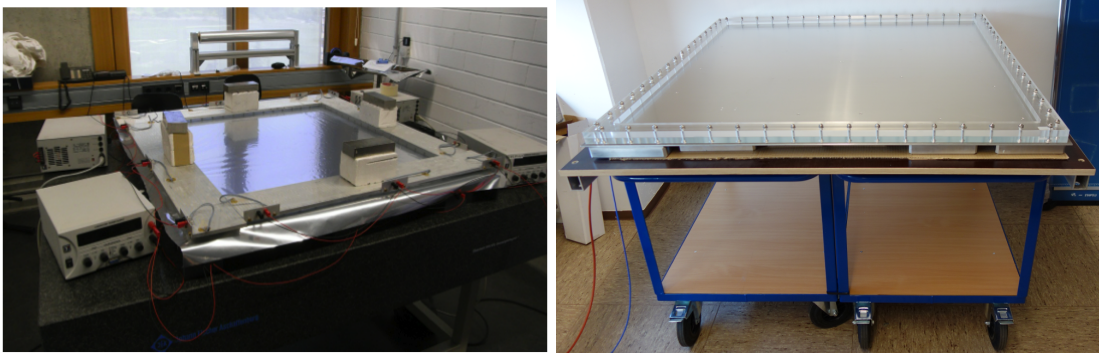


Figure 5.11: Devices to prepare the cathode foil for the entrance window at a well defined tension. The left picture shows the frame with heating coils and power supplies. A PMMA stretching frame on a aluminium heating plate for up to  $1 \text{ m}^2$  foils is presented on the right figure.

The largest  $25 \mu\text{m}$  Kapton foil dimension with a maximum deformation of  $1 \text{ mm}$  at a pressure difference of  $1 \text{ mbar}$  was estimated in tests to be  $10 \times 10 \text{ cm}^2$ , which thus defines the spacing of the carbon lattice grid. To this grid a foil of  $25 \mu\text{m}$  Kapton with  $0.05 \mu\text{m}$  aluminum on one side will be attached. The foil can be stretched by the thermal expansion of a Plexiglas, PMMA (PolyMethylMethAcrylate), frame from  $20^\circ \text{C}$  to  $50^\circ \text{C}$ . This procedure is based on a development for GEM foils and in principle described in [S<sup>+</sup>11]. In the version foreseen for the CBM-TRD the foil prepositioning is done using Kapton adhesive tape. It is fixated in the frame by 52 screws, which are tightened with  $20 \text{ Nm}$  per screw. The thermal expansion coefficient  $\alpha$  at  $25^\circ \text{C}$  is  $82.8 \cdot 10^{-6} \text{ K}^{-1}$  for PMMA. The heat deflection temperature of PMMA is between  $65 - 105^\circ \text{C}$  which gives the upper temperature limit for this procedure. The total expansion of the frame ( $(69.0 \pm 0.1) \times (69.0 \pm 0.1) \text{ cm}^2$  at  $20 \pm 1^\circ \text{C}$ ) from  $20^\circ \text{C}$  to  $50^\circ \text{C}$  is calculated to  $0.17 \pm 0.01 \text{ cm}$  ( $0.207 \pm 0.009 \%$ ). The Kapton foil has a thermal expansion coefficient of  $20.0 \cdot 10^{-6} \text{ K}^{-1}$ . The Kapton foil itself expands about  $0.04 \pm 0.01 \text{ cm}$  ( $0.06 \pm 0.002 \%$ ). The difference between both materials gives the elongation of the Kapton foil. A first version of a foil stretching device working according to this principle has already been used for the production of prototype TRD modules [Sei14]. Figure 5.11 shows the device, which consists of an aluminum frame that is attached to the foil and can be heated by electrical heating elements to a well defined temperature (here

typically  $55^{\circ}\text{C}$ ). This approach can easily be applied to the large-scale production of the MWPCs of the CBM-TRD.

This gas window is glued to the chamber body to enclose the gas volume. The electrical connection to the aluminized Kapton gas window is realized by an overlapping part of the Kapton foil crimped over a copper strip covered on both sides with silver glue. The drift HV cable is soldered to this copper strip after hardening. The copper strip is afterwards covered by a Kapton adhesive tape to ensure electrical isolation to the outside. The chamber is closed by glueing the support grid gas window on top of the active detector volume. The gaps on the two wire ledge stack sides are filled with AW 106 to ensure gas tightness and increase mechanical stability. The anode, cathode and drift cables are soldered to the HV filter board, one first order low-pass pre-filter ( $1\text{ M}\Omega$  resistor and  $4.7\text{ nF}/3\text{ kV}$  capacitor) followed by eight channel individual first order low-pass filter ( $1\text{ M}\Omega$  resistor and  $2.2\text{ nF}/3\text{ kV}$  capacitor) on the anode section and one first order low-pass filter ( $1\text{ M}\Omega$  resistor and  $4.7\text{ nF}/3\text{ kV}$  capacitor) for the drift HV. The common ground potential bar for the drift and anode filter sections is connected via one  $1\text{ k}\Omega$  resistor on each side to the floating ground of each HV power supply. The filter board is mounted on the backside of the backpanel inside of a cable shaft.

### 5.2.2.1 Entrance window stress test

Since the  $25\text{ }\mu\text{m}$  Kapton foil entrance window is the mechanically most fragile part of the detector, it had to undergo a one year mechanical stress test operation. The main mechanical stress to this component is provoked by pressure variations due to weather changes. An estimate on the distribution of air pressure variations within time windows of 10 min is given by a measurement of the atmospherical pressure. The presented maximum pressure variations within time windows of 10 min (see Fig. 5.12) have been extrapolated to a full year.

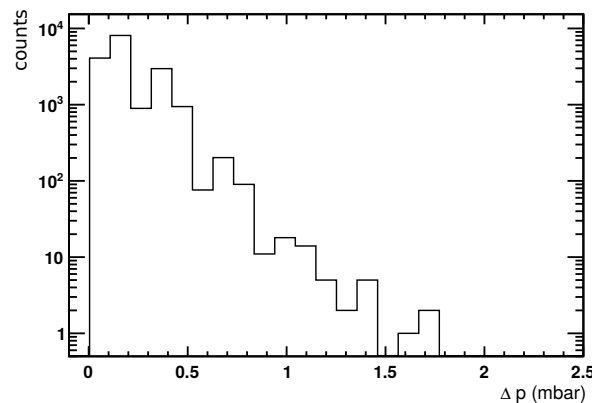


Figure 5.12: The maximum air pressure variations within 10 minute intervals measured over about four months are presented. The following stress test simulates the variations assumed for one year of operation and is based on an extrapolated version of this distribution. The detector gas flow through the detector is adjusted to  $31/\text{h}$  Ar/CO<sub>2</sub> (82/18). The test sequence is started with the lowest pressure variations on the left side of the histogram. The pressure variations have been applied at constant gas flow by closing an electric valve at the gas exhaust pipe behind the chamber.

The differential gas pressure has been measured in front and behind the chamber. As observable for the condition of the foil window, the oxygen content of the gas mixture at the exhaust has been continuously monitored. The pressure variation was realized using an electric valve, closing the gas exhaust. An example for a 1.5 mbar overpressure sequence is presented in Fig. 5.13. The short spikes in the oxygen content at the exhaust of the chamber have been

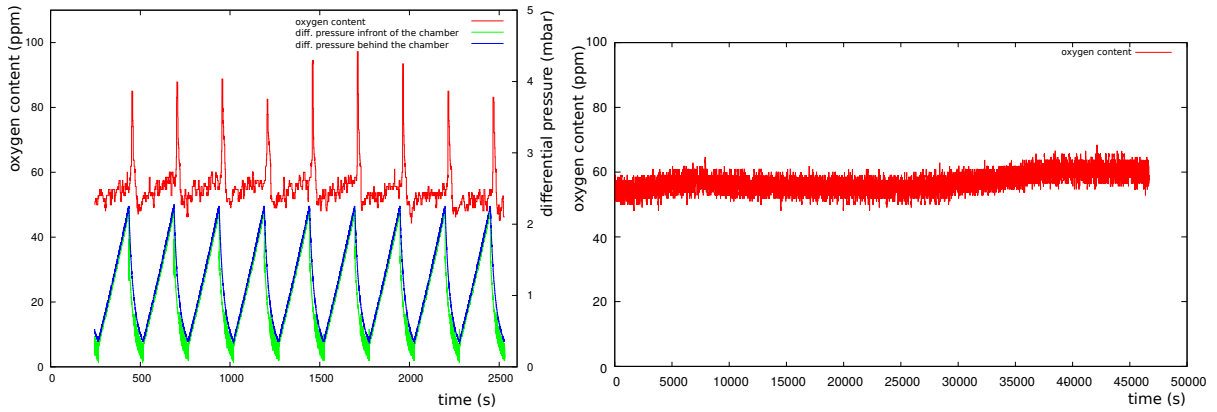


Figure 5.13: Left: A fraction of a 1.5 mbar pressure sequence is presented. The differential pressure in the gas system in front (blue) and behind (green) the chamber is presented in combination with the oxygen content (red) of the gas mixture after passing the chamber. Right: The leakage rate of the detector under test has been tested after the full one year test sequence. The oxygen content is at the same level compared to a measurement before the stress test.

identified as gas backflow during the retain of the gas within the chamber. As result of this procedure, the chamber has been found to be in the same condition after one year of operation since the leakage test before and after the test showed the same level of oxygen contamination.

### 5.2.3 Electrostatic calculations

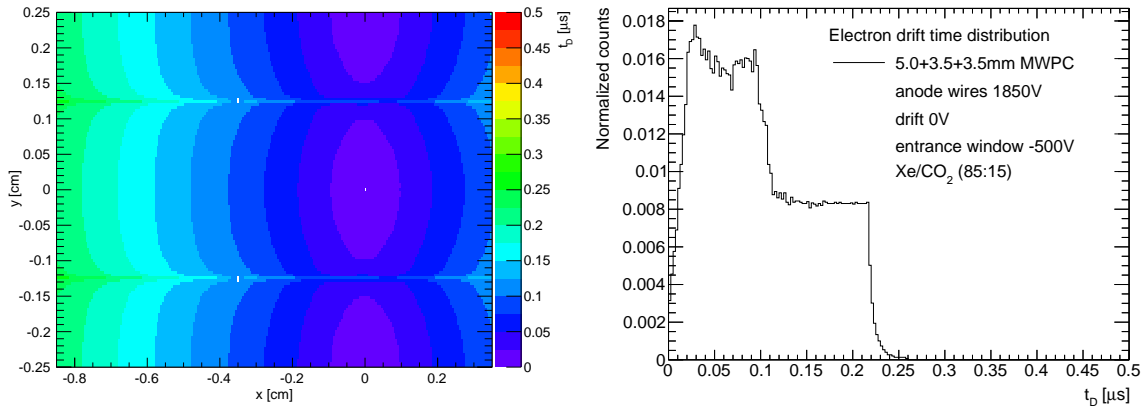


Figure 5.14: GARFIELD calculation of the electron drift times  $t_D$  in the default chamber geometry (3.5 + 3.5 mm amplification and 5.0 mm drift region) for an anode voltage of 1850 V and a drift voltage of  $-500$  V. Shown is  $t_D$  as a function of the spatial coordinates  $x$  (drift direction) and  $y$  inside a drift cell (left) and the projected  $t_D$  distribution (right).

The GARFIELD simulation program [Vee98] was used to determine the properties of the proposed ROC design. The default wire geometry of 3.5 + 3.5 + 5.0 mm results in electron drift time distributions as shown in Fig. 5.14. Inside the amplification region the electrons are collected on the anode wires within  $0.1 \mu\text{m}$ . To this the drift region adds further  $0.125 \mu\text{m}$ . These drift times depend on the position of the primary ionization relative to the corresponding anode wire, as illustrated in the two-dimensional distribution shown in the left panel of Fig. 5.14.

An important point that needs to be addressed with these calculations is to which extend

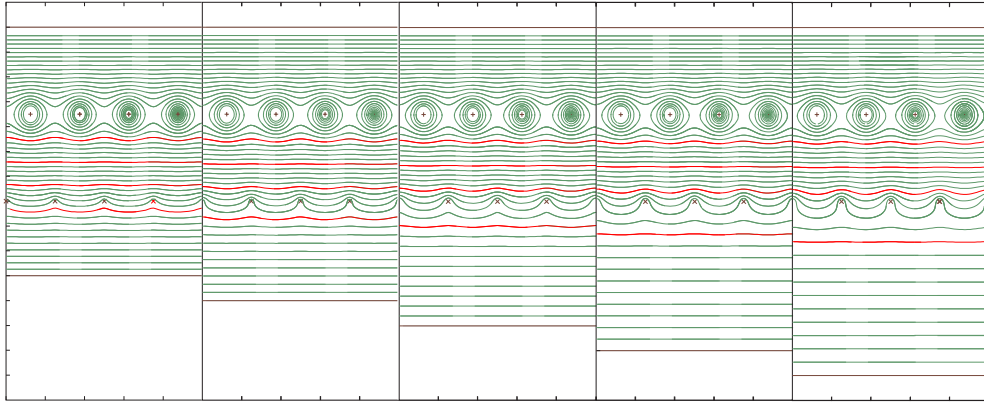


Figure 5.15: GARFIELD drift field scan for deformed gas windows of  $\pm 1$  mm and  $\pm 2$  mm for a constant drift voltage of  $-500$  V. The nominal geometry is  $3.5 + 3.5 + 5$  mm (central panel). From left to right the deformation is  $-2$  mm,  $-1$  mm,  $0$  mm,  $+1$  mm, and  $+2$  mm. The potential lines for  $0$ ,  $250$ ,  $500$ , and  $750$  V between the anode and cathode wire plane are highlighted in red.

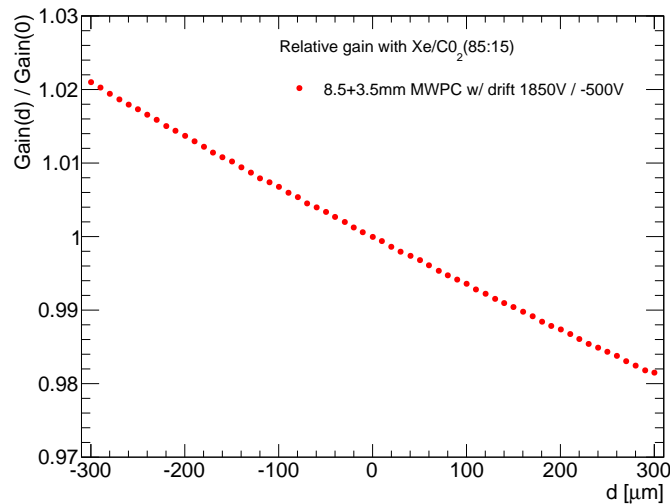


Figure 5.16: The relative gain variation as a function of the displacement  $d$  of the entrance window position as calculated with GARFIELD.

mechanical deformations of the entrance window foil modify the electric field and thus the corresponding gas gain. Figure 5.15 shows the field lines as simulated with GARFIELD. The middle panel displays the configuration for the nominal geometry, i.e. an  $3.5+3.5$  mm amplification and  $5$  mm drift region. To the left (right) the effect of a  $-1$  mm and  $-2$  mm ( $+1$  mm and  $+2$  mm) deformation of the entrance window is shown. As can be seen, a deformation of  $\pm 1$  mm already leads to visible distortions of the electric fields also inside the amplification region and thus alters the resulting gain. This effect is further quantified in Fig. 5.16, which displays the expected relative variation of the gain factor as a function of the displacement of the entrance window. A shift of its position by  $\pm 300$   $\mu\text{m}$  results in gain variations of around  $\pm 2\%$ . Restricting the deformations to below  $1$  mm will therefore ensure that local gain changes will be significantly smaller than  $10\%$ . These remaining gain variations can easily be corrected by the corresponding calibration method (see Sect. 9.4).

### 5.3 Pad planes and front end boards

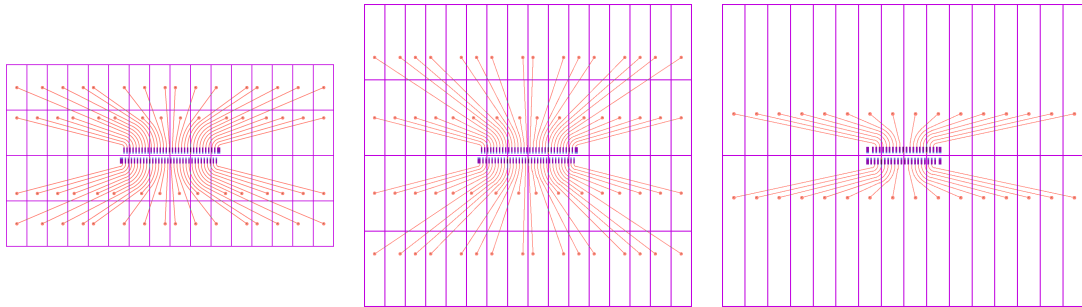


Figure 5.17: Layout of the different pad plane traces (shown at different scales). Left: 64 channel footprint, module type 1 (4 rows of 16 pads, *super density*). Middle: 64 channel footprint, module type 2 (4 rows of 16 pads, *super density*). Right: 32 channel footprint, module types 3,6,7 and 8 (2 rows of 16 pads, *regular density*).

The charge generated in the amplification region induces a signal on the segmented pad plane, which constitutes the part of the TRD backpanel that faces the chamber interior. The signals seen by the individual pads are directly fed into the FEBs, which will be mounted on the outer side of the backpanels. The FEBs provide the readout and infrastructure for the SPADIC ASICs, as described in Chap. 7.

#### 5.3.1 Pad plane layout

Module type	# Columns	# Rows	# Pads	Height (cm)	Width (cm)	Area (cm <sup>2</sup> )
1	80	36	2880	1.5	0.68	1.01
2	80	20	1600	2.5 / 2.75	0.68	1.69 / 1.86
3	80	12	960	4.5	0.68	3.04
6	128	16	2048	5.75	0.72	4.13
7	128	8	1024	11.50	0.72	8.27
8	128	6	768	15.50 / 15.25	0.72	11.14 / 10.96

Table 5.3: The parameters characterizing the pad plane layout for the different TRD module types. Given are the number of pads in row and column direction, as well as the corresponding pad dimensions. The module types 2 and 8 have pads of 2 different heights in their middle and outer sectors.

The pad plane layout has to respect several constraints. While for the smaller modules in the inner detector regions they can still be produced as a single PCB, for the large modules they will have to be constructed from two or more separate PCB pieces, since they cannot be produced in the required size. The dimensions of the pads depend on the configuration of the wire grid. E.g. the length of the pads needs to be an integer multiple of the anode wire spacing. Also, it should be ensured that the length of the traces leading from the pads to the connectors is minimal in order to reduce cross talk. Therefore, the pads from two or four different pad rows will be grouped onto a single connector. In order to achieve the necessary channel integration for the different pad sizes, 64 pads (*super density*, see left and middle panels of Fig. 5.17), and blocks of 32 pads (*regular density*, see right panel of Fig. 5.17) are currently foreseen. The shown layouts provide the shortest possible trace lengths from the connector to the pad locations. By

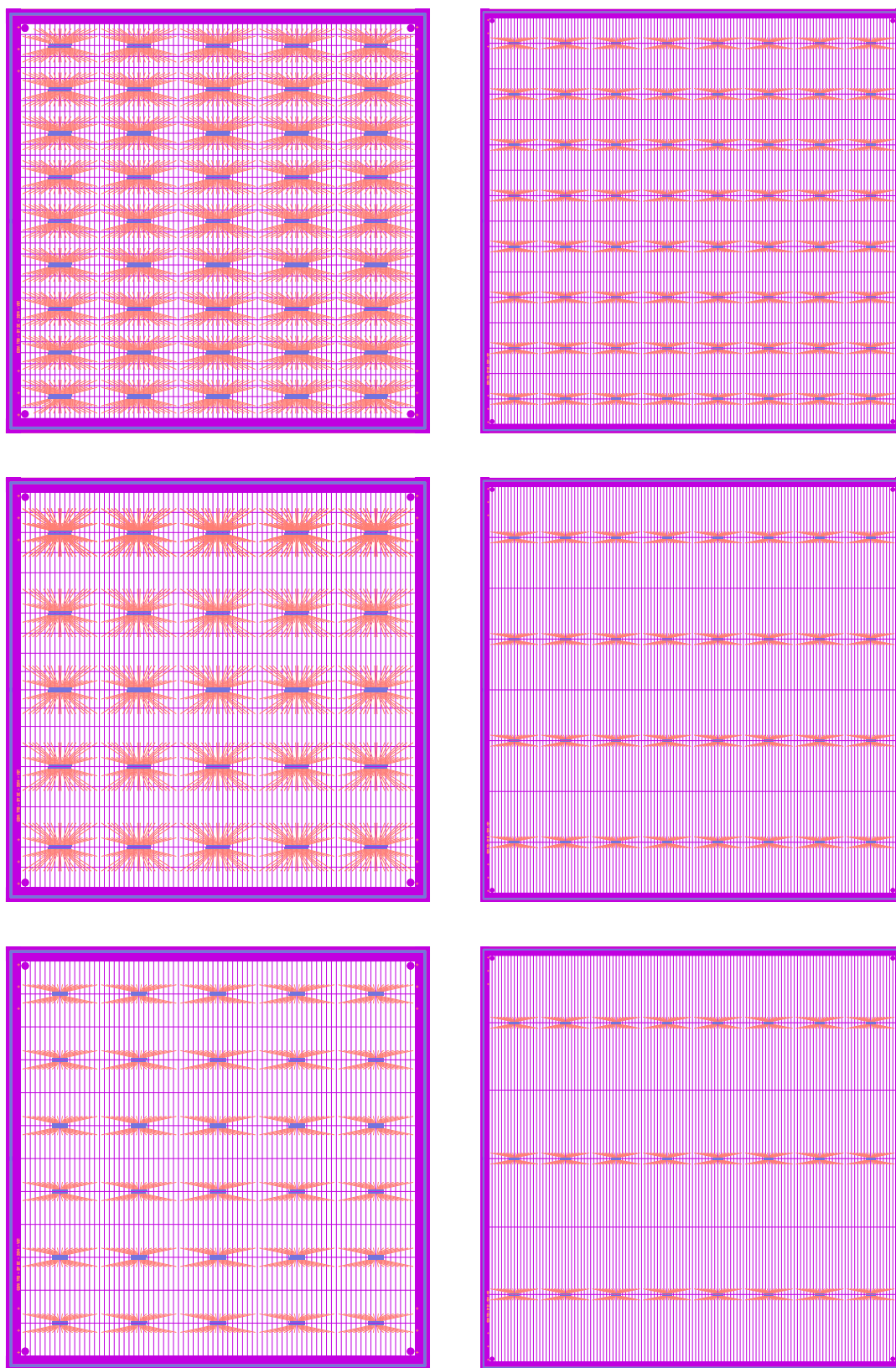


Figure 5.18: The pad plane layout for all six module types. From top to bottom in the left column the small module types 1, 2 and 3 are shown, while in the right column, at a different scale, the large module types 6, 7 and 8 are presented.

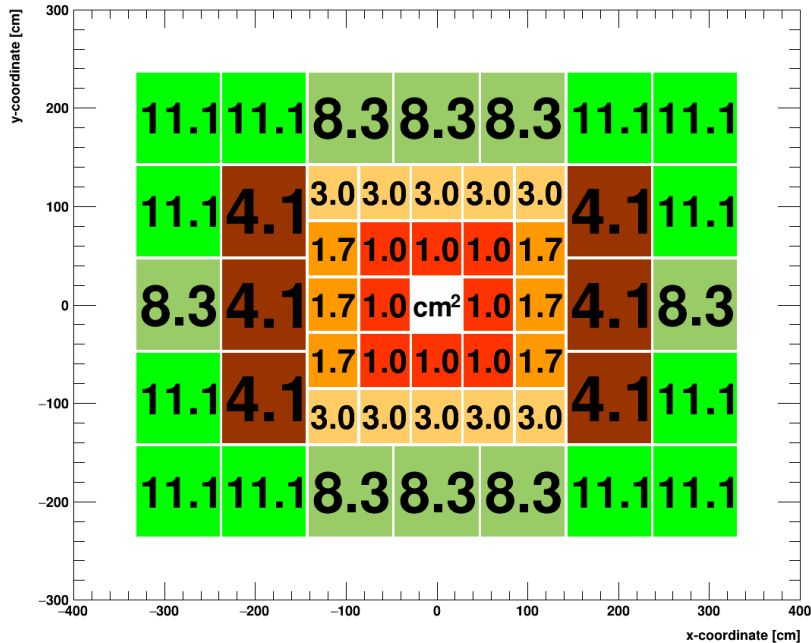


Figure 5.19: The distribution of pad sizes in the CBM-TRD geometry. The values correspond to the pad areas in  $\text{cm}^2$ .

grouping the pads this way the number of pads in a given row will be fixed to a multiple of 16, while the connectors and cables will be for 32 or 64 channels.

The sizes of the readout pads have to be adjusted to the expected hit densities in the different areas of the CBM-TRD. Based on simulations using UrQMD events for Au + Au collisions at 10 AGeV, using the latest CBM geometry with a realistic material budget, the pad sizes have been determined such that the trigger rate always stays below 100 kHz (see Sect. 4.5). On the other side, one would like to avoid to have too many different pad plane layouts in the whole detector design in order to facilitate the module production. In the current design only six different pad planes (see Fig. 5.18) are needed, three for the smaller modules and three for the larger ones. The result of this optimization procedure is summarized in Tab. 5.3 and the arrangement of the different pad plane types in one CBM-TRD plane is shown in Fig. 5.19.

### 5.3.2 Front end board arrangement

The FEB design has to reflect the different channel densities. One ASIC is designed for 32 channels. In the case of a 64 channel connector and cable, two ASICs have to be grouped. To minimize the amount of material introduced by the FEBs into the detector setup, the number of channels per FEB should be chosen as high as technically possible. Currently foreseen are two different FEB types for the small modules with 160 and 320 channels (notation: FEB\_05n and FEB\_10s, respectively). For the large modules only one type of FEB with 256 channels (notation: FEB\_08n) is planned. Figure 5.20 shows the corresponding configurations together with the small and the large detector module.

The six different module types of the CBM-TRD together with their corresponding FEB types mounted on the back are shown in Fig. 5.21. The upper row shows the small modules, the lower row the large ones. While for the small modules FEBs with regular and super density are needed, for the large ones the regular density FEB is sufficient. The number of mounted

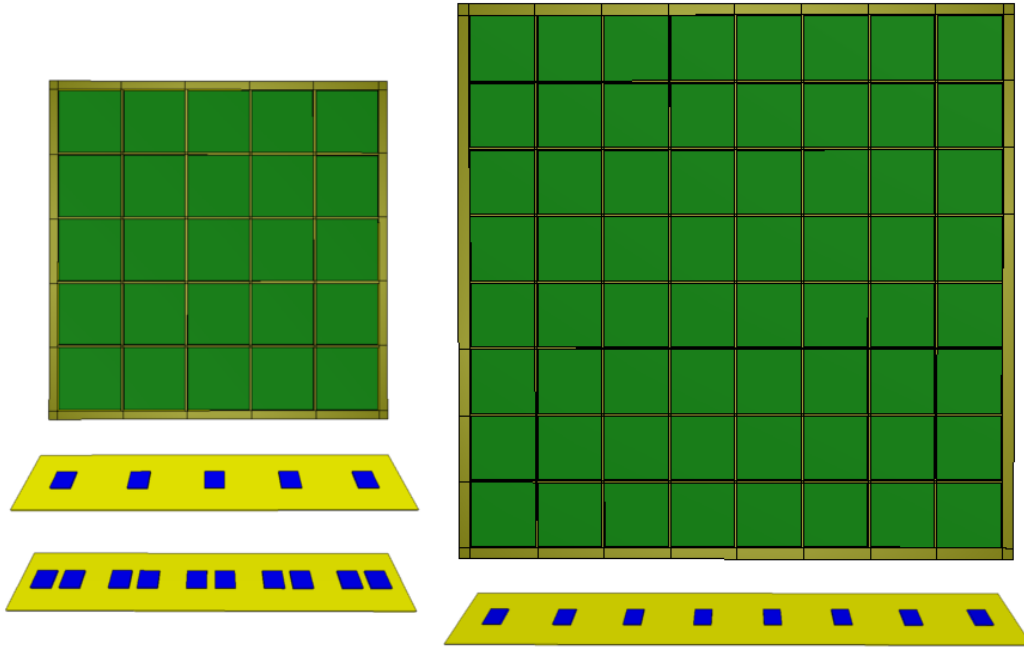


Figure 5.20: TRD modules and related FEB types: regular and super density, with  $5 \times$  and  $10 \times$  32-channel ASICs (notation: FEB\_05n, FEB\_10s) for the small and  $8 \times$  32-channel ASICs (notation: FEB\_08n) for the large module type.

FEBs increases with decreasing pad size. A more detailed view on the six different module types equipped with FEBs is also shown in Appendix C in the Figs. C.1 and C.2. Table 5.4 summarizes the essential parameters of the different FEB types and also lists the number of FEBs and ASICs needed.

FEB type	Module types	ASICs/FEB	Channels/FEB	FEBs/module	No. of FEBs
FEB_10s	1 / 2	10	320	9 / 5	408
FEB_05n	3	5	160	6	240
FEB_08n	6 / 7 / 8	8	256	8 / 4 / 3	464
<b>Total number of ASICs:</b>		<b>8,992</b>			

Table 5.4: Summary on the different FEB types together with the total number of needed ASICs.

It is planned to directly mount the FEBs to the backpanel of the ROCs. Due to their relatively small area only lightweight holding structures will be needed, which can be glued to the backpanel. For the mounting of the FEBs several options with different tilting angles  $\alpha$  are possible. Assuming a height of the PCB board of 6.0 cm, all TRD module types would in principle provide enough space to install the FEBs flatly at the outer side of the backpanel (i.e.  $\alpha = 0$ ). This arrangement would provide the most evenly distributed material budget. However, in order to be able to properly route cables and also cooling lines where needed, the FEBs might have to be installed with a tilting angle  $\alpha > 0$ , especially for modules with a higher integration density, e.g. type 1, 2, 3 or 6, see Fig. 5.21. For these cases,  $\alpha$  should be chosen such to ensure a minimal non-uniformity of the resulting material budget. In the current simulations  $\alpha = 45^\circ$  is assumed for all module types.

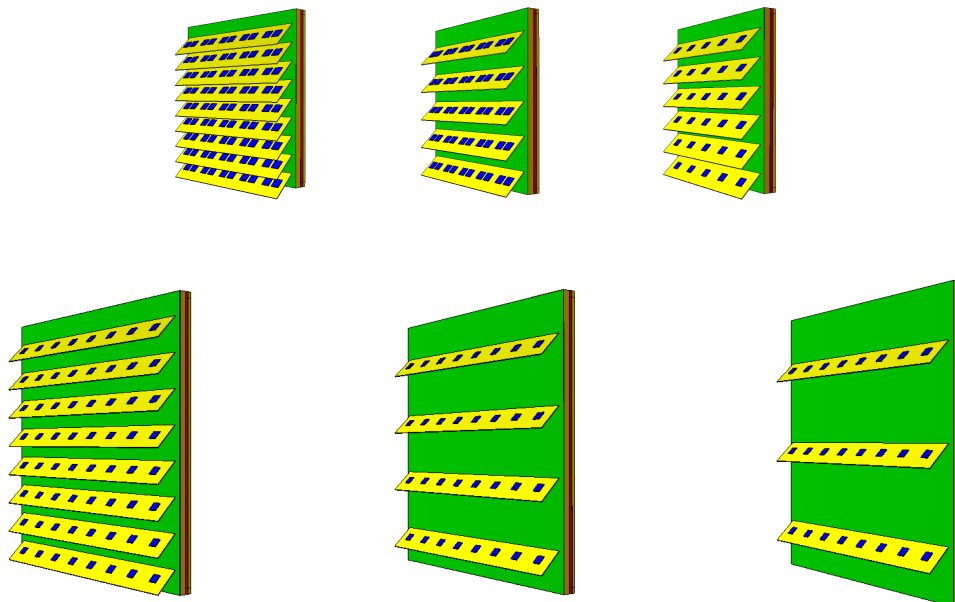


Figure 5.21: Rear views of the six different TRD module types 1, 2, 3 (top row), and 6, 7, 8 (bottom row), equipped with the corresponding FEBS shown in yellow, as implemented in the simulation software.

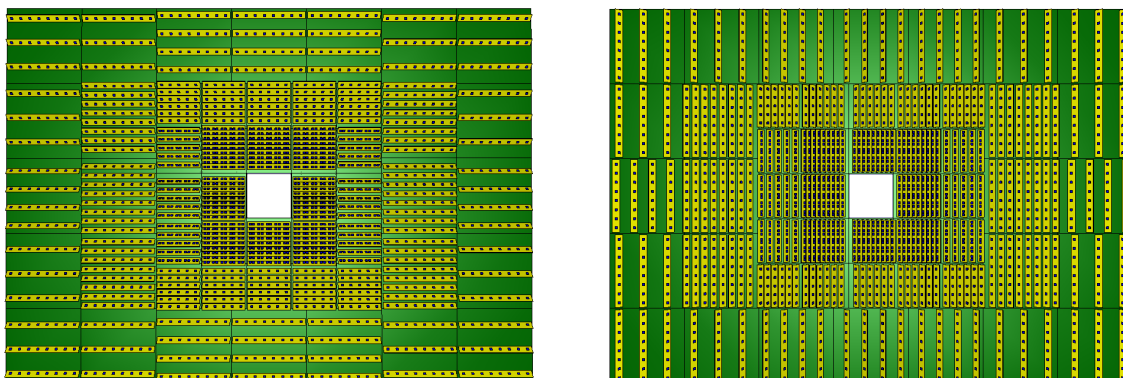


Figure 5.22: Rear view of two different TRD layers, illustrating the orientation of FEBS on the modules.

## Chapter 6

# Radiator

This chapter summarizes the approaches to theoretically describe the behaviour of different radiator types. These effective descriptions are on one hand the basis for the simulation of the TRD detector response, as described in Sect. 9.2. On the other hand, they have been employed to identify the optimal radiator solution and to match the design of the readout chambers to the spectral distribution of the produced TR-photons. Finally, the most promising radiator options for the CBM-TRD are presented and their properties discussed.

### 6.1 Theoretical description of radiators

Radiators are devices used to produce TR-photons emitted at periodic material boundaries between materials with different dielectric constants  $\epsilon$ . Such boundaries can be realized in different ways: regular foil, foam and fiber radiators. The essential property of the radiator material is the plasma frequency  $\omega_P$ . To calculate this property the average electron density  $n_e$  is needed, which is correlated to the average atomic number  $Z$  of the material. The  $Z$ ,  $A$  (atomic mass number),  $\rho$  (density), and  $\omega_P$  values of different materials can be found in Tab. 6.1. There are two main classes of radiators, the regular radiators mostly made from equally spaced foils and the irregular radiators made from foams or fiber mats. The regular radiators utilize coherent interference and produce a larger number of photons per incident electron and boundary, while the mean number of photons is lower in case of irregular radiators due to the missing coherent interference and/or the smaller structure size in foams or fiber mats. This lower number of photons and smaller mean photon energy can partially be compensated by a higher number of boundaries per unit length, since the average structure sizes are smaller.

#### 6.1.1 Regular radiators

The simplest scenario of TR production by a relativistic particle with a Lorentz factor  $\gamma$  considers a single interface which is crossed by the charged particle. The expected double differential photon spectrum is

$$\left( \frac{d^2 N}{d\omega d\vartheta} \right)_{\text{interface}} = \frac{\alpha}{\pi} \cdot \left( \frac{\vartheta}{\gamma^{-2} + \vartheta^2 + (\omega_{P,1}/\omega)^2} - \frac{\vartheta}{\gamma^{-2} + \vartheta^2 + (\omega_{P,2}/\omega)^2} \right)^2 \quad (6.1)$$

with the emission angle relative to the direction of motion  $\vartheta$ , the foil ( $i = 1$ ) and gap ( $i = 2$ ) plasma frequency  $\omega_{P,i}$  and the fine structure constant  $\alpha$ . The plasma frequency is given by

$$\omega_{P,i} = \sqrt{\frac{n_e \cdot e^2}{\epsilon_0 \cdot m_e}} = \sqrt{\frac{4\pi\alpha n_e \hbar c}{m_e/c^2}} \quad (6.2)$$

where  $m_e$  is the electron mass [AW12]. The average electron density  $n_e$  can be calculated as follows

$$n_e = \frac{\rho \cdot N_A \cdot Z}{A} \quad (6.3)$$

where  $\rho$  is the density,  $N_A$  the Avogadro constant and  $A$  the average mass number. The average atomic number  $Z$  can be approximated for  $i$  materials by using the relative weighting factor  $w_i$

$$Z = \sum_i w_i \cdot Z_i \quad (6.4)$$

This scenario can be extended to a foil with two surfaces

$$\left( \frac{d^2 N}{d\omega d\vartheta} \right)_{\text{foil}} = \left( \frac{d^2 N}{d\omega d\vartheta} \right)_{\text{interface}} \cdot 4 \sin^2 \left( \frac{l_1}{2z_i} \right) \quad (6.5)$$

with  $z_i$  being the formation zone (Eq. 6.6) for the two media [CHMP74]. Both, foil thickness  $l_1$  and gap dimension  $l_2$ , should be greater than the formation zone  $z_i$ , which is typically of the order of 10  $\mu\text{m}$  for plastic and 700  $\mu\text{m}$  for gases like air.  $z_i$  is given by

$$z_i = \frac{2\beta c}{\omega} \cdot \left( \gamma^{-2} + \vartheta^2 + \left( \frac{\omega_{P,i}}{\omega} \right)^2 \right)^{-1} \quad (6.6)$$

where  $\omega$  is the photon frequency and  $\vartheta$  the photon emission angle with respect to the particle trajectory. All formulas up to now do not include self-absorption within the radiator material. Self-absorption is relevant in the low energy part of the spectrum, i.e. below a few keV. The production probability for a photon at a single foil is of the order of  $1/\alpha$ . To increase the particle separation performance, the number of interfaces has to be enhanced within a given radiator. A periodic radiator with  $N_f$  layers of thickness  $l_1$  and spacing  $l_2$  can be described by

$$\left( \frac{d^2 N}{d\omega d\vartheta} \right)_{\text{stack}} = \left( \frac{d^2 N}{d\omega d\vartheta} \right)_{\text{foil}} \cdot \exp \left( \frac{(1 - N_f)\sigma}{2} \right) \frac{\sin^2 \left( \frac{N_f \phi_{12}}{2} \right) + \sinh^2 \left( \frac{N_f \sigma}{4} \right)}{\sin^2 \left( \frac{\phi_{12}}{2} \right) + \sinh^2 \left( \frac{\sigma}{4} \right)} \quad (6.7)$$

with  $\phi_{12} = \phi_1 + \phi_2$  and

$$\phi_i \simeq \frac{1}{2} \left( \gamma^{-2} + \vartheta^2 + \left( \frac{\omega_{P,i}}{\omega} \right)^2 \right) \omega l_i \quad (6.8)$$

and  $\sigma$  being the total photon absorption cross section  $\sigma$  ( $\sigma = \mu_1 \cdot l_1 + \mu_2 \cdot l_2$ ) for one foil and gap layer. The mass attenuation coefficient  $\mu/\rho$  for different elements, compounds and mixtures can be found in the National Institute of Standards and Technology (NIST) XCOM database [BO98]. The emission angle  $\vartheta$  integral of this formula can be approximated as:

$$\frac{dN}{d\omega} = \frac{4\alpha}{\omega(\kappa + 1)} \frac{(1 - e^{-N\sigma})}{(1 - e^{-\sigma})} \cdot \sum_n \Theta_n \left( \frac{1}{\varrho_1 + \Theta_n} - \frac{1}{\varrho_2 + \Theta_n} \right)^2 [1 - \cos(\varrho_1 + \Theta_n)] \quad (6.9)$$

according to [Maz00]. This equation includes coherent and incoherent effects as well as the self-absorption of gap and foil material. Therefore it was used to calculate the total yield per keV in the following section. Equation 6.9 provides an accurate description of the spectra within  $\pm 15\%$  [FS75]. It uses the relation

$$\varrho_i = \frac{\omega l_1}{2c} \left( \gamma^{-2} + \left( \frac{\omega_{P,i}}{\omega} \right)^2 \right), \quad (6.10)$$

with the definitions

$$\kappa = \frac{l_2}{l_1} \quad (6.11)$$

and

$$\Theta_n = \frac{2\pi n - (\varrho_1 + \kappa\varrho_2)}{1 + \kappa} > 0. \quad (6.12)$$

Systematic deviations between measurements and theoretical predictions arising from the material budget of the radiator and the MWPC and possible irregularities of the radiator can be compensated by introducing an attenuation factor  $a$ , defined in the range  $[0,1]$ :

$$\left(\frac{dN}{d\omega}\right)_{\text{measurement}} = a \cdot \left(\frac{dN}{d\omega}\right)_{\text{theoretical}}. \quad (6.13)$$

### 6.1.2 Irregular radiators

A spectral distribution of TR-photon production in an irregular radiator, consisting of parallel plates of random thickness, is given by Garibian et al. [GGY75]. This formulation can be modified to take into account the presence of a material in the gap. However, the usage of this model is quite challenging, since it implies a perfect knowledge of the two distributions of the foil and gap thicknesses. In reality this causes problems especially in the case of foam radiator materials. The bubble size depends on several parameters and varies within the same foam over a wide range. These distributions are not homogeneous in all three dimensions within the same foam sample. The bubble diameters can also vary due to gravitation. Large bubbles accumulate at the top of the foam, since they have lower average material density, and smaller bubbles at the bottom. Such density gradients are more distinct for foams with longer hardening time and/or low viscosity of the solid, respectively liquid, components. The most homogeneous distribution in commercial Polyethylene (PE) foams have been found for rather thin foam sheets (sheet thickness only up to 1 – 3 times larger as the average bubble size) which are not produced as parts of a larger piece. A schematic drawing illustrating the characteristics of a liquid/gas or solid/gas foam bubble is presented in Fig. 6.1. The films are thin sheets of liquid (solid, after hardening)

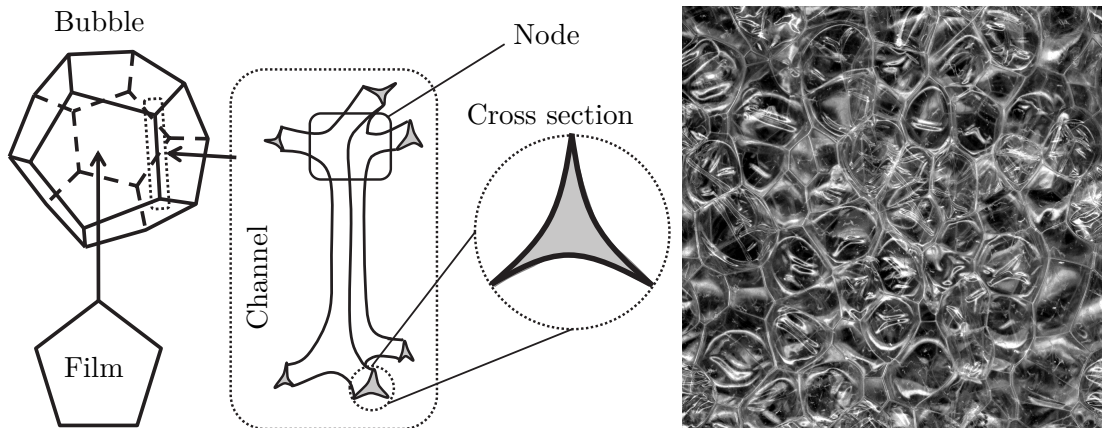


Figure 6.1: Left: Schematic of a dodecahedral bubble and the wall channel based on [C<sup>+</sup>13a]. Right: Foam structure of a  $19 \times 19 \text{ mm}^2$  and 5 mm thick Cell-air polyethylene foam sample.

separating two bubbles. The channels are thin liquid or solid columns formed at the intersection of three bubbles. The channels are also known as plateau borders. The cross section of a channel resembles a triangle with edges curved towards the interior. The channels form a network of pipes that allow liquid to flow through the foam. The junctions where the channels intersect are called nodes, and four channels meet at a single node [C<sup>+</sup>13a]. This description implies a very

complex inner structure of the foam with thin film structures, relatively thick channels and more or less spheric bubbles.

The description of the solid fiber or fleece components is in most cases easier. In [Ber14] it was observed that the fiber diameters showed only a small variation within the same sample that was investigated, but at the same time have a broad spectrum of gap spacings as presented in Fig. 6.2. Nevertheless, the description of gap distributions is very complex in case of fleece

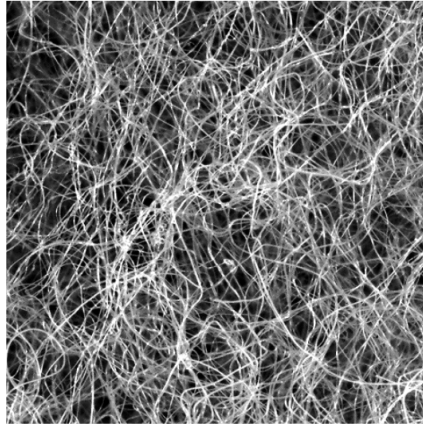


Figure 6.2: Fiber structure of a  $10 \times 10 \text{ mm}^2$  Polypropylene fleece sheet.

materials and depends on too many parameters such as fiber length, diameter, bendability and production process, and would thus demand a three dimensional measurement without any outer forces on the material disturbing the material properties.

Based on the previous argumentation and the fact that the pure photon spectrum defies any attempt of direct measurement with a MWPC, a description of irregular radiators is not used here. Instead, the emission and absorption spectra, presented in the following, are based on a realistic material budget, but are calculated for a regular toy model radiator using Eq. 6.9 with average parameters  $\langle l_1 \rangle$ ,  $\langle l_2 \rangle$  and  $\langle N_f \rangle$ . The resulting spectra are scaled by a weighting factor  $a$  to describe the measured total energy loss spectra ( $dE/dx + \text{TR}$ ) as good as possible. The full material budget between radiator and backpanel, i.e. the single sided aluminized Kapton foil, the wires and the Xe/CO<sub>2</sub> gas mixtures, are taken into account. The absorption maximum  $\omega_{\text{max}}^{\text{abs.}}$  of the 2012 prototypes is at 5.66 keV, as presented in Fig. 6.3. It is essential to understand the influence of radiator parameters like material, number of foils and foil as well as gap thickness to optimize the TR-yield with respect to the absorbed spectrum seen by a readout chamber. The materials, which constitute the main components of possible radiators, have different properties like stability, conductivity, and cross section. The material properties, which are essential for this optimization, are shown in Tab. 6.1. The different material parameters, such as density and plasme frequency, are chosen over a wide range of values, corresponding to the tested radiator prototypes.

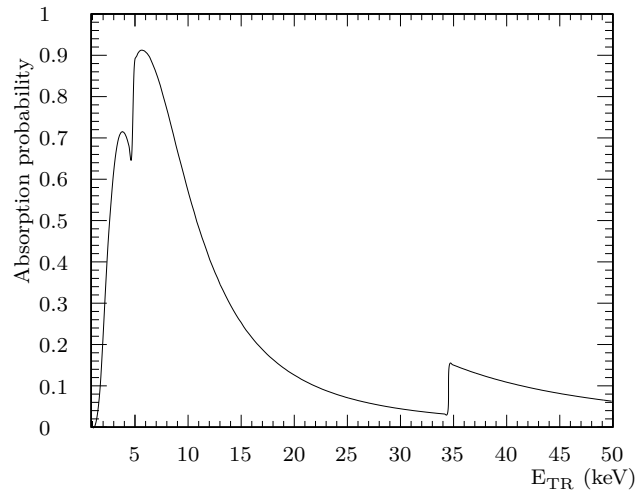


Figure 6.3: The absorbed photon spectrum as seen by one readout chamber including the transmission of the frontpanel components.

Table 6.1: Gap and foil material properties:  $Z$ ,  $A$ ,  $\rho$  and  $\omega_P$  at a pressure of 101.325 kPa and a temperature of 293.15 K. The properties of mixed materials are not presented in case of foams or fibers. The gaseous and solid components are presented separately within the first part of the table and are used as simulation input.

Material	$Z$	$A$	$\rho$ (g/cm <sup>3</sup> )	$\omega_P$ (eV)
Air	14.49	29.02	$1.2 \cdot 10^{-3}$	0.71
Mylar	4.55	8.73	1.393	24.53
POKALON N470	4.06	7.71	1.150	22.43
Polyethylene (PE)	2.67	4.68	0.900	20.65
Polypropylene (PP)	2.67	4.68	0.900	20.65
Polymethylmethacrylate (PMMA)	3.18	5.89	1.180	22.99

## 6.2 Optimization procedure

The optimal radiator parameters are strongly correlated with the detector characteristics. A good matching between the photon absorption probability spectrum (presented in Fig. 6.3) and the TR-photon production spectrum leads to an optimal PID performance of the entire detector system. The shape of the TR-spectrum is mainly influenced by the foil and gap thickness. The total yield can be modified by the used number of foils. A numerical approach has been chosen to optimize the energy loss due to TR-photon emission per electron as presented in Fig. 6.4 for different radiator materials. The optimization was done numerically by varying the parameters  $l_1$  in the range between 0 and 100  $\mu\text{m}$  and  $l_2$  between 0 and 10 mm. The resulting optimized parameters  $l_1^{\text{opt}}$  and  $l_2^{\text{opt}}$  for POKALON N470, PP and PE are listed in Tab. 6.2.

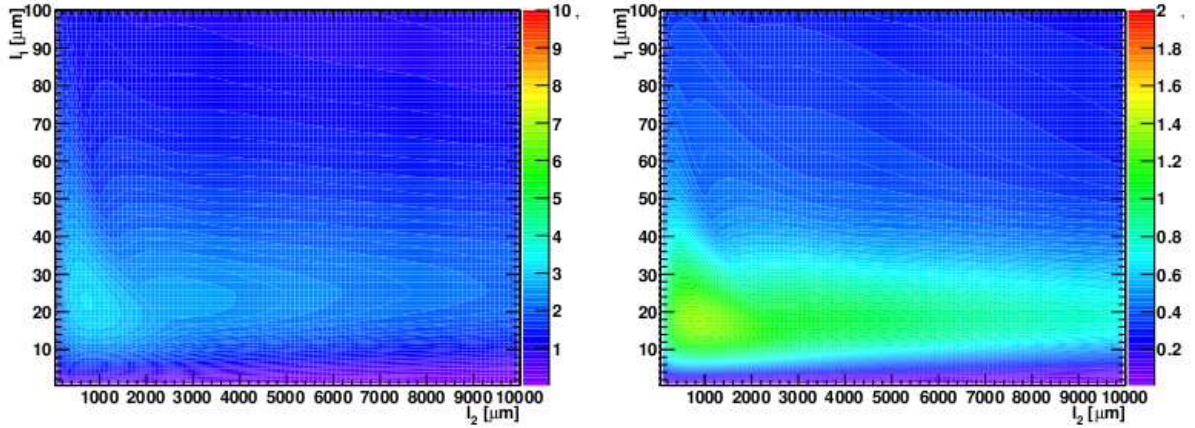


Figure 6.4: Integrated TR-yield emission spectrum (right) and spectrum of photons absorbed within the detector (left) calculated for 200 PE foils of variable foil thickness  $l_1$  and gap thickness  $l_2$  for 2 GeV/ $c$  electrons.

Table 6.2: Numerically optimized radiator parameters for a total number of foil layers of 200 at an electron momentum of 2 GeV/ $c$ . The parameters for the three most promising radiator materials are presented. The presented optimized values are rounded to commercial available material thicknesses. The parameters of prototype radiators are in case of irregular materials averaged values.

Material	$l_1^{\text{opt}}$ ( $\mu\text{m}$ ) $\pm 1 \mu\text{m}$	$l_2^{\text{opt}}$ ( $\mu\text{m}$ ) $\pm 100 \mu\text{m}$	$l_1^{\text{real}}$ ( $\mu\text{m}$ )	$l_2^{\text{real}}$ ( $\mu\text{m}$ )
POKALON N470 (K)	20	800	24	700
Polyethylene (H)	20	800	12	900
Polypropylene (G30)	20	800	17	50

The granularity of the used histogram (compare Fig. 6.4) is the main origin of the uncertainties presented in Tab. 6.2. A variation of the chamber thickness resulting in a modification of the chamber absorption characteristic results in strong modification of the optimal radiator parameter  $l_1$  and  $l_2$ . The exact matching of the parameters for the three most promising materials is therefore a special feature resulting from the absorption characteristic of our detector.

Since a too small foil thickness ( $l_1$ ) can provide the same TR-yield as a too large foil thickness, the smaller parameter  $l_1$  should always be preferred in order to minimize the material budget. A similar argument can be found for the foil spacing. In this case a shorter distance is leading to a more compact radiator and is therefore to be preferred if the optimal parameter can not be realized. In the end, the results of this optimization procedure have been used to classify new commercially available radiator materials into candidates worthwhile to be tested.

### 6.3 Three best radiator options

The following section will focus on the description on what we currently consider to be of the three best radiator options (presented in Fig. 6.5). The best compromise between performance, mechanical stability and cost efficiency was found for:

1. PolyEthylene (PE) foam foil radiator (H:  $125 \times 2.0$  mm layers) with a radiation length of 1.39 – 1.75 % and a total weight of 334 g. The 2.0 mm thick foam foil had the highest

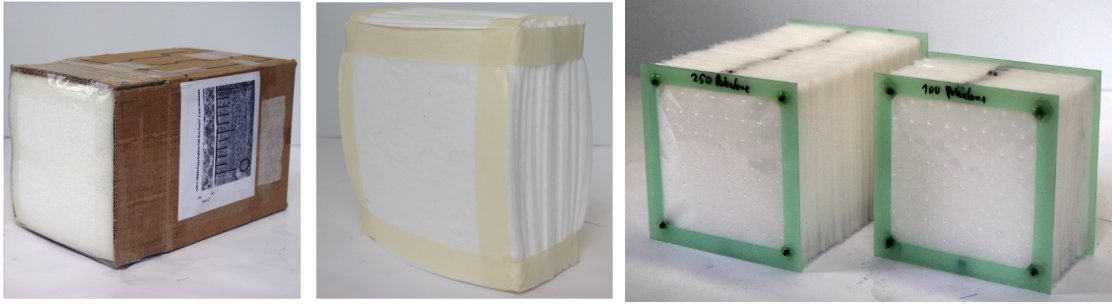


Figure 6.5: The three best radiator options **left:** *H*,  $125 \times 2.0$  mm PE foam foils, **center:** *G30*,  $30 \times 4$  mm PP LRP 375 BK fiber fleece layers and **right:** *K*, self-supporting micro-structured POKALON N470 foil radiator.

performance among the irregular radiators, which is also in reasonable agreement with simulations. The highest regularity of the bubble sizes correlated to radiator parameters  $l_1$  and  $l_2$  was also observed for this material (compare to Tab. 6.2).

2. A low weight (176 g) frame-less option combining the advantages of a regular radiator with the mechanical stability of an irregular radiator is the micro-structured self-supporting POKALON radiator (*K++*) made from 350 foil layers. The radiation length (3.09 %) is higher due to the oxygen content. However, the high price of POKALON renders this option uneconomical.
3. The same argument applies to the PP fiber radiator *G30* (made from 30 fiber fleece layers) which also exhibited a good performance at a radiation length of 1.70 – 1.96 %. The fiber diameter distribution is very uniform, while their spacing is completely chaotic. The pure amount of interfaces between fibers and gas per unit volume is most likely leading to the high performance.

### 6.3.1 Test beam results on radiator performance

A test of the PID performance was carried out in 2012 at the CERN-PS. A combination of two identical MWPC prototypes with different radiators was under test. The measurements were performed with a Xe/CO<sub>2</sub> (80/20) mixture, a particle momentum of 3 GeV/*c*, 100 V/mm drift voltage and 1775 V anode voltage. The electron and pion energy loss spectra are measured for each detector radiator combination using an external reference PID system composed of two air-Cherenkov counters and one lead-glass calorimeter. Based on the spectra measured in one TRD module, the final PID performance at a fixed electron efficiency can be approximated for a four layer detector using a likelihood on total charge as described in Sect. 9.3.2.2. The approximated pion efficiency at 90 % electron efficiency with four detector hits (see Fig. 6.6) indicates a good agreement for most regular prototypes between simulation and measurement within the errors. It can be seen that the most efficient radiator is a regular radiator made from PE-foil ("FFM0.7×350"), as expected. However, such a radiator is not an option for the CBM experiment, since the foil support frames increase the material budget of the TRD to a value which can not be tolerated. Furthermore, it would be a non-trivial task to produce these kind of radiators in sufficient quantity and sizes. The best self-supporting candidates in terms of performance are *G30* (PP-Fibers), *H* (PE foam foils) and *K++* (regular micro-structured POKALON foil). However, a consideration of the pure material price would exclude the PP-Fibers as well as the POKALON foil, thus leaving the radiator type *H* as preferred option.

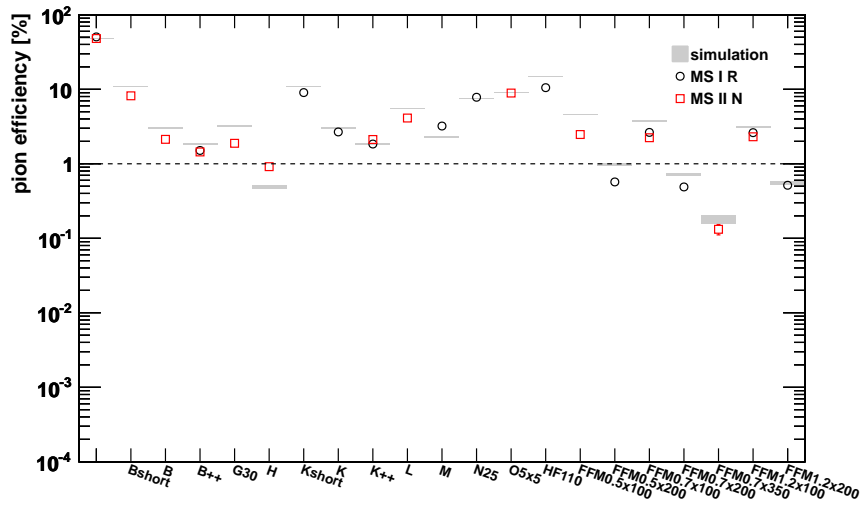


Figure 6.6: The pion efficiency at 90% electron efficiency at  $p = 3 \text{ GeV}/c$ , extrapolated to four measured detector hits per particles. Shown are different radiator prototypes.

### 6.3.2 Mechanical layout of the radiators

The radiator is composed of a hard foam box (PMMA or PE hard foam) of 10 mm thickness. The box has an aspect ratio of  $57 \times 57 \text{ cm}^2$ , resp.  $95 \times 95 \text{ cm}^2$ , at the front and a depth of 36 cm. First prototypes are presented in Fig. 6.7.



Figure 6.7: Full size radiator prototypes (left: PE hard foam box, right: PMMA hard foam box) for small detector modules.

The boxes are filled with PE foam foil layers of 2 mm thickness each. The last foam foil layer is glued to the box outer frames to keep the inner foil layers in position. The small volumes within the carbon lattice window of the ROCs are filled individually with the same foam foils. The surface of the lattice structure is afterwards closed by a last full surface foam foil layer like the radiator box. The weight will be  $\sim 3.5 \text{ kg}$  for the small radiator boxes and  $\sim 9 \text{ kg}$  for the large radiator boxes. The boxes (total weight  $\sim 320 \text{ kg}$  per layer) will be carried by a separate mounting structure in the final setup.

## Chapter 7

# Front End Electronics and Readout Chain

The TRD readout architecture is based on the SPADIC front-end ASIC, which will be integrated on the FEBs, directly mounted on the back of the readout chambers. From the frontend, the data will be transported to a DPB layer using the GBTx technology. After feature extraction in the FPGAs of the DPBs, the preprocessed data is shipped via optical links to the FLIB/FLES data acquisition for further analysis and storage.

### 7.1 The SPADIC front-end ASIC

#### 7.1.1 Overview

The SPADIC chip (*Self-triggered Pulse Amplification and Digitization ASIC*) is a mixed-signal readout ASIC with 32 input channels developed explicitly for the readout of the TRD of CBM [Arm13]. Figure 7.1 shows a simplified block diagram: Each channel contains a charge sensitive amplifier (CSA), a continuously running ADC sampling the amplifier output, a programmable digital filter (‘DSP’) and a hit detection logic. When a hit occurs (the digital amplitude value crosses a programmable threshold or a steep slope is observed), the sampled data of the hit pulse shape is stored for later readout. The amount of data to read out per hit can be programmed in a very flexible way by choosing a set of sample values (relative to the trigger moment) with a programmable mask pattern. This flexibility allows a trade-off between data volume and the amount of information. The zero suppressed data is then aggregated and distributed to two high speed serial links. Events are timestamped for later time event association, and they contain some other meta-information and error checking bits. The chip is controlled with one serial control ‘down’ link, carrying configuration data and fast commands like test injections or timestamp synchronization signals.

The described architecture has been encouraged by the TRD group because it offers the possibility to analyze the shape of individual chamber pulses. This feature may allow a discrimination between different particle types, depending on the radiator design. As it was not clear which shape parameters are relevant, the pulse picking mechanism was introduced for a maximum of flexibility. No on-chip data processing (for instance a summation of ADC samples or the determination of the temporal pulse width) has been included yet, because such a dedicated hardware solution requires prior evaluation of the algorithm with real detector data.

The programmable digital IIR filter has been included in order to pre-process possible complex detector pulse shapes. It may be used for ion tail cancellation or double hit discrimination.

Another important feature of SPADIC is a neighbor logic which allows to force trigger channels by hits in neighboring channels. The amplitude information of adjacent channels can

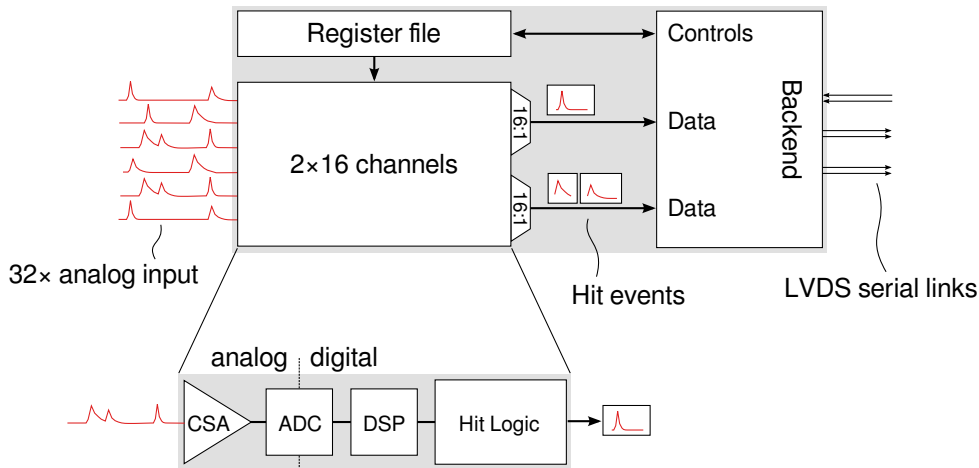


Figure 7.1: Conceptual block diagram of the SPADIC chip. The ‘Backend’ block is CBMnet in SPADIC 1.x and an E-link interface in SPADIC 2.x.

be used to improve position resolution so that also small amplitudes should be known. In a self triggered operation, this would require very low thresholds so that data volume would be increased by noise hits. The neighbor mechanisms allows to set a conveniently high threshold in all channels and still obtain the amplitude of neighbors (even below threshold) by force triggering. In order to provide a maximum flexibility for different pad plane designs, the neighbor association can be programmed to a large extent. SPADIC also allows to pass trigger information from chip to chip (which is not trivial due to signal propagation times) and therefore provides three neighbor trigger inputs and outputs at both the ‘top’ and ‘bottom’ sides of the chip.

Table 7.1 summarizes the most important chip properties, Fig. 7.2 shows the layout of the chip. A website has been set up to distribute information about the chips [AK].

Chip size	$5 \times 5 \text{ mm}^2$
Channels	32
Total power	600 mW
Peaking time of analogue part	80/160 ns
ADC resolution	9 bits
ADC sampling frequency	25/16 MHz
IIR filter stages (1st order)	4
Technology	UMC 180 nm
Transistor count	$\approx 2.5 \text{ M}$

Table 7.1: Most important parameters of the SPADIC chips. Multiple values refer to different chip versions.

### 7.1.2 Chip versions and history

After prototyping five test chips with few channels, the first full size chip SPADIC 1.0 has been submitted end of 2011 [AFP10, AFKP12]. The analogue shaper in that chip has a peaking time of 80 ns, the ADC samples at 25 MSps, and the digital interface uses the CBMnet protocol [LB13] (this part has later been used as a basis for the digital interface of the first STS-XYTER chip [KKO<sup>+</sup>14]). Apart from few minor bugs, SPADIC 1.0 is fully functional and has been used for

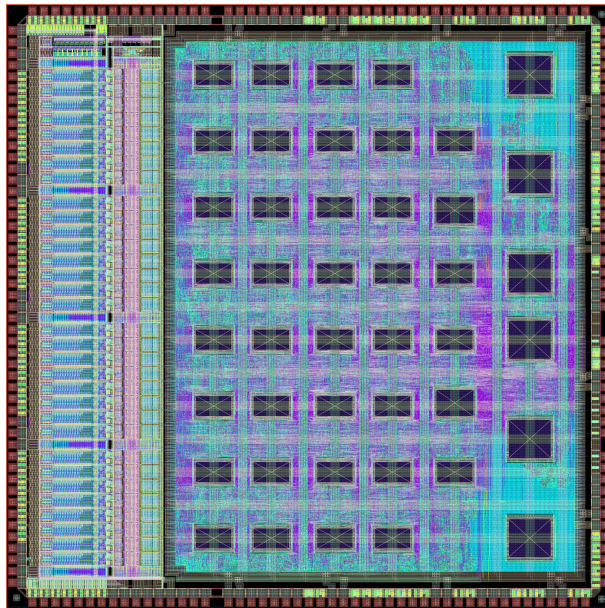


Figure 7.2: Top-level layout of the SPADIC 1.0 chip. The chip has a size of  $5 \times 5 \text{ mm}^2$ . The 32 analog channels occupy the first quarter of the chip area from the left side, the synthesized digital part is to the right. The black boxes are larger memory blocks.

intensive lab characterizations. A small number of chips has been packaged into 176 pin ceramic carriers (Fig. 7.3) which were then mounted on various versions of the FEBs used to read out detector prototypes. Several test beam campaigns were carried out with these packaged chips.

Because no more SPADIC 1.0 chips were available at some point, a slightly updated version, SPADIC 1.1, has been submitted in 2015. The three known bugs (instability in analogue part, unwanted behavior of comparator under certain conditions, timing issue in serial output stream) were fixed. This chip will be used in 2016 for further test beam measurements.

After CBM had decided to move from the special CBMnet protocol to a format using the GigaBit Transceiver chips (GBT) from CERN, the entire digital interface of the SPADIC 1.x chips had to be exchanged. This has been carried out in late 2015 and early 2016 (very much based on an E-link implementation for the STS-XYTER developed by the group in Krakow) and the new chip SPADIC 2.0 has been submitted in June 2016 on an engineering run together with other CBM ASICs. While the major change is an ‘E-link’ compatible data/control interface, the opportunity was used to change a few chip parameters: the shaping time of the analogue part has been increased to 160 ns to match the longer drift paths in the latest TRD chambers, the ADC sampling rate has been slowed down correspondingly to 16 MSps (this is also driven by changes in the clock speeds of the CBM DAQ) and the number of ‘pre-samples’ (ADC values *before* trigger has occurred) has been increased. SPADIC 2.0 will be packaged in a low cost 208 pin plastic package suited for large volume production. It is expected that mass production for the full detector will use a further, final iteration SPADIC 2.1.

Table 7.2 shows some key parameters of the different chip versions.

### 7.1.3 Charge Sensitive Amplifier (CSA) and ADC

The analogue front-end consists of a classical arrangement of a charge sensitive amplifier, a pole-zero compensation network and a shaping amplifier. The overall structure shown in Fig. 7.4 generates a pulse of shape

$$f(t) = A \cdot \frac{t}{\tau} \cdot \exp\left(-\frac{t}{\tau}\right) \quad (\text{for } t \geq 0)$$

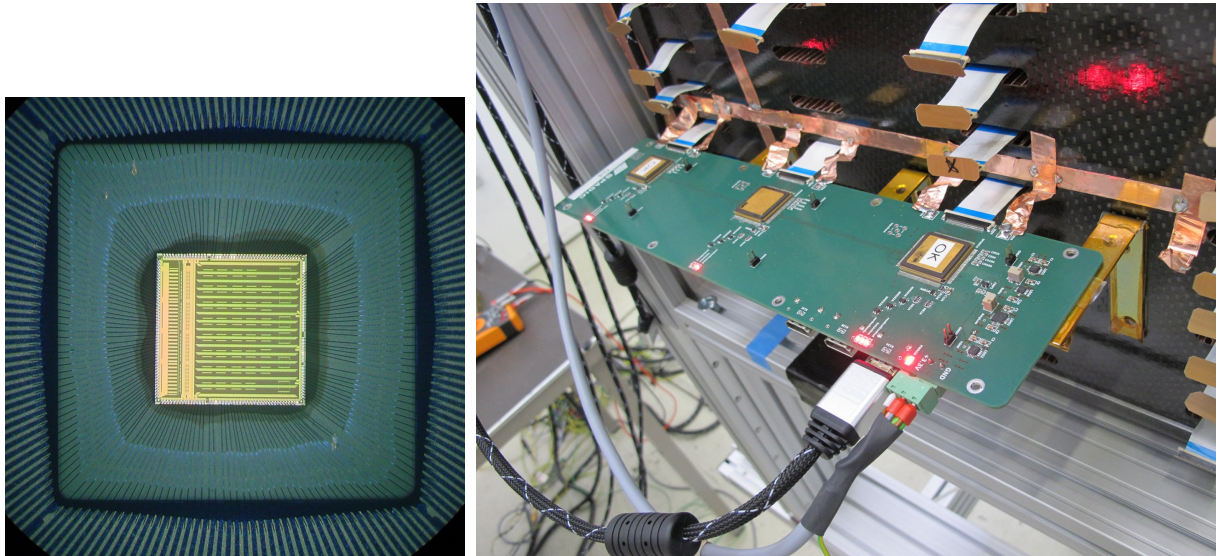


Figure 7.3: Left: Bonding detail of a SPADIC 1.0 mounted in a QFP176 ceramic carrier. Right: FEB using packaged chips during a beam test.

	SPADIC 1.0	SPADIC 1.1	SPADIC 2.0	SPADIC 2.1
Year	2011	2015	2016	2017/18
Peaking time	80 ns	80 ns	160 ns	tbd.
ADC sampling frequency	25 MHz	25 MHz	16 MHz	16/8 MHz
Master clock	250 MHz	250 MHz	160 MHz	160 MHz
Interface	CBMnet	CBMnet	E-Link	E-Link
Package	QFP176	QFP176	QFP208	QFP208
Notes	first full size chip	bug fixes	new interface	production design

Table 7.2: Comparison of the different full size SPADIC versions.

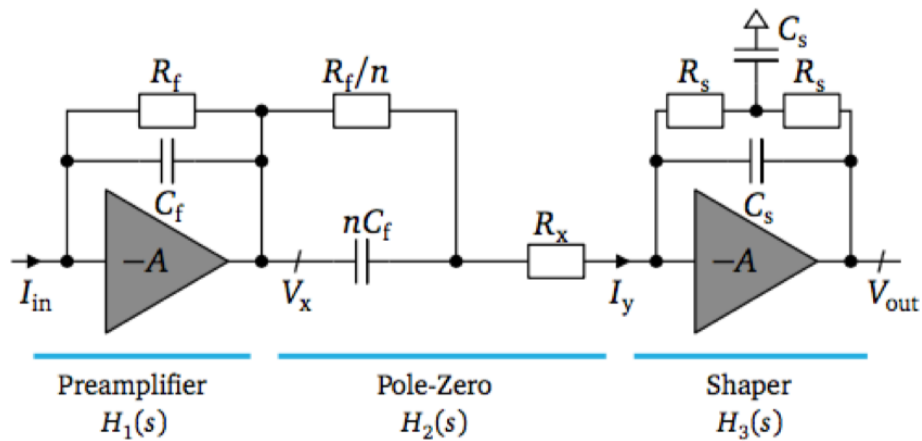


Figure 7.4: Principle of the charge amplifier, pole-zero correction and shaping in SPADIC.

with peaking times  $\tau = 80/160$  ns for SPADIC 1.x and SPADIC 2.x. Pulses digitized with the internal ADC at a sampling rate of 20 MHz<sup>1</sup> are shown in Fig. 7.5. The pulse shape matches very well the prediction.

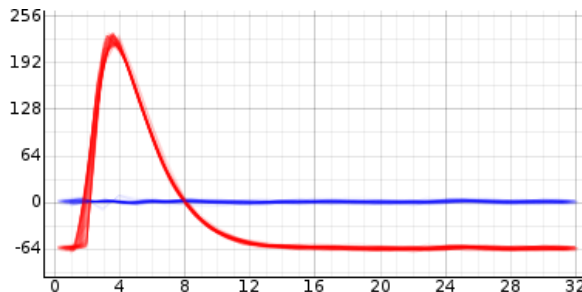


Figure 7.5: Digitized pulses generated by test injection. The flat blue lines are the residuals of fits to the predicted pulse shape.

The amplifier/shaper has been optimized for positive inputs signals. It consumes a power of  $\approx 5$  mW. In order to be able to also process negative signals from other detector types a less power-optimized front-end for negative input signals is available, consuming  $\approx 10$  mW. The type of front-end to be used can be configured by software.

The input referred noise expressed in electronics, i.e. the equivalent noise charge (ENC) has been determined on test chips as a function of input capacitance. Figure 7.6 shows simulations and measurements for a range of lengths of the input transistor. The best performance of  $\approx 200 e^- + 20 e^-/pF$  is obtained for a length of 320 nm (dark blue curve with crosses). This choice is used for all later SPADIC versions.

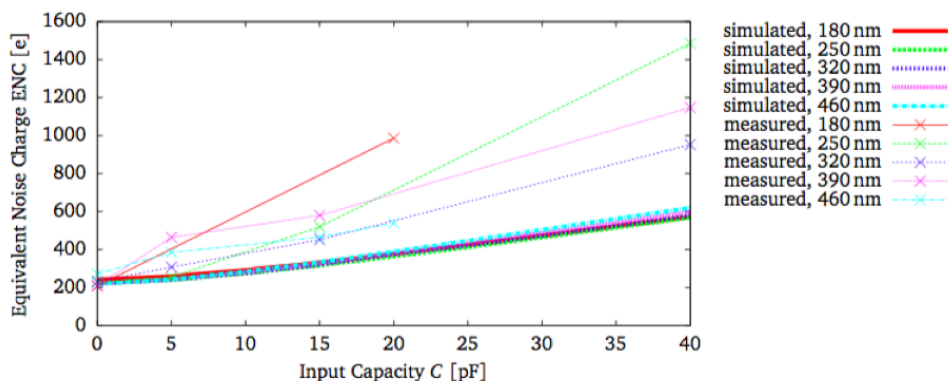


Figure 7.6: Simulated and measured ENC measured in SPADIC prototype chips for various lengths of the input transistor. The simulations (lower, solid curves) predict lower values than the measurements (upper curves with crosses). The observation that no dependence on transistor length is predicted by the simulations while a clear effect is measured indicates that the provided noise simulation models are inaccurate.

The ADC is a custom pipelined design based on a special current memory cell [PAK<sup>+</sup>10]. It digitizes the shaper output with 9 bits at a rate of up to 25 MHz. The effective resolution, considering nonlinearities, is roughly 8 bits. The gain of the CSA in combination with the dynamic range of the ADC has been chosen so that a charge of  $\approx 75$  fC leads to a full scale ADC signal.

Table 7.3 summarizes the most important parameters of the CSA/ADC part.

<sup>1</sup>The sampling rate is linked to the master clock frequency which was limited in the test setup.

Shaper Type	CR-RC
Pulse shape	$\propto t \exp(-t/\tau)$
Shaping time	$\tau = 80/160$ ns
Noise	$\approx 200 e^- + 20 e^- / \text{pF}$
Input range	$\approx 75$ fC
Front end power	3.8 mW
Max. sampling frequency	25 MHz
Resolution	9 bits
ENOB	$\approx 8$ bits
ADC power	4.8 mW

Table 7.3: SPADIC Parameters of CSA and ADC.

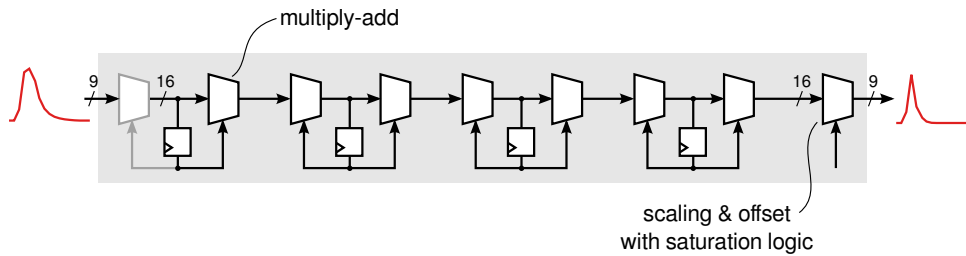


Figure 7.7: Topology of the IIR Filter. The first coefficient is hard-wired to zero, reducing the number of poles by one.

#### 7.1.4 Digital signal processing

The digitized data is filtered by a digital Infinite-Impulse-Response (IIR) filter with the topology shown in Fig. 7.7. Four first order stages are followed by a final stage which scales and shifts the signal into a suited range and which handles overflow signals. Intensive simulations have been carried out to determine a good choice of the internal resolutions (affecting significantly the required hardware resources, in particular for the multiplier blocks) [Kri11]. The main parameters of the filter are given in Tab. 7.4.

Parameter	Value
Order	4 zeros, 3 poles
Internal resolution	16 bits
Width of coefficients	6 bits
Available coefficients	$-1 \dots 0.96875$ (in steps of $\frac{1}{32}$ )
Width of scaling factor	9 bits
Available scaling factors	$-8 \dots 7.96875$ (in steps of $\frac{1}{32}$ )
Width of offset value	9 bits
Available offset values	$-256 \dots 255$

Table 7.4: Properties of the digital filter part.

An example of filter action is shown in Fig. 7.8: The bottom left curve shows a digitized pulse obtained with standard charge injection. The upper left pulse shape is obtained by degrading the pulse intentionally with an additional injection. The shape of this distorted pulse can be

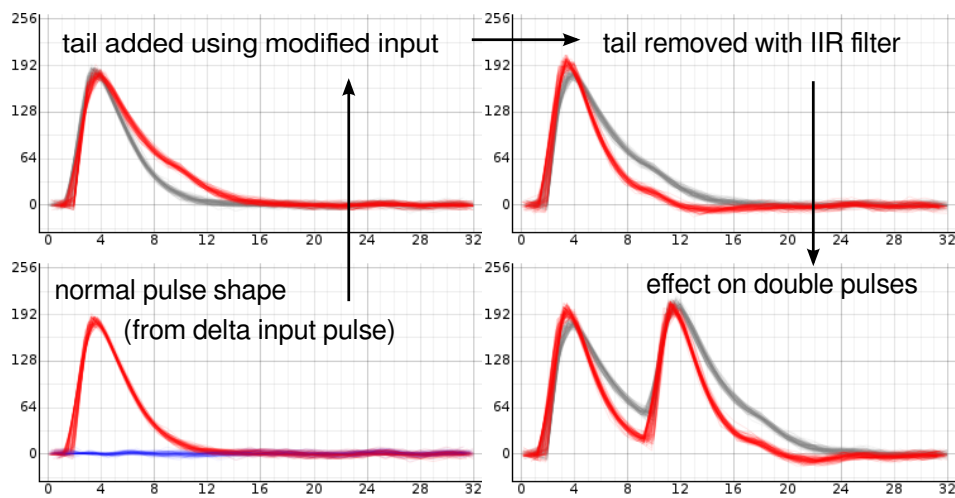


Figure 7.8: Measured pulse shape improvement achieved by the IIR filter (see text).

improved by choosing suited coefficients in the IIR filter. The resulting signal (a real chip output is shown) is shown in the upper right curve. The lower right curve shows the filter action on a distorted double pulse.

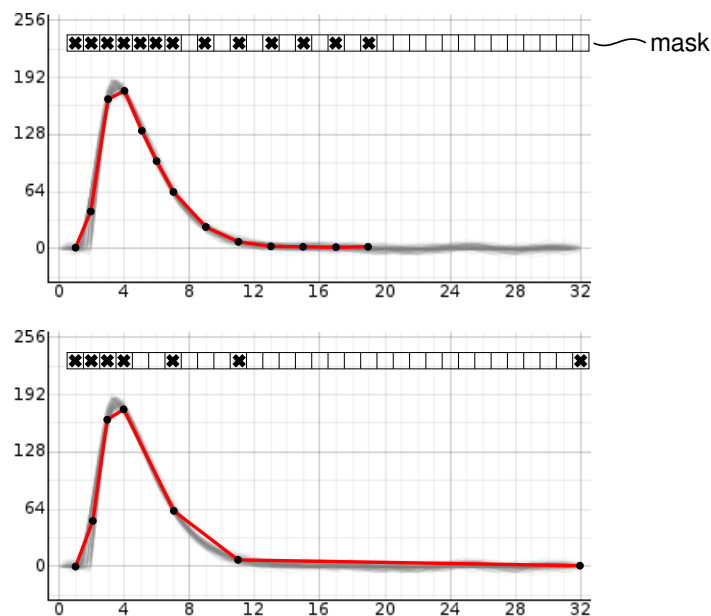


Figure 7.9: For each detected hit, a freely programmable set of signal samples are read out. Two examples sets are shown.

The filtered digital signal is fed to a discriminator section which detects hits. A fixed threshold can be set, or the slope of the pulse (obtained as the difference of consecutive samples) can be used. Triggers from neighbor channels arriving either chip-internally or through dedicated chip pins, can initiate a pulse readout as well. When a pulse is detected, several sampled data values (up to 32) are tagged for readout. The pattern of values is freely programmable so that a compromise between information content and data volume can be found. Figure 7.9 shows this unique pulse picking feature for two cases. The pulse picking is implemented such that it maintains the full information also in the case of multiple hits during the time interval in which samples are picked.

Field	Size (Bits)	Purpose
Group number	8	Globally identify one group of 16 channels
Channel number	4	Locally identify one channel within a group
Timestamp	12	Event time within one ‘epoch’
No. of samples	6	Cannot be unambiguously determined from the event size
Hit type	2	Trigger source (e.g. self, neighbor)
Stop type	3	Reason for unexpectedly small event size (e.g. multi hit)

Table 7.5: Metadata contained in a regular hit event.

Number of samples	data words (16 bits)
0	3
1	4
$1 \leq N \leq 32$	$3 + \left\lceil \frac{9N+3}{15} \right\rceil$
32	23

Table 7.6: Event size as a function of the number of requested samples per hit. The offset is caused by timestamps, flags, headers and trailers. Each sample adds 9 bits.

Apart from the pulse shape information, further data like a timestamp or the trigger type that caused the hit is combined to a hit event (see Tab. 7.5). Some of these fields are not strictly required and can be omitted in later versions of the chip in order to minimize the event size. Table 7.6 shows the size of one such event as it leaves the chip, as a function of event samples. The smallest events that can be achieved, containing no sample at all (i.e., only a binary hit information) consist of three 16-bit words. For each sample included in the event, the size increases according to the formula shown in Tab. 7.6, up to a maximum size of 23 words for 32 samples contained.

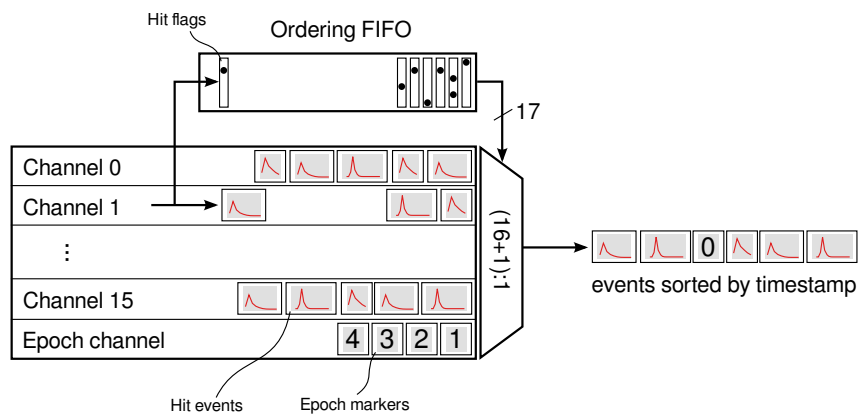


Figure 7.10: Principle of the time-ordering feature of events, implemented per group of 16 channels.

The hits are buffered in a FIFO in each channel. 16 of these FIFO data streams are merged to one serial data stream, two of these streams leave the chip via the CBMnet or E-link interface. CBM has requested that the events leaving the chip are ordered according to their hit-time. This complicates the merging of the FIFO information into a single data stream (a simple round-robin

arbitration is not possible). A special time ordering FIFO has been introduced to control the event selection. This circuitry, sketched in Fig. 7.10, is quite complicated, because it has to cope with different event sizes, with multiple events per timestamp, and it must correctly react and recover from FIFO overflow conditions.

Besides the regular hit events there are other, exceptional, types of messages sent to data acquisition which notify about timestamp wraparounds ('epoch markers'), missed events due to full buffers, or other error conditions.

## 7.2 Data transport

The components of the data transport chain are listed in the following Tabs. 7.7 and 7.8. It has been configured such that for the initial phases of detector operation an uncompressed data stream can be transported, in order to be able to fully debug the system. Therefore, this chain will on one side allow the transmission of the data rate expected at the SIS100 after online reduction (see Sect. 4.5) without problems, but on the other side would also still be sufficient for an operation at the SIS300.

Table 7.7: Defintion of the foreseen DAQ components.

	GBTx	VTR	VTT	Optical links
ROB3	2+1	1	1	4
ROB5	4+1	1	2	6
ROB7	6+1	1	3	8

A total number of 1664 simplex fibers will be needed for the CBM-TRD, subdivided into 256 downlinks ( $12 \times 12$ -fold MPO) and 1408 uplink ( $118 \times 12$ -fold MPO) fibers.

Table 7.8: DAQ components required for the full system.

Module type	1	2	3	6	7	8
Number of modules	32	24	40	24	32	48
FEB type	10s	10s	05n	08n	08n	08n
ASICs/FEB	10	10	5	8	8	8
FEB/module	9	5	6	8	4	3
ROB3/module	0	1	0	0	0	1
ROB5/module	0	1	1	2	1	0
ROB7/module	2	0	0	0	0	0
optical fibers	512	240	240	288	192	192

## 7.3 The readout chain

In this section the readout chain is summarized. The structure is as follows: first, the general concept of the readout scheme is presented followed by the readout proposal for the TRD. Second, the readout prototype implementation with a detailed overview of the processing blocks is presented. Finally, the feature extraction preprocessing stage is introduced and explained.

### 7.3.1 The TRD readout concept

The general concept of the readout chain is summarized in Fig. 7.11. The main components are the FEE, the Readout ConTroler (RCT) and the event building and selection. The communication between those main blocks is made by different data transport links that depend on the hardware

used. The FEE converts the TRD detector signals into discrete messages. As presented before in Sect. 7.1, the SPADIC v1.0 chip has been used up to now as front-end ASIC for the TRD however the final version will be based on the v2.x ASIC revision.



Figure 7.11: Schematic view of the TRD readout chain.

The RCT has multiple functionalities. It provides the interface between the FEE and the data taking system. It also provides communication with the Experiment Control System (ECS) and Timing and Flow Control system (TFC). The RCT also implements a data preprocessing stage, better known as feature extraction. The feature extraction stage implements preprocessing algorithms in order to extract a relevant set of features from the input signals, such as total integrated charge, time-over-threshold and cluster finding. The feature extraction is based on the information provided by the SPADIC message format. A SPADIC message is conformed by multiple message words as previously explained. Therefore, a message would normally be made of a couple of metawords (e.g. timestamp, channel ID, group ID, and hit type) and the raw data from the ADC, which can be configured to provide a maximum of 32 bins. A detailed description of the feature extraction is presented in Sect. 7.3.4. Finally, the data is shipped to the event building and selection stage.

### 7.3.2 TRD readout proposal

The TRD readout proposal is summarized in Fig. 7.11. The FEE will be based on the SPADIC v2.x ASIC. The data transport link between the SPADIC v2.x and the DPB layer is performed using the GBTx transport technology. The Data Processing Board (DPB) is a FPGA that acts as a RCT between the FEE and the First-Level Event Selector (FLES). Optical fibers are used to transport data between the DPB, located in the CBM experiment cave, and the FLES that will be located in the Green Cube. The FLES Interface Module (FLIM) transport link is used to transport the data as well as control commands. The FLIM provides a data transfer rate of 10 GB/s. A detailed description of the current common DAQ system development can be found in the CBM Online TDR [E<sup>+</sup>17].



Figure 7.12: TRD readout chain using the SPADIC v2.x ASIC and AFCK boards.

The latest readout development is the SPADIC v2.0 in combination with a AFCK RCT board as presented in Fig. 7.12. This readout chain is the first one compatible with the final GBTx e-Link readout schema.

A detailed overview of the internal structure of the AFCK RCT is shown in Fig. 7.13. It comprises also a feature extraction stage following the front end GBTx eLink and the data concentrator.

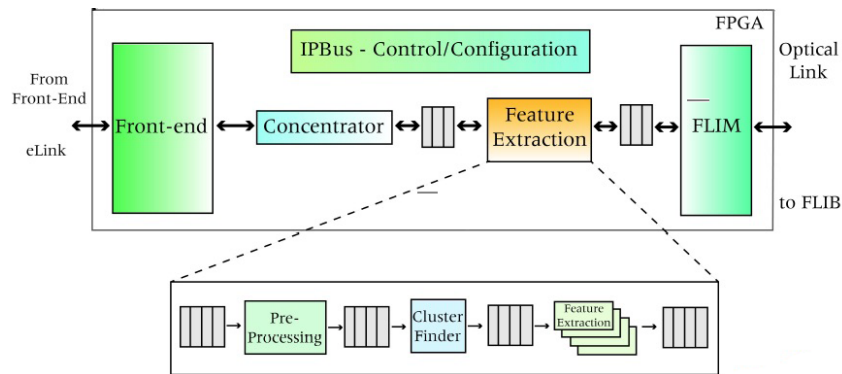


Figure 7.13: Detailed view of the components implemented on the AFCK boards. The front end transfer link is based on GBTx and the back end is based on FLIM.

### 7.3.3 TRD readout prototype

Multiple FEE configurations have been tested during previous beamtest campaigns during the last years. The SPADIC v0.3 was the first chip tested and was followed by the SPADIC v1.0 ASIC. This later would use a CBMnet 2.0 data transfer link. The RCT was implemented on a FPGA development platform, the SysCore3. The design loaded into the SysCore3 allowed to communicate with up to three SPADIC v1.0 by means of the CBMnet 2.0 protocol and provided a down-link communication to the FLIB/FLES at a data transfer rate of 4.8 GB/s. The SysCore3 also included a preprocessing stage where a feature extraction core would calculate parameters based on the channel signals such as total charge, time-over-threshold and center-of-gravity in time direction.

### 7.3.4 Feature extraction

The feature extraction is a data preprocessing stage of the TRD DAQ chain. The feature extraction aims at delivering event-filtered and bandwidth reduced data to the FLES. The feature extraction stage implements multiple processing algorithms in order to find and extract regions of interest within time series signals. For the requirements of the TRD the signal processing stages can be summarized as: baseline correction and cluster finder. Possible implementations of the algorithms are described in the following subsections.

#### 7.3.4.1 Baseline correction

The purpose of the baseline correction is to decrease the noise and systematic effects. The module has three operation modes:

- a Fixed mode: A constant value stored in a register is subtracted.
- b Bin dependent: For every value of the current message, a value stored in a memory is subtracted.
- c.1 Variable: The last three time bins of the time dependent signals are averaged. This average value is then subtracted from all the message time bins. The calculation is performed for every message independently.
- c.2 Variable: The first sample in front of the rising edge is subtracted from all the message time bins. The calculation is performed for every message independently.

Depending on the SPADIC message or more precise message stop type there are different default methods to be applied in order to perform a robust online baseline subtraction. The default case is a normal message stop type. These messages have a predefined number of samples (between 1 and 32). For sample numbers larger two (one sample of the maximum amplitude and one pre-sample or one with maximum distance relative to the maximum to measure the current baseline of each individual channel) the pre- or last message sample(s) is/are used to calculate and subtract the up-to-date channel baseline. The second case is the so-called multi-hit scenario (compare to Sect. 7.1). These messages have a number of samples smaller than the normal predefined one. This is due to the appearance of a new detector signal during the message building within the predefined hit time window. The second signal is therefore positioned on top of the ion-tail slope of the previous one. Subtracting of the last time bins average would lead to an overcompensation of the baseline. This can be avoided by three different approaches:

- Subtraction of the pre-sample.
- Subtraction of a fixed measured baseline value.
- Subtraction a fitted baseline offset using the SPADIC response function.

The described scenario can be minimized by applying the digital IRR filter as mentioned in the previous chapter. Therefore it is also an option to avoid online processing of multi-hits within the DPB layer and just transporting them into the FLES for detailed analysis.

#### 7.3.4.2 Signal preprocessing

There are on-going studies concerning the ability and performance of online data compression in the DPB layer by integrating the signal amplitude over a fixed number of samples. An other alternative is fitting of the measured signal samples to the SPADIC response function to extract the exact time of the maximum amplitude, the maximum amplitude and the baseline offset. The evaluation of both approaches is currently in progress.

#### 7.3.4.3 Cluster finder

The cluster finding in space and time is also a promising option of data preprocessing, since the data from each SPADIC ASIC is already time sorted. The memory consumption for the cluster finding in time direction can be efficiently reduced compared to other ASICs without time sorted data transport. The FNR trigger logic guaranties an equal time stamp for the messages of a physical charge cluster measured by a single ASIC. The ability of cluster merging between different ASICs of the same FEB or even the full chamber within the DPB layer is at the moment investigated in details. An online cluster finding would create the possibility of further data compression by calculating the hit position based on the full charge information of the cluster.

## Chapter 8

# System Integration and Services

This chapter will summarize the services integrated in CBM-TRD as mechanical structure, gas system, Low Voltage (LV), High Voltage (HV) and cooling. A detailed description of the individual design options and construction is given, if already available.

### 8.1 CBM-TRD commissioning and installation

The individual chamber produced by the three institutes will be collected at Frankfurt and/or GSI. The FEE will be mounted on the chamber and first tests of the mounted full equipped detector modules will be done. The tested ROCs are shipped afterwards to the CBM location on the FAIR area, to be integrated into layer slices. This structures are composed of  $2 \times 5$  large modules in the outer region and  $3 \times 1$  large modules plus  $5 \times 5 - 1$  small modules in the inner region (see Fig. 8.2). The slice integration will be done at the ground level of the CBM building (see Fig. 8.1).

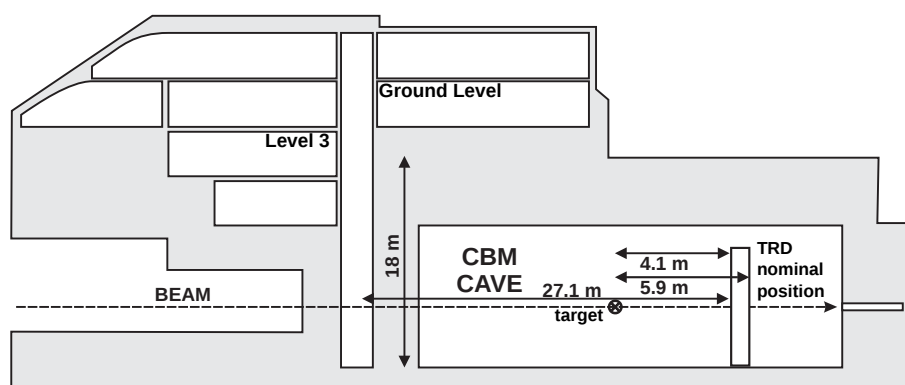


Figure 8.1: Schematic layout of the CBM building.

A temporal mounting structure is needed in this area to build the slice in a hanging way, since the slice is constructed to carry the load only vertically. First gas tightness tests will also be performed here. The TRD gassystem constructed for the test beams will be used for this purpose and installed during the installation time on the ground level of the CBM building. A minimal HV/LV and DAQ system will also be needed at this location. As additional infrastructure a lifting platform will be required as well. The finally assembled and tested slices are craned from the ground level of the CBM building into the cave and there integrated into full layers. The radiator box modules are mounted afterwards in a separate mechanical structure in front of each layer.

## 8.2 Mechanical structure

The total weight of the TRD (disregarding the outer support frame structure) is estimated to be 3.26 t. The ROCs contribute with 1.51 t, while the radiators weigh 1.14 t, the FEBs 222 kg (disregarding the FEB mounting) and the mounting ledges 45 kg (disregarding screws). This weight has to be supported by the frame structure, which has to be stable within  $\pm 1$  mm.

### 8.2.1 ROC mounting

8	8	7		7		7		8	8
8	6	3	3	3	3	3	6	8	
		2	1	1	1	2			
7	6	2	1		1	2	6	7	
		2	1	1	1	2			
8	6	3	3	3	3	3	6	8	
		3	3	3	3	3			
8	8	7		7		7		8	8

Figure 8.2: The arrangement of the different module types in one TRD layer. A layer can be separated into three vertical sections, two outer ones (shown in light gray), consisting of large modules, and a center one (shown in dark gray), containing small modules in the middle and large modules at the top and bottom.

Each TRD layer is mechanically subdivided into three building blocks as presented in Fig. 8.2. The light gray colored outer building blocks consist of two ROC columns connected to two FR4 mounting ledges each. The inner building block (dark gray colored) can be further subdivided into the upper and lower large modules and the inner sub-frame, build of the small ROCs.

A cross section of the interconnection between two adjacent ROCs is presented in Fig. 8.3.

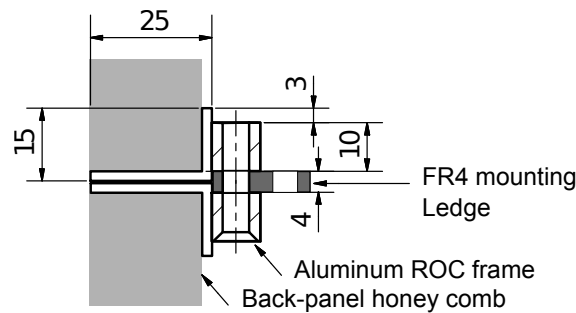


Figure 8.3: The module mounting structure is a 4 mm thick FR4 ledge (dark gray) positioned between the two aluminum frames of two adjacent detector modules. The mechanical fixation is realized by four lock screws, which are here shown from above. The mounting structure is positioned vertically between detector slices. The second drilling in the mounting ledge is later used to mount the LV power bus bars.

### 8.2.2 Radiator mounting

There are two mounting options considered for the radiator:

- (1) A hard foam like EF700 is used to build an individual radiator nesting (four or five sides closed) for each chamber with a depth of 27 cm for the radiator type H (12 cm for radiator type G30). The box provides mechanical support and, being a foam, acts to some extent as a radiator at the same time. The foam foil stack is piled inside of the box. The open side of the box is orientated towards the entrance window of the chamber and the support grid, which keeps the first foil in position. At the same time the radiator box limits the flexibility of the support grid in direction of the radiator.
- (2) The foam foil radiator can be mounted like a theater curtain in slices of 1.5 m width in front of each detector layer. This option is cost and production efficient. The slices are mechanically compressed above and below the detector layer and stretched by the own weight of the material and the bottom clip.

Comparing both options, the advantage of option (1) is the minimal additional material budget, since only a very reduced mechanical support inside the active area is required. The drawbacks are the exposure of the foam foil to external influences and difficulties in providing the required mechanical stability and uniformity. Solution (2) would imply a bit more construction work, but has the benefit of giving additional mechanical protection to the entrance foil window, the most fragile component of the detector. Also, it provides a more flexible design and would require less complicated mounting devices. Therefore, we currently foresee option (2) as default solution.

### 8.2.3 FEB mounting

The FEBs will be mounted at an angle relative to the chamber backpanel surface, which is defined by the depth of the FEB and the distance between the readout cable holes of the chamber with the highest channel granularity, i.e. module type 1 (compare Sect. 5.3.2). The angle has to be chosen such that it distributes the FEB material as homogeneously as possible on the back of the ROC. A commercially available solution for the FEB clamp will be preferred if available. If the optimal angle cannot be covered by commercial clamps we would design a specific clamp which could be produced by injection moulding by a external service provider.

### 8.3 Gas system

The CBM-TRD has an overall gas volume of  $1.39 \text{ m}^3$  in the SIS100 configuration with four layers. The total number of gas enclosures (detector modules) in the system is in this case 200. There are two different module sizes  $57 \times 57 \text{ cm}^2$  and  $95 \times 95 \text{ cm}^2$  (see Sect. 4.4). The total gas depth in  $z$ -direction is 12 mm for both module types. This results in a rather disadvantageous, from the gas tightness point of view, volume-to-surface ratio of  $1.39 \text{ m}^3 / 125.05 \text{ m}^2 = 0.011 \text{ m}$ . For this reason, special provisions have to be taken in order to minimize gas leakage (see Sect 5.2). In addition, a low-mass construction of the detectors is needed for minimizing multiple scattering and TR-photon absorption in the materials between radiator and active gas volume. The light construction mechanically limits the relative overpressure of the chambers to 2 – 3 mbar. In order to avoid electrostatic distortions due to deformation of the enclosing drift and pad electrodes, the overpressure at which the chambers are operated is limited at 1 mbar.

#### 8.3.1 Gas choice

The choice of xenon as the noble gas in the mixture used for standard operation is determined by its large absorption, and subsequent ionization, cross section for transition radiation X-rays produced in a suitable radiator material. Because xenon is a high-cost gas (ca. 12 Euro/l), recirculation in a closed loop, purification, and recovery of the purged gas are mandatory. In addition, xenon is a rather heavy gas (density 5.58 g/l). The density difference between the chamber volume and the surrounding air is 4.67 g/l. This means that the overpressure gradient of 0.46 mbar/m over a volume which extends over a height of 4.75 m is 2.19 mbar. In order to avoid significant deformations of the thin entrance foil and pad plane structure, and to achieve an uniformity of operation of the whole system in terms of  $E/p$  (see Sect. 5.2 and Fig. 8.4), the maximum overpressure in each individual chamber should not be higher than 1 mbar. Thus, a suitable segmentation of the pressure regulation in the height of the detector is imposed by the choice of the noble gas. The typical quencher used in other TRD systems is methane, since its well known transport and quenching properties makes it a rather convenient choice. However, safety aspects, neutron interactions, and lifetime considerations make  $\text{CH}_4$  a gas to be avoided. Therefore, the quencher of choice is  $\text{CO}_2$ , because it is non-flammable, contains no hydrogen, is a low-cost gas, and performs adequately. The concentration of quencher will be chosen as 15%, as it has been operated in the ALICE-TRD. Because the maximum drift distance in a TRD module is only 5 mm, problems associated with electron attachment due to oxygen contamination in the presence of  $\text{CO}_2$  are expected to be negligible. Concentrations of  $\text{O}_2$  as high as 100 ppm are therefore affordable, since such a contamination would only affect the signal by  $< 10\%$ . Other contaminants from air such as  $\text{N}_2$  will be removed from the mixture in the recovery process (see Sect. 8.3.2.4).

#### 8.3.2 Layout

As explained in the previous section, the use of a high-cost gas component makes a closed loop circulation system mandatory. The proposed system will consist of functional modules that are designed as standardized units for all LHC gas systems like ALICE-TRD. Table 8.1 indicates the location of these modules. The mixing, purifying, and gas recovery are located in the gas handling area of the CBM building on level E30. The component sizes and ranges will be adapted to meet the specific requirements of the TRD gas system. An overview of the distribution system can be seen in Fig. 8.5. The basic function of the gas system is to mix the components in the appropriate proportions and circulate the gas through the TRD chambers at a pressure of  $< 1$  mbar above atmospheric pressure. Some of the basic parameters of the TRD gas system are given in Tab. 8.2

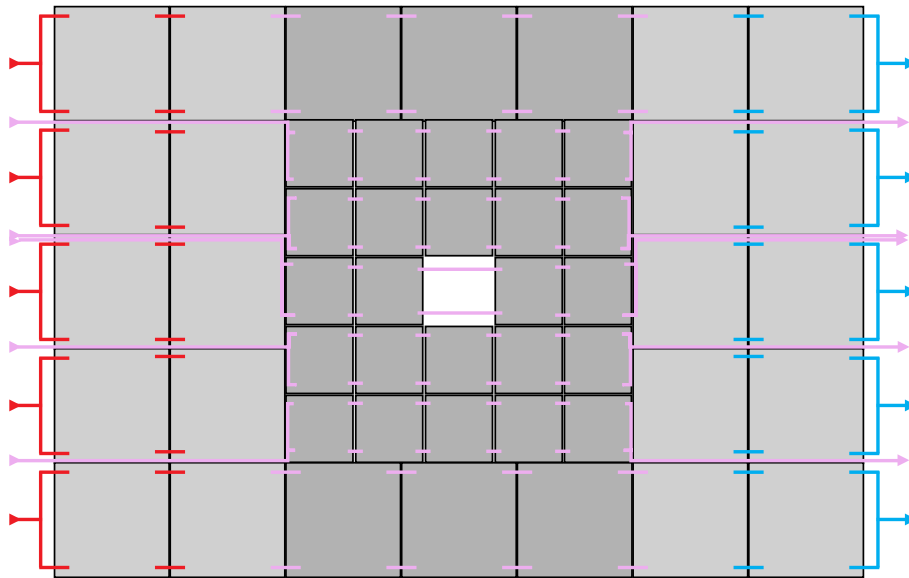


Figure 8.4: Schematic layout of the TRD gas supply chain. Red gas tubes correspond to the left building block, pink is used for the central building block, and blue indicates the gas tubes of the right building block.

Table 8.1: Functional modules of the TRD gas system and their location.

Functional module	Use
E6C0SR002/Farnell	Purifier
XF-329/Farnell	Purifier
E6C0SR002/Farnell	Dryer
XF-329/Farnell	Dryer
8711/Burkert	CO <sub>2</sub> mass controller
8711/Burkert	Xe mass controller
N87TTE/KNF	Recirculating compressor
HB1-M/Tectra	Purifier/dryer heaters
O2XI-29-0/PAMETRICS	Oxygen analyzer
MIS35-331-1-000/PANAMETRICS	Water analyzer
600D/California Anal. Inc	Carbon dioxide analyzer

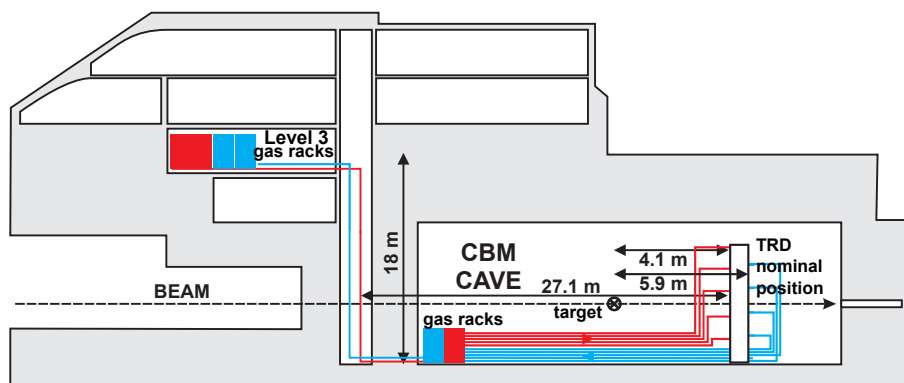


Figure 8.5: Schematic layout of the TRD gas system, showing the location of the different modules.

Table 8.2: Basic parameters of the TRD gas system.

Maximum number of modules	200
Maximum volume	$1.37 + 0.5 \text{ m}^3$
Gas mixture	Xe/CO <sub>2</sub>
Working overpressure	1 mbar
Filling rate	$5 \times 0.003 \text{ m}^3/\text{h}$
Circulation flow rate	$\text{m}^3/\text{h}$

### 8.3.2.1 Mixing unit

The gas mixing will be done based on the mass flow of the individual components (see Fig. 8.6).

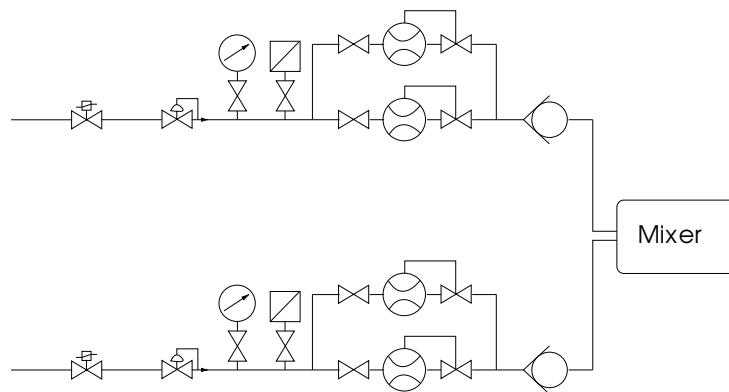


Figure 8.6: Gas mixing unit, located in the gas handling area of the CBM building. The substantially different gas flows in the filling and running modes are controlled by two different mass flowmeters per gas line [C<sup>+</sup>01].

The flows of component gases are metered by mass-flow controllers, which have an absolute stability of 0.3 % over one year, and a medium term stability of 0.1 % under steady state conditions [C<sup>+</sup>01]. Flows are monitored by a process flow control computer, which continually calculates the mixture percentages supplied to the system. The anticipated fresh gas flow at operating conditions, which depends strongly on the leak rate, is expected to be not higher than 2 l/h per flush line. Filling of the detector will be done in a closed loop circulation mode, where the purging gases N<sub>2</sub> and O<sub>2</sub> are gradually replaced by the operation mixture. The separation and recovery of the Xe/CO<sub>2</sub> mixture will be done in the recovery plant. Under normal operating conditions the mixing unit will top up the gas which is removed from the system for purification purposes or by losses due to leaks within the circuit.

### 8.3.2.2 Circulation and purification system

The gas mixture is circulated in a closed loop as shown in Fig. 8.5. Return gas from the detector must be compressed well above atmospheric pressure to pump it back to the gas handling area where it will be recycled through the purifier. The hydrostatic pressure over the total height of the detector is approximatively 2.19 mbar. Since the detector working pressure is limited due to mechanical reasons to 1 mbar, a subdivision of the full detector into height sections is necessary. Furthermore, the flow and pressure regulation must be done in each section independently. In particular, the sensor for the pressure regulation must be as close as possible to the detector inlet or outlet, in order to minimize hydrostatic and hydrodynamical pressure differences between the chamber and the sensor. On the other hand, due to space limitations around the experimental

setup, it is desirable to place as much hardware as possible in other areas. Taking into account these considerations, the following gas distribution into the detectors is proposed and shown in Figs. 8.7 and 8.8:

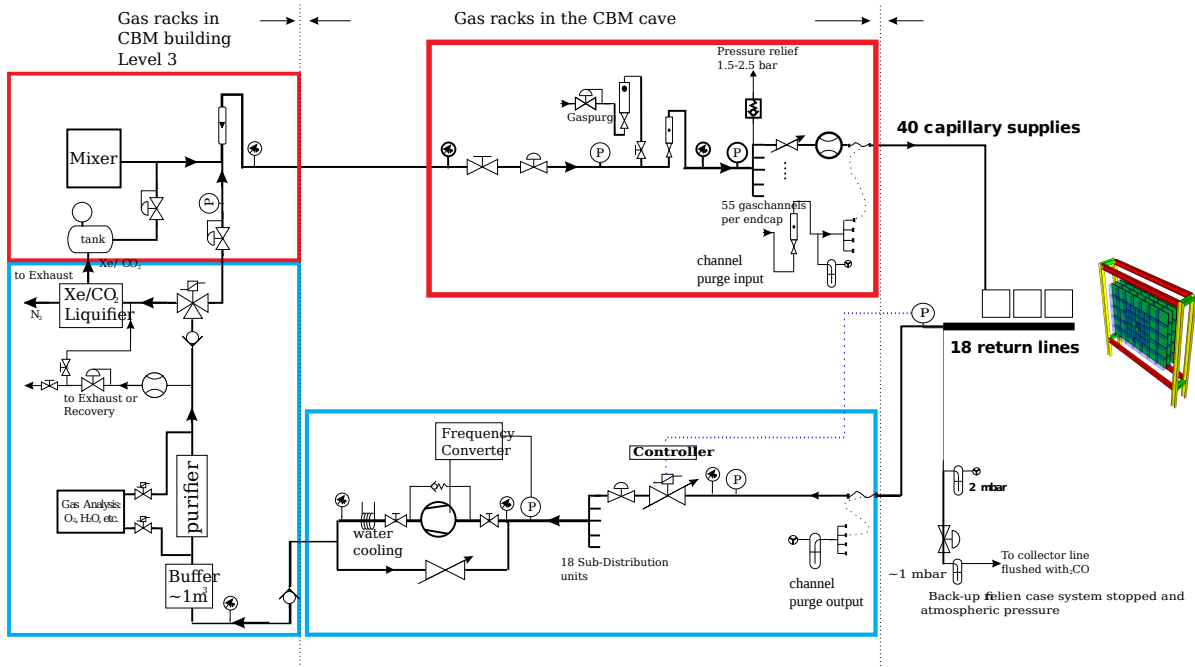


Figure 8.7: General layout of the circulation gas loop [C<sup>+</sup>01].

Gas in the recirculation unit (see Fig. 8.5) is distributed through a 40-line manifold where the lines going to the detector are thin enough (4 mm inner diameter) in order to achieve a uniform, substantial pressure drop of almost 100 mbar. If all the lines have the same length, the pressure drop in each line will be much larger than the hydrostatic differences between sectors. In this manner, the individual flow regulation can be skipped. Each line serves one set of 5 – 10 chambers (two layers back and forth in beam direction) and the pressure regulation sensor is placed at the outlet, thus being the only component inside the experimental area. All the other components will be located at the plug. The feedthrough from chamber to chamber is foreseen to be realized by a short (3 cm) pipe with an inner diameter of 18 mm, which results in a negligible (of the order of 0.04 mbar) total impedance to the gas along the 10 served chambers. The pressure regulation will be performed at the outlet of each sub-circuit (three per sector) by placing the pressure sensor near the last chamber. Still inside the experimental area a threefold manifold will merge the lines from each sector into one 60 mm line. Therefore, a total of 18 outlet lines will run up to an accessible area, where the rest of the instruments for flow and pressure regulation will be installed. The loop pressure regulation is performed by acting on the suction speed of the compressor. A pressure sensor located at the detector outlet drives the reaction mechanism. In addition, gas losses are compensated for by acting on the mixing unit flowmeters according to a pressure sensor located at the high pressure buffer after the compressor. In this manner, the regeneration rate can be chosen anywhere within the range of the mixing flowmeters, and the unrecoverable gas is limited to the leaks. The purification system will remove, as usual, oxygen and water contamination in the gas. This will be done with cartridges filled with activated copper. A configuration in parallel allows one to run gas through one purification cylinder while the other one is being regenerated. Regeneration is done by heating the cartridges to 200 °C under an Ar/H<sub>2</sub> (7%) (Noxal) mixture.

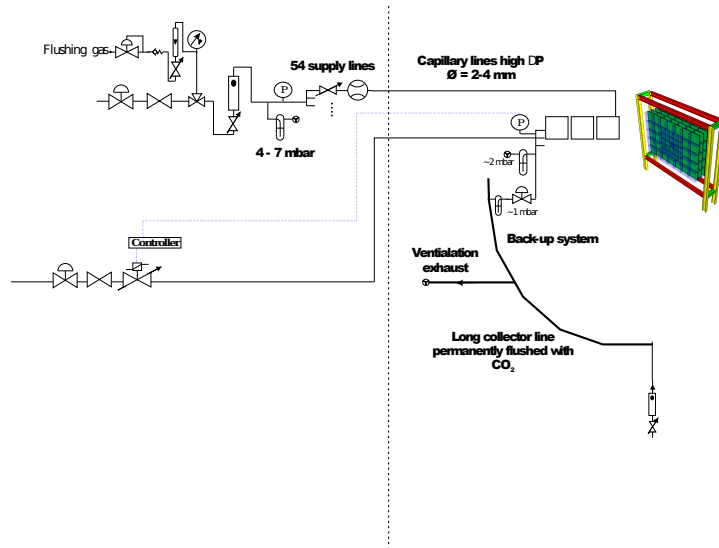


Figure 8.8: The distribution of the gas mixture into the four layers of the detector by thin lines, with the flow and pressure regulation, and the backup system [C<sup>+</sup>01].

### 8.3.2.3 Backup system

In case of a malfunctioning of the pressure regulation, for example due to a power failure, the two-way safety bubblers, located near the detectors, shall ensure that the maximum over- and underpressures that the detectors can stand does not exceed 2 – 3 mbar. However, this mechanism should be regarded as the ultimate measure for the system. In case of an increase of the atmospheric pressure during such periods, the safety bubblers would allow air to be sucked into the detectors thus deteriorating the purity of the operating gas. The purifiers and the recovery station might therefore get rapidly saturated. In order to prevent air to enter the gas loop, a backup system for cases of failure has been foreseen. It consists of a permanent flow of CO<sub>2</sub> that circulates to an exhaust which passes by one of the sides of a bubbler. In this manner, positive fluctuations of the ambient pressure results in an enrichment of CO<sub>2</sub> in the mixture, which can be gradually compensated for by the fresh gas injection mechanism as the experiment is restarted. Negative fluctuations of the ambient pressure will lead, in any case, to the loss of some xenon. The flow of backup CO<sub>2</sub>, and the expected rate of xenon loss, is estimated from experience to be driven by short maximum pressure fluctuations of 5 mbar/h.

### 8.3.2.4 Recovery station

Nitrogen, which enters the recirculation loop through leaks, cannot be removed by the purification system. Thus, a separation station is needed in order to extract the N<sub>2</sub> from the system and recover the xenon for recycling. The precise gas purge rate into the recovery unit, estimated to be 0.1% of the detector volume per hour (2.4l/h), will be determined by the actual leak rate of the system. The proposed cryogenic recovery unit is shown in Fig. 8.9.

Table 8.3: Freezing and boiling points, of some gases relevant to the present gas system.

Gas	Freezing point (°C)	Boiling point (°C)
N <sub>2</sub>	-209.86	-195.8
Xe	-111.9	-108.1
CO <sub>2</sub>	-78.4 (subl.)	

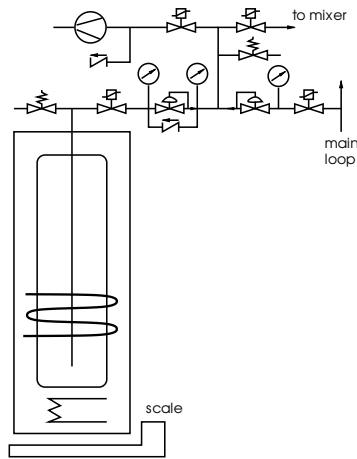


Figure 8.9: Schematic layout of the cryogenic plant used to separate the nitrogen from the components of the gas mixture [C<sup>+</sup>01].

The same concept has already been used by the ALICE experiment. The operating principle is based on the selective distillation of the gas by cooling it down to nearly the temperature of liquid nitrogen (LN<sub>2</sub>). Because the freezing point of both, the xenon and the CO<sub>2</sub>, are above that of the nitrogen, as shown in Tab. 8.3, by cooling down with LN<sub>2</sub> a storage vessel, one can freeze both the xenon and the CO<sub>2</sub> as the gas enters the vessel, while still keeping the nitrogen in the gas phase. A scale that weighs the vessel is used to control the amount of gas that enters the vessel. Once the desired amount - such that at room temperature the pressure would not exceed 200 bars - has been frozen, the gas left in the vessel is pumped and vented out until the pressure drops to essentially zero. Then, the vessel is brought back to room temperature.

## 8.4 High voltage and low voltage

### 8.4.1 Low voltage power distribution

Table 8.4: LV power consumption of individual components

Device	Power consumption (W)
ASIC	0.75
FEB_10s	7.50
FEB_05n	3.75
FEB_08n	6.00
GBTx	2.20
VTR	0.63
VTT	1.00
ROB3	8.23
ROB5	13.63
ROB7	19.03

All following values are estimated based on the current prototype DAQ components. The final versions will be further optimized and the power consumption is expected to be lower. For the CBM-TRD it is mainly caused by the components listed in Tab. 8.4, resulting in a total electric power consumption of the order of 11.23 kW or 2.8 kW per detector layer, as summarized in Tab. 8.5.

Table 8.5: LV Power Consumption (PC) per module and for the full system

Module type	1	2	3	6	7	8
Number of modules	32	24	40	24	32	48
FEB type	10s	10s	05n	08n	08n	08n
ASICs/FEB	10	10	5	8	8	8
FEB/module	9	5	6	8	4	3
ROB3/module	0	1	0	0	0	1
ROB5/module	0	1	1	2	1	0
ROB7/module	2	0	0	0	0	0
FEB PC (W)	71.7	41.0	26.7	53.6	26.8	20.1
ROB PC (W)	38.1	21.9	13.6	27.3	13.6	8.2
<b>Module PC (W)</b>	<b>109.8</b>	<b>62.9</b>	<b>40.3</b>	<b>80.9</b>	<b>40.4</b>	<b>28.3</b>
<b>TRD PC (kW)</b>						<b>11.23</b>

Two possible solutions are being considered for supplying power to the detector FEE.

1. Power supplies located outside of the cave (e.g. at Level 3), delivering the required voltages and currents directly to the FEBs and ROBs. In this case the power cable cross-section must be large enough to limit the voltage drop. However, cable bulk as well as copper conductor weight and material budget are the limiting factors for this solution.
2. DC-DC converters placed on each ROC or even FEB close to the load. In this case the cross-section of the input power cables (power bus bars) can be significantly reduced. However, the converters must be able to operate in a radiation environment. The possible effects of radiated or conducted noise from the switching supplies need to be investigated.

In both cases low-drop voltage regulators are installed on the electronics boards. The second solution has been worked out in detail and is presented here. The first one is being investigated as fall-back solution only. The SPADIC FEBs are operated at 3.3 V where the GBTx ROBs will be operated at 1.5 V (GBTx) and 2.5 V (VTT and VTR). This results in the power consumption per layer presented in Fig. 8.10.

The low voltage system will be subdivided into independent low voltage channels. The actual number of 40 LV channels is a compromise between cost and performance. Each of them will power a vertical slice of a full layer, that corresponds to 3 – 7 chambers (see Fig. 8.11).

This results in a total number of 40 power bus bars plus 40 supply and their respective return lines. The power supplies will be located inside of the cave beneath the magnet platform in an area not accessible during beam operation (see Fig. 8.12).

In this scenario a cable length of about 30 m is needed, from the power supplies to the actual copper power bus bars. The cable and bus bar characteristics are summarized in Tab. 8.6.

Each of the listed LV bus bars (A – J) is needed eight times (one supply and one return for each layer) and for each bus bar two supply cables are installed between the power supplies and the bus bar. The total weight of the 80 copper LV supply cables (2140.80 kg) and 80 bus bars (314.55 kg) for the CBM-TRD is of the order of 850 kg. The bus bars, which are mounted together with the ROCs, contribute by 9.64 % to the total weight of the detector. Figure 8.13 illustrates one option to mount the LV power bus bars on the global detector mounting structure.

The total amount of LV components is listed in Tab. 8.7.

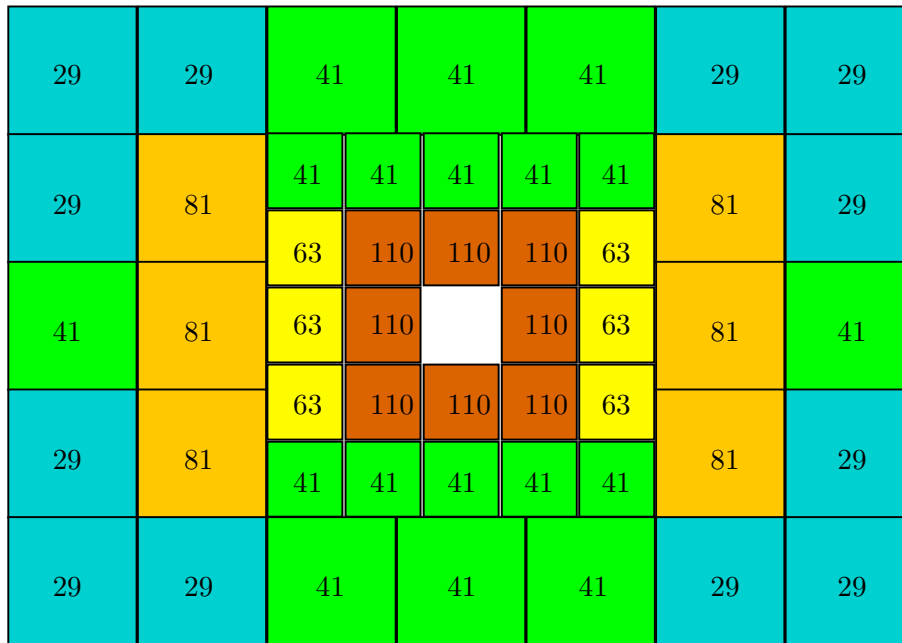


Figure 8.10: Schematic of the ASIC and GBTx power consumption per module given in Watt.

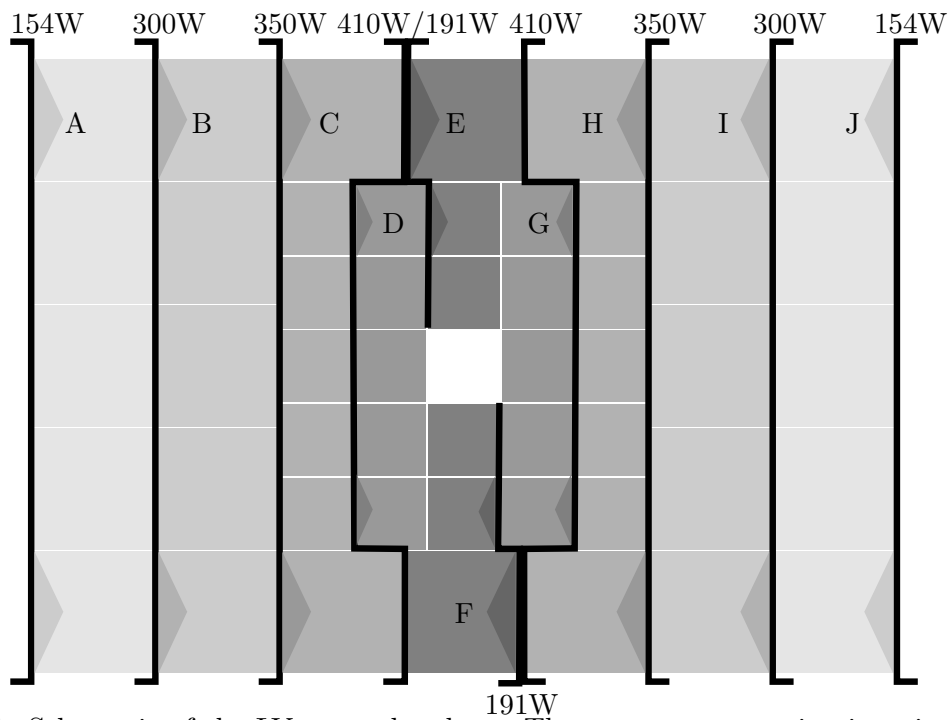


Figure 8.11: Schematic of the LV power bus bars. The power consumption is estimated only including the ASICs and GBTx.

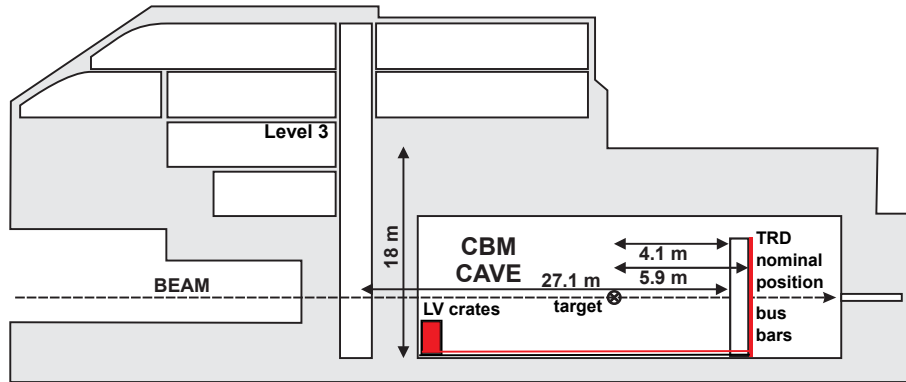


Figure 8.12: Schematic layout of the TRD LV system, showing the location of the different components.

Table 8.6: Characteristics of each cable ( $c$ ) for a low voltage system based on 40 channels.  $I_c$ : Current carried in each cable.  $S$  and  $L_c$ : Cross section and length of each cable.  $W_c$ : Cable weight,  $R_c$ : Cable resistance.  $P_c^{\text{total}}$ : Total power dissipated on the cables. The slices are labeled from A to J from left to center. The right half is identical to the left half and is therefore not presented. We assume a bus bar voltage of 48 V on the power bus bars.

Slice	Total No.	$I_c$ (A)	$S$ (mm <sup>2</sup> )	$L_c$ (m)	$W_c$ (kg)	$R_c$ (m $\Omega$ )	$P_c^{\text{total}}$ (W)
2 supply cables	40		100	$2 \times 30$	53.52	10.50	0.22
A and J bus bar	$2 \times 8$	3.21	100	4.75	4.24	0.83	153.96
B and I bus bar	$2 \times 8$	6.24	100	4.75	4.24	0.83	299.46
C and H bus bar	$2 \times 8$	7.30	100	4.75	4.24	0.83	350.32
D and G bus bar	$2 \times 8$	8.55	100	5.51	4.91	0.96	410.16
E and F bus bar	$2 \times 8$	3.97	100	2.28	2.03	0.40	190.74

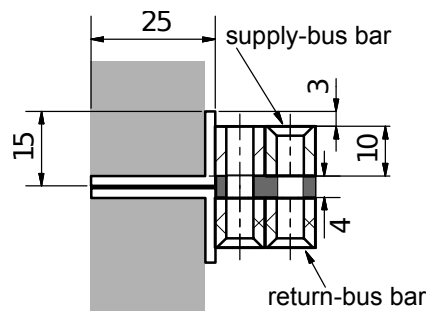


Figure 8.13: Module LV copper bus bar mounted on the FR4 module slice mounting ledge. They follow the vertical run which is only discontinued in the inner part of the detector layer.

Table 8.7: Main LV components.

Number	Device	Length (m)	Comment
	LV power supplies		
80	LV supply cables	30	between racks and detector
80	LV copper bus bars	2.28 – 5.51	on backside of each layer
1696	DC-DC converter		1208 for FEBs and 488 for ROBs
1016	LV-FEB cables	0.6 – 1.0	

## 8.4.2 High voltage power distribution

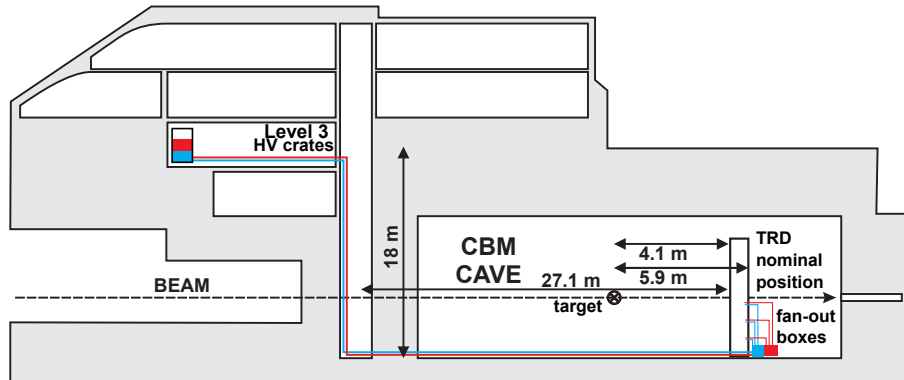


Figure 8.14: Schematic layout of the TRD HV system, showing the location of the different modules.

The foreseen chamber design requires two HV potentials to separate the primary ionized ions from the electrons, accelerate and amplify the electrons. These potentials are of the order of 1700 – 2000 V with positive and 500 V with negative polarity. The negative potential is applied to the Kapton entrance foil window, while the positive potential is connected to the anode wires. To operate 200 individual detector modules 200 positive and 200 negative HV power supply channels are needed. The most cost efficient low noise power supply for this purpose is the ISEG HV EDS F025n/p 504 SHV Redel (32 or 48 channels). In order to get a maximum channel utilization a 32 channel power supply would be the favored option. Therefore, seven ISEG HV EDS modules with 32 channels with positive and seven with negative polarity powered by two Wiener MPOD or ISEG ECH 44A (10 slot) crates are a solution for the CBM-TRD.

The interconnection of the HV power supplies positioned on Level 3 of the CBM building and the modules in the cave is done via  $37 \times 0.14 \text{ mm}^2$  3 kV HT cables (with 37 litz wires each), as presented in Fig. 8.14. The 32 channels are split into individual channels using fan-out boxes positioned close to the nominal position of the TRD in the cave. Each fan-out box can serve 32 detectors with one polarity, resulting in four fan-out boxes serving one detector layer with 50 modules for both polarities each. The full positive and negative HV distribution system for the CBM-TRD will be composed of  $16 \times 37 \times 0.14 \text{ mm}^2$  3 kV HT cables and fan-out boxes with 400 coaxial high voltage cables 5 kV interconnecting the fan-out boxes with the individual modules. The main components are summarized in Tab. 8.8.

Table 8.8: Main HV components

Number	Device	Length (m)	Comment
2	MPOD or ECH 44A		10 slots
7	ISEG HV EDS F025n 504		32 channels/module
7	ISEG HV EDS F025p 504		32 channels/module
16	$37 \times 0.14 \text{ mm}^2$ cable	45 – 50	32 channels
16	HV fan-out boxes		32 channels
400	Coaxial HV cables	15	single channel
200	HV filter boards		up to 9 anode segments & 1 drift

A low pass filter PCB board close to the chamber will be used to enhance the potential stability and reduce external noise. At the same time it allows to decouple up to nine anode wire

segments, thus enhancing the fail tolerance of the module with respect to mechanical and/or electrical anode wire failures. The electrical interconnection between the HV-filter board and the drift electrode/anode wires segment is realized using a coaxial high voltage cable which is transferred through holes at the edges of the honeycomb backpanel and the pad plane. The gas tightness is ensured by usage of Araldite glue.

## 8.5 Cooling

Cooling of the FEBs and/or ROBs will be organized according to the power consumption of the individual ROC (compare to Fig. 8.10). A total power dissipation of  $400 \text{ W/m}^2$  is assumed to be the limit for passive air cooling. As already pointed out, the presented power consumption values are based on measurements with DAQ prototype components and should be interpreted as upper limits. Since the limit for passive air cooling is just reached in the inner part of the detector layers, and a decrease of power consumption in the range of 10% is reasonable we assume that passive air cooling will be the most probable solution for CBM-TRD. If it finally turns out that the electronics of certain modules will be above this limit these will be cooled by active water cooling.

### 8.5.1 Cooling distribution

The pipes used to bring the cool water to the ROCs as well as the return lines will be positioned between the beam pipe and the inner modules of type 1, which have to be actively cooled. Nine FEBs of type 10s are mounted on the chamber with two ROB7 resulting in a minimum cooling pipe length per module of 5.0 m. The heat radiator and pumping system will be positioned in the cave below the HADES platform. This results in additional 27 m pipes between the modules and the service station in average. The supply and return lines between the service station and the individual detector layers will be covered by aluminum pipes with a diameter of 32 mm for each layer. The pipes within each layer will be aluminum with an outer diameter of 6 mm. Based on the experience gained with the ALICE-TRD it was defined that the full system has to be driven by under pressure to avoid a damage of the electronic in case of a cooling system leak.

## 8.6 Monitoring and detector control

The safe and stable operation of the TRD requires the continuous monitoring of several quantities which are summarized in Tab. 8.9. The system should be able to either safely switch off critical hardware components (e.g. HV supplies) to prevent damages, if certain predefined parameter thresholds are exceeded (hardware threshold), or to issue alarms to the operators (software alarm) when other essential observables reach values which would compromise the detector operation. The detector control system should also provide the possibility to switch on and off all detector components and to change all their relevant system parameters, such as HV and LV settings.

## 8.7 Safety aspects

The CBM-TRD detector will follow the GSI/FAIR safety rules and codes. Specifically, the following risks and actions are to be considered and will be discussed with the GSI/FAIR Technical Inspection and Safety commission:

- The gas mixtures for the TRD, Xe/CO<sub>2</sub> and Ar/CO<sub>2</sub>, are non flammable and have UN classification 2.2 (non-toxic and non-flammable substances). Due to the non-negligible quantity of these gases in the CBM cave, the TRD volume is about  $1.9 \text{ m}^3$ , and the high

Group	Observable	Logging frequency	Operation safety
Environment	Air humidity	1/h	Software alarm
	Air pressure	1/h	Software alarm
	Ambient temperature	1/h	Software alarm
Gas mixture	Temperature at chambers	1/min.	Software alarm
	Pressure per height level	1/min.	Hardware threshold
	H <sub>2</sub> O content	1/min.	Software alarm
	CO <sub>2</sub> content	1/min.	Software alarm
	O <sub>2</sub> content	1/min.	Software alarm
	Flow	1/min.	Software alarm
Low voltage	Potentials	1/min.	Hardware threshold
	Currents	1/min.	Hardware threshold
High voltage	Potentials	1/s	Hardware threshold
	Currents	1/s	Hardware threshold
FEBS	Temperatures	1/min.	Hardware threshold
Cooling	Temperatures	1/min.	Hardware threshold
	Pressure	1/min.	Hardware threshold

Table 8.9: List of observables to be monitored during TRD operation.

densities of xenon (5.58 g/l), argon (1.78 g/l) and CO<sub>2</sub> (1.98 g/l), oxygen deficiency meters will be installed near to the detector.

- The TRD detector will be operated with an overpressure of a 1 mbar above the atmospheric pressure and is designed for a maximum over-pressure of 2 – 3 mbar. Thus, the TRD modules are not classified as pressure vessels.
- The high pressure part of the gas system is located in E30, near the surface. The gas system will be constructed according to the appropriate rules.
- The MWPCs will operate with high voltages at around 1 – 2 kV, the total current for each individual supply line will be limited to few mA. The low voltage supply to the detector readout is below 50 V. The total power dissipation on the detector is below 12 kW. Appropriate interlocks and current monitoring systems will be installed enabling to interrupt power at the source.
- Work will occasionally be done in the electronics area inside the CBM cave in E10, close to the detector. After beam shut down adequate waiting times are necessary to ensure that the air activation is below 3  $\mu$ Sv/h.

## Chapter 9

# Simulation and Reconstruction

The software developments for the simulation of the TRD detector and for the reconstruction of its data are presented in the following. A detailed and realistic description of the detector response is mandatory for reliable studies of the detector performance and is therefore based on input from test beam measurements as much as possible. In the following, results on the expected trigger rates and occupancy, as well as on the tracking and electron identification performance are presented.

### 9.1 Simulation framework

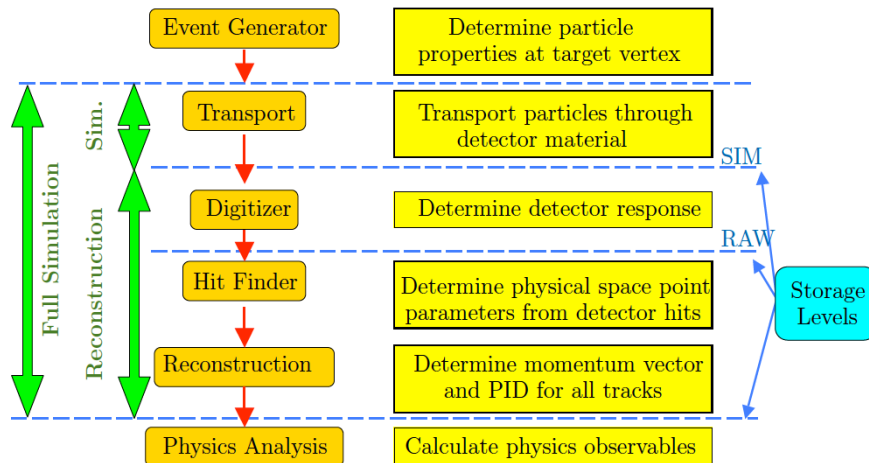


Figure 9.1: Summary of the different simulation and reconstruction steps implemented in the CBMROOT framework (picture taken from [Ber14]).

The simulations presented here were performed within the CBMROOT framework, which contains all components necessary to perform a full detector simulation and reconstruction (see Fig. 9.1). As standard event generator UrQMD [B<sup>+</sup>98] is used. The detector setup used in the simulations is the same as described in Chap. 3. The particle transport through the geometry is performed with GEANT3 [B<sup>+</sup>87]. The details of the TRD response simulation, which describes the signal generation related to the specific energy loss and TR-photon absorption, and the details of the hit finding and reconstruction step are described in the following sections.

## 9.2 Detector simulation

The fundamental processes responsible for the signal creation and evolution within a TRD can in principle be included in all microscopic details in a MC detector response simulation framework, however, at the price of a relatively high CPU time consumption. To achieve an adequate compromise between a detailed physics simulation and an efficient detector response, both parts are decoupled in the CBMROOT simulation framework. The particle production and transport, as well as all relevant energy loss effects, except TR-photon production, are calculated within the simulation part. Only the total energy loss per active detector volume is stored. The detector response, DAQ, data transport, event building and the physics analysis is done in the second step, the reconstruction part. The output of the simulation is pure MC information, like the ionization energy loss or the position of the entrance and exit points of particle trajectories crossing active detector volumes.

### 9.2.1 Energy loss in the detector gas

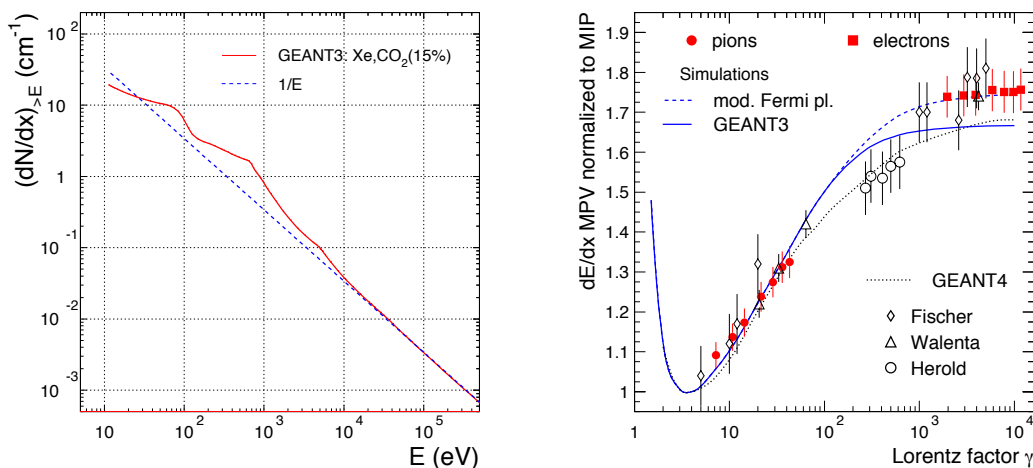


Figure 9.2: Left: The integral spectrum of the energy transfer in primary collisions of charged particles simulated with GEANT3 (red line). Right: The MPV of the energy loss, normalized to the MIP value, as a function of the Lorentz-factor  $\gamma$ . Both figures are taken from [A<sup>+</sup>04].

The energy loss of all particles, including  $\delta$ -electron production, is calculated (in the simulation step) using GEANT3. In the context of the developments performed for the ALICE-TRD, the performance of GEANT3 in terms of energy loss for xenon as counting gas was evaluated [A<sup>+</sup>04]. The left panel of Fig. 9.2 displays the energy spectrum of primary electrons released in inelastic collisions of a minimum ionizing particle (MIP,  $\gamma = 4$ ) with a Xe/CO<sub>2</sub> (85/15) mixture. GEANT3 uses an implementation of the photo-absorption ionization model [AC80] to calculate this process. The structures correspond to the atomic shells of xenon. For comparison also the Rutherford spectrum is shown, which, in its integral form, corresponds to a  $1/E$  dependence. Both shown distributions start at the first ionization potential of xenon,  $I_{\text{pot}} = 12.1$  eV, and extend up to the energy above which the released primary electrons are treated as  $\delta$ -rays that are transported as separate tracks by GEANT3. The threshold for this transition was chosen as 10 keV.

A comparison of the GEANT3 result for the most probable value (MPV) of the  $dE/dx$  (blue solid line) to data is shown in the right panel of Fig. 9.2. Generally, a good agreement was found up to the relativistic rise, while the unmodified GEANT3 slightly under-predicts the

measurements in the region of the Fermi-plateau.

### 9.2.2 Transition radiation

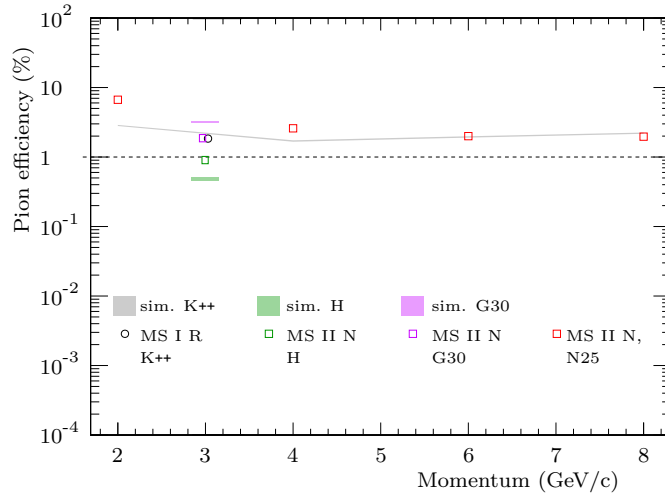


Figure 9.3: The pion efficiency, i.e. the probability to misidentify pions as electrons, for a TRD with four detector layers as a function of the particle momentum. Shown are test beam results for four different radiator types (K++, H, G30 and N25) in comparison to simulations [Ber14]. The labels “MS I R” and “MS II N” refer to two different version of ROCs (amplification and drift region thicknesses 3.5+3.5+5 mm).

The simulation of the TR-photon production is done based on Eq. 6.9 as described in Chap. 6.1. The self-absorption of the radiator is taken into account as well as the absorption of the aluminized entrance window and the active gas volume. Losses due to TR-photon absorption within the FR4 lattice grid between the radiator and the entrance window foil are also implemented. The final deposited energy due to TR-photon absorption within the sensitive gas volume is added to the ionization energy loss coming from the simulation part. The radiators which have been tested in beam between 2010 and 2012 are all implemented in the framework and modeled according to the in beam test results. Figure 9.3 shows a comparison of pion efficiencies measured in beam tests and simulated with the above described approach.

Since for the radiators H and G30 the momentum dependence of their performance has not yet been experimentally determined, we rely in the performance studies on the momentum dependent prediction for the K++ type, tuned to the measurement at 3 GeV/c (gray band in Fig. 9.3). The radiator K++ is a self-supporting regular foil stack type. At a momentum of 3 GeV/c its performance is very similar to the radiator G30 and slightly worse than the radiator H, which are both discussed in Sect. 6.3 in detail. For the baseline TRD setup radiator type H is currently foreseen as the default solution.

The comparison with the measurements for the radiator N25, which is an irregular type (PE foam) with properties similar to H (PE foam foils) and K++, illustrates that the calculated momentum dependence used here should be realistic, also for an irregular radiator. In any case, only a moderate change of the pion suppression factor with increasing momenta is expected, while the evolution towards lower momenta is rather dominated by the contribution from the energy loss due to ionization. The measurement for the radiator type H at 3 GeV/c might indicate that our currently employed model is even underestimating the achievable performance of the final detector design and that therefore the performance studies discussed in the following and in Chap. 3 can be considered as conservative.

### 9.2.3 Signal generation

The signal generation is partitioned into three stages: digitization, clustering and hit production.

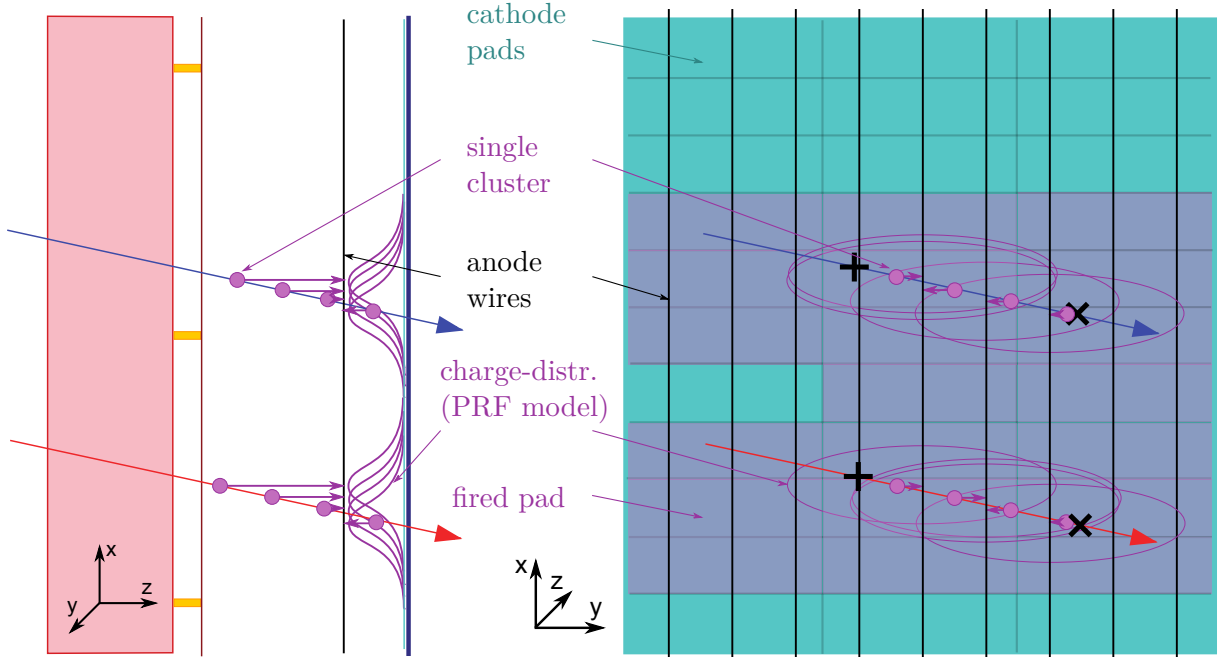


Figure 9.4: Schematic view of the CBM-TRD detector response simulation as implemented in CBMROOT. The algorithm splits the total MC energy loss into several equal single clusters per unit track length inside the active detector volume. These single clusters are transported towards the closest anode wire position. The induced charge fraction as function of the displacement of the single cluster position with respect to the center of the underlying pad is calculated in  $x$ - and  $y$ -direction based on the PRF model (Eq. 9.1). The product of the  $x$  and  $y$  charge fraction per pad is multiplied with the single cluster charge to evaluate the induced charge on each pad. The signal of two or more single clusters of the same or different MC tracks within the same event are summed up.

#### 9.2.3.1 Digitization

The digitization comprises the detector response up to the charge distribution on the pad plane and charge integration and/or preprocessing by the ASIC. Up to now, there is no detailed time evolution of the signal and further detailed ASIC features implemented. The charge distribution is estimated based on the Pad Response Function (PRF)

$$\begin{aligned}
 PRF(d/h) &= \int_{d/h-W/2}^{d/h+W/2} \rho(d'/h) d(d'/h) \\
 &= - \frac{\arctan\left(\sqrt{K_3} \tanh\left(\pi(\sqrt{K_3}-2) \cdot \frac{W-2 \cdot d}{8h}\right)\right)}{2 \arctan(\sqrt{K_3})} \\
 &\quad - \frac{\arctan\left(\sqrt{K_3} \tanh\left(\pi(\sqrt{K_3}-2) \cdot \frac{W+2 \cdot d}{8h}\right)\right)}{2 \arctan(\sqrt{K_3})}.
 \end{aligned} \tag{9.1}$$

which is given by the spatial integral of the charge density distribution presented by Mathieson [Mat88]

$$\rho(d/h) = q_a \cdot \frac{\frac{\pi}{2} \cdot \left(1 - \frac{\sqrt{K_3}}{2}\right) \sqrt{K_3}}{4 \arctan(\sqrt{K_3})} \cdot \frac{1 - \tanh^2\left(\frac{\pi}{2} \cdot \left(1 - \frac{\sqrt{K_3}}{2}\right) \frac{d}{h}\right)}{1 + K_3 \tanh^2\left(\frac{\pi}{2} \cdot \left(1 - \frac{\sqrt{K_3}}{2}\right) \frac{d}{h}\right)}. \quad (9.2)$$

Equation 9.1 describes the normalized induced charge fraction as a function of one parameter representing the chamber geometry  $K_3$ , the pad width  $W$ , the distance between anode wire plane and pad plane  $h$  and the displacement  $d$  of the cluster relative to the pad center. This description is valid parallel and perpendicular to the anode wire direction for quadratic or squared pad geometries and therefore used to calculate the charge sharing on adjacent pads in the CBM-TRD. A detailed description of the charge sharing for other pad geometries is not available in the framework at the moment. Since the simulation stores only the total energy loss per particle track segment, the clustering of the primary ionization processes along the particle trajectory has to be recovered in the reconstruction step to obtain a realistic detector response in a MWPC, specially for tracks with a large impact angle, which are found in the outer part of the detector layers. The total energy loss is therefore subdivided into  $n$  equal fractions, which is also done for the track path in the active volume. The individual primary ionization clusters are projected towards the closest anode wire. The induced charge fraction is calculated based on Eq. 9.1, multiplied by the primary cluster energy loss fraction and summed up on the channel (“digi”) level. The fired digis are summed up after each event, since a given pad can be fired by more than one track in a collision. In addition, the SPADIC response can be simulated, which is useful to study the DPB feature extraction based on simulated data.

### 9.2.3.2 Clustering and hit reconstruction

In a following step the continuous and mixed digi stream is sorted. This is done based on a detector and channel unique ID. This analysis step corresponds to ASIC (time sorting) and the DPB/FLES (spatial sorting) in the experiment. All digis above a threshold of 1 keV total energy loss are used as cluster seed. All digis sharing at least one edge along the anode wire direction with a seed digi are merged into a cluster, where different seeds can share digis. Since the detector design is optimized for an average cluster size of 2.5 channels per cluster in anode wire direction, only first neighbor generation digis are merged to the seeds. This feature is also realized in the SPADIC by a neighbor channel triggered readout. This algorithm allows therefore for detailed detector studies, including occupancy and physics performance. The DPB readout layer is also implemented. It is foreseen to merge clusters of adjacent rows which overlap in column, if the weighted center of charge of both agree within a fixed window. The procedure reduces significantly the amount of ghost hits in the last step.

A hit corresponds to a charge cluster with a position information assigned to it. The position in the  $x$ - $y$ -plane is determined by calculating the center-of-gravity of the charges associated with a given cluster. The  $z$ -position of the hit is set to the  $z$ -position of the pad plane of the corresponding chamber.

A two-dimensional position reconstruction based on the charge measured with rectangular pads of the size  $5 \times 10 \text{ mm}^2$  has been demonstrated based on data from the in-beam test of 2006 at GSI [Ber09]. The reconstructed beam profile is presented in Fig. 9.5. From this data a lower limit of 20 mm pad height can be estimated for a two-dimensional position reconstruction on rectangular pad geometries.

The reconstruction algorithm is based on the assumption of a Gaussian shaped charge

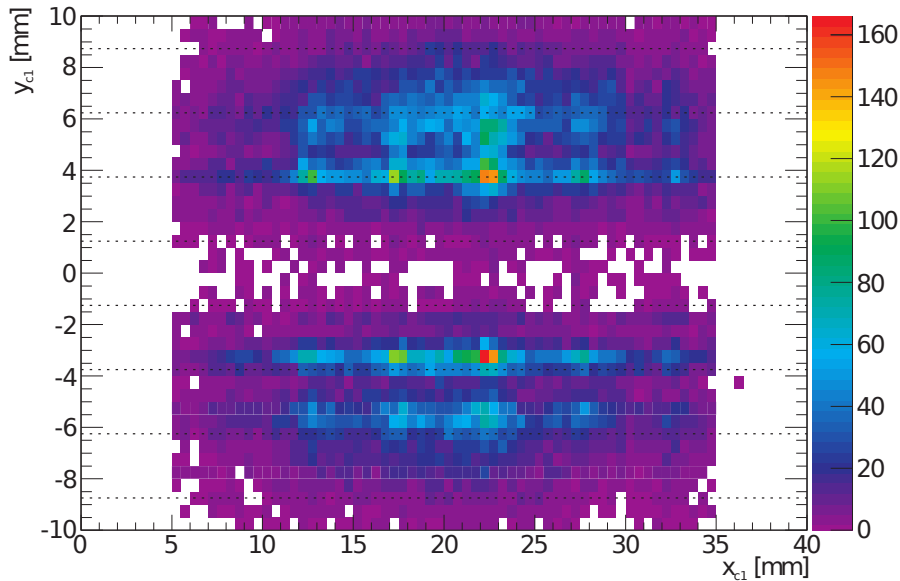


Figure 9.5: Beam profile as reconstructed in two dimensions using a rectangular pad plane geometry ( $5 \times 10 \text{ mm}^2$ ) for a test beam in 2006 at GSI [Ber09]. The gray dashed lines represent the anode wire positions.

distribution  $Q^{\text{Fit}}(y)$  between two adjacent pad rows.

$$Q^{\text{Fit}}(y) = A \cdot \exp\left(-\frac{y^2}{2\sigma^2}\right). \quad (9.3)$$

The charge ratio between the two rows can be fitted by Eq. 9.3 resulting in the presented distribution. The accumulation points within the spectrum are due to the wire positions. Thus, the position along the pad columns can be determined with a resolution of the order of the wire distance  $2.5 \text{ mm}$  divided by  $\sqrt{12}$ .

## 9.3 Reconstruction routines

This section describes technical details and performance tests on the hit and track reconstruction routines implemented in CBMROOT which are the basis for all physics feasibility studies and TRD performance simulations presented in the physics performance chapter (see Chap. 3).

The main challenge of the hit reconstruction and track recognition in the CBM-TRD detector results from the large multiplicity in heavy-ion collisions, which leads to a high track and hit density in the TRD detector. As an example Fig. 9.6 shows an event display with a simulated Au + Au collision at  $10 \text{ AGeV}$ . Displayed are geometries of the CBM detectors, the tracks of the particles generated with UrQMD, and the produced hits in the sensitive volumes of the detectors.

### 9.3.1 Track reconstruction

The track reconstruction algorithm developed for the TRD is based on a track following algorithm using the tracks reconstructed in the STS as seeds. The STS tracking employs the cellular automaton method [Kis06] and the STS track parameters are used as a starting point for the following track prolongation. This track following is based on the standard Kalman filter technique [Kal60] and is used for the estimation of track parameters [Fru87] and trajectory

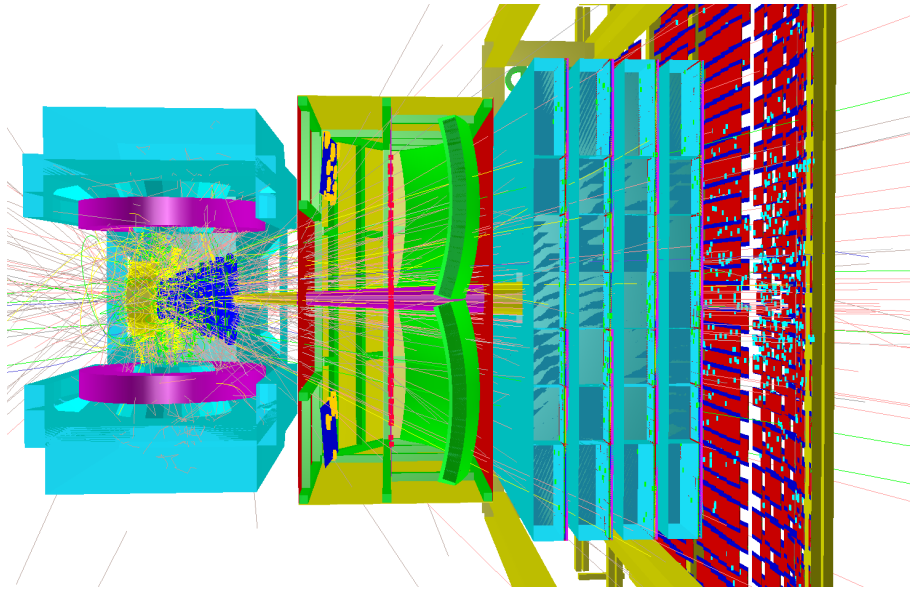


Figure 9.6: Visualization of one simulated central Au + Au collision at 10 AGeV.

recognition. The main logical components are track propagation, track finding, track fitting and, finally, a selection of good tracks. Each of these steps will be described in the following in more detail.

### 9.3.1.1 Track propagation

The track propagation algorithm estimates the particle trajectory and its errors, while taking into account three physics processes which influence the trajectory: energy loss, multiple scattering and the magnetic field. The effect of the material on the track momentum is taken into account by calculating the expected average energy loss due to ionization (Bethe-Bloch formula) and bremsstrahlung (Bethe-Heitler formula) [O<sup>+</sup>14]. The influence of multiple scattering on the error, which is propagated via the covariance matrix, is included by adding process noise in the track propagation. Here, a Gaussian approximation employing the Highland formula [O<sup>+</sup>14] is used to estimate the average scattering angle. The propagation of the trajectory is done according to the equation of motion. If the track passes a magnetic field the equation of motion for a charged particle is solved applying the 4<sup>th</sup> order Runge-Kutta method [Pre07]. If it passes a field free region a straight line is used for propagation and transport matrix calculation. The transport matrix is calculated by integrating the derivatives along the so-called zero trajectory [F<sup>+</sup>00]. A detailed description of the track propagation developed for the TRD can be found in [LO08].

### 9.3.1.2 Track finding

In the track finding algorithm hits are attached to the propagated tracks at each detector station using two different methods. Either just the nearest hit is attached to the track, or all hits within a certain environment are included in the branching method. For the first method, only one track is propagated further. The branching method allows for several track branches to be followed, one for each attached hit. Techniques common to both methods are the above described track following, the Kalman filter and the calculation of the validation region for hits.

The assignment of new hits is done step by step at each detector station. After the track has been propagated to the next station, possible hits are attached and track parameters are updated by the Kalman filter. For the attachment of hits a validation gate is calculated in order

to allow for a high degree of confidence in the hit-to-track assignment. The validation gate is defined based on the residual vector  $r$  (distance between the fitted track and the hit) and the residual covariance matrix  $\mathbf{R}$ . In the context of Kalman-based tracking filters, a validation gate can be expressed as  $v = r \mathbf{R}^{-1} r^T < d$ . The cut value  $d$  is chosen such that a defined probability of rejecting the correct hit is achieved, here this probability is chosen to be 0.001. Values for  $d$  are taken from  $\chi^2$  tables, determined as a function of the number of effective degrees of freedom. The algorithm takes into account the possibility of hits missing due to detector inefficiencies, dead zones in the detector, inefficiencies of the hit finder algorithm, and other effects.

The two methods that are used to assign hits to tracks differ in the way how they treat the situation in which several hits lie within the validation gate. In case of the branching method, a new track branch is created for each hit lying within the validation gate. Since the number of branches can grow exponentially, the  $\chi^2$  value is calculated for each track branch and unlikely ones are rejected. For each input track seed the number of created branches is also calculated and, if it exceeds a certain limit, the tracking continues by using the nearest neighbor approach instead. For the second method no track branches are created. The nearest neighbor method attaches the hit with the smallest  $v$ , if it is lying in the validation region at all.

### 9.3.1.3 Track selection

After track finding so-called clone tracks (consisting of very similar sets of hits) and ghost tracks (consisting of a random set of hits) have to be rejected while keeping correctly found tracks with high efficiency. The selection algorithm works in two steps. First, tracks are sorted by their quality, which is defined by the track length and their  $\chi^2$ . Then, starting with the highest quality tracks, all hits belonging to a track are checked. In particular, the number of hits shared with other tracks is calculated and the track is rejected, if more than 15% of its hits are shared.

## 9.3.2 Electron identification

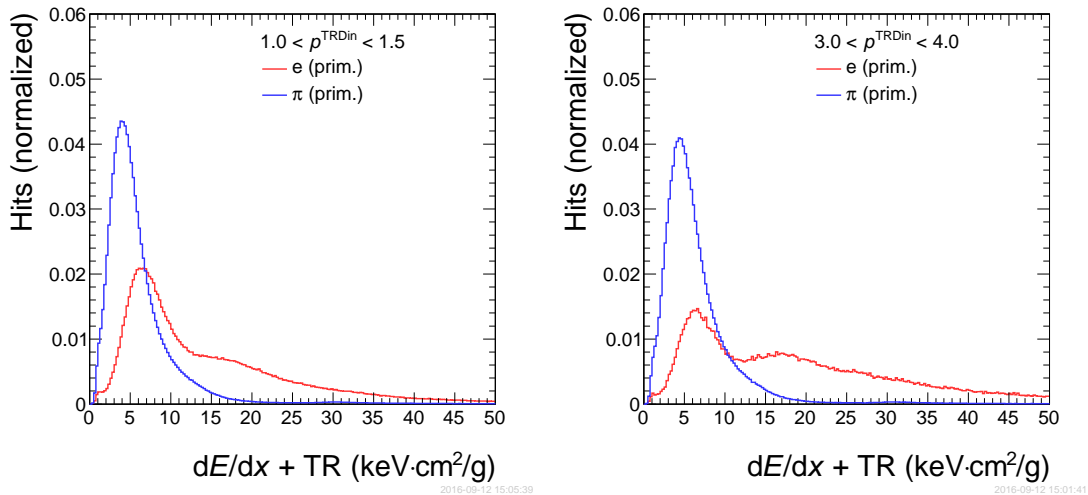


Figure 9.7: The simulated signal distributions for a single TRD layer in two different momentum intervals. Primary electrons are shown in red and pions in blue color.

The goal of the electron identification algorithms is to distinguish electrons and pions using a set of energy loss measurements. The simulated signal distributions in a single TRD layer are displayed for two different momentum intervals in Fig. 9.7. The values are corrected for the different path lengths the tracks can have when passing through the gas volume at different

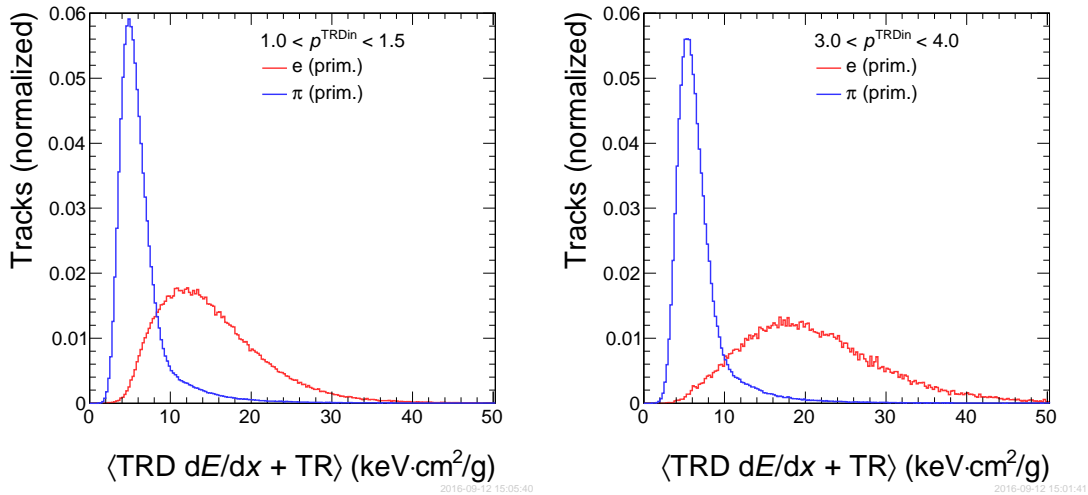


Figure 9.8: The simulated distributions of the average energy loss signal for tracks reconstructed with at least three hits in the TRD for two different momentum intervals. Primary electrons are shown in red and pions in blue color.

incidence angles. The distributions for pions reflect the deposited charge due to energy loss alone. As the pion momentum increases, the average of the distribution move to slightly higher values due to the increase of the specific energy loss  $dE/dx$  in the relativistic rise region of the Bethe-Bloch curve. For electrons the distributions have a more complex shape, since in addition to the specific energy loss also the TR component contributes and causes the second maximum at higher momenta. While the specific energy loss of electrons is already in the plateau region of the Bethe-Bloch curve throughout the whole relevant momentum range and thus the position of the first peak does not change, the TR contribution still rises between the two momentum intervals shown.

The TRD in the SIS100 configuration will deliver up to four independent measurements of the  $dE/dx + TR$  signals. The distributions of the averaged signals for tracks with at least three hits is shown in Fig. 9.8. Even though a clear separation of electrons and pions is visible in both momentum intervals, applying simple cuts on the average signal for all layers usually does not provide a sufficiently high pion suppression level, so that more sophisticated algorithms have to be used. For this purpose several methods for electron identification were implemented. The two main methods are the Likelihood Function Ratio (LFR) and an Artificial Neural Network (ANN). Other methods, that were also implemented and tested, are Ordered Statistics (Median) and an algorithm based on the usage of a Boosted Decision Tree (BDT) classifier.

### 9.3.2.1 Artificial neural network

As the default electron identification method, which is also used for the simulations prepared for the performance studies shown in Chap. 3, an algorithm based on an ANN is employed. Here the ANN implementation of the multilayer perceptron type from the ROOT package [BR97] was used. The number of input neurons corresponds to the number of energy loss measurements (number of hits in a track). The number of neurons in the hidden layer is the doubled number of the input neurons. The ANN has one output neuron. Simply using a set of energy loss measurements as input to the ANN did not allow to train the ANN in a robust way and to obtain reasonable pion suppression factors. To solve this problem it was proposed [A<sup>+</sup>07] to transform the initial energy

loss measurement set to a new set of variables  $\lambda_i$ , according to the equation:

$$\lambda_i = \frac{E_i - E_{\text{mp}}}{\xi} - 0.225, \quad (9.4)$$

where  $E_i$  is the measured value of energy loss in the  $i$ th TRD station,  $E_{\text{mp}}$  is the most probable value, and  $\xi$  corresponds to  $\frac{1}{4.02}$   $FWHM$  of the distribution of energy loss for pions. The sample of the obtained  $\lambda_i$  values is sorted according to their magnitude and for each of them the corresponding values of a Landau distribution function  $\varphi(\lambda)$  are calculated. This new set of is used as the input to the ANN.

The left panel of Fig. 9.9 illustrates the distributions of the ANN output values from the training sample for electrons and pions. A cut on the ANN output value defines the required electron identification efficiency (90 % by default).

### 9.3.2.2 Likelihood function ratio

The likelihood for a measured track to be an electron is defined as

$$L = \frac{P_e}{P_e + P_\pi}, \quad (9.5)$$

where  $P_e$  is the probability that the track is an electron and  $P_\pi$  its probability to be a pion.

$$P_e = \prod_{i=1}^N P(E_i|e), \quad P_\pi = \prod_{i=1}^N P(E_i|\pi). \quad (9.6)$$

Here,  $P(E_i|e)$  and  $P(E_i|\pi)$  are the probabilities that the energy deposit in the  $i$ th layer was produced by an electron or a pion, respectively.  $N$  is the number of hits assigned to a given track.

The right panel of Fig. 9.9 shows the distributions of the likelihood values for electrons and pions. The cut on the likelihood values defines a certain electron identification efficiency (90 % by default).

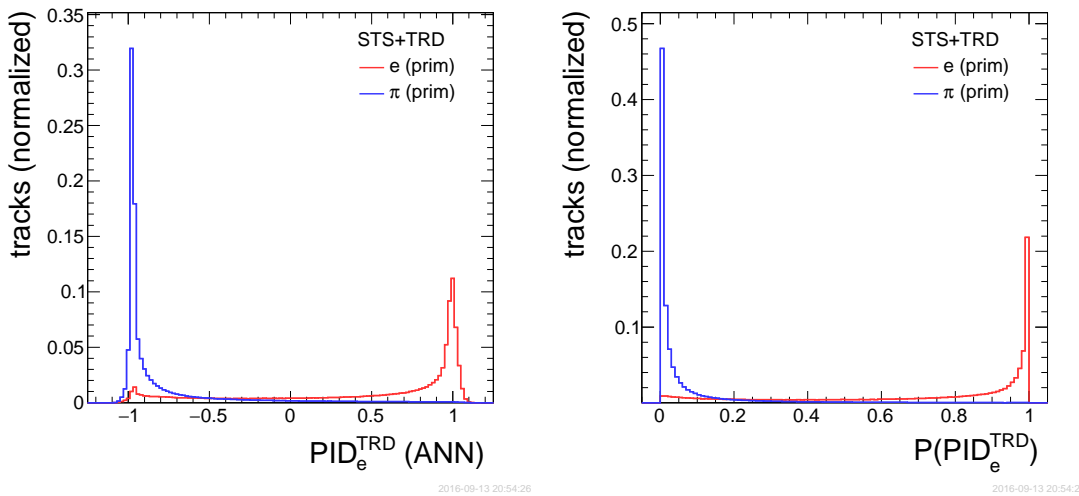


Figure 9.9: Left: The distributions of the ANN output values for electrons and pions, integrated over all momenta. Right: The momentum integrated distributions of the likelihood values for electrons and pions. Electrons are shown in red, pions are shown in blue color.

### 9.3.2.3 Ordered statistics (median)

For each reconstructed TRD track the median value of the corresponding array of energy loss measurements is calculated by rearranging all the measurements from the lowest to the highest value and selecting the middle one. If there is an even number of measurements, the median is defined to be the mean of the two middle values. Using a cut on the median value one can distinguish between electrons and pions. The main advantage of this algorithm is its simplicity and extremely fast calculation speed, while at the same time it gives reasonable results. The median method is more robust in comparison to a simple cut on the sum of energy loss measurements, as it helps to overcome difficulties with long tails of the energy loss distributions.

### 9.3.2.4 Boosted decision tree

First a preparation step is performed in order to construct Probability Density Functions (PDF), which are needed for the energy loss transformation. PDFs are obtained separately for pions and electrons in the following way: For each TRD track the assigned set of energy loss measurements is sorted from the lowest value to the highest one. Then a set of histograms is filled such that the lowest energy loss value goes to the first histogram, the next one to the second and so on. Finally, these histograms are normalized to an integral of unity and kept for the further analysis.

During the reconstruction step the array of measured energy loss values, assigned to a given track, is sorted by its magnitude. Then for each energy loss  $E_i$  a new "normalized" value  $L_i$  is calculated according to the equation:

$$L_i = \frac{PDF_i^\pi(E_i)}{PDF_i^\pi(E_i) + PDF_i^e(E_i)}, \quad (9.7)$$

where  $PDF_i^\pi(E_i)$  corresponds to the value of the PDF for pions and  $PDF_i^e(E_i)$  to the value of the PDF for electrons for the  $i$ -th energy loss. The resulting array of "normalized" energy losses is used as input for a BDT classifier [BR97]. The cut on evaluated BDT output value is set assuming 90 % electron identification efficiency.

## 9.3.3 Performance of the tracking and electron identification.

The results presented in this section are based on studies performed with standard simulations for central Au + Au collisions at 8 AGeV beam energy. Events were generated with the UrQMD event generator [B<sup>+</sup>98] to which various dielectron sources have been added as described in Sect. 3.1.2. The detector setup which is described in Sect. 3.1.1 was used for simulations.

### 9.3.3.1 Reconstruction efficiency and resolution in the TRD

The performance of the reconstruction algorithms was determined using information on the MC input. For the efficiency calculation the level of correspondence between found and simulated tracks is estimated. A track is defined as correctly found, if more than 50 % of the reconstructed hits match to hits of a MC track. The track reconstruction efficiency is defined as  $\epsilon = N_{\text{rec}}/N_{\text{acc}}$ , where  $N_{\text{rec}}$  is the number of tracks correctly reconstructed in the TRD and  $N_{\text{acc}}$  is the number of reconstructable tracks lying in the TRD acceptance, i.e. having a minimal number of MC hits in the TRD. They should also be reconstructed in the MVD and the STS with at least four points in total, of which one has to be in the first MVD layer. In addition, they must fulfil the requirement to point to the primary vertex with a  $\chi^2/ndf < 3$ .

Figure 9.10 shows the track reconstruction efficiencies for the TRD as a function of their momentum and polar angle at the first TRD layer  $\theta^{\text{TRDin}}$  in Au + Au collisions at 8 AGeV beam energy. It is defined for tracks inside the TRD acceptance (producing at least three MC

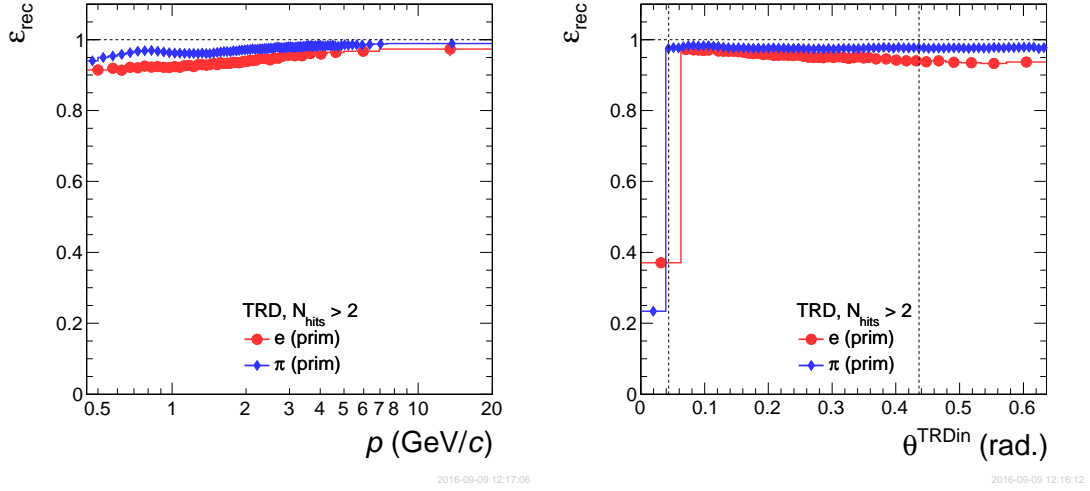


Figure 9.10: Reconstruction efficiency for primary  $e^\pm$  (red) and pion (blue) tracks measured with at least three points in the TRD as a function of their momentum (left) and polar angle at the first TRD layer (right) in Au + Au collisions at 8 AGeV. The vertical dashed lines indicate the nominal CBM acceptance ( $2.5^\circ - 25^\circ$ ).

hits) and a minimal number of reconstructed TRD points of three. The efficiencies are well above 90% at all momenta and  $\theta^{\text{TRDin}}$ . A slight increase towards higher momenta and smaller angles is visible. These dependencies are more pronounced for the electrons than for pions. This difference is caused by the fact that electrons, in addition to multiple scattering, suffer from bremsstrahlung in the detector material in front of the TRD. This effect significantly alters their trajectories and cannot directly be incorporated in the treatment of the track errors within the Kalman filter approach, due to its highly non-Gaussian energy loss distribution as described by the Bethe-Heitler formula. However, overall the differences between the electron and pion efficiency are not very large (maximally 5%).

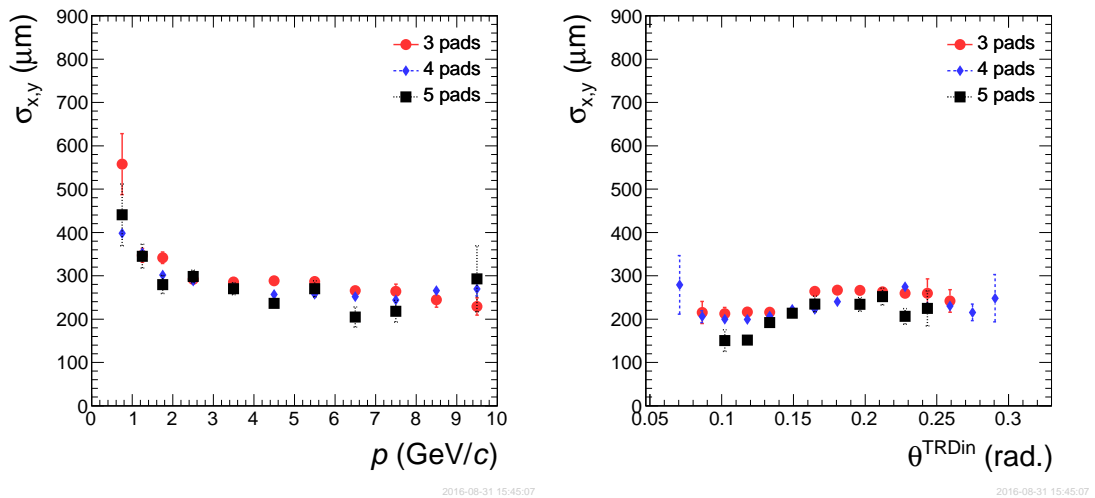


Figure 9.11: Point resolution for different cluster sizes (3 – 5 pads) as a function of momentum and polar angle at the first TRD layer of the tracks reconstructed in the innermost, small TRD modules in central Au + Au collisions at 8 AGeV.

The spatial resolution of reconstructed points is displayed in Fig. 9.11. It is obtained by comparing the reconstructed cluster (3 – 5 pad cluster) position along a pad row to the one of the corresponding MC point. For the innermost modules (small module types 1, 2 and 3) a very good position resolution below 300  $\mu\text{m}$  for  $p > 2 \text{ GeV}/c$  is found, irrespective of the incidence angle of the track on the first TRD layer and of the cluster size. For the larger outer modules (module types 6, 7 and 8) the position resolution is found to be slightly worse and is  $\sim 400 \mu\text{m}$ .

In the current CBM global track reconstruction scheme the TRD points are not included in the momentum fits. Therefore, the momentum resolution is entirely determined by the STS alone and the TRD has no impact here.

### 9.3.3.2 Matching efficiency between TRD and TOF

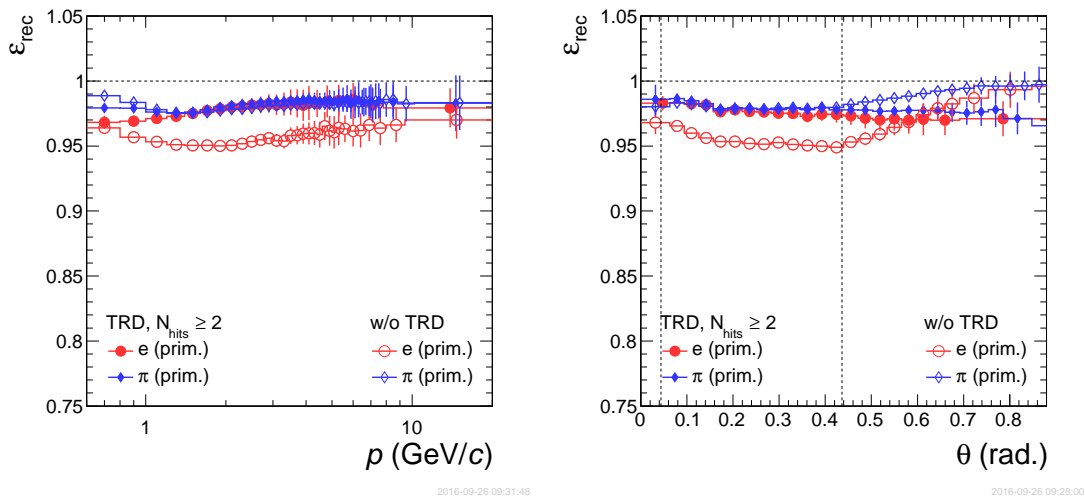


Figure 9.12: The efficiency to match tracks reconstructed in STS and TRD with at least three reconstructed TRD points to hits found in TOF for primary  $e^\pm$  (red) and  $\pi^\pm$  (blue) as a function of momentum (left) and polar angle (right) in Au + Au collisions at 8 AGeV beam energy (filled symbols). The vertical dashed lines indicate the nominal CBM acceptance ( $2.5^\circ - 25^\circ$ ). Also shown is the matching efficiency between STS and TOF alone, without a TRD in between (open symbols).

An important question that needs to be addressed is whether the additional material introduced by the TRD will affect the matching efficiency between the tracks reconstructed by STS and TRD and the corresponding points found in the TOF detector. The additional multiple scattering caused by the TRD material should ideally at least be compensated by the additional point measurements with the TRD.

The results of a dedicated study are displayed in Fig. 9.12. A high matching efficiency for pion tracks (filled blue diamonds) of  $\epsilon_{\text{rec}} > 97\%$  is obtained with a TRD geometry including the complete material budget. This efficiency exhibits no strong dependence on momentum or polar angle. For electrons (filled red circles) it is found to be slightly less at low momenta and larger polar angles, but also never drops below 97%.

To investigate whether the material introduced by the TRD outweighs the improvement of the pointing accuracy due to the TRD points, an additional calculation was performed where the TRD geometry was completely removed from the simulation. The results, which now correspond to the efficiencies to match tracks reconstructed by STS alone to TOF points over the empty space between the detectors, are shown as the open symbols in Fig. 9.12. For low momenta ( $p \lesssim 1 \text{ GeV}/c$ ), the TRD in fact causes a slight deterioration for pions. However, for higher

momenta no effect is seen for pions while the electron matching efficiency is significantly improved by the presence of the TRD at all momenta. This can be explained by the effect of Bremsstrahlung on the electron trajectories in the STS and RICH material, which can to some extent be corrected by adding the intermediate point measurements of the TRD.

### 9.3.3.3 Electron identification efficiency

The electron identification efficiency is defined as the number of electrons which were correctly identified in the detectors STS(+RICH)(+TRD), divided by the number of electrons being properly reconstructed in the corresponding detectors. In this analysis the tracks are required to have the following minimal number of reconstructed points:  $N_{\text{hits}}^{\text{STS}} \geq 6$ ,  $N_{\text{hits}}^{\text{RICH}} \geq 6$  and  $N_{\text{hits}}^{\text{TRD}} \geq 3$ .

The pion suppression factor is defined as the number of pions which were reconstructed in the STS and TRD, divided by the number of pions identified as electrons in the corresponding PID detectors. The electron identification in the TRD applies a momentum dependent selection on the output of the ANN in order to achieve a momentum independent electron efficiency. The left panel of Fig. 9.13 shows as an example the case for 80 % electron efficiency. In the case of the RICH detector, however, a momentum independent cut on the ANN-output is applied with the consequence that the electron efficiency of the RICH varies with particle momentum (see left panel of Fig. 9.13).

The pion suppression factor as a function of momentum together with the corresponding electron efficiency is summarized in Fig. 9.13 and in Tab. 9.1 for Au + Au collisions at 8 AGeV beam energy. The TRD alone, in its standard four layer configuration will provide in the high momentum region ( $p > 8 \text{ GeV}/c$ ) a pion suppression factor of up to  $\sim 15$  ( $\sim 50$ ) at 90 % (80 %) electron efficiency. In this momentum region the addition of RICH and TOF information increases this value further to  $\sim 80$ , however at a reduced electron efficiency of 80 %, due to the combination of the inefficiencies of the contributing detectors.

In addition to the standard TRD configuration with four layers, also a setup consisting of five identical detector layer was investigated. Since this layout will provide an additional measurement of energy loss and TR production to a given track, it will naturally improve the electron identification capabilities of the TRD. The resulting numbers on the pion suppression for the five layer setup are also included in Tab. 9.13. They are higher by more than a factor of two in comparison to the four layer configuration, however, at the expense of a 25 % increase of the overall detector cost.

Detector combination	Momentum region	Electron efficiency	Pion suppression factor
TRD	2 – 8 GeV/ $c$	80 %	30
	> 8 GeV/ $c$	80 %	50
	2 – 8 GeV/ $c$	90 %	10
	> 8 GeV/ $c$	90 %	15
RICH+TRD+TOF	2 – 8 GeV/ $c$	60 %	$8 \times 10^3$
	> 8 GeV/ $c$	55 %	80
	2 – 8 GeV/ $c$	70 %	$5 \times 10^3$
	> 8 GeV/ $c$	65 %	20
TRD(5L)	2 – 8 GeV/ $c$	80 %	70
	> 8 GeV/ $c$	80 %	130
RICH+TRD(5L)+TOF	2 – 8 GeV/ $c$	60 %	$8 \times 10^3$
	> 8 GeV/ $c$	55 %	230

Table 9.1: The pion suppression factors for different electron identification efficiencies in different momentum intervals and for different detector combinations. Also included are the values for a TRD setup with an additional fifth layer (5L).

### 9.3.4 Reconstruction efficiency of the TRD in the muon setup

As described in Sect. 4.4.2, the TRD is also foreseen as part of the CBM muon setup together with the MUCH detectors (see Fig. 4.7). In the SIS100-C configuration, muons will be reconstructed by the STS in combination with MUCH, consisting of one carbon (60 cm thickness) and three iron absorbers (20 cm, 20 cm and 30 cm thickness), instrumented with three GEM stations, followed by the four layer TRD station as final tracking station. Additional muon identification will be provided by the TOF detector. Figure 9.14 illustrates that the TRD is indeed very well suited as tracking device in the muon spectrometer. Shown is a comparison of the signal-to-background ratios obtained for reconstructed muon pairs from  $\omega$  mesons embedded into UrQMD events in the low mass region with two different setups: one (blue line) includes additional GEM detectors as final tracking device behind the last absorber layer of the MUCH, while the other (red line) employs the four layer TRD station for this purpose as described above. A significantly higher signal-to-background ratio with the setup including the TRD is visible in this comparison ( $S/B \approx 0.5$  relative to  $S/B \approx 0.3$  in the  $\omega$  mass region). In this analysis at least seven STS hits, 11 MUCH hits, resp. 8 MUCH and two TRD hits are required. For the particle identification in TOF a cut at  $m^2 < 0.1 \text{ (GeV}/c^2)^2$  is imposed.

Figure 9.15 illustrates that the four layer TRD station matches the acceptance of the MUCH quite well. The acceptance, shown here as blue diamonds, is defined by muon tracks reconstructed in more than seven layers of the MUCH tracking detectors which generate at least one MC point in one of the TRD layers. While tracks below  $p \approx 3.2 \text{ GeV}/c$  are stopped in the last absorber, those above this momentum are in principle all findable with the TRD. For these tracks also the efficiency has been determined (red dots in Fig. 9.15) by requiring that at least two matching hits have to be reconstructed in the TRD. It is found to be  $\sim 95\%$  and independent of the muon track momentum.

## 9.4 Calibration and alignment

An important prerequisite for a good reconstruction performance is the availability of accurate calibration and alignment procedures. With respect to the envisaged PID capabilities of the TRD, especially the gain stability is of crucial importance. Therefore, we address in this section in

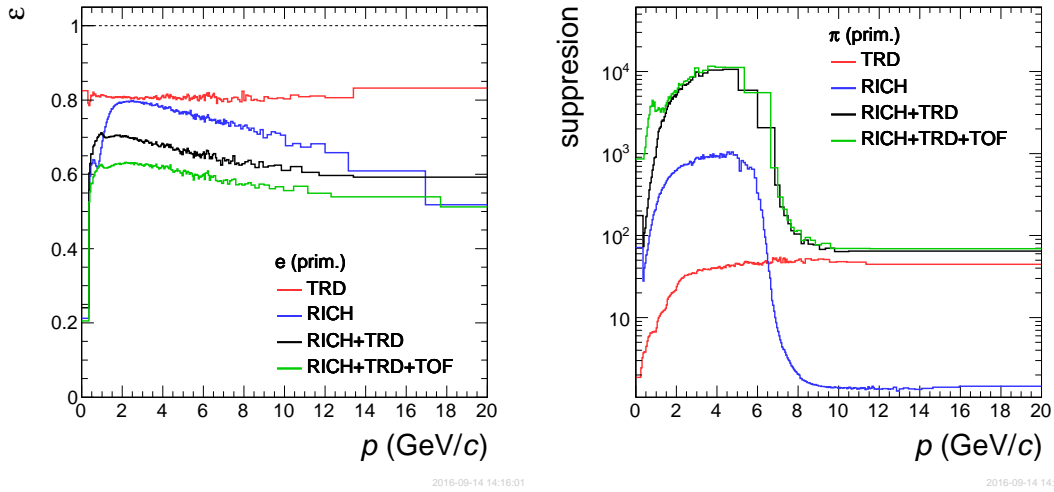


Figure 9.13: The electron identification efficiency (left panel) and the pion suppression factor (right panel) as a function of momentum. Both are calculated for the 10 % most central Au + Au collisions at 8 AGeV beam energy. Different colors represent the performance for different detector combinations included in the electron identification procedure: TRD (red), RICH (blue), RICH+TRD (black) and RICH+TRD+TOF (green).

particular the possible strategies for gain calibration, which will be the main challenge depending on the chosen readout chamber type. In the high rate environment of CBM a proper alignment of the different TRD chambers is also essential to ensure a high matching efficiency between STS, TRD, and TOF. For both, calibration and alignment, one can build on the large amount of experience gathered in the recent years with the ALICE-TRD.

#### 9.4.1 Gain calibration procedures

The gain of the TRD readout chambers will be influenced by several factors. Parameters such as temperature and pressure of the gas mixtures will have a direct effect on the overall gain, but can in principle be controlled to a certain extent by the gas system. Still, residual time dependent changes will remain, which need to be corrected within the reconstruction procedure. On top of this, every chamber will have a local variations of the gain that need to be known in order to achieve a uniform performance. Time dependent pressure differences between the inside and the outside of the chambers will modify these gain uniformities, since they can deform the entrance window that also serves as a cathode plane. E.g. for the ALICE-TRD variations over one year of  $\pm 7\%$  were observed [A<sup>+</sup>16]. Therefore, a careful gain calibration strategy is mandatory and we foresee the following procedures:

##### 9.4.1.1 Krypton calibration

The local gain variations of the chambers can be mapped during a dedicated run where  $^{83}\text{Kr}$  is added to the gas mixture. This procedure is well established and has been employed several times to calibrate TPCs [LW98, A<sup>+</sup>99], as well as the ALICE-TRD [AH10, Sti11]. The procedure requires the introduction of solid  $^{83}\text{Rb}$  into the gas system, which decays by electron capture into gaseous Kr. Hereby also the isomer state  $^{83m}\text{Kr}$  is populated, which has an excitation energy of 41.6 keV, a half-life of 1.8 hours and decays into the ground state by the emission of electrons. By reconstructing the energy deposited by them inside the gas of the chambers a local gain calibration can be achieved. Previous experiences with the ALICE-TRD show that several days

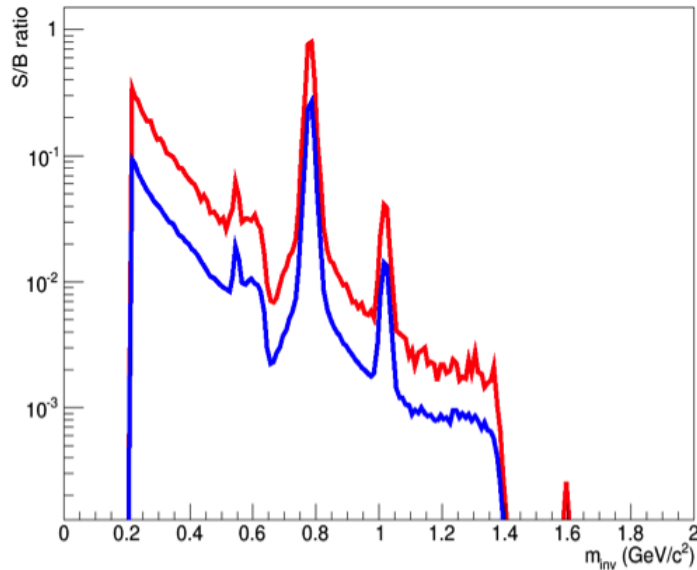


Figure 9.14: The signal-to-background ratios as a function of the dimuon invariant mass for two different muon arm layouts in Au + Au collisions at 8 AGeV. The blue line shows a configuration with GEM detectors as the last MUCH tracking station, while the red line depicts a setup where this task is taken over by a four layer TRD station.

of measurement with a  $^{83}\text{Rb}$  source of 5 MBq intensity are sufficient to register in the order of thousand counts per pad. This allows to establish two-dimensional gain factor maps with high enough accuracy ( $\sim 1\%$ ), which can then serve as a starting point for a time-dependent gain calibration procedure. The Kr-calibration procedure would at least be required after each new module installation or rearrangement.

#### 9.4.1.2 Online gain monitoring

A first correction of time dependent gain variations should be possible based on the online measurement of the pressure differences between inside and outside of the readout chamber. This measurement can be used to calculate variations of the gain factor by combining its known effect on the deformation of the entrance window and the induced change of the electric field (both taken from simulation, see e.g. Sect. 12.5.3). This online gain correction can serve as a starting point for a first reconstruction pass.

#### 9.4.1.3 Calibration with data

A further refinement of the gain calibration can be achieved by a calibration using collision data. By analyzing the pulse height spectra collected within a given time interval, a time dependent calibration can be performed. As a minimal option, this will allow to calculate one pad averaged gain factor per readout chamber which can be used to correct the two-dimensional gain factor maps obtained by the Kr-calibration by a time dependent correction factor. For the ALICE-TRD a precision of 1.4% was achieved with this kind of procedure [A<sup>+</sup>16]. However, the high interaction rates measured with CBM might allow to accumulate much higher statistics than available to ALICE within the relevant time intervals (typically in the range of 1 – 6 hours). Therefore a time dependent calibration of more local regions of a given ROC (groups of pads or even single pads) could be possible.

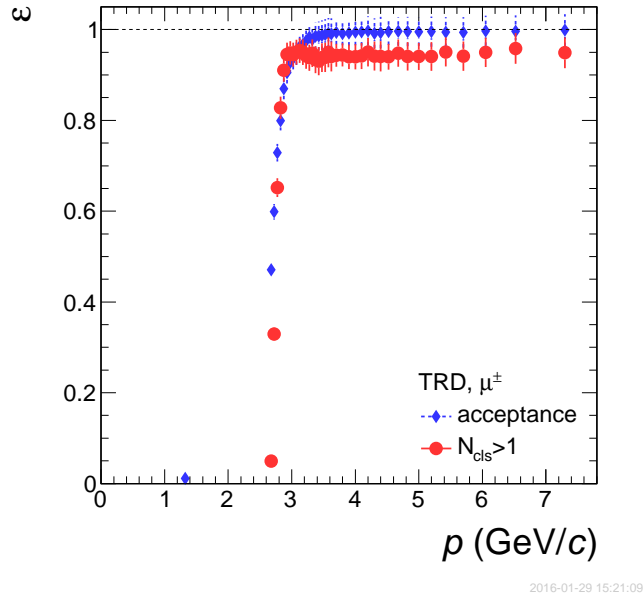


Figure 9.15: Acceptance (blue diamonds) and matching efficiency (red dots) of the TRD as part of the MUCH setup SIS100-C as a function of muon momentum for minimum bias Au + Au collisions at 8 AGeV. The efficiency is determined for tracks inside the acceptance having at least two reconstructed hits in the TRD.

In addition to the gain calibration, it will be possible to monitor time depending variations of the status and noise level of a given readout channel.

#### 9.4.2 Alignment procedure

The alignment of the TRD chamber relative to each other and relative the STS can be performed using either tracks from cosmic rays or from collisions in the target. The procedure is in principle based on a minimization of space point residuals with respect to reconstructed tracks, as can be implemented within. e.g., the MILLPEDE package [BK02]. Since the tracks passing through the TRD layers are straight, due to the absence of any magnetic field in this region, this minimization procedure should pose no principal problems. Generally, the alignment should be updated before each data taking period, especially if the detector setup has been modified.

Using cosmic ray tracks has the advantage, that an alignment can be performed before the actual data taking. This is important for the online data reconstruction, whose performance will otherwise be limited. A possible disadvantage of this approach is that it might be difficult to obtain sufficient statistics for cosmic ray tracks that pass horizontally through all detector layers. In any case, this requires a dedicated trigger setup (using e.g. the TOF detector). With the ALICE-TRD a typical precision of the relative chamber alignment with cosmic ray tracks of 0.13 mm was achieved, requiring a statistics in the order of  $10^3$  tracks per chamber [A<sup>+</sup>16].

A higher accuracy of the alignment will be achievable with real collision data, since a much higher statistics of usable tracks will be available. However, this procedure will only be possible during, or even after the data taking. An online implementation of the procedure might allow to determine the alignment parameter iteratively before any online reconstruction and might also be used to monitor time dependent variations of the relative chamber alignment.

## Chapter 10

# Mass Production

As described in Chap. 4 the CBM-TRD for SIS100 will consist in total of 200 individual detectors (not including spares), which need to be constructed, tested, and finally installed in the experimental setup of CBM. These tasks can naturally not be handled by a single institution. Therefore, it is currently foreseen to involve several major construction sites in the assembly of the individual detectors or major parts of it. In order to keep the production fast and cost efficient, it is planned to use industrial pre-produced components as often as possible. The production of the individual ROCs can be subdivided into three major component groups: Entrance window, wires and FR4 ledges and backpanel. This modularity opens up the possibility to assembly subcomponents at individual institutes. Alternatively, the production can be subdivided according to ROC module types (see e.g. Fig. 5.21). Further work packages are the production of the radiators, as well as the electronics integration and test.

### 10.1 Production equipment

For the production and test of the ROCs the following basic equipment is required:

- **Clean room:** The mounting and adjusting of the wires should be performed in a room which provides a sufficiently dust free environment.
- **Granite or glass table:** Tables with sufficient planarity (precision below 50  $\mu\text{m}$ ) are required for the ROC frame assembly.
- **Winding machine:** Special machines for the production of wire planes with controlled wire tension are needed. The wires are wound onto aluminum frames of sufficient rigidity, which then can be transferred to the ROC frames to allow glueing of the wires onto the frames.
- **Optical alignment and tension measurement devices:** In order to properly align the wires with a precision better than 10  $\mu\text{m}$  a setup with a microscopic device is required. After glueing, the tension of the wires needs to be measured by an additional setup.
- **Plexiglas frame:** These frames are needed to stretch the Kapton foils for the ROC entrance windows. The frames are heated, e.g. by an oven of sufficient size providing temperatures up to 60 °C, and therefore expand, thus providing the necessary tension to the foils.
- **Test stand:** For a first performance test of the completed ROCs they are scanned with an  $^{55}\text{Fe}$ -source in a special test stand. This requires the availability of a simplified gas system and a data acquisition in order to operate the chambers in the laboratory under realistic conditions.

- **Storage space:** Appropriate space for storage of raw materials and finished detector modules should be available at the construction sites.

### 10.1.1 Existing laboratory infrastructure

The following calculation is based on the existing CBM TRD collaboration. However the production can be redistributed between additional institution which may join the collaboration in the future. Up to now, it is foreseen to distribute the ROC production between the laboratories in Bucharest, Frankfurt and Münster. All sites were already involved in the construction and integration of chambers of the ALICE-TRD. Therefore, they have not only collected a considerable experience in the mass production of MWPCs, but also have already installed fully equipped detector laboratories for this purpose.

#### 10.1.1.1 Bucharest laboratory

The laboratory for gas detectors at the Hadron Physics Department "Horia Hulubei" National Institute of Physics and Nuclear Engineering, Bucharest (HPD/IFIN-HH) has originally been set up for the construction of ROCs for the ALICE-TRD and provides all the necessary equipment. Its infrastructure consists of five clean rooms ( $2 \times \text{ISO6}$ ,  $1 \times \text{ISO7}$  and  $2 \times \text{ISO8}$ ), one wire winding machine, two vacuum tables, one glass table, and the necessary devices for mounting and adjusting the wires and for measuring their tension. For testing the completed chambers a special chamber test stand available in a separate room.

#### 10.1.1.2 Frankfurt laboratory

The laboratory for gas detectors at the Institut für Kernphysik, Frankfurt (IKF) has originally been set up for the construction of readout chambers for the ALICE-TRD and provides all the necessary equipment. Its infrastructure consists of a clean room equipped with a wire winding machine, a portal crane for the transport of the wire frames, and the necessary devices for mounting and adjusting the wires and for measuring their tension. In a second room a granite table (dimensions:  $180 \text{ cm} \times 120 \text{ cm} \times 25 \text{ cm}$ ) with a mechanical precision below  $12 \mu\text{m}$  underneath an airflow box is available for the final assembly of a given chamber. For testing the completed chambers a special test stand has been set up in a separate room, which allows to scan the chambers in two dimensions with a radioactive or a X-ray source. In addition, other rooms are available for preparing the chamber frames and backpanels and for performing tests of the mounted frontend electronics. All the described equipment is free to be used for the chamber production for the CBM-TRD.

#### 10.1.1.3 Münster laboratory

The laboratory for gas detectors at the Institut für Kernphysik, Münster (IKP) has originally been set up for the integration of readout chambers for the ALICE-TRD into so-called super-modules and provides all the necessary equipment for final integration and hardware tests. Its infrastructure consists of a test gas system, a portal crane for the transport of larger chamber structures, and a water cooling system. In a second room a granite table with a mechanical precision below  $12 \mu\text{m}$  underneath an airflow box is available for the final assembly of a given chamber. It is planned to move a wire winding machine from Heidelberg ALICE-TRD equipment to Münster for the time of the detector production for CBM. A cleanroom, which was used for the production of wire frames for the KATRIN experiment, will then be available for the final chamber assembly. In addition, other rooms are available for preparing the chamber frames and backpanels and for performing tests of the mounted frontend electronics. All the described

equipment is free to be used for the chamber production for the CBM-TRD. Cooperations with local industries have been established and developed further during the prototype production.

## 10.2 Production timeline

### 10.2.1 Human resources

The available human resource in the three participating institutions is listed in Tab. 10.1. The total working hours per week of 760 h has to be divided corresponding to the construction tasks described below and the project plan given in Sect. 11.3.

Table 10.1: Working Hour Per Day (WHPD) and Working Hour Per Week (WHPW) based on the available human resource of the participating institutes. We distinguish engineers (Eng.), permanent staff physicists (Phys.), technicians (Techn.), Postdocs (P.docs), PhD students, master students (MSc), bachelor students (BSc), part time employed scientists (WHK) and part time employed students (SHK).

Institute	Eng.	Phys.	Techn.	P.docs	PhD	MSc	BSc	WHK	SHK
Bucharest	5.00	6.00	5.00	0.00	1.00	1.00	0.00	0.00	0.00
Frankfurt	0.00	0.00	1.00	1.00	2.00	1.00	2.00	0.00	3.00
Münster	0.00	0.00	1.50	1.00	2.00	0.00	2.00	0.00	0.00
WHPD	8.50	8.50	8.50	8.50	8.50	8.50	8.50	4.00	2.00
scale factor	0.75	0.75	0.75	0.50	0.33	0.33	0.00	1.00	1.00
WHPW	159.38	191.25	239.06	42.50	70.13	28.05	0.00	0.00	30.00
CBM-TRD WHPW									<b>760.36</b>

### 10.2.2 Time consumption

We have relatively good estimates on the time consumption for the production of ROCs based on experiences with the ALICE-TRD ROC mass production and CBM-TRD prototype construction. From this we estimate the total production time for one ROC including wire position and tension tests, as well as final HV stability and gas tightness tests done by two persons to be 77 hours and 170 hours for hardening of the glue. This breaks down into three main building blocks: entrance window, backpanel, wire plane and ledges. Since the most time consuming part of the ROC production is the hardening of the glue (12 h) and the wire winding (4 h) and each wire winding process results in two identical wire planes it is more efficient to build two ROCs in parallel. For the following estimations we will use abbreviation for Glueing Hours (GH) and Working Hours (WH). With an adequate work planning it is possible to move most of the GH towards night which makes production more efficient.

#### 10.2.2.1 Entrance window

The production of one entrance window composed of a 25  $\mu\text{m}$  single sided aluminized Kapton foil, outer FR4 frame and CFRP lattice takes for two persons three days or 17 WH and 36 GH. The parallel production can only be realized if critical infrastructure like the oven for thermal stretching of the foil and the Plexiglas stretching frame is also available two times.

**10.2.2.2 Backpanel**

The production of one backpanel composed of aluminum frame, honeycomb and pad plane takes for two persons five days or 35 WH and 48 GH. A vacuum table with a sufficient surface is necessary for the parallel production of two backpanels.

**10.2.2.3 Wiring and glueing to ledges**

The final completion of the ROC, joining of the two pre-produced building blocks, wiring and glueing of the wired distance ledges takes for two persons seven days or 25 WH and 86 GH.

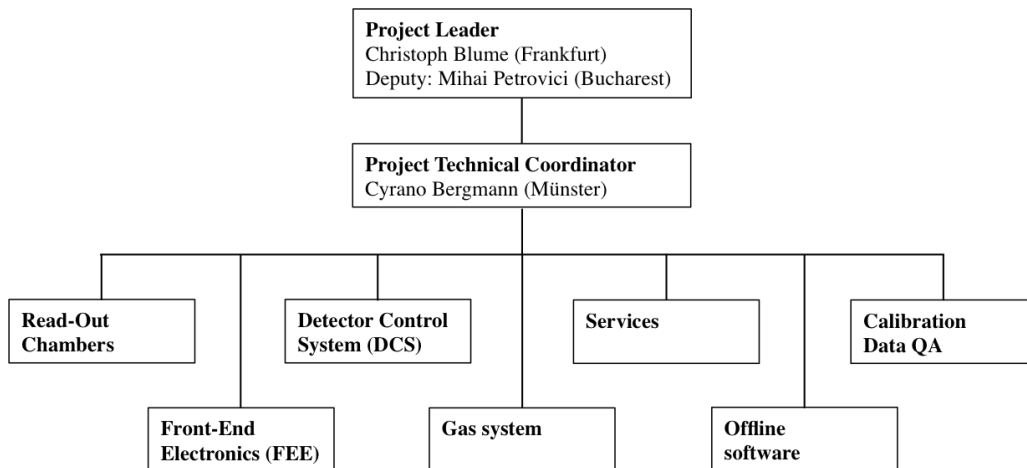
**10.2.2.4 Total production time**

This results in a total time consumption for two ROCs built by two persons of 77 WH and 170 GH or three weeks (154 WHPW in all three institutes together). Including the assumption of 250 working days per year we come up with an estimated production time for three participating production sides producing two ROCs in parallel of two years. The detailed project time plan can be found in Sect. 11.3.

## Chapter 11

# Project Organization

The CBM-TRD project is organized as follows: in addition to a project leader (Christoph Blume), a deputy project leader (Mihai Petrovici) and a project technical coordinator (Cyrano Bergmann, before David Emschermann), seven sub-projects have been defined:



These sub-projects encompass the following activities and responsibilities, which should be organized by one dedicated coordinating person:

- **Read-out chamber:** Installation, commissioning, and operation of the readout chambers, including the radiators.
- **Front-End Electronics (FEE):** Integration, commissioning, and operation of the TRD FFE and the following readout chain. Implementation and maintenance of feature extraction and other online signal processing algorithms.
- **Detector Control System (DCS):** Integration of the TRD in the CBM-DCS.
- **Gas system:** Development, installation, and operation of the TRD gas system.
- **Services:** Installation and maintenance of the LV, HV, and cooling system.
- **Offline software:** Implementation and maintenance of the TRD offline software. This includes the detector specific simulation software, as well as the TRD related reconstruction algorithms (tracking, PID).

- **Calibration:** Implementation and operation of the TRD calibration algorithms (e.g. gain calibration). Also, included are procedures to perform a quality assessment of the raw and reconstructed data.

## 11.1 Responsibilities

### 11.1.1 Participating institutes

The following institutions are participating in the construction of the CBM-TRD:

- Bucharest, Romania, National Institute of Physics and Nuclear Engineering (IFIN-HH).
- Frankfurt am Main, Germany, Institut für Kernphysik (IKF), Goethe-Universität.
- Frankfurt am Main, Germany, Institut für Informatik, Infrastruktur und Rechnersysteme in der Informationsverarbeitung (IRI), Goethe-Universität.
- Heidelberg, Germany, Institut für technische Informatik (ZITI), Ruprecht-Karls-Universität.
- Münster, Germany, Institut für Kernphysik (IKP), Westfälische Wilhelms-Universität.

### 11.1.2 Sharing of tasks

The following table summarizes how the responsibilities for the construction of the TRD will be shared. It reflects the current assignments for the TRD part of the CBM hardware components list, which is being prepared as a basis for a future memorandum of understanding.

Item	Institutions
ROCs	Bucharest (IFIN-HH) Frankfurt (IKF) Münster (IKP)
Radiators	Münster (IKP)
ASIC	Heidelberg (ZITI)
FEBs	Frankfurt (IKF)
ROBs	Münster (IKP)
Gas system	Münster (IKP)
Cooling	Münster (IKP)
LV system	Frankfurt (IKF)
HV system	Münster (IKP)
On-detector & environment monitoring	Frankfurt (IKF)
CRI layer (firmware design)	Frankfurt (IRI)
Offline software	Frankfurt (IKF)

### 11.1.3 TRD task force

The following persons have contributed to the work presented in this Technical Design Report:

A. Andronic, W. Amend, H. Appelshäuser, V. Aprodu, A. Arend, T. Armbruster, A. Bercuci, T. Ballé, D. Bartoş, C. Baumann, E. Bechtel, I. Berceanu, R. Berendes, C. Bergmann, T. Bel, C. Blume, J. Book, G. Caragheorgheopol, V. Cătănescu, J. de Cuveland, F. Constantin, P. Dillenseger, D. Emschermann, P. Fischer, T. Galatyuk, S. Gläsel, M. Hartig, N. Heine, E. Hellbär, C. Höhne, D. Hutter, C. de Jesus Garcia Chavez, P. Kähler, U. Keschull, M. Kohn, M. Krieger,



For the readout electronics the cost per readout channel is estimated to be:

Item	Cost/channel (Euro)	Cost (Euro)
ASICs	3.59	130,384.00
FEBs	0.33	93,880.00
GBTx	0.79	227,440.00
DPB	0.19	156,116.00
Optical fibers	0.36	104,000.00
Total	5.09	711,820.00

### 11.2.2 Total TRD setup

Based on cost estimate for a single ROC and the readout electronics presented above, the total cost for the CBM-TRD is estimated. This does currently not include the costs for the external support structures, which are at the moment difficult to assess. For the SIS100 configuration (four layers) we thus arrive at the following list:

SIS100 version	
Item	Cost (kEuro)
ROC (200 chambers)	731.0
FEE (287,744 channels)	711.8
Xe/CO <sub>2</sub> (1.4 m <sup>3</sup> )	11.0
HV (400 channels)	145.4
LV PS FEB & ROB	359.5
HV cables	3.5
LV cable & bus bars	150.0
DC-DC converter	67.8
Gas system	23.0
Total	2,112.2

Thus, the total cost estimation of the full CBM-TRD setup in the four layer configuration, without support structure, external services and spare ROCs, amounts to 2,112.2 kEuro.

### 11.3 Schedule

The overall work program and schedule is shown in Fig. 11.1. It is based on the current FAIR planning (2016) and assumes that the CBM cave will be available for detector installation in Dec. 2021 and envisages that the TRD will latest be ready for installation middle of 2023. The schedule is planned to ensure that the TRD detector is fully commissioned and operating by this time. It is also adjusted to the envisaged funding profile for the project and embedded in the official FAIR planning scheme. Here it is assumed that Romanian in-kind contact will be finalized Nov. 2017 and the corresponding funding will be available in Mar. 2018, while the German BMBF-funding can be expected for the coming funding period starting in Oct. 2018.

#### 11.3.0.1 Milestones

Currently, we foresee the following basic milestones for the production and commissioning of the CBM-TRD:

Milestone	Date
Start of production	31.12.2017
End of small modules production	31.12.2020
End of large modules production	31.12.2021
End of SPADIC production	28.12.2018
End of FEB production	27.03.2020
End of detector pre-assembly	31.03.2023
End of detector commissioning	30.06.2023
Ready for installation	30.06.2023

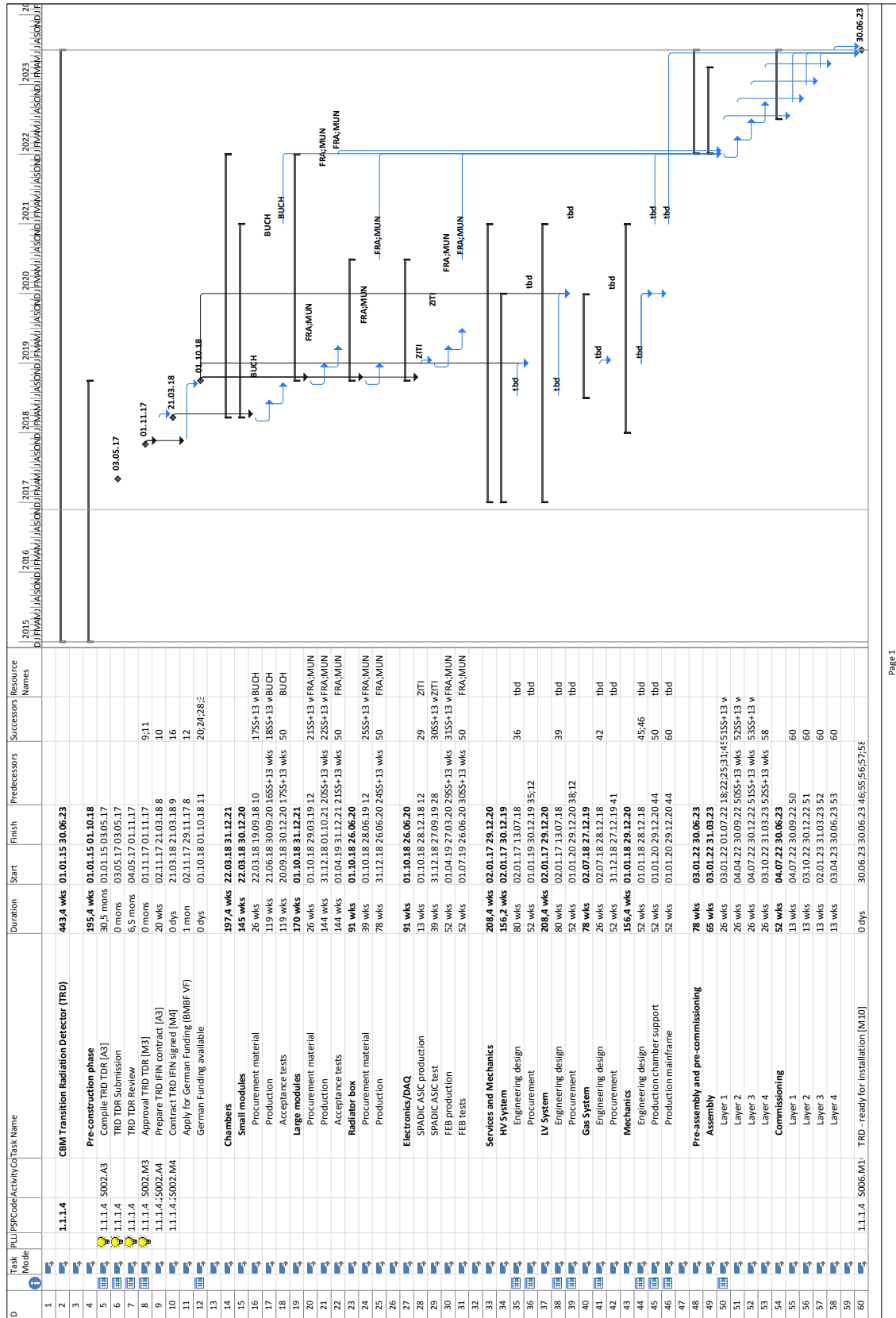


Figure 11.1: Project plan outlining the production schedule and the corresponding milestones.

## Chapter 12

# Alternative Design Options

### 12.1 Overview on alternative TRD design options

In addition to the standard baseline configuration of the CBM-TRD, as outlined in the Chaps. 4 and 7, other options for the ROCs architecture and the readout electronics have been investigated during the R&D period.

#### **Read-out chamber design for optimum performance PID**

In order to develop a TRD which fulfills the requirements of a fixed target and high interaction rate heavy-ion experiment as CBM, many different designs [P<sup>+</sup>07a], some of them with original architecture [P<sup>+</sup>07b, P<sup>+</sup>13a] have been investigated. The prototype called Double-Sided Transition Radiation Detector (DSTRD), with a symmetric structure relativ to the central readout electrode, almost transparent to TR-photons, common to two multi wire proportional chambers with only amplification zones [P<sup>+</sup>07b] turn out to be the most performant in terms of electron-pion discrimination for a given electron efficiency. However, due to the readout of the signals on the lateral sides of the detector, the estimated geometrical efficiency of a large area detector is  $\sim 76\%$  for a single layer. In addition, a rather significant material budget is introduced by the frames of individual chambers. In order to overcome this drawback, a compromise solution was a TRD chamber based on a single MWPC coupled with a small drift region.

The architecture based on a multiwire proportional chamber coupled with a drift region, read out by a pad-plane with triangular shaped pads turned out to be performant in both two-dimensional position resolution as well in the electron-pion discrimination requirements, in high counting rate and multi-hit environment for large area detector systems.

Based on the results obtained in a series of tests, this architecture could be foreseen for the inner zones of the CBM-TRD at small polar angles.

#### **TRD pad plane design for optimum position information**

The standard pad plane layout for the baseline ROC design with rectangular pads, as described in Chap. 4, provides high position resolution only in pad row direction, since the pad width is generally smaller than its height. Instead, it is conceivable to use a pad plane with triangular pads, which can be paired in two different ways (straight and inclined) such that also a significantly higher position resolution along the pad column direction can be achieved. This might be advantageous in the inner part of the detector which is exposed to high hit counting rates and has therefore been explored with prototypes developed in Bucharest.

**Fast Analog Signal Processor (FASP)**

The experimental results using mixed electron and pion beams at SIS18 and front-end electronics delivering semi-Gaussian signals [S<sup>+</sup>05] have demonstrated that the position information and electron-pion discrimination in high counting rate environment is less deteriorated using pulse height information than integrated values. Based on this an alternative readout electronics, the FASP (Fast Signal Processor) ASIC has been developed in Bucharest. It provides signal amplification, shaping and pulse height information with a very high signal to noise ratio.

**Fast ROC design**

The high rate capabilities of the default ROC design are limited due to the short drift region of the MWPCs. Therefore it was investigated whether it is possible to omit the drift region and use chambers that contain only an amplification region and thus inherently provide much shorter signal collection times. A potential disadvantage is the higher sensitivity of the chamber gain to external pressure variations. However, it turns out that this can be significantly reduced by a different layout of the wire planes (alternating high voltages) as proposed in [VHK11]. Another advantage of this ROC design is a potentially higher stability in a high rate environment, since the absence of a drift region implies less accumulated charge due to slow moving ions.

## 12.2 Readout chamber design for optimum performance PID and tracking

### 12.2.1 Single MWPC prototype

The first solution for a fast TRD detector which conserves the response function in high counting rates was a simple Multiwire Proportional Chamber (MWPC) [P<sup>+</sup>07a]. It was designed and built with a symmetric  $2 \times 3$  mm amplification region and 2.5 mm anode wire pitch, in order to reach the required speed of the readout of the signals and to reduce the possible space charge effects.

A very good energy resolution of 8.6 % using an <sup>55</sup>Fe source was obtained in the laboratory tests. In-beam tests were performed at the SIS18 accelerator of GSI, Darmstadt. The obtained pion efficiency for a six layer configuration and a Rohacell HF71 radiator was 12.5 % and of 2.9 % for ten TRD layers at 90 % electron efficiency. These results were obtained using Xe/CO<sub>2</sub>(85/15) gas mixture for 1 GeV/*c* particle momentum. Obviously, such efficiency could be reached with less layers (lower material budget, lower cost) using a much performant radiator in terms of TR yield, but the main reason for the large number of layers needed with such an architecture is the low conversion efficiency of TR in the thin gas layer.

The effect of the high counting rate was estimated in terms of pulse height and integrated charge. The relative degradation of the pulse height (3.2 %) was smaller than that of the integrated charge (5.0 %) at the highest rate reached in these tests of  $10^5$  particles/(cm<sup>2</sup>·s) for an exposure of the chamber. The signals were processed using the preamplifier/shaper PASA [CC<sup>+</sup>01] based on discrete components, developed during the R&D phase of the ALICE-TRD. The experimental results using mixed electron and pion beams at SIS18-GSI and front-end electronics delivering semi-Gaussian signals showed that the position information and electron-pion discrimination in a high counting rate environment is robustly recovered using the induced signal via pulse height information rather than several time samples of it. The better behavior of pulse height information led to the development of a new front-end electronics called Fast Analog Signal Processor (FASP) for signal processing in high counting rate environment, described in Sect. 12.4. It provides signal amplification, shaping and pulse height information with a very high signal to noise ratio.

### 12.2.2 Double-sided MWPC prototype

In order to maintain the counting rate performance and increase the conversion efficiency of the TR in a single TRD layer, we designed and built an original TRD architecture for electron/pion discrimination in high counting rate environment [P<sup>+</sup>07b]. It is based on two multiwire proportional chambers with a common double-sided pad structure readout electrode, almost transparent to the TRs. The configuration of this prototype is symmetric relative to the central readout electrode with identical pad structure on both sides. The corresponding pads on the upper and lower surface are electrically connected together. In this configuration a TR photon produced in a radiator by an incident high momentum electron can be absorbed either in the first MWPC or in the second MWPC after crossing the readout electrode with low TR absorption. Therefore, the conversion probability significantly increases relative to the single sided configuration.

First Double-Sided TRD prototype (DSTRD-V0) had 3 mm anode-cathode distance, resulting in  $2 \times 6$  mm gas thickness for TRs. Double-sided copper pad readout structure was obtained etching the evaporated copper layer on a 25 μm kapton foil. Two anode wire planes with 2.5 mm wire pitch were disposed symmetrically relative to the central readout electrode. The size of the rectangular shaped pads was of 0.5 cm x 1 cm each. The chamber was closed on both sides by an aluminized kapton foil.

Before the in-beam tests, laboratory  $^{55}\text{Fe}$  source tests showed a chamber energy resolution of 8.5% using the anode signal. The in-beam tests were performed at SIS18 accelerator of GSI Darmstadt. The signals were processed using an updated version of the PASA ASIC [S<sup>+</sup>05]. For a regularly spaced foil radiator (120 foils, 20  $\mu\text{m}$  thickness and 500  $\mu\text{m}$  gap) the extrapolated pion efficiency was of 1% for a six TRD layer configuration. The pulse height as a function of counting rate did not show a significant deterioration up to a counting rate of  $200 \times 10^3$  particles/( $\text{cm}^2 \cdot \text{s}$ ) exposing the detector directly in the beam.

The active area of this prototype, i.e.  $4.5 \times 2.0 \text{ cm}^2$ , is too small for a large array based on such chambers. Therefore, a larger size prototype with the same inner architecture was developed. The larger active area was achieved by increasing the sizes of the rectangular pads of the central double sided readout electrode. Obviously, this conflicts with the requirements of a high granularity and appropriate position resolution. Therefore, the rectangular pads of the readout electrode were split along the diagonal, each triangle being readout separately. This choice of a triangular pad geometry allows for position determination in both coordinates: across and along the pads, respectively, as is shown in Sect. 12.3 with a single TRD layer.

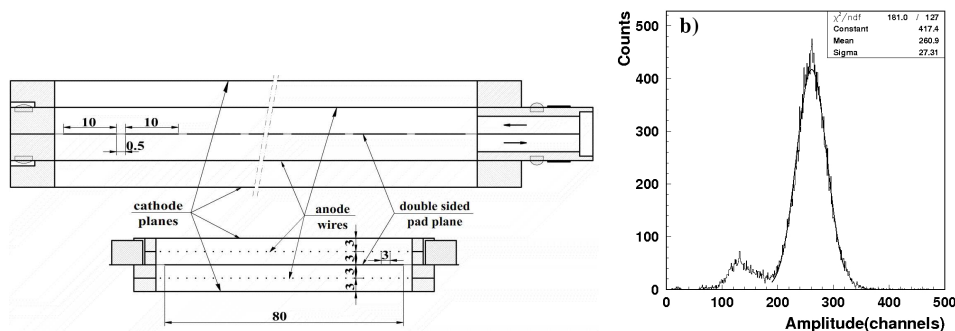


Figure 12.1: Schematic view of the detector structure (left). The pulse height spectrum of a  $^{55}\text{Fe}$  source at 1750 V and Ar/CO<sub>2</sub>(70/30) gas mixture using FASP-V01 (right).

The inner geometry of the detector can be seen in Fig. 12.1 [P<sup>+</sup>11, P<sup>+</sup>13b]. The prototype architecture is similar to the one described in the previous paragraph. The readout electrode is made from a 25  $\mu\text{m}$  thick kapton foil covered on both sides with evaporated Al/Cr (200 nm/20 nm) layers. It is almost "transparent" to the transition radiation (it has a negligible absorption of about 1% for 5.9 keV X-ray of  $^{55}\text{Fe}$  source). It has a row of 72 triangular pads along the anode wires. The corresponding pads on the opposite sides of the pad plane are electrically connected and use a single readout channel. Each pad has a width of 10 mm and a height of 80 mm with a readout cell area of  $4 \text{ cm}^2$ . Two versions of the prototype, with the same active area of  $8 \times 36 \text{ cm}^2$ , defined by 72 triangular pads were used in these tests. The first version of the prototype (DSTRD-V1) was built with a  $4 \times 3 \text{ mm}$  gain region. In order to improve the charge sharing between adjacent pads for better position reconstruction, the second version (DSTRD-V2) was built with a  $4 \times 4 \text{ mm}$  gain region. In both cases the anode pitch wire was 3 mm. The functionality of the prototype was tested in the laboratory using the  $^{55}\text{Fe}$  source. For pad signal processing the new dedicated FEE called FASP-V01 [C<sup>+</sup>10, C<sup>+</sup>11] (see Sect. 12.4), with 40 ns shaping time and peak-sensing ("flat top") output has been used for the first time. The flat top output was directly digitized by an ORTEC ADC811 converter. Typical amplitude (energy) spectra obtained in  $^{55}\text{Fe}$  source tests for DSTRD-V1 (presented in Fig. 12.1-right) showed 10% energy resolution.

The detectors were tested with a mixed electron/pion beam of 1 – 5 GeV/c momenta at the T10 beam line of the CERN-PS accelerator. The signals were processed by the FASP-V01 ASIC and digitized by Mesytec MADC converters. The electrons and pions were selected using the

information from a Cherenkov detector installed in the front of the tested detector prototypes and a Pb-glass calorimeter positioned at the end of the beam line. Two regular foil radiators were used in the measurements. The first one, called Reg1 (20/500/120) is a multilayer foil structure of 120 foils of 20  $\mu\text{m}$  thickness and 500  $\mu\text{m}$  air gap. The second one called Reg2 (20/250/220) is a stack of 220 foils of 20  $\mu\text{m}$  thickness and 250  $\mu\text{m}$  air spacing. DSTRD-V1 was operated at 1700 V anode voltage with Reg2 while DSTRD-V2 was operated at 2000 V with Reg1 radiator. The detectors were flushed with Xe/CO<sub>2</sub>(80/20) gas mixture at atmospheric pressure at a flow of 3l/h. The measured pulse height distributions for electrons and pions at 2 GeV/c with DSTRD-V2+Reg1 are shown in Fig. 12.2-left.

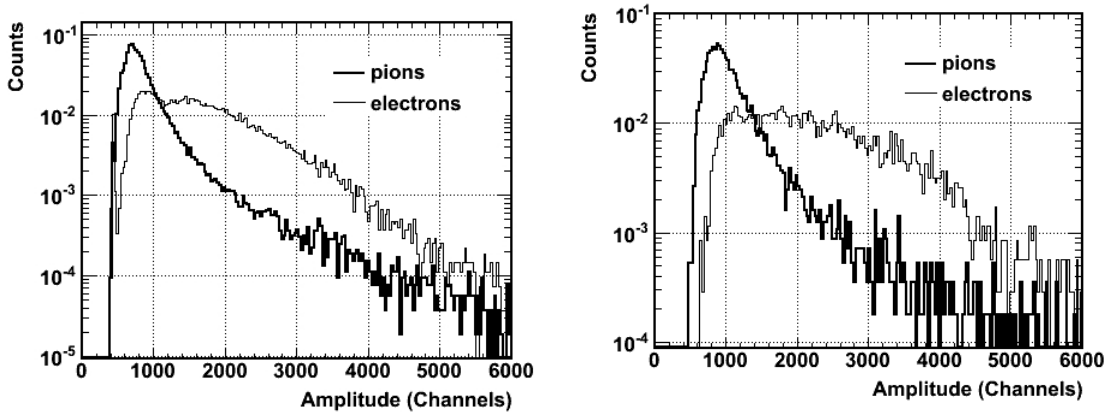


Figure 12.2: Energy loss spectra for 2 GeV/c electrons (thin line) and pions (thick line) measured with DSTRD-V1+Reg2 (left) and DSTRD-V2+Reg1 (right).

Although it has a very good  $e/\pi$  discrimination performance (see Sect. 12.2.5) [P<sup>+</sup>11, P<sup>+</sup>13b], the size of the DSTRD is limited by the topology of the signal extraction in the same plane as the readout electrode. Therefore, the geometrical efficiency of a single layer large area detector based on such architecture is in the region of of  $\sim 76\%$ . In addition a rather significant material budget is introduced by the frames of individual chambers. For these reasons, this architecture is not recommended for large area multi-layer TRDs.

### 12.2.3 Single-sided MWPC prototype with drift section

In order to overcome this problem we proposed a standard TRD architecture [P<sup>+</sup>13a] of  $2 \times 4$  mm amplification region coupled with a 4 mm drift zone (Single - Sided Transition Radiation Detector - SSTRD). It has a gas thickness identical to the  $4 \times 3$  mm double-sided TRD prototype. The size of the drift zone was a compromise between the drift time of the ionization clusters inside the active volume and a TR conversion efficiency as large as possible. Design details of this prototype (SSTRD-V0) are presented in Fig. 12.3-left.

The detector is closed on one side by the drift electrode, made from an aluminized kapton foil of 25  $\mu\text{m}$  thickness stretched on a 8 mm HF71 Rohacell plate. On the other side the gas volume is enclosed by the readout electrode made from a printed circuit board of 300  $\mu\text{m}$  thickness glued on a honeycomb layer which confers the mechanical stability and planarity. The cathode wire (75  $\mu\text{m}$  diameter, Cu-Be alloy) plane with a 1.5 mm pitch separates the amplification region from the drift zone. The anode wire (20  $\mu\text{m}$  diameter, Au-plated tungsten) plane with 3 mm pitch is positioned in the middle of the amplification region. The readout electrode has the same structure as used for the prototypes described in Sect. 12.2.2.

The detector performance was first tested in the laboratory using an <sup>55</sup>Fe source. An Ar/CO<sub>2</sub>(80/20) gas mixture was flushed through the counter at atmospheric pressure. The pad

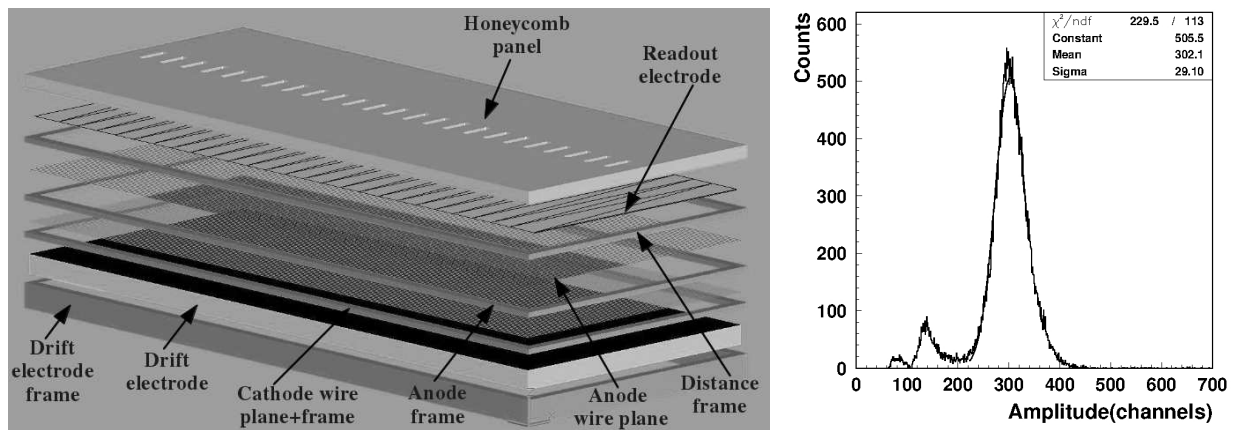


Figure 12.3: 3D view of the SSTRD-V0 prototype (left). The pulse height spectrum of a  $^{55}\text{Fe}$  source for Ar/CO<sub>2</sub>(70/30) gas mixture using FASP-V01 (right).

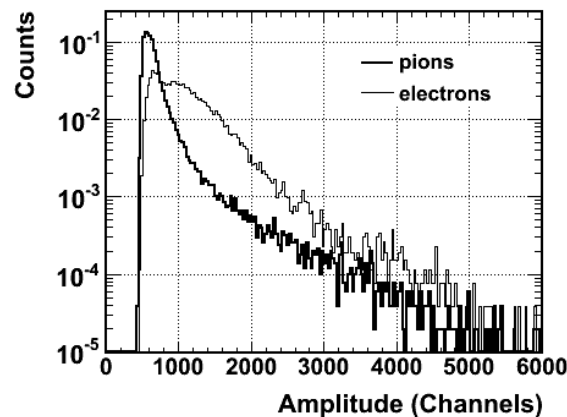


Figure 12.4: Energy loss spectra for 2 GeV/ $c$  electrons (thin line) and for pions (thick line) measured with SSTRD-V0.

signals were processed using the same FASP-V01 ASIC with a shaping time of 40 ns and flat-top output selection. The measured energy resolutions for the obtained spectrum (Fig. 12.3-right) was 10% for 5.9 keV X-rays.

In-beam tests with a mixed electron-pion beam of 1 – 5 GeV/ $c$  momentum were performed at the T10 beam line of the CERN-PS accelerator as part of the same experimental set-up in which DSTRDs prototypes were tested. The SSTRD, flushed with Xe/CO<sub>2</sub>(80/20) gas mixture at atmospheric pressure, was operated with 1900 V anode and 400 V drift voltages. The regular radiator Reg1, described in Sect. 12.2.2, was positioned in front of the drift electrode. The signals of triangular pads were processed by FASP based FEE, using the flat top outputs and the same shaping time of 40 ns as in the  $^{55}\text{Fe}$  source laboratory tests. The outputs were digitized by 32-channel peak-sensing Mesytec ADCs.

Using the information from the Cherenkov detector and the Pb-glass calorimeter, both part of the experimental setup, the pulse height distributions for electrons and pions of 2 GeV/ $c$  momentum were obtained, as shown in Fig. 12.4. The electron-pion discrimination performance of the prototype is presented in Sect. 12.2.5. The obtained position resolutions in both direction, which define the plane of the readout electrode, are presented in Sect. 12.3.1.2.

### 12.2.4 ROC simulations

The maximum drift time of the ionization clusters is an important parameter for the optimization of the counter geometry and also for defining the operational parameters of the FEE (i.e. shaping time). We define the maximum drift time as the longest time needed of an ionization cluster to travel from the furthest generation point relativ to the anode wire to the anode wire plane. A minimization of this parameter is required by the operation in a high counting rate environment.

We used the GARFIELD/MAGBOLTZ [Vee98] software package for calculating the maximum drift time of ionization clusters randomly generated inside the detector volume, for different applied anode voltages. Both DSTRD and SSTRD detector architectures were considered in the simulations for two gas mixtures of Ar/CO<sub>2</sub>(80/20) and Xe/CO<sub>2</sub>(80/20).

The obtained results for the chamber with 3 mm anode wire pitch and 4 × 4 mm detector gas thickness (DSTRD-V2) are presented in Fig. 12.5-left. For the chamber with the same anode pitch, but 2 × 4 mm amplification zone coupled with 4 mm drift zone (SSTRD-V0) the obtained results are shown in the right panel of Fig. 12.5 for three values of the drift voltage.

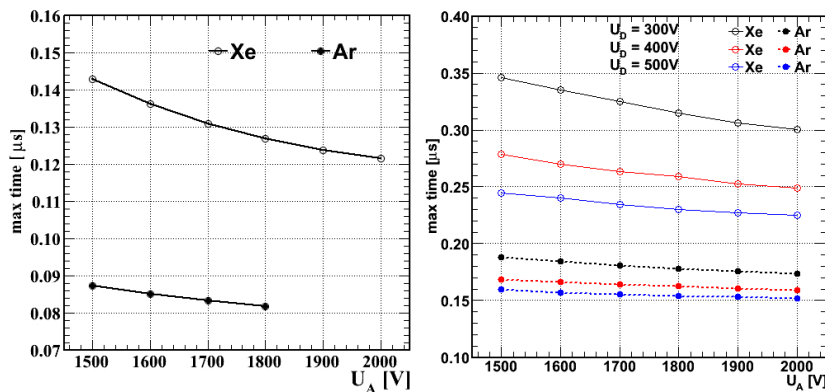


Figure 12.5: The dependence of the maximum drift time of ionization clusters drifting in the gas volume on the applied anode voltage for: DSTRD-V02 (left) and SSTRD-V0 (right) architectures.

In the Xe based gas mixture a maximum drift time around 120 ns for an anode voltage larger than 1900 V for DSTRD architecture with 4 × 4 mm amplification zone, was estimated. As expected, the electron drift time is much shorter in an Ar based gas mixture due to its larger drift velocity. For the SSTRD architecture, a maximum drift time of 230 ns was estimated for Xe based gas mixture and 500 V drift voltage. The larger drift time is explained by the presence of the drift region with a much lower field and larger drift path length to the anode wires.

### 12.2.5 PID performance comparison

A likelihood method [CMP74] was used in order to calculate the pion misidentification probability as a function of number of layers for 90 % electron efficiency for both detector architectures discussed in Sects. 12.2.2 and 12.2.3.

As could be seen in Fig. 12.6 a pion misidentification probability of  $(0.82 \pm 0.05) \%$  is obtained for a six layer configuration based on DSTRD-V1 using Reg2 radiator and 1700 V anode voltage. For a six layer configuration based on DSTRD-V2 and Reg1 foil radiator, the pion misidentification probability is improved by a factor of 1.6, i.e.  $(0.50 \pm 0.04) \%$  at 2000 V applied high voltage. The better pion suppression obtained with the second chamber is due to the thicker gas layer of DSTRD-V2 (4 × 4 mm) relative to DSTRD-V1 chamber (4 × 3 mm). A value of  $(1.18 \pm 0.07) \%$  for the misidentification probability was estimated for a six layer configuration based on SSTRD-V0 using Reg1 foil radiator, for 1900 V anode and 400 V drift voltages. The

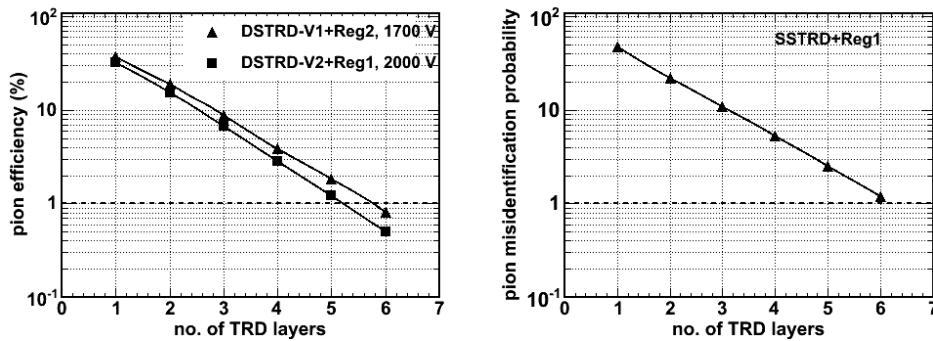


Figure 12.6: a) Pion misidentification probability as a function of the number of TRD layers for 90 % electron efficiency (the errors are at the level of the symbol size) for DSTRDs prototypes (left) and SSTRD-V0 prototype (right).

errors are at the level of the symbol size. This SSTRD chamber has the same gas thickness for TR absorption as the double-sided architecture with 3 mm anode-cathode distance for which a 0.8 % pion misidentification probability was reported. For the SSTRD prototype, however, the consecutive ionization clusters with a large drift time difference between them are not integrated by the FASP-V01 version (see Sect. 12.4).

### 12.2.6 Real size TRD prototype

The SSTRD architecture allows the construction of large area TRD systems with a better geometrical efficiency. In order to reach the granularity required by the innermost zone of the first TRD station, a new readout electrode with the area of a triangular pad of  $\sim 1 \text{ cm}^2$  (2.7 cm height times 0.7 cm width) was designed.

Two identical small chambers of  $23 \times 8.5 \text{ cm}^2$  active area with this readout pad plane geometry, called SSTRD-V1A and SSTRD-V1B were built and used in the in-beam tests. The results are presented in Sect. 12.3. A third readout chamber with the same inner geometry as SSTRD-V1 chambers, but of a size of  $60 \times 60 \text{ cm}^2$ , called SSTRD-V2, has the readout electrode made from 300  $\mu\text{m}$  thickness FR4. The sizes of this prototype are identical with the ones of the readout chambers which are foreseen to be implemented in the inner zones of the TRD stations.

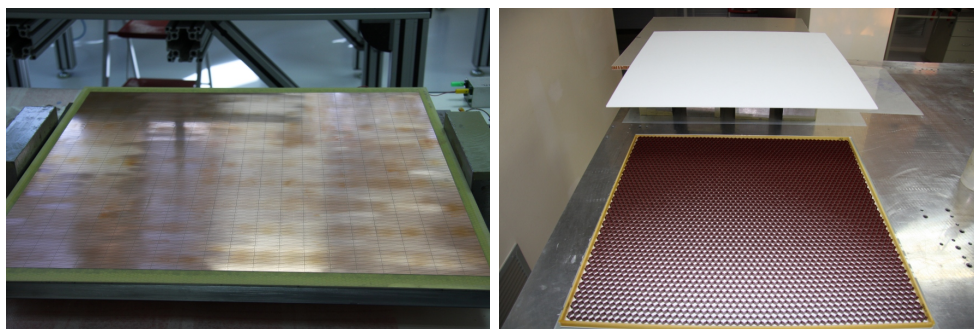


Figure 12.7: Photo of the readout pad plane (left). Details on the construction of the drift-electrode (right).

In order to have a drift electrode with a minimum absorption of transition radiation in front of the active gas volume but also with a good mechanical rigidity, the drift electrode was built as a sandwich structure with a honeycomb material of 9 mm thickness reinforced on each side by two Rohacell plates of 3 mm thickness.

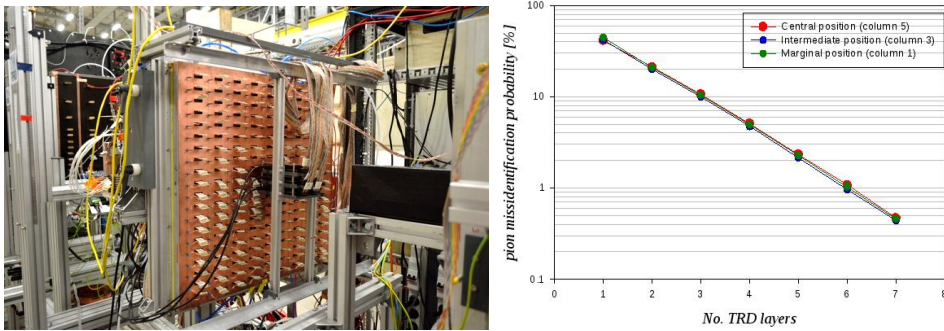


Figure 12.8: Real size TRD prototype within CERN-PS experimental setup (left). Pion misidentification probability as a function of the number of TRD layers for 90% electron efficiency for three different positions across the TRD surface (right).

The prototypes presented in Sects. 12.2.2 and 12.2.3 have the drift electrode made from a Rohacell plate with aluminized kapton foil stretched on both sides. The measured absorption of such a drift electrode for  $^{55}\text{Fe}$  X-rays was 62%. For the composite structure based on honeycomb sandwiched between the 3 mm Rohacell plates, the measured absorption for the same radioactive source was 57.5%.

In order to maintain the mechanical stability and decrease even further the TR absorption, a new structure for the drift electrode support was developed. It is based on a honeycomb layer sandwiched between two 100  $\mu\text{m}$  carbon foils. The measured absorption for  $^{55}\text{Fe}$  X-rays is of 52.4%. This configuration has also a very good mechanical stability against the deformation due to the slight overpressure of the circulated gas.

The in-beam test of this prototype was performed also at the CERN-PS. The detector coupled with the Reg2 foil radiator (see Fig. 12.8-left), was flushed with Xe/CO<sub>2</sub>(80/20) gas mixture and operated with 2000 V anode voltage and 800 V drift voltage. A newly designed FEB with two ASICs per board was used for signal processing. The pion efficiency obtained with the real size TRD prototype was of 1% for a 3 GeV/c momentum, independent on the position. This shows, besides the detector performance, the fact that the drift and/or readout electrodes are not deformed anymore due to the slight overpressure of the circulated gas mixture. The pion suppression performance could be further improved using FASP-V02 version with 100 ns shaping time (see Sect. 12.4) for signal processing.

### 12.3 TRD pad plane design for optimum position information

It is rather obvious that the position resolution based only on rectangular pads suffers due to poor resolution along the pads. A possible solution based on slightly tilted pads as used in the ALICE-TRD [C<sup>+</sup>01] only alleviates the problem by giving up on the good resolution across pads and adding further complications to the reconstruction. For a net improvement of position resolution using such pad geometries, a two layer set-up with layers rotated by 90° relative to each other seems to be the natural choice. However, doubling the amount of detector stations increases the material budget of the whole set-up and costs. A possible solution within the rectangular pad architecture would be to readout also the anode wires, but such design would be rather poor in disentangling multi-hit events in a relatively large ROC and would require a substantial increase of the number of electronic channels. Therefore, a new pad plane architecture was sought which can deliver two dimensional position information with good resolution keeping the benefits of inductive readout and optimizing the amount of measured data.

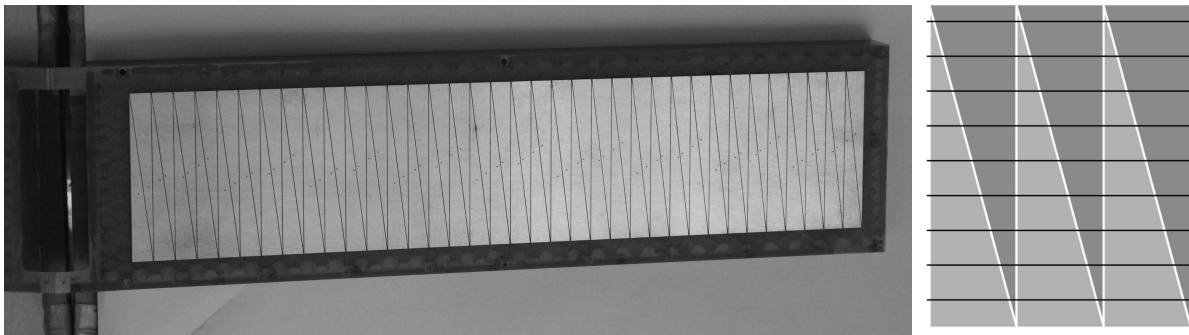


Figure 12.9: Photo of the readout electrode showing the triangular shaped pads (left) and a schematic view of the pad plane architecture emphasizing the triangular pad readout and the anode wire grid (right).

In introducing the new pad plane architecture we start from the observation that by contrast to the position measured across pads, which is continuous in character, the positions of ionizations along the pads are discreet, with a step equal to the anode pitch. This imposes a new limitation on the resolution along the pads, although to an acceptable value. To identify the anode(s) hit by a crossing particle one needs besides the independent position measured by the rectangular pad architecture also an observable sensitive to the position along pads. Such an aim can be accomplished by splitting the rectangular pads of the readout electrodes diagonally. The old pad plane architecture and position information, respectively, can be recovered by summing up the charge in two triangles, coupled to a rectangle, while the extra information can be obtained by coupling triangular pads from adjacent rectangles. For clearness we will denote the coupling of triangular pads to a rectangle as *column*.

Two triangular pad architectures of the readout electrode were used to read out the ROC. A large pad size of  $80 \times 10 \text{ mm}^2$  for the DSTRD-V1 and -V2 and SSTRD-V0, respectively. For the later ROCs, i.e. SSTRD-V1 and -V2, the pad size was reduced to  $7.5 \times 27.7 \text{ mm}^2$  and 0.2 mm spacing, all together yielding a pad area of  $1 \text{ cm}^2$  as suggested by detailed detector simulations (see Sect. 9). A schematic view of the pad plane and of the anode wires used to produce the signal (thick horizontal lines) is presented in Fig. 12.9-right. The induced signal can be read out from single pads, which can be coined as *triangular read-out*, but also, by coupling pads to rectangles, in a so-called *rectangular read-out* similar to the usual set-up.

### 12.3.1 Triangular pad readout

The first readout strategy implemented in FASP-01 (see Sect. 12.4) is to read out individual triangular pads. If the charge induced on the upper triangular pads is  $\{q_i^\nabla\}_{i=\overline{1,5}}$  (see Fig. 12.9-right - dark gray pads) and on the lower triangular pads  $\{q_i^\Delta\}_{i=\overline{1,5}}$  (see Fig. 12.9-right - gray pads), respectively, then the position across columns of width  $w$  is obtained by recovering the rectangular signals by:

$$Q_i = q_i^\nabla + q_i^\Delta, \text{ for } i = \overline{1,5} \quad (12.1)$$

and fitting them with a normal distribution. If no background from multi-hits is considered then, following a method described in [BR94], the standard deviation  $\sigma$ , obtained by a fit with a Gaussian to the column response function, is used to calculate the displacement  $d$  of a hit from the center of the column  $i$  with the maximum charge deposition  $Q_i$ :

$$d = \frac{1}{Q_{i-1}^2 + Q_{i+1}^2} (W_1 + W_2), \quad (12.2)$$

with

$$W_1 = Q_{i-1}^2 \left( \frac{\sigma^2}{w} \ln \left( \frac{Q_i}{Q_{i-1}} - \frac{w}{2} \right) \right) \quad (12.3)$$

$$W_2 = Q_{i+1}^2 \left( \frac{\sigma^2}{w} \ln \left( \frac{Q_{i+1}}{Q_i} + \frac{w}{2} \right) \right). \quad (12.4)$$

For a given track the reconstructed position across the columns,  $x_{\text{rec}}$ , is obtained as

$$x_{\text{rec}} = d + \left( i + \frac{1}{2} \right) w. \quad (12.5)$$

If a constant background is also considered the signals are fitted directly with the function from Eq. 12.6

$$\mathcal{G}(d, PRF | \{Q_i\}_{i=\overline{1,5}}) + P_0 \quad (12.6)$$

The Gaussian mean value  $d$  is selected as position observable and the reconstructed track position is given by Eq. 12.5; an estimator for Pad Response Function (PRF) is the sigma parameter of the Gaussian.

The position along the pads can be measured by constructing the observable:

$$qq = (Q^\nabla - Q^\Delta) / (Q^\nabla + Q^\Delta) \text{ with} \quad (12.7)$$

$$Q^k = \sum_{i=1}^5 q_i^k; \quad k = \nabla, \Delta \quad (12.8)$$

The correlation of  $x_{\text{rec}}$  (in units of  $w$ ) from Eq. 12.5 and  $qq$  can be seen in Fig. 12.10-left for an uniform illumination of the detector with X-rays from an  $^{55}\text{Fe}$  source. The sine pattern of the  $qq$  maxima as a function of  $x_{\text{rec}}$  can be used to identify individual anode wires;  $n = 8$  being the number of anode wires covered by a pad row. The observed maxima in the  $(x_{\text{rec}}, qq)$  correlation plot can be fitted with:

$$qq(x) = A + B \cdot \sin(C \cdot (x + D)) \quad (12.9)$$

with  $A$ ,  $B$ ,  $C$  and  $D$  as parameters. Out of these, the  $A$  and  $D$  parameters are identifying the class as they describe the mean  $qq$  value ( $A$ ) and the phase shift ( $D$ ). The parameters  $B$  and  $C$  are related to the geometry of the pad plane and have typical values  $B \approx 0.1$  and  $C \approx 2\pi$ . We identify the reconstructed pairs  $(x_{\text{rec}}, qq)$ , which are found around such maxima as coming from the hits amplified around a specific anode wire and thus measuring the position along the pads with the resolution of the anode wire pitch. The method for anode wire identification just described is coined Anode Wire Response Function (AWRF).

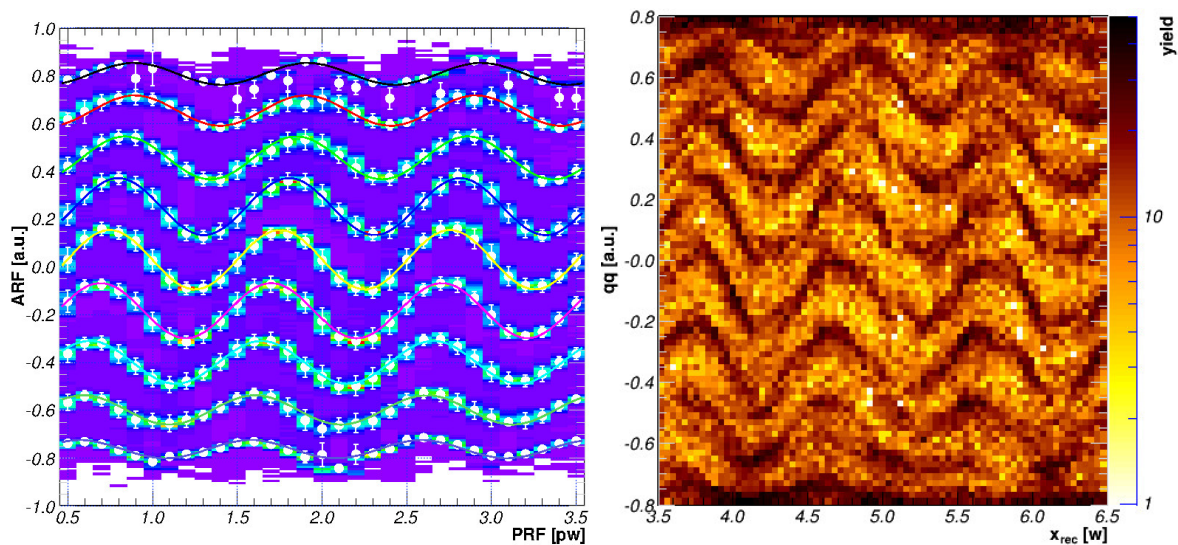


Figure 12.10: The correlation of the  $x_{\text{rec}}$  (horizontal axis) and  $qq$  (vertical axis) position observables from Eq. 12.7 as measured with the SSTRD-V1/FASP-01 for a uniform illumination with  $^{55}\text{Fe}$  (left) and in a high counting rate environment at the CERN-SPS (right).

### 12.3.1.1 Laboratory tests using $^{55}\text{Fe}$ X-rays

The SSTRD-V1 prototype was operated in the laboratory using an Ar/CO<sub>2</sub>(80/20) gas mixture at atmospheric pressure and 1900 V anode and 500 V drift voltages, respectively. The detector was mounted on a  $(x, y)$  scanning device, having attached a  $^{55}\text{Fe}$  source of 1.1 GBq. The experimental setup allows uniform illumination measurements by placing the uncollimated  $^{55}\text{Fe}$  source at a large ( $\approx 40$  cm) distance from the detector or localized illumination by placing the source close ( $\approx 1$  cm) to the TRD. Additionally, position scans along and across pads were performed using the source close to the detector. The detector was operated on an area of 5 pad columns  $\times$  3 pad rows and was self triggered by the OR signal obtained based on channel wise trigger signals delivered by FASP-01. The outputs were digitized by 32-channel peak-sensing Mesytec ADCs controlled by an GSI-MBS DAQ. In order to measure also the semi-Gaussian signals (see Sect. 12.4.1) all channels were delayed by 100 ns to match the readout gate. The uniform illumination run was used to calibrate the position of anode wires as identified with the AWRP method (see Fig. 12.10-left).

### 12.3.1.2 Low-rate tests at the CERN-PS

In-beam tests with a mixed electron-pion beam of 1 – 5 GeV/ $c$  momentum were performed at the T10 beam line at the CERN-PS accelerator. Three prototypes were part of the experimental setup, two versions of a double-sided TRD prototype [P<sup>+</sup>13b] (here denoted as DSTRD-V1 and DSTRD-V2, see Sect. 12.2.2) and the single-sided prototype SSTRD-V0, see Sect. 12.2.3. They were flushed with an Xe/CO<sub>2</sub>(80/20) gas mixture at atmospheric pressure. Their operation parameters and the details about the experimental set-up are given in Sects. 12.2.2 and 12.2.3. The analysis performed to reconstruct the position is described in [P<sup>+</sup>11, P<sup>+</sup>13b].

The distribution of the residuals between the reconstructed positions across the pads in the SSTRD-V0 prototype and in the DSTRD-V2 prototype is shown in Fig. 12.11.a. From this distribution a position resolution *across the pads* of  $327 \pm 4 \mu\text{m}$  was obtained, assuming equal contributions of both chamber types. Using a different set-up in which DSTRD-V1 ROC was rotated by  $90^\circ$  relative to the SSTRD-V0 prototype, the resolution *along the pads* can be obtained. Using DSTRD-V1 as reference a position resolution *along the pads* of  $6.29 \pm 0.09$  mm

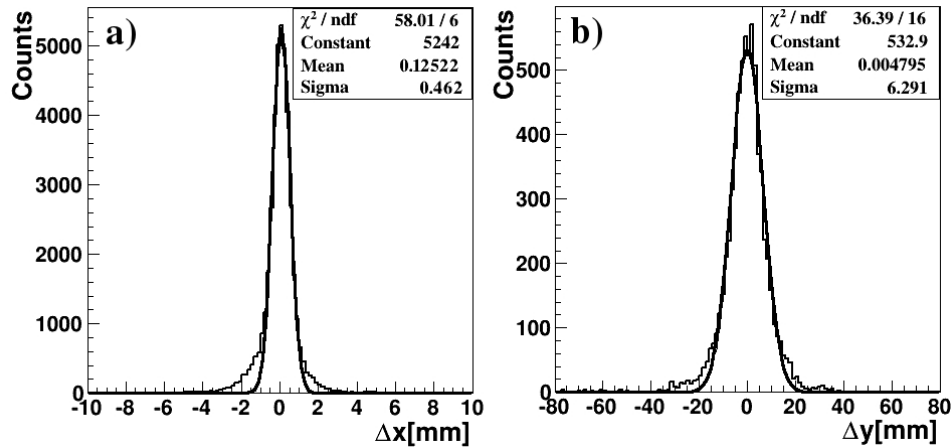


Figure 12.11: The distribution of the residuals between the reconstructed positions in SSTRD-V0 and in DSTRD-V2: a) across the pads; b) along the pads.

[P<sup>+</sup>13a] was thus determined as shown in Fig. 12.11.b.

#### i. Validation of Anode Wire Response Function method

For the most forward polar angles covered by the CBM-TRD, where the counting rates could reach values up to 100 kHz/cm<sup>2</sup> and the charged particle multiplicity is high, new TRD prototypes with the same ROC geometry as SSTRD-V0, but with the increased granularity of the readout pads ( $7.5 \times 27.7 \text{ mm}^2 = 1 \text{ cm}^2$  (see Sect. 12.2.6) - as suggested by the results in Chap. 9), were tested.

In a second campaign of tests at the CERN-PS the TRD prototype using the finer granularity pad plane architecture were tested with collimated mono-energetic mixed beams of electrons and pions. Here the SSTRD-V1 and -V2 ROC were used, operated with a Xe/CO<sub>2</sub>(80/20) gas mixture. The experimental setup was arranged to provide position scanning along the pads for the TRD prototype. A reference SSTRD-V1 operated in the rectangular read-out was mounted in front of the tested SSTRD-V2 rotated by 90°. Each of the two detectors were operated on three rows and eight columns yielding 24 channels for SSTRD-V1 and two times more for SSTRD-V2. The acquisition was triggered by plastic scintillators and RPC detectors positioned along the beam line.

The observable  $x$  reconstructed by SSTRD-V1 can be correlated with the identified anode wire of the SSTRD-V2. Assuming parallel straight tracks crossing both detectors, the correlation between the anode index (in the increasing order of  $qq$  values) measured with SSTRD-V2 on the horizontal axis and the reconstructed position  $x$  from SSTRD-V1 on the vertical axis are correlated as shown in Fig. 12.12. The color code in the picture represents the yield distribution of tracks crossing both detectors. For each anode index a normal fit is performed and the correlation of all maxima is deduced by a linear fit. From the slope of the fit (see box) of  $p_1 = 0.298 \pm 0.005 \text{ cm}$  we can deduce the distance between each anode wire of SSTRD-V2 as measured by the reference detector SSTRD-V1, which is identical within the error bars with the anode wire pitch of 0.3 cm (see Sect. 12.2).

#### ii. Position resolution along pads

The resolution along the pads is based on the deconvolution of the position spectrum measured with SSTRD-V1 for events conditioned by an anode wire identification in SSTRD-V2. A quality cut on the  $qq$  observable was also imposed with respect to the distribution shown in Fig. 12.10. If the one-dimensionally conditioned spectrum measured by SSTRD-V1 is fitted with the convolution of a Gauss distribution, modeling the cumulated resolution of the TRD across pads and the beam spread on the vertical axis, and a box accounting for the anode wire projected width  $r$ , the latter

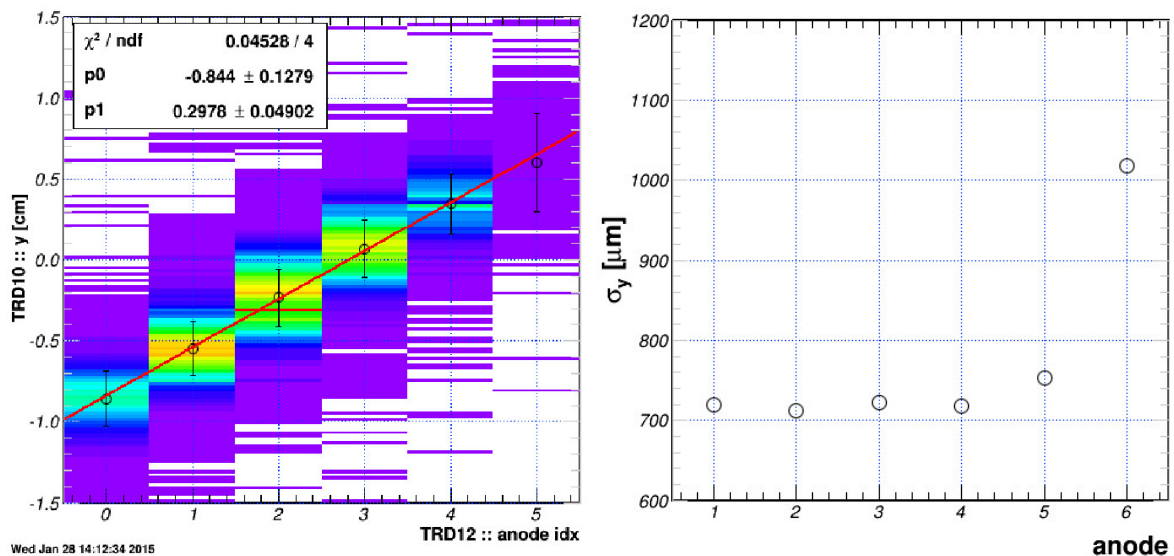


Figure 12.12: The measurement of the anode wire pitch using a reference TRD (SSTRD-V1) with MIPs (left); the slope ( $p1$ ) of the fit gives the distance between anodes in cm. The position resolution along the pads as function of anode wire index (right).

parameter can be estimated from the expression  $\sigma_y = r/\sqrt{12}$ . The results for conditioning on all identifiable anode wires of SSTRD-V2 is presented in Fig. 12.12-right. A rather constant behavior is obtained for the central wires (index 1 – 5) with values close to 720  $\mu\text{m}$ . The geometrical limit on the resolution can be determined from the anode pitch and has a value of 866  $\mu\text{m}$ , which is close to the measured value for the difference being generated by the extra conditioning in  $qq$ . For wires close to row boundaries (index 6 in Fig. 12.12-right) the results deteriorates as the image of the avalanche is shared between pad rows. For such cases a different approach should be applied, which is for the moment outside the scope of the present report.

### 12.3.1.3 Tests in realistic CBM conditions at CERN-SPS

The final tests for the TRD prototypes were performed in conditions close to those which are foreseen for the CBM experiment at SIS100, i.e. high counting rates and hit multiplicities in the detectors and a large range of particle species of various momenta. Extreme illumination conditions triggered by pile-up effects in the detector can lead to (local) signal saturation. Such effects cannot be inferred in an assumption free fashion from low rate data and therefore experimental data are needed. The CERN-SPS facility can provide such conditions. Two interaction systems of 13 AGeV Ar and 30 AGeV Pb beams on Pb targets were used to bridge the gap from the low multiplicity conditions obtained at CERN-PS. In both cases the detector setup consisted of two SSTRD-V1 used as reference detectors and one SSTRD-V2 as detector under test. In all cases the acquisition trigger was provided from outside (e.g. diamond detector, RPC, and plastic scintillator) and the triangular readout was used. ROCs were always operated with an Ar/CO<sub>2</sub>(80/20) gas mixture.

The detector setup used for the intermediate conditions (13 AGeV Ar beams) was operated with one pad row equipped with FASP-01 on each detector. The SSTRD-V2, the most upstream in beam, was operated on 42 columns (84 readout channels), while the reference prototypes on 12 columns (24 readout channels) each. All three detectors were mounted parallel to each other and aligned relative to the operated rows and the whole setup was aligned orthogonally to the target position at a polar angle of 15°.

The experimental setup was used to investigate the position resolution in both coordinates

under extreme conditions. To render the data as clean as possible from external assumptions only the linear track model is considered as the linear correlation of the hits reconstructed in the three stations which include also the misalignments between detectors. In order to assure proper track identification only events with one cluster per detector were selected. Additionally, a cut on the energy per cluster was imposed to clean the data sample from e.g. secondary  $\delta$ -electrons. To calculate resolutions the linear correlation of the position residuals between (SSTRD-V2, SSTRD-V1A) and (SSTRD-V2, SSTRD-V1B) was investigated [B<sup>+</sup>16a]. Solving the distribution for its eigenvectors is equivalent to finding two uncorrelated observables, one proportional to the mean resolution of the TRDs and the other to the illumination profile of the detectors. In order to account for pad-to-pad variations, misalignments of the detector and dependence of the resolution on the track inclination the distribution was differentiated with respect to the SSTRD-V2 column. Such a method provides robust results relevant for systematic effects in the ROC-RO-DAQ chain.

If  $x_2$ ,  $x_0$  and  $x_1$  are the reconstructed position across pads in the SSTRD-V2, SSTRD-V1A and SSTRD-V1B, respectively, and if the correlation  $A = x_2 - x_0$  with  $B = x_2 - x_1$  is observed then the quantity:

$$V = e_0 * A + e_1 * B \quad (12.10)$$

with  $e_0$  and  $e_1$  as eigenvalues, is proportional to the TRDs resolution. Assuming that all three detectors have equal resolution one obtains:

$$\sigma_x = \sigma_V / \sqrt{(e_0 + e_1)^2 + e_0^2 + e_1^2} \quad (12.11)$$

with  $\sigma_V$  being accessible experimentally via a Gauss fit of the  $V$  distribution.

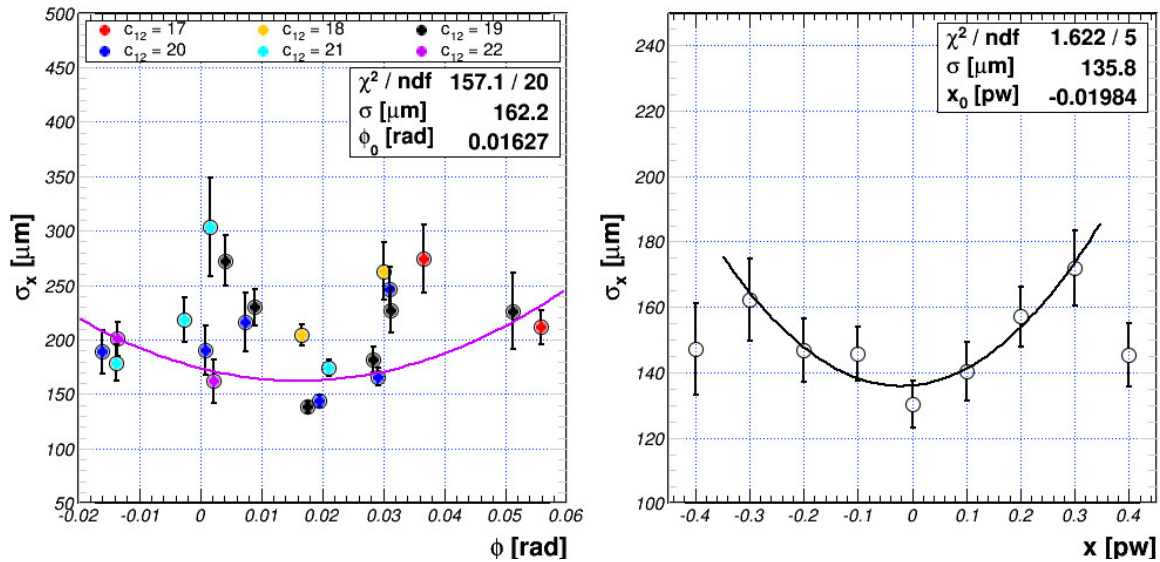


Figure 12.13: Mean TRD resolution across pads as a function of track inclination based on SSTRD-V2 column selection (left, see color mapping detailed in the legend) and as a function of charge sharing detailed by the deviation from pad center (right).

In Fig. 12.13 the mean resolution of the TRD (all prototypes being considered identical) is presented as calculated based on Eq. 12.11 for different data selections based on the largest column signal measured in the SSTRD-V2. Using vertex to detector mechanical measurements and the normalization to vertex direction with respect to detector setup obtained from analyzing the shape of the yield distribution as function of SSTRD-V2 column index one can estimate track inclination. The results obtained for each SSTRD-V2 column selection are emphasized

by a different color as detailed in the legend of Fig. 12.13-left. Error bars are determined from the Gauss fit to  $V$ . As one can see, the reaction products are seen simultaneously in the three detectors for six columns of SSTRD-V2 running from column 17 to column 22 with a maximum on 19 – 20. A parabolic fit is also shown in Fig. 12.13-left which yields a maximum resolution of  $162\ \mu\text{m}$  at normal incidence.

The same quantity was analyzed with respect to the incidence per TRD column, as shown in Fig. 12.13-right, in units of 10% of pad width i.e.  $770\ \mu\text{m}$ . The data were conditioned such that only clusters within the specified range expressed in pad width units were selected in all three detectors. The distribution over  $\phi$  was integrated. A clear minimum is observed in the middle of the pad ( $x_0 \approx 2\% \text{ pw}$ ) with a value of  $135\ \mu\text{m}$ . From the two dependencies shown in Fig. 12.13 one can see that the best detector resolution at  $\phi = 0$  and  $x[\text{pw}] = 0$  for single track events in high rate/multi-hit environments is slightly larger than  $100\ \mu\text{m}$ .

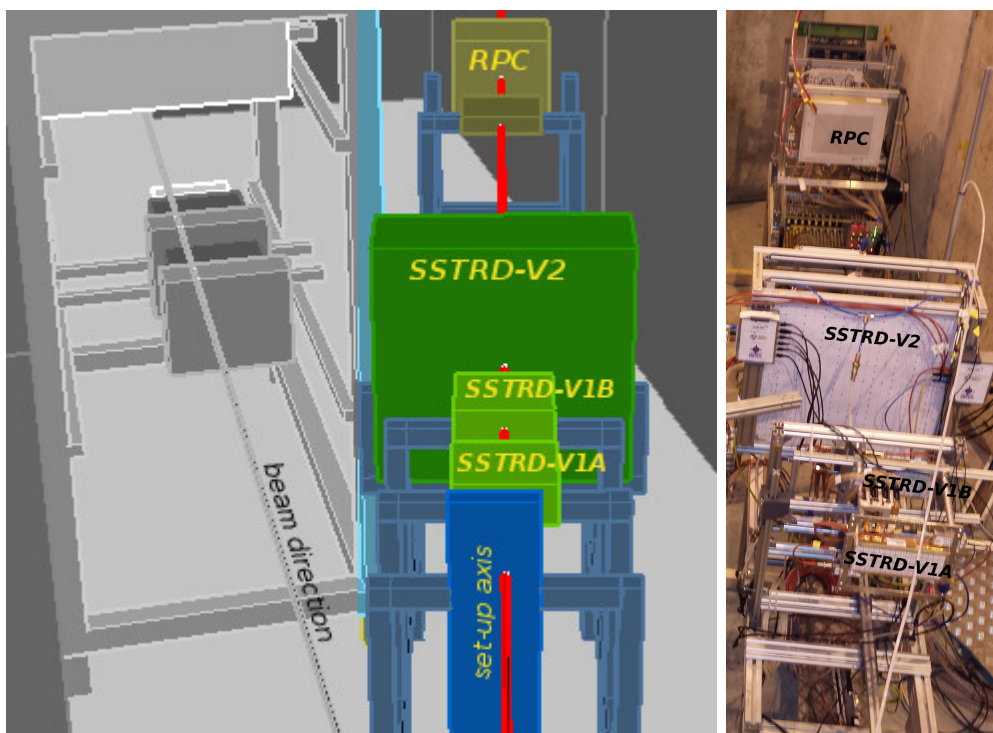


Figure 12.14: Detector setup tested at 30 AGeV Pb+Pb interactions at the CERN-SPS. Schematic view (left) and photo (right).

The detector setup used for 30 AGeV Pb-beams is presented as both, sketch and photo, in Fig. 12.14. The SSTRD-V2, positioned this time downstream in beam, was operated on three pad rows equipped with FASP-01/02 and 16 columns/row (96 readout channels), while the reference prototypes (SSTRD-V1) on one row of 12 columns (24 FASP-01 readout channels) each. All three detectors were mounted parallel to each other and aligned relative to the operated rows.

A detailed calibration procedure was implemented to adjust the gain of each FEE channel based on injecting a given signal on the anode grid. A specific calibrated signal spectrum is shown in Fig. 12.15-left, for each channel of two FEE boards equipped with the FASP-02 ASICs. A constant signal at 1200 ADC channels is observed, which is produced by a pulser running in parallel with data acquisition. The pedestals are also calibrated as can be observed in the band centered at ADC 0 channels.

Using the position of reconstructed clusters in the three stations and a simple matching algorithm one can reconstruct straight tracks. Details of the analysis can be found elsewhere [B<sup>+</sup>16b]. Worth mentioning here is the vertex reconstruction result which is shown in Fig. 12.15-

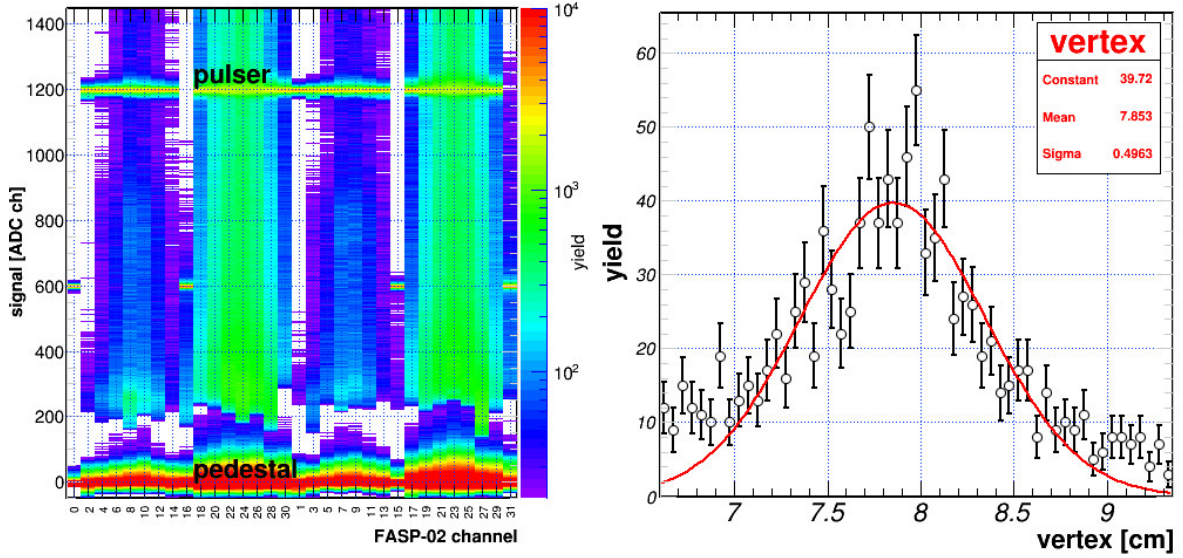


Figure 12.15: Calibration of FASP-02 channels at 30 AGeV Pb+Pb interactions at the CERN-SPS (left) and the interaction profile from the target reconstructed using the TRD stations (right).

right. The Pb target is placed at 160 cm from SSTRD-V1A and the whole TRD setup is tilted with  $15^\circ$  with respect to the beam axis. Aligning the TRD detectors with respect to each other and extrapolating TRD tracks to such distance a peak of 0.5 cm width is observed.

### 12.3.2 Two-ways paired pads readout

Reading out triangular pads, although versatile, has the drawback of variable  $S/B$  ratio and pad-to-pad cross talk along pads (see Sect. 12.3.3.1). In order to cure these problems a new readout was developed in which the charge summing is performed before entering the amplification level. Thus a major improvement was introduced with the second version of FASP (see Sect. 12.4.2). The charge is summed for each column on the even FASP-02 channels  $\{Q_i\}_{i=\overline{1,3}}$  (see Fig. 12.16-left - gray columns) and for each parallelogram on the odd channel  $\{Q_i^{//}\}_{i=\overline{1,3}}$  (see Fig. 12.16-left - hatched parallelograms), respectively. The signal obtained for each channel after calibration is shown in Fig. 12.15 (left), for the rectangular columns first (even channel index) and for tilted columns (odd channel index) last.

Reconstruction of the position across pads follows from Eqs. 12.5 and 12.6 with  $P_0 = 0$ , while for tilted pads one can apply

$$\mathcal{G}(\Delta, PRF | \{Q_i^{//}\}_{i=\overline{1,3}}) \quad (12.12)$$

$$qq^{//} = \Delta + j/2 - d, \text{ with} \quad (12.13)$$

$j = -1$ , if tilted maximum happens before the rectangular and  $j = 1$  otherwise and  $d$  from Eq. 12.2.

#### 12.3.2.1 Laboratory tests using $^{55}\text{Fe}$ X-rays

The two-dimensional reconstruction was tested with FASP-02 using the uniform illumination with an  $^{55}\text{Fe}$  source. The results are presented in Fig. 12.16, which shows a better separation of the anode wires with respect to FASP-01 (see Fig. 12.10). Besides the improvements mentioned above the channel wise logic marker generated by FASP-02 (see Sect. 12.4.2) used in the reconstruction eliminates some of the random pile-up events rendering a better  $S/N$  ratio for anode identification. Such readout configuration appears to be the best candidate for operating the central part of the

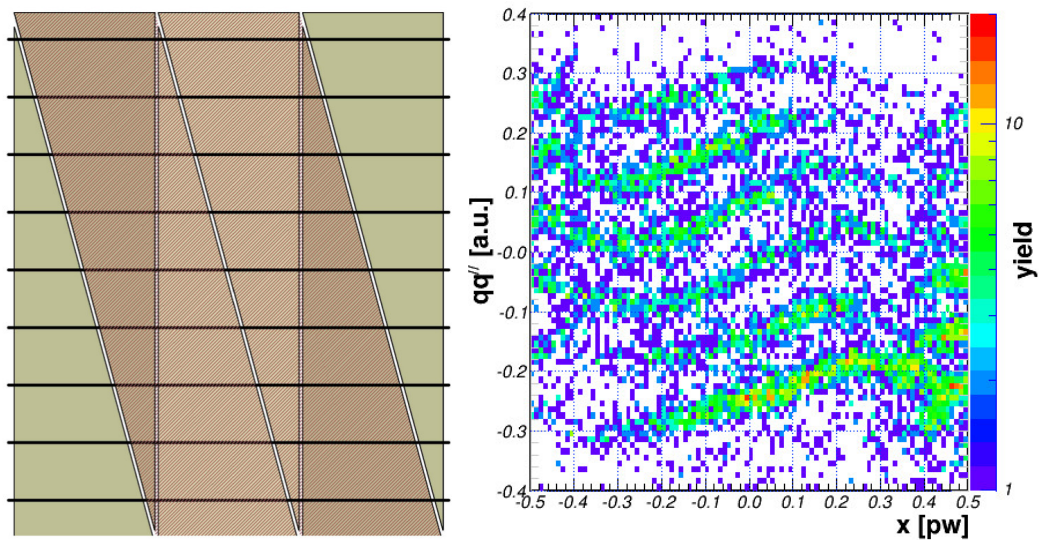


Figure 12.16: A schematic view of the pad plane architecture emphasizing the tilted/rectangular pairing readout and the anode wire grid (left) and the corresponding AWRF plot obtained for  $^{55}\text{Fe}$  illumination (right).

TRD wall, as it inherits all features of the triangular/FASP-01 readout, but adds the possibility to disentangle pile-up events, which are produced in extreme illumination conditions and allows for a better position resolution along wires due to the very good separation of anode wire characteristic lines. Such a goal can be easily reached by decreasing the anode pitch [B<sup>+</sup>16b].

### 12.3.3 Simulation of the detector response

The charge seen by each triangular pad was modeled by considering a point-like charge multiplication located on the anode wire and its electrostatic image induced on the conductive pads described by two orthogonal independent normal distributions centered on it. Their integral over a pad area is proportional to the measured signal. The free parameters of the model are  $\sigma_x$  and  $\sigma_y$ , describing the charge distribution across pads for variable  $x$  and along the pads  $y$ , respectively. The integration was performed on a rectangular grid of size  $dx \times dy = 0.04 \times (w \times h)$ <sup>1</sup>. Modeling a uniform illumination of one column was performed by scanning all anode wires span by a column in steps of 1% of pad width (i.e. 77  $\mu\text{m}$ ). The charge seen for each triangular pad was therefore calculated according to the approximation

$$q^{\nabla/\Delta} = \int_{-w/2}^{w/2} dx \int_{-kx}^{kx} dy \mathcal{G}(x|x_0, \sigma_x) \mathcal{G}(y|y_0, \sigma_y) \quad (12.14)$$

$$\approx \sum_{i_x} \sum_{i_y} \mathcal{G}(x(i_x)|x_0, \sigma_x) \mathcal{G}(y(i_y)|y_0, \sigma_y) d\mathcal{A}(i_x, i_y) \quad (12.15)$$

where  $k$  is the slope of the boundary between upper and lower triangular pads,  $(x_0, y_0)$  is the charge multiplication center,  $(x(i_x), y(i_y))$  is the center of bin indexed  $(i_x, i_y)$  and  $d\mathcal{A}$  its effective area i.e.

$$d\mathcal{A} = dx dy \quad \text{if } (x(i_x), y(i_y)) \in \text{pad} \quad (12.16)$$

$$= dx dy / 2 \quad \text{if } (x(i_x), y(i_y)) \in \text{boundary} \quad (12.17)$$

$$= 0 \quad \text{rest} \quad (12.18)$$

<sup>1</sup>Calculations were performed for  $w = (7.5 + 0.2)$  mm and  $h = (27.5 + 0.2)$  mm corresponding to SSTRD pad plane.

Applying the Eq. 12.5 for position across pads and Eq. 12.7 or 12.13 along pads for triangular

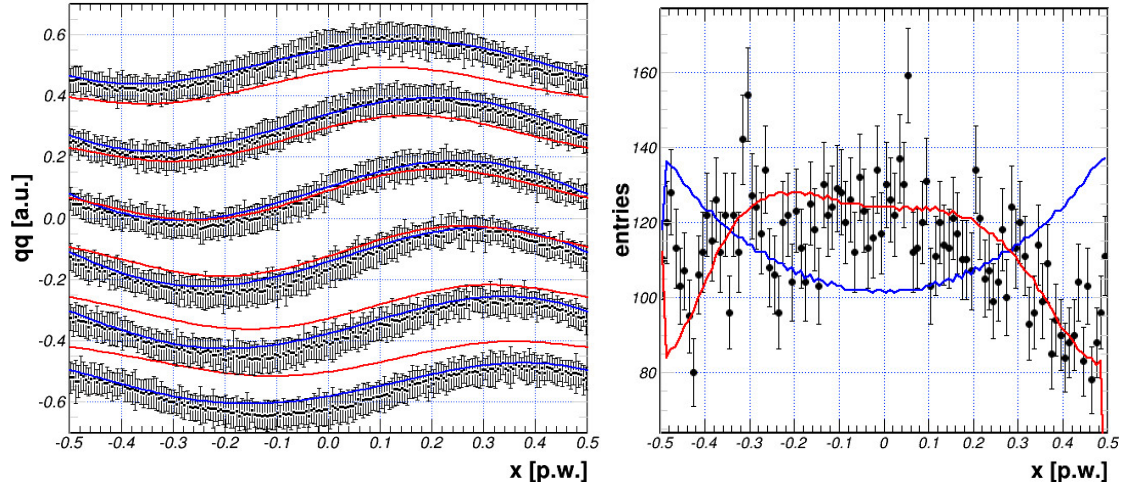


Figure 12.17: Comparison between 13 AGeV Ar+Pb data (black) measured with the SSTRD-V1 prototype and simulations with  $XT = 4\%$  (red) and without  $XT$  (blue) for the 2D position observables of the TRD (left) and the measured yield/column for uniform illumination as function of  $x_{\text{rec}}$  (right).

or paired readout, respectively, one can render observables similar to the measurements<sup>2</sup>. In Fig. 12.17 a fit (with respect to  $\sigma_x$  and  $\sigma_y$  model parameters) of 13 AGeV Ar+Pb data is shown for triangular readout on two correlation plots; the  $(qq, x)$  (left panel) and the  $(\text{yield}, x)$  (right panel). Data are shown in black as  $(\text{mean}, \text{RMS})$  quantized with respect to  $x_{\text{rec}}$  expressed in pad width (p.w.) units for identified anode wires. The model correlations are shown in blue. In order to avoid secondary effects not covered by the model, only single cluster events on all TRD stations were selected.

The results presented in Fig. 12.17 show a very good agreement for the  $(qq, x)$  plot for all<sup>3</sup> anode wires simultaneously and for the full width of a column. On the other hand we observe that trend of the measured yield per column and for an anode wire is not explained. The opposite trend of the model with respect to data suggests a strong effect when an interaction happens close to the column boundaries where the relative width of the pads with respect to anode wire differ the most. Such effect can be modeled by introducing a cross talk ( $XT$ ) parameter<sup>4</sup>.

### 12.3.3.1 Cross talk effects

The cross talk ( $XT$ ) of signal between adjacent triangular pads due to capacitive coupling is defined by the effective charge seen by a triangular pad altered by its neighbors according to:

$$q^m = q_0^m + \chi \cdot q_0^l + \chi \cdot q_0^r \quad (12.19)$$

where  $q_0$  is the charge seen by the triangular pad as calculated before (see Sect. 12.3.3), upper indexes are shorthands from *middle*, *left* and *right* and  $\chi$  is the  $XT$  parameter<sup>5</sup>. The results

<sup>2</sup>The model neglects effects like varying signal with charge deposit, charge amplification on two anode wires by inclined trajectories, multi-hits on single pad, etc. Such effects will be studied in details as soon as a frozen detector architecture is selected.

<sup>3</sup>Actually only the central six out of eight anode wires are shown. For the other two boundary effects between pad rows start to be important and modeling become technical complicated. Nevertheless, the heuristic performance of the model is not affected.

<sup>4</sup>Such effect is relevant for the triangular readout. Using paired readout the effect should be significantly diminished by construction.

<sup>5</sup>The model is simple but rather general as it uses one  $XT$  parameter to describe the full detector (i.e. independent of anode wire or position across pads). It is also symmetric with respect to the left and right neighbors

obtained with a value  $XT = 4\%$  are displayed as the red curve in Fig. 12.17. Although the matching from the  $qq - x$  correlation plot deteriorates (Fig. 12.17-left) the  $yield - x$  trend is described much better thus confirming our assumption. A more explanatory model covering a larger range of data correlations is beyond the scope of this report.

### 12.3.3.2 Systematic effects of position reconstruction across pads

The reconstruction of position across pads using the Eq. 12.5 is biased (see e.g. [BR94]). Using the model described above one can estimate and correct them.

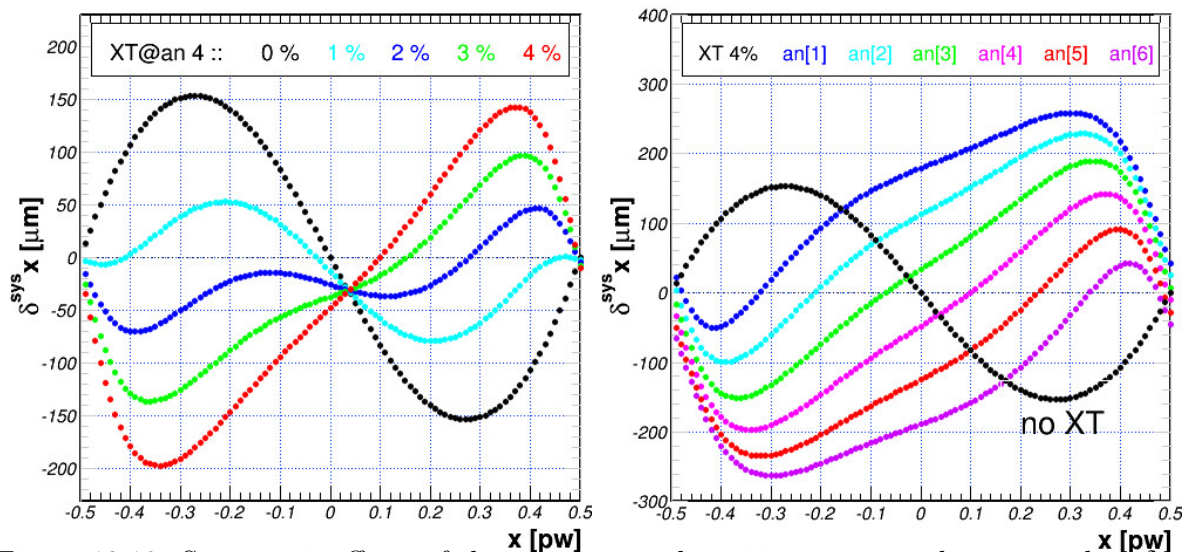


Figure 12.18: Systematic effects of the reconstructed position across pads expressed as  $\delta x = x_0 - x_{\text{rec}}$  as a function of  $x_{\text{rec}}$  in units of pad width for the fourth anode and  $XT$  range 0 – 4% (left) and their dependence on the anode wire for fixed  $XT = 4\%$  (right).

In Fig. 12.18 the residuals  $\delta x^{\text{sys}}(x_{\text{rec}}) = x_0 - x_{\text{rec}}$  between the center of the charge multiplication (see Eq. 12.14) and the reconstructed value obtained from Eq. 12.5 are shown as function of the reconstructed position  $x_{\text{rec}}$  for various anode wires and  $XT$  values. By selecting a particular anode (e.g. the fourth in Fig. 12.18-left) one can evaluate the systematic shift for  $XT$  values in the range 0 – 4%. A non negligible (with respect to position resolution, see Sect. 12.3.1.3) correction to the reconstructed position across pads is identified, which has the effect of e.g. deforming a flat spectrum as seen in Fig. 12.17-right. The dependence of the shift in case of  $XT \neq 0$  is asymmetric with respect to the center pad and is anode wire dependent (see Fig. 12.18-right). Moreover the position for which the systematic effect is independent of  $XT$  is defined by the intersection of the anode wire with the diagonal slit between adjacent triangular pads.

In order to produce unbiased results for the reconstructed position across pads the observable  $x_{\text{rec}}$  is corrected to:

$$x_{\text{rec}}^{\text{unbiased}} = x_{\text{rec}}^{\text{rec}} + \delta x^{\text{sys}}(x_{\text{rec}}|XT) \quad (12.20)$$

with the  $XT$  parameter as found from a fit to the data (see the red curve in Fig. 12.17-right).

We have determined the parameters of the model  $\sigma_x$ ,  $\sigma_y$  and  $XT$  from fitting simultaneously the correlation plots from Fig. 12.17 on data for all operated prototypes. The data used for the fit were selected events with one cluster for each TRD station from measurements at the CERN-SPS

and it assumes non zero values only for first order neighbors. A dedicated electromagnetic modeling of the capacitive coupling between triangular pads and subsequently estimation of the  $XT$  from first principles is beyond the scope of present TDR.

with the 13 AGeV Ar+Pb system. The results for the three prototypes ( $2\times$  SSTRD-V1 and SSTRD-V2) over the full column range operated in the test beam show for the  $(qq-x)$  correlation plot values of  $\sigma_x \approx 2.5$  mm and  $XT \approx 2\%$ . They are also independent of the TRD column/FEE channel due to the way they are constructed. The fit to the  $(yield, x)$  correlation plot depends on the position along the prototype and is best explained by  $\sigma_x \approx 3.2$  mm and  $XT \approx 4\%$ . The least sensitive parameters of the model,  $\sigma_y$ , best describes the data for a value of  $\approx 3.5$  mm. More details are presented elsewhere [B<sup>+</sup>16a].

## 12.4 Electronic readout based on the FASP ASIC

The concept of the Fast Analog Signal Processor (FASP) as an ASIC is based on the high counting rate in-beam results obtained with the very first prototypes of TRDs developed for CBM Experiment at FAIR. The final target is to have a fast amplifier for MWPC or GEM detectors used in high counting rate environments, which delivers minimum information without deteriorating the detectors performance.

The first two prototypes designed by the Bucharest group uses AMS 0.35  $\mu\text{m}$  N-well technology [Col05].

The FASP ASIC has eight (v0.1), respectively sixteen (v0.2), identical channels, each processing one TRD pad (see Fig. 12.19-left *in*-channels). The current signal is amplified and shaped optimizing the signal to noise ratio. The chip provides two types of output for each channel: a semi-Gaussian shaped output and a peak-sensing output (see Fig. 12.19-right top two responses).

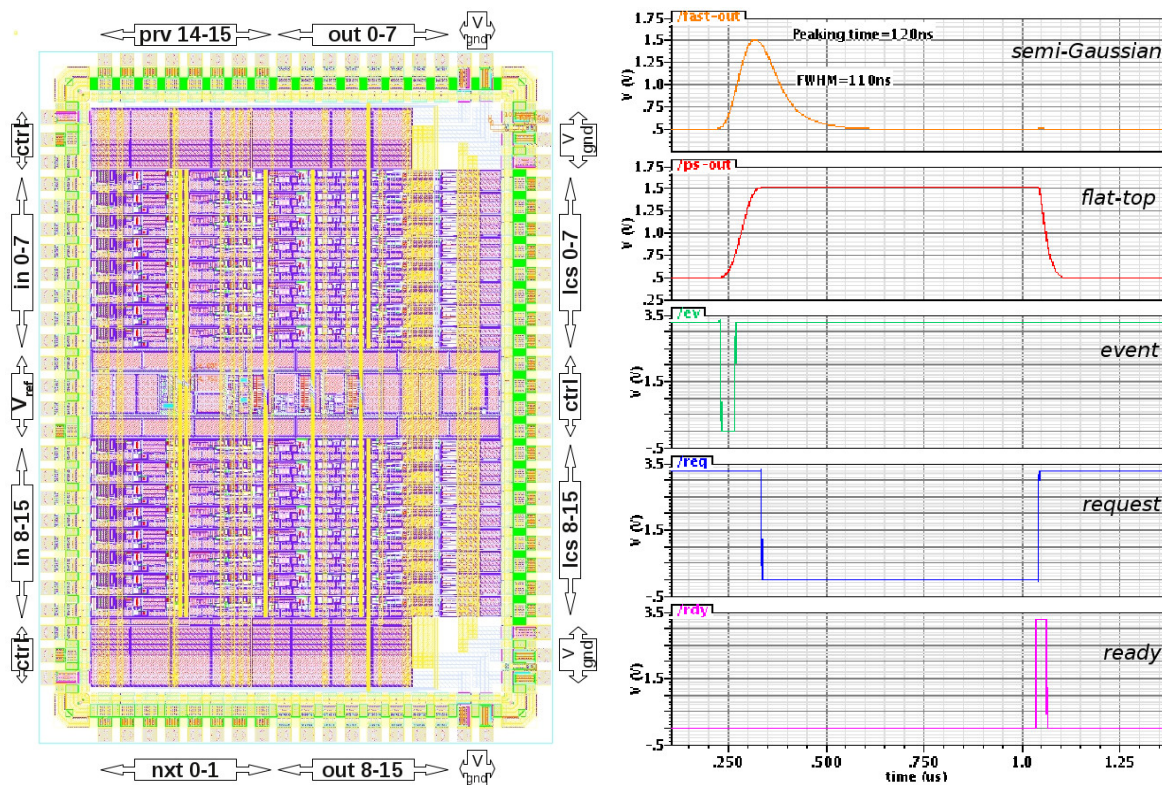


Figure 12.19: The layout of the FASP-0.2 ASIC with its in/out pads connections (left) and the typical analogue/logic response to a delta current for one FASP channel (right).

An I/O interface inside the chip, working on request/grant basis, assures a correct data transfer between the output of each channel and the data acquisition system. All channels have a self trigger capability with variable threshold [C07, CBC09] coined *chip select* (see Fig. 12.19-left *lcs*-channels and -right the *request* signal). For testing purposes a test pulse generator is implemented into the ASIC. The most important features of the FASP ASIC [C07, CBC09] are summarized in Tab. 12.1.

Table 12.1: The general FASP ASIC features

Average pulse rate	over 300 kcps
Charge input range	0.15 fC ... 165 fC
Input coupling / type	DC / single ended
Channel gain	6.1 mV/fC
Shaping time, (CR-RC**4, semi-Gaussian, 1-bit selection)	20 ns or 40 ns
Semi-Gaussian output pulse FWHM	62 ns (shaping time 20 ns) 110 ns (shaping time 40 ns)
Output type (semi-Gaussian or peak-sensing)	single ended
Output voltage swing (semi-Gaussian or peak-sensing)	0 ... 1 V
Output pulse variation (semi-Gaussian or peak-sensing)	
- with temperature $T = 0 \dots 70 \text{ C}$	$< 0.03 \text{ \%}/\text{C}$
- with power supply $V_d = 3.0 \text{ V} \dots 3.6 \text{ V}$	$< 0.18 \text{ \%}/\text{V}$
Output baseline shift (semi-Gaussian or peak-sensing)	
- with temperature $T = 0 \dots 70 \text{ C}$	$< 8 \text{ }\mu\text{V}/\text{C}$
- with power supply $V_d = 3.0 \text{ V} \dots 3.6 \text{ V}$	$< 0.07 \text{ \%}$
- with detector leakage current	$< 5 \text{ }\mu\text{V}/\text{nA}$
Channel ENC ( $C_{\text{det}} = 25 \text{ pF}$ )	
- for shaping time 40 ns	980 e
- for shaping time 20 ns	1170 e
Integral nonlinearity (semi-Gaussian or peak-sensing)	
- for shaping time 40 ns	$< 0.21 \text{ \%}$
- for shaping time 20 ns	$< 0.90 \text{ \%}$
Overshoot / undershoot (semi-Gaussian)	
- for shaping time 40 ns	$< 0.20 \text{ \%}$
- for shaping time 20 ns	$< 0.80 \text{ \%}$
Peak-sensing output settling time to 0.1 % of final value	$< 450 \text{ ns}$
Peak-sensing output decay	$< 25 \text{ }\mu\text{V}/\mu\text{s}$
Self trigger capability	
- variable threshold (cont. adj.)	0 ... 165 fC (full range)
- hit occurrence signal	logic level
Power consumption	11 mW/channel

### 12.4.1 Features of the FASP-0.1 ASIC

The FASP-0.1 version ASIC of  $3.15 \times 2.10 \text{ mm}^2$  has the following characteristics:

- i. **Good response to double pulses and high rates** was obtained using an appropriate number of shapers and values for the shaping time. In Fig. 12.20-left one can observe the performance on the semi-Gaussian output to a pair of delta pulses of amplitude 1.0 and 0.2 separated by 1  $\mu\text{s}$ .
- ii. A special circuitry in each analog channel allows a very **fast and clean recovery to charge overload**. In Fig. 12.20-middle the performance is shown when signal overloads of ten times the nominal range are simulated. The situation is worse when such precautions are not considered (see Fig. 12.20-right). The fast recovery circuits reduce the dead time of the analog channels and result in a very good double pulse separation and an excellent response to high pulse rates without baseline perturbation.

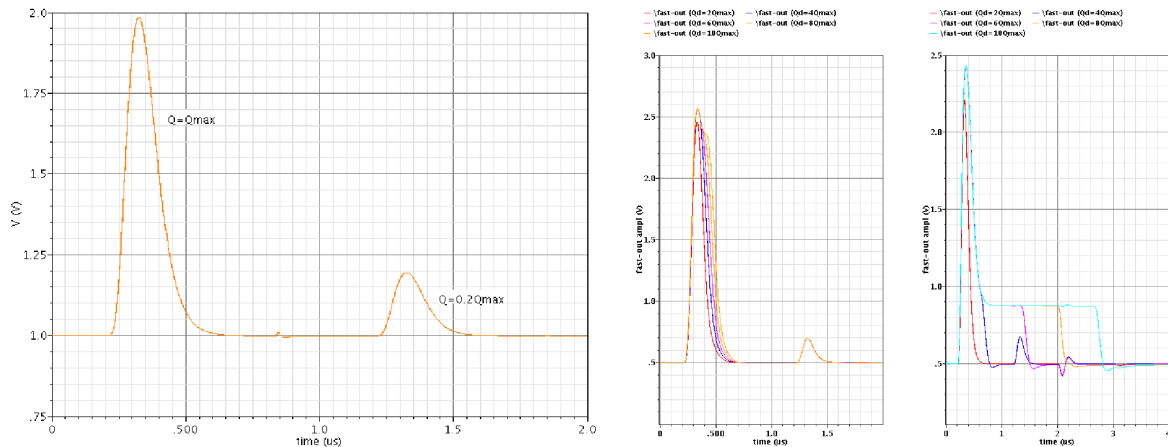


Figure 12.20: Semi-Gaussian output response of one analog channel to delta pair pulses. Semi-Gaussian output response of one analog channel to delta pair pulses with fast recovery circuits (left) and without fast recovery circuits (right).

- iii. Specific circuits are implemented for the **restoration of output baseline** which allows to compensate the effects of detector leakage currents. For example a pad leakage current in the range of  $\pm 50$  nA the output baseline shift is reduced from shifts of  $0.8$  mV/nA to below  $3$   $\mu$ V/nA as detailed CADENCE [Eur] simulations show. The same circuits are also very efficient to avoid a baseline displacement due to high counting rates.
- iv. A **shaping time selection** is implemented with a 1-bit logic input line. Two possible values of  $20$  ns and  $40$  ns are available depending on the results obtained during the tests of the TRD prototypes.
- v. For each channel, a second **peak-sensing self-trigger** output (Fig. 12.19-right second signal), offers a flat top pulse with a value corresponding to the peak of its semi-Gaussian output. The peak-sensing output is generated only for pulses with an amplitude above a defined threshold, generating also a self-trigger logic signal (Fig. 12.19-right fourth signal). The peak-sensing signal is maintained until a ready is received from the acquisition unit (Fig. 12.19-right fifth signal). The threshold level is common to all analog channels but its value can be adjusted within the full output range of the analog channels.

Besides the features mentioned above there are also additional circuits such as: calibration pulse generator, reference and bias circuits, and also a fast input/output interface for data processing.

### 12.4.2 Features of the FASP-0.2 ASIC

The second version of the FASP-0.2 ASIC with die size  $4.65 \times 3.45$  mm<sup>2</sup> was developed also in the AMS  $0.35$   $\mu$ m N-well technology. It preserves all specifications of the previous version, but includes some additional features summarized below:

- i. **16 input channels** for detector signal processing (see Fig. 12.19-left in pad entries).
- ii. User **selectable polarity for the inputs**.
- iii. **Multiplexed analog inputs** allowing for different pad pairing (see Fig. 12.16-left).
- iv. Capability of each data processing channel to generate a **separate chip-select, clock-synchronized logic signal** and to act as its individual ADC.

- v. **Channel wise logic time signal** allows to transmit the variable threshold level or can be used for the signal peak detection according to the selection by the user.
- vi. Selectable **channel neighbor trigger** to increase cluster size. Such facility is used to force flat-top generation on under threshold channels and thus increase position resolution performance.

The input channel signal polarity, the shape of output signal (semi-Gaussian or flat-top), the logic time signal generation (threshold or peak-sensing), and the neighbor trigger can all be selected by the user, each via a 1-bit selection line (see Fig. 12.19-left `ctrl` pad entries) resulting in 16 different working modes of the FASP-0.2 chip. The user can modify dynamically the control parameters via a dedicated `ctrl` link.

The main specifications of FASP-0.1 and FASP-0.2 are listed in Tab. 12.2, while the whole layout of the FASP-0.2 ASIC is presented in Fig. 12.19.

Table 12.2: The specifications of the FASP-0.1 and FASP-0.2 ASICs.

Specifications	FASP-0.1	FASP-0.2
Average pulse rate	> 300 kHz	> 300 kHz
Detector pad capacitance	25 pF	25 pF
Number of analog channels	8	16
Input polarity (1-bit selection)	positive	positive / negative
Channel pairing	no	yes
Charge input range	0.15 fC ... 165 fC	0.15 fC ... 165 fC
Input type	DC single ended	DC single ended
Channel gain	6.2 mV/fC	6.2 mV/fC
Shaping time / (1-bit selection)	20 ns and 40 ns / yes	100 ns <sup>6</sup> n.a.
Analog output type (1-bit selection)	semi-Gaussian or peak-sensing	semi-Gaussian or peak-sensing
Analog output polarity	Positive (single ended)	Positive (single ended)
Analog output voltage swing	0 ... 1 V	0 ... 1 V
Analog output DC voltage level baseline (cont. adj.)	0.2 V ... 1 V	0.2 V ... 1 V
Semi-Gaussian output FWHM	62 ns / 110 ns	290 ns
Peak-sensing output plateau	typ. 400 ns (cont. adj.)	typ. 400 ns (clock dependent)
Channel ENC ( $C_{\text{det}} = 25$ pF)	980 e (ST = 40 ns), 1170 e (ST = 20 ns)	940 e
Crosstalk (max. signal in only one ch., no signals in others)	0.5 %	0.012 %
Crosstalk (max. signal in 15 ch., no signal in one channel)	0.7 %	0.022 %

Self-trigger capability: variable threshold (cont. adj.)	0 ... 165 fC	0 ... 165 fC
Logic common event output	neg. 20 ns width	neg. 20 ns width
External clock synchronization	no	max. 50 MHz
Logic signal channel wise, clock synchronized, output	no	yes
Channel synchronized logic signal for semi-Gaussian output	n.a.	to thres. level / to max. ampl.
Channel-wise synchronized logic signal for semi-Gaussian output	n.a.	neg. 20 ns to thres. level / to max. ampl.
Channel-wise synchronized logic signal for peak-sensing output	n.a.	neg. 20 ns to thres. level / neg. 14 clock cycle to max. ampl.
Channel neighbors trigger enable / disable	n.a.	yes

### 12.4.3 Simulations of the FEE

The response of the FASP ASIC was tested using CADENCE [Eur] simulations. The main results are summarized as follows:

- i. The **typical response to delta current signals of one self-triggered analog channel signals** is shown in Fig. 12.19-right for an input charge of 165 fC, a shaping time constant of 40 ns, and for a channel threshold of 6 fC.
- ii. The **integral nonlinearity**, for both type of outputs (semi-Gaussian and peak-sensing) and for shaping times of either 20 ns or 40 ns are below a 1 % as summarized below: In

Shaping time [ns]/Output	20	40
Semi-Gaussian	< 0.47 %	< 0.21 %
Peak-sensing	< 0.91 %	< 0.19 %

Fig. 12.21-left the semi-Gaussian output as a function of the input charge for one analog channel with a shaping time of 40 ns is shown. The corresponding integral nonlinearity is 0.21 %.

- iii. The **noise characteristics** were carried out for a typical input pad capacitance of 25 pF, as well as for varying capacitances  $C_{in}$  in the range [0,40] pF as shown in Fig. 12.21-right for both 20 ns ( $\approx 31$  e/pF) and 40 ns ( $\approx 22$  e/pF) shaping time values. For the typical value the simulated channel noise is 980 e and 1170 e for a shaping time of 40 ns and 20 ns, respectively.

#### 12.4.3.1 Analog channel response to GARFIELD input

The FASP design has to be optimized with respect to two opposite requirements derived from the operation conditions of the TRD prototype: it has to be fast enough for running in high rate environments without dead time truncation and has to conserve energy deposit by particles crossing the active area as the basic requirement for PID and position performances. An optimum was searched for by simulating the response of the FASP channel using the CADENCE software [Eur] with realistic detector signals simulated with GARFIELD [Vee98] (see Sect. 12.2.4).

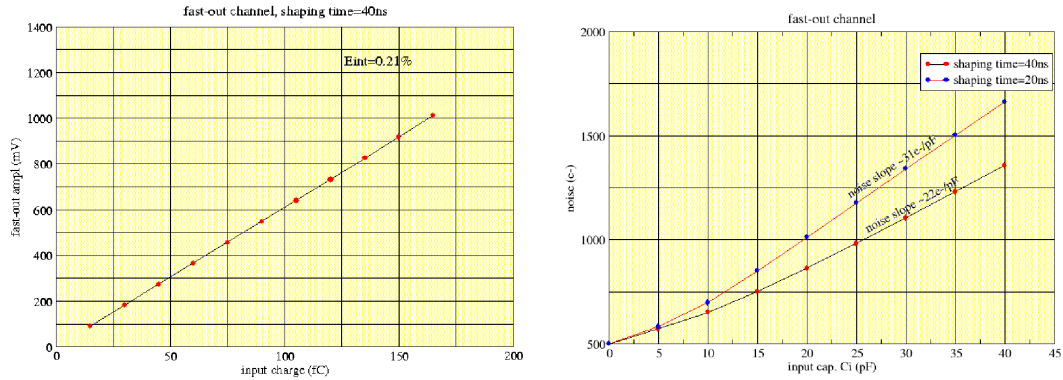


Figure 12.21: Integral nonlinearity for the semi-Gaussian output with a shaping time of 40 ns (left) and the ENC for the semi-Gaussian output as a function of the input capacitance  $C_{in}$  (right).

In Fig. 12.22 the transient responses of the analog channels to simulated input current signals are presented. The length of the simulated signal is 3  $\mu$ s. In the upper panel the detector current signal simulated with GARFIELD is shown, which is used as input to the analog channel. The middle panel displays the results of the semi-Gaussian output (red line) and of the peak-sensing output (blue line) for a shaping time of 40 ns. In the lower panel the same two outputs are shown for a shaping time of 20 ns. For both peak-sensing cases (40 ns and 20 ns shaping time) the threshold is adjusted such that it allows only the analysis of the peaks of interest.

The two main constructive ROC prototypes for which FASP was designed are presented in Sect. 12.2.2 for the DSTRD and in Sect. 12.2.3 for the SSTRD, respectively. It was shown (see Fig. 12.5-left) that the maximum drift time of an ionization cluster produced by a charged particle inside the gas volume, calculated with GARFIELD, was about 100 ns for DSTRD and 250 ns (see Fig. 12.5-right) for SSTRD, respectively. Since the FASP amplifier was originally designed for DSTRD [P<sup>+</sup>13b], the shaping time (ST) of this version was optimized to 40 ns, in order to process the fast signals delivered by this prototype. The linearity of the FASP output signal processed with a shaping time of 40 ns is shown in Fig. 12.23-left, where the ionization clusters are randomly distributed inside the drift volume over a drift time window (DTW) of 100 ns (triangle markers). A very good proportionality and linearity of the signal to the input charge is observed. The extracted slope of 5.97 mV/fC is very close to the conversion gain and the offset of 2.43 mV is small. For comparison the FASP performance on a SSTRD prototype with maximum drift time 250 ns (square markers) is included. The observed slope of 5.17 mV/fC is lower than the conversion gain and an offset of about  $\sim$  50 mV is observed. In Fig. 12.23-right the uniformity of the FASP response to tracks depositing a constant  $E_{dep} = 65$  fC for the same configurations as used in the left panel. The standard deviation of 5 mV around a mean output value of 392 mV, which is very close to the theoretical mean of 402 mV, is small for the DSTRD architecture. For a DTW of 100 ns the average FASP output conserves the gain and the fluctuations are rather small. For the SSTRD geometry, the rather large standard deviation of 40 mV around a mean of 289 mV shows that the FASP ST has to be optimized for an undistorted processing of such signals.

It is obvious that the operation of SSTRD requires an increase of the shaping time to accommodate the larger DTW of such ROC architectures. The improvements in the linearity of the output signal due to an increase of the shaping time from 40 ns to 80 ns, resp. 100 ns, for a DTW of 250 ns are shown in Fig. 12.24-left. For a shaping time of 100 ns, the slope of 5.88 mV/fC, obtained with a linear fit, approaches the conversion gain and the offset is reduced to  $\sim$  12 mV.

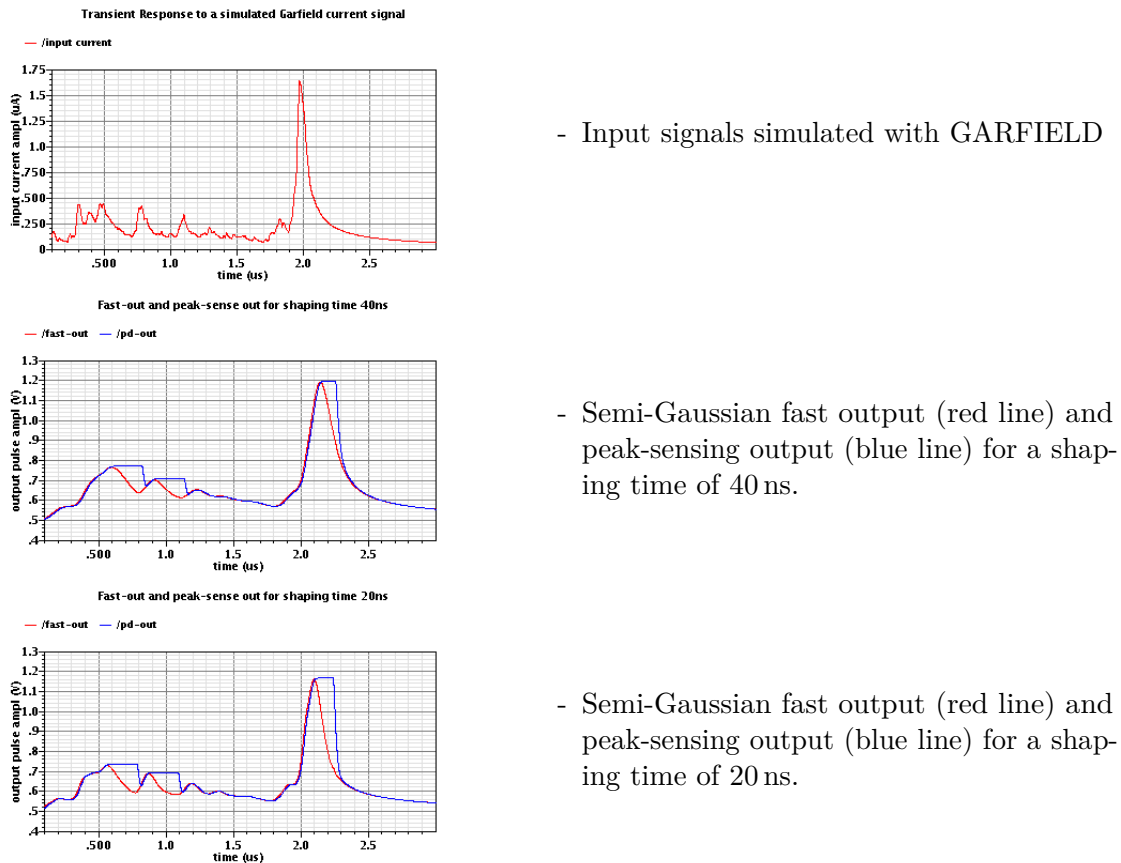


Figure 12.22: Analog channel response to simulated GARFIELD signals.

Figure 12.24-right demonstrates the improvements in the fluctuations achieved by an increase of the shaping time for a constant  $E_{\text{dep}} = 65 \text{ fC}$  delivered by various track parameters. The mean value of the distribution increases to 371 mV for a shaping time of 100 ns, and the standard deviation of the distribution is reduced to 16 mV. Based on these results, a second version (v0.2) of the FASP amplifier has been developed with a larger shaping time of 100 ns. This value can still cope with the  $100 \text{ kHz/cm}^2$  counting rate expected in the innermost zone of the CBM-TRD at SIS100.

#### 12.4.4 FEE integration

FASP ASICs were integrated on prototype FEBs developed by the Bucharest group to interface between DSTRD and SSTRD ROC architectures on one end and various DAQ systems. In order to cope with both triggered and free-running DAQs sitting at large distances (several meters) the single-ended output of FASP is converted to differential and shipped over twisted pair cables.

##### 12.4.4.1 FASP FEB

The FASP-0.1 ASIC has been integrated on various FEBs housing one or two chips. In Fig. 12.25-left an example with two chips is shown.

The largest part of the FEB is dedicated to Analog Buffers (see Fig. 12.25) which besides transforming the single ended output to differential have also functions for DC compensation and extra gain such to optimally match the ADC range used to digitize the signals. For this FEB version a common request REQ TTL signal is provided for both chips which might be used

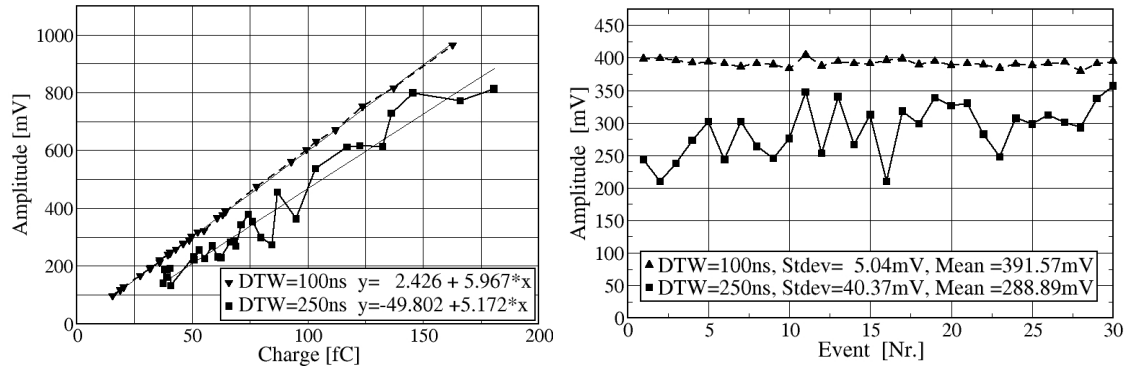


Figure 12.23: Linearity of the FASP response (shaping time of 40 ns) for particles of various  $E_{\text{dep}}$  in [fC] in DSTRD (triangles max drift time 100 ns) and for the SSTRD (squares max. drift time 250 ns) prototype respectively (left) and the uniformity of the signal for various tracks with fixed  $E_{\text{dep}} = 65$  fC (right).

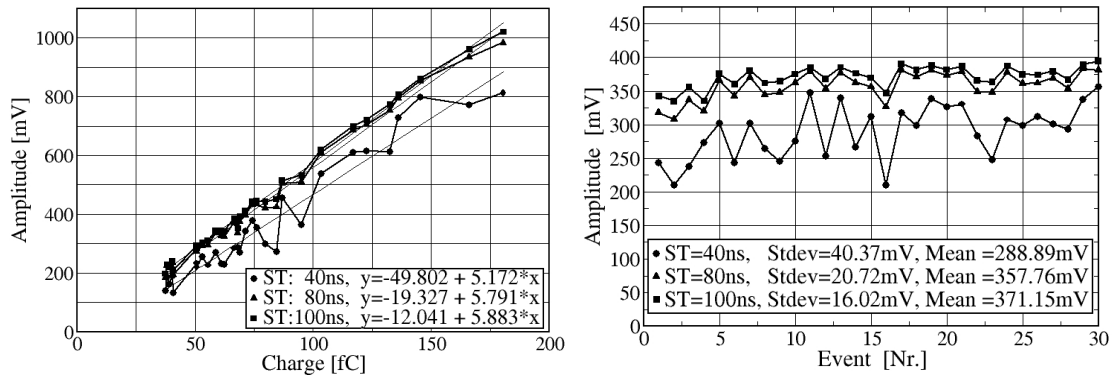


Figure 12.24: Linearity of the FASP response for the SSTRD prototype for particles of various  $E_{\text{dep}}$  in [fC] for 40, 80 and 100 ns shaping times (left) and its uniformity for various tracks with fixed  $E_{\text{dep}} = 65$  fC (right).

to self trigger the DAQ. Control functions for threshold adjustment  $\text{THR}$  and for flat-top  $\text{FT}$  duration are located on board and are interfaced via simple mechanical devices. The board is powered via a USB socket  $\text{PWR}$ .

For the second version of the FASP a version of FEB housing one chip is presented in Fig. 12.25-right. As this board house its own 33 MHz CLK the flat-top adjustment  $\text{FT}$  and external reset  $\text{RST}$  are omitted and are replaced by phasing the chip output with the CLK. Threshold adjustment is still kept. From the central/top area of the chip (see also Fig. 12.19-left) the channel wise *chip select* logical signals produced by FASP.02 when generating the flat-top are temporarily combined in a general *OR* to cope with the triggered DAQ used in tests. The chip-wise  $\text{REQ}$  signal can be used for self triggered data acquisition (see e.g. Sects. 12.3.1.1 or 12.3.2.1).

#### 12.4.4.2 Free running DAQ

The CBM-DAQ is foreseen to operate in a free streaming regime. In order to connect the FEB housing the FASP to such system two Free Running Data Acquisition (frDAQ) system prototypes were developed. The first, based on the Virtex-6 FPGA ML605 Evaluation Kit, (see Fig. 12.26-left) [C<sup>+</sup>13b] was used to operate FEBs based on FASP.01. The signals delivered by the ROC prototypes were amplified on the FEB [C<sup>0</sup>7, C<sup>+</sup>10] and transported via twisted

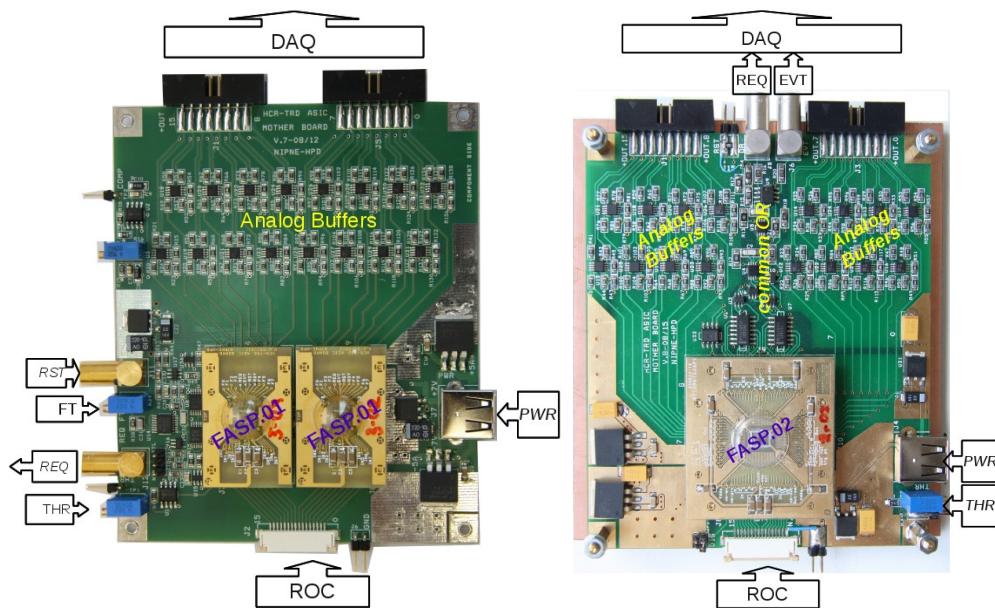


Figure 12.25: Two FEB versions for housing FASP ASICs and their *in/out/ctrl* functions with 2 FASP.01 chips (left) and 1 FASP.02 (right).

pair cable to fast MAX1434 ADCs. The MAX1434 is a 10-bit analog-to-digital converter which features fully differential inputs, a pipelined architecture and digital error correction incorporating a fully differential signal path. The MAX1434 offers a maximum sample rate of 50 Msps.

The system was successfully tested in the in-beam test campaigns at CERN-PS. A sync signal delivered by the triggered MBS-DAQ (Multi-Branch Data Acquisition System) was used to correlate the data delivered by the MAX1434 ADC with those delivered by the converters incorporated in the MBS system (mainly QDC converters used to read external PID detectors like the lead glass and Cherenkov detectors).

Using only events measured in coincidence with the triggered MBS system one can access PID information from external detectors. Such correlations are shown in Fig. 12.27 where the pulse height spectra reconstructed using frDAQ system for electrons and pions tagged events are shown for 1 GeV/ $c$  and 1.5 GeV/ $c$ . Similar performance plots for the triggered systems are presented in Sect. 12.2.3. In spite of qualitative differences between the two DAQ systems, which are due also to different measuring conditions like different types of radiators and particle momenta, we conclude that frDAQ can well operate the FASP.01.

Based on these results, a more elaborated frDAQ system using four *Spartan 6* (SP601) evaluation boards and a custom designed motherboard for analogue conversion with 2 Msps and 12 bits MAX11105 ADCs [Int16, INC16] was developed (see Fig. 12.26-right), which can operate up to 128 readout channels. The MAX11105 analog converters are foreseen to be implemented in a later stage in a hybrid upgraded version of FASP and thus this represent a good test for farther integrations. The main tasks assumed by the system are: data unpacking from the  $2 \times 32$  MAX11105 and time synchronization management, synchronization with the triggered MBS DAQ via a  $MBS_{sync}$  signal, data packing and transmission via UDP protocol. The correlated information from the two DAQ systems can be used to perform analysis as e.g. suggested in Fig. 12.27.

The system was tested during the CERN-SPS tests of 30 AGeV Pb+Pb collisions (see Sect. 12.3.1.3). In Fig. 12.28 a qualitative representation of  $\approx 500 \mu s$  of data taking is shown. For each marker on the time axis (vertical red/blue lines) representing the acquisition time measured with 10 ns precision by the system a sketch of the data registered by two acquisition boards is

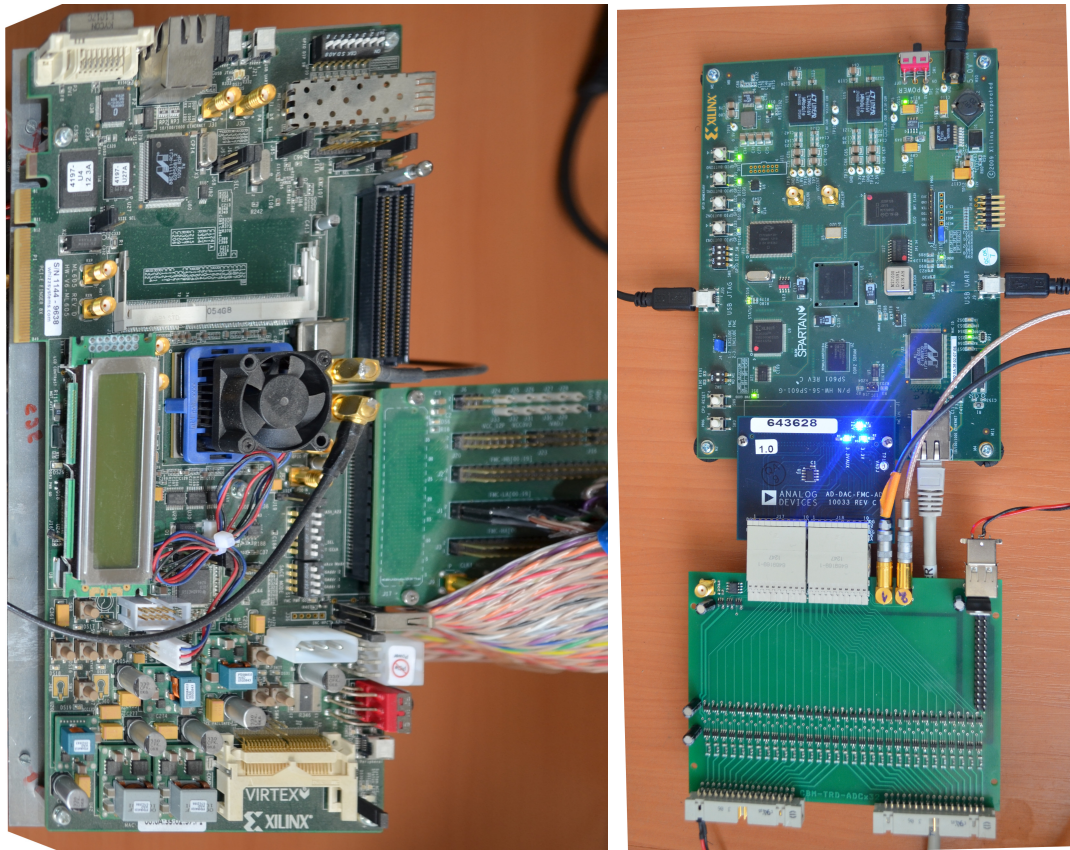


Figure 12.26: Free Running DAQ system based on Virtex-6 FPGA ML605 Evaluation Kit (left) and Spartan 6, SP601 evaluation board (right).

shown. The amount of charge collected on each rectangular column is proportional to the size of the rectangle in the sketch and its position within the detector is indicated by the *row-col* axis on each plot. Since one Spartan board was used to read out one row of eight columns, events having data simultaneously in two rows represent synchronous events between the two acquisition boards. For clarity such events are displayed in red while the single board/row are drawn in blue. From the distribution of signal between adjacent columns one can nicely identify clusters with the right shape and size. Due to the limitations of the FASP.02 FEB design (see Sect. 12.4.4.1) the acquisition was triggered by the REQ signal of one chip (i.e. 16 electronic channels). Such limitations obscure eventual pile-ups in the detector and large signals such as that produced at  $t \approx 180 \mu\text{s}$  (see Fig. 12.28) are hard to disentangle. The next generation of FEB-frDAQ systems will deal with individual *CS* signals (see Fig. 12.19-left) and thus overcoming current limitations. A more detailed analysis is under preparation based on the 30 AGeV Pb+Pb data and in-house tests with high rate X-ray tube illumination of full detector surface.

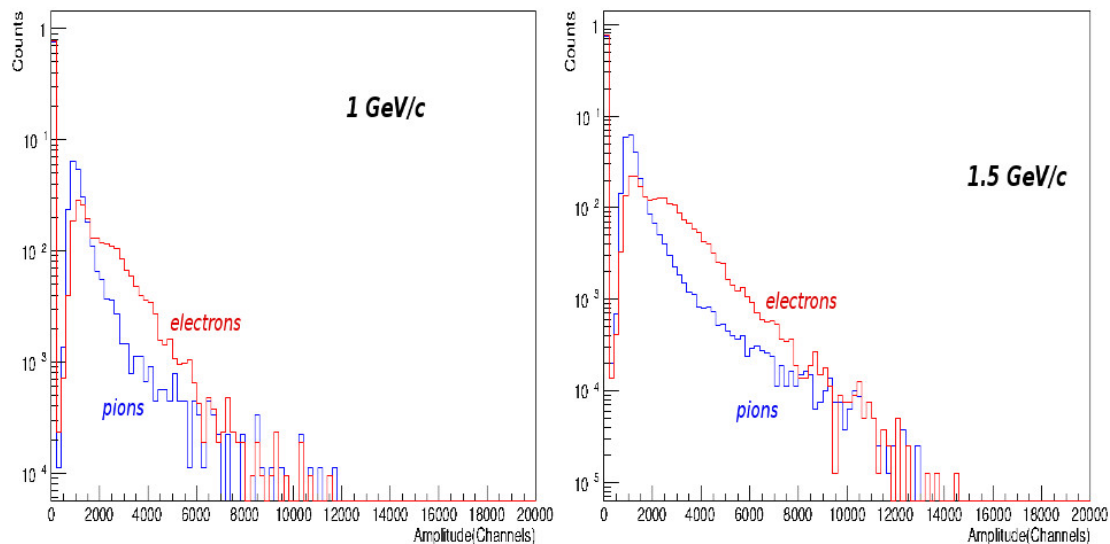


Figure 12.27: The pulse height distribution of electrons and pions of 1 GeV/c (left) and 1.5 GeV/c (right) momenta using a SSTRD prototype described in Sect. 12.2.3 coupled with a fiber radiator.

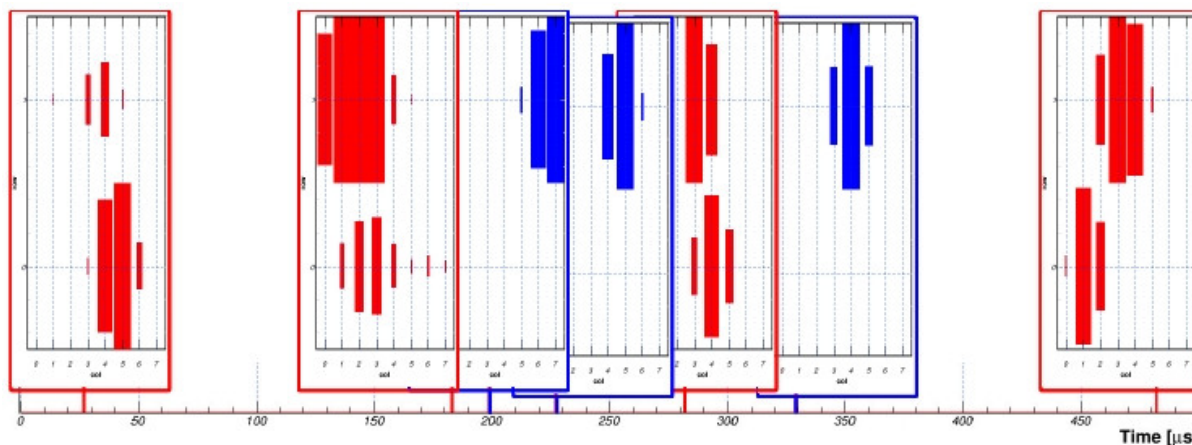


Figure 12.28: Time evolution of TRD events measured on 2 rows  $\times$  8 cols with one Spartan board/row synchronized with a 100 MHz clock; synchronous single row events in red, single row events in blue. The event acquisition time is marked on the horizontal axis in units of 10  $\mu$ s.

## 12.5 Fast ROC design

The ROCs situated closer to the beam axis will be exposed to very high hit rates. In order to be able to separate different hits in time direction a fast signal collection in the MWPCs is mandatory. Since the drift region, as foreseen in the baseline design of the CBM-TRD, contributes substantially to the overall time needed to collect the deposited charge, a faster design might be necessary for the inner chambers in order to avoid overlaps between hits from different events. This would in particular apply to the situation at the SIS300 where the interaction rates will be much higher than at the SIS100. Therefore, a fast MWPC prototype was investigated by the groups in Frankfurt and GSI, which consists only of an amplification region. This simplified design allows electron drift times below  $0.15\ \mu\text{s}$  and can thus be considered as an alternative option for the innermost chambers in an upgrade scenario for the SIS300.

The following sections describe conceptual design ideas, the mechanical layout of the detector, the mechanical simulation of the entrance window and its construction, as well as electrostatic simulations and laboratory measurements with an  $^{55}\text{Fe}$  source.

### 12.5.1 Conceptual chamber design

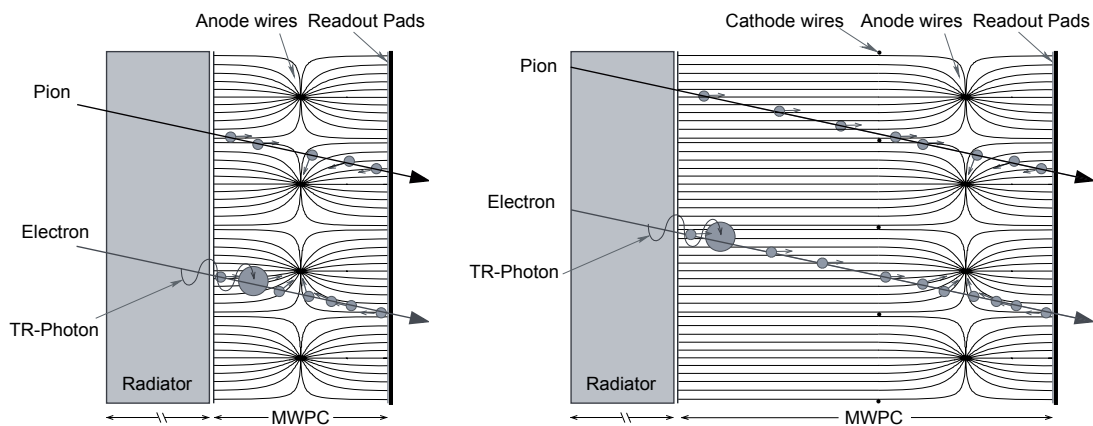


Figure 12.29: Sketch of a TRD without (left) and with additional drift region (right). The fast TRD design corresponds to the setup without drift region.

Figure 12.29 shows in the left panel a cross section of the fast TRD design. It consists, from left to right, of a radiator, the entrance window, the gas region with only one wire plane, and the pad plane. To minimize the absorption probability for the incoming particles and especially TR-photons, only a thin aluminized Mylar or Kapton foil serves as entrance window of the detector and as a cathode for the electric field, similar as in the baseline TRD design. The main advantages of the fast TRD are the following:

- The reduced thickness of the MWPC and the omission of an additional drift region will allow for a very fast signal collection time (the electron drift times are below  $0.15\ \mu\text{s}$ ).
- The construction of this type of MWPCs will be much simpler, since only a single wire plane needs to be prepared for each chamber.

On the other hand, this concept will introduce some complications that need to be addressed if this design is to be used in the final experimental setup:

- Deformations of the entrance window will cause significant gain instabilities, since the electric field in the amplification region is directly coupled to the window foil.

- Due to the reduced thickness the absorption probability for TR-photons might be lower than in the baseline design, possibly causing a reduced electron identification performance.
- The pad response cannot easily be chosen independently from the MWPC thickness in a symmetric layout, i.e. with the anode wire plane in the middle between the cathodes. However, this can be achieved by using an asymmetric configuration.

The in-beam and laboratory tests described below were therefore aiming at determining the level of performance which can be achieved with this kind of design and whether a stable operation within the experiment will be possible. On one side, it is necessary to establish that this approach will not compromise the PID capabilities and the position resolution. On the other side, methods need to be developed that stabilize the gas gain during detector operation as much as possible, such that the need for additional calibration efforts is minimized.

### 12.5.2 Layout of the fast TRD prototype

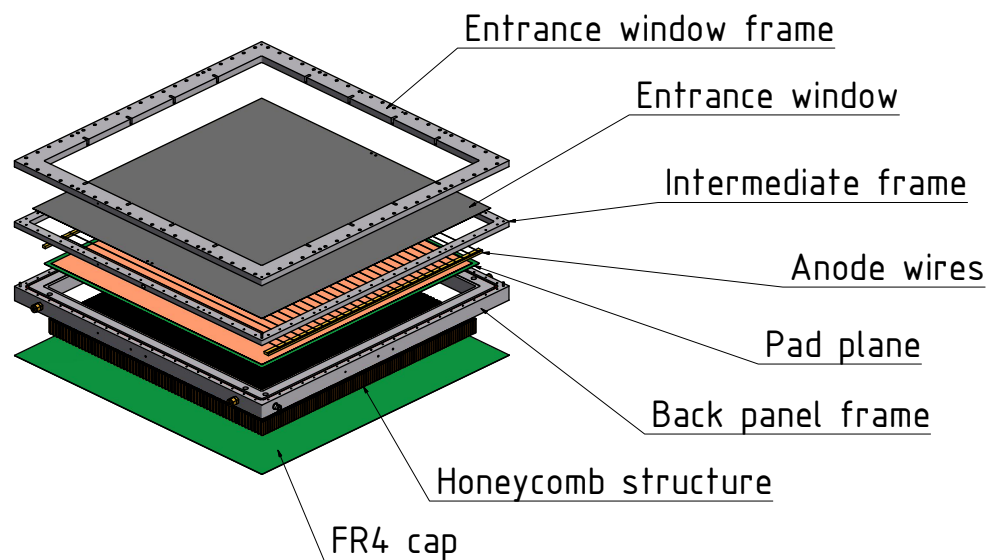


Figure 12.30: Technical drawing of a fast TRD prototype as used during the 2012 test beam at the CERN-PS. Its inner dimensions are  $59 \times 59 \text{ cm}^2$ , which thus correspond to the full size of an inner TRD module.

Figure 12.30 displays a technical drawing of a fast TRD prototype. Two of these prototypes with dimensions corresponding to the final envisaged size of the inner TRD modules have been tested during the 2012 test beam at the CERN-PS. They are constructed in a modular way in order to be able to easily modify the setup, e.g. by replacing the wire plane by different designs. Therefore, the outer frame was made from aluminum so that it can be dismantled and reassembled quickly. The backpanel is a composite structure of the pad plane PCB, a honeycomb layer, and an outer layer made of the glass-reinforced epoxy material FR4.

A cross section of the prototype is shown in Fig. 12.31. Visible is the aluminum frame, the wire plane and the honeycomb structure of the backpanel. The prototypes were designed in two different configurations: in one case a 4 mm distance between the wire plane and the entrance window, respectively the pad plane was chosen (“4+4”), in the other case it was 5 mm (“5+5”). The wire pitch was in both cases 2.5 mm. The thickness of the honeycomb structure was 30 mm. The total thickness of the chamber prototype, including the aluminum frame, was 55.2 mm for the 5+5 version (53.2 mm for the 4+4 type).

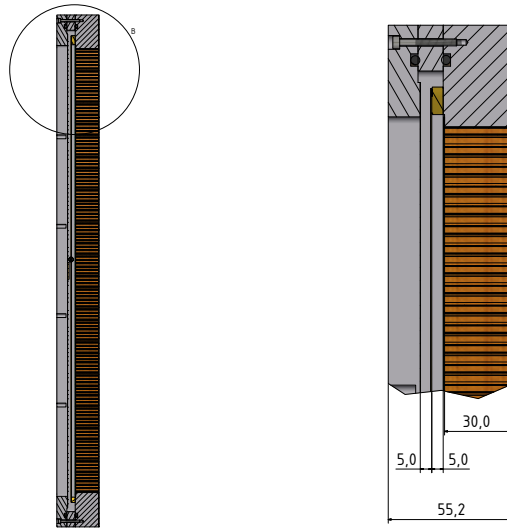


Figure 12.31: Cross section of the fast TRD prototype in the 5+5 mm configuration.

### 12.5.3 Electrostatic simulations

For the above described MWPC design several simulations of the electric field configuration, of the drift time distributions, and of the gas gain variations have been performed [Hel13] using the GARFIELD program [Vee98]. Figure 12.32 shows the calculated field configuration for the 4+4 type MWPC.

The electron drift times for the fast TRD design are displayed in Fig. 12.33 for the 4+4 and 5+5 type MWPCs at nominal anode voltages ( $U_A = 1940$  V (4+4) and  $U_A = 2220$  V (5+5)). For these chamber types electron arrival times averaged over one drift cell of  $\langle t_D \rangle = 0.054$   $\mu\text{s}$  (4+4) and  $\langle t_D \rangle = 0.065$   $\mu\text{s}$  (5+5) are obtained. In both cases the maximum arrival time does not significantly exceed 0.12  $\mu\text{s}$  (see also left panel of Fig. 12.39). This means that the maximal signal collection time for the fast TRD will be significantly less than the one achievable for a MWPC with an additional drift region of 4 mm thickness (corresponding to 0.16  $\mu\text{s}$  electron drift time).

The other important aspect that has been addressed with GARFIELD simulations is the variation of the gas gain. Figure 12.34 shows the local variations inside a given drift cell, due to the different drift paths of the electrons. For the 4+4 MWPC with Xe/CO<sub>2</sub> (80/20) gas mixture and an anode voltage of  $U_A = 1940$  V an averaged gain factor of  $\langle G \rangle = 2224$  is obtained (5+5 MWPC:  $\langle G \rangle = 2227$  at  $U_A = 2220$  V). The dependence of the gain factors on the applied anode voltages is summarized in the left panel of Fig. 12.35.

The main disadvantage of the fast TRD design is the strong sensitivity of the field in the amplification region to deformations of the cathode foil. Due to changes in the difference between the internal and the ambient pressure, the foil can deform and therefore the distance between the anode wire plane and the cathode changes. To quantify this effect, simulations have been repeated for different distances between cathode foil and wire plane and the relative change of the gas gain determined. As shown in the right panel of Fig. 12.35, a variation of the distance by 100  $\mu\text{m}$  will cause a change of the gas gain by about 10 %.

### 12.5.4 Simulations and measurements of the gain stability

From the electrostatic simulations described in the previous section follows that any deformation of the entrance window will directly affect the gas gain. In order to limit these deformations

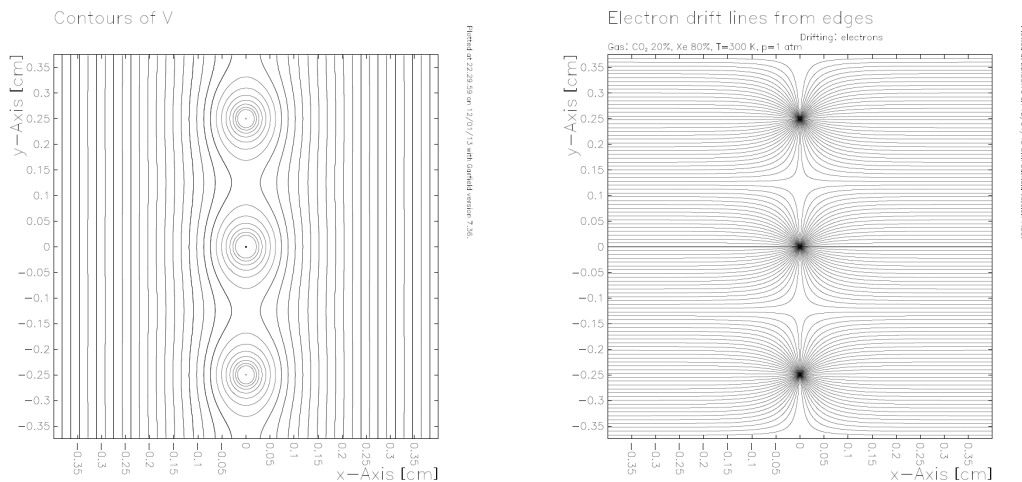


Figure 12.32: Lines of constant potential (left) and electron drift lines (right), as calculated with GARFIELD [Vee98, Hel13] for the 4+4 prototype with a wire pitch of 2.5 mm at an anode voltage of  $U = 1940$  V.

to a tolerable level, the pressure difference will have to be kept as constant as possible, which would require a corresponding performance of the gas system. In order to obtain a relation of the simulated gas gain change at a given deformation to a pressure difference measurements of the behavior of stretched foils have been performed and compared to calculations [Reu13].

The calculations have been done with the finite-elements program ABAQUS [Gmb13] and are based on the corresponding elasticity modulus and thickness of the used Mylar foil. The left panel of Fig. 12.36 shows the resulting deformation pattern of a stretched  $60 \times 60$  cm<sup>2</sup> foil, if a pressure difference of 250  $\mu$ bar is applied. For a pressure difference of 100  $\mu$ bar the maximal deformation at the center of the foil was calculated to be  $1.55 \pm 0.16$  mm. The simulation results were cross checked by a measurement on a real size Mylar foil window (see right panel of Fig. 12.36) and a very good agreement was found for pressure differences below 250  $\mu$ bar. Based on these results the spatial distribution of the foil deformation can also be calculated in advance within some uncertainty and will thus allow to generate a map of gain distortions as a function of position and pressure difference. This map could then be used in online and offline calibration procedures.

Combining these results with the electrostatic simulation described in the previous section (12.5.3) leads to the conclusion that already a pressure difference of 10  $\mu$ bar, corresponding to the achieved stability of the gas system used for the HERMES-TRD [Thi96], might cause a maximal relative change of the gain factors of more than 10%. As a consequence this fast MWPC design will result in time dependent residual gain variations of this order. In principle, these variations can be corrected by a corresponding calibration procedure, which can also make use of the simulated position dependence of the foil deformation as described above. However, it would be desirable to limit these variations by other means, in order to reduce the dependence on the calibration accuracy. One option is to stabilize the entrance foil by choosing a mechanically rigid radiator to be placed directly in front of it. First laboratory tests with an <sup>55</sup>Fe source have shown that this approach allows to significantly reduce the gain variations [Bal13]. However,

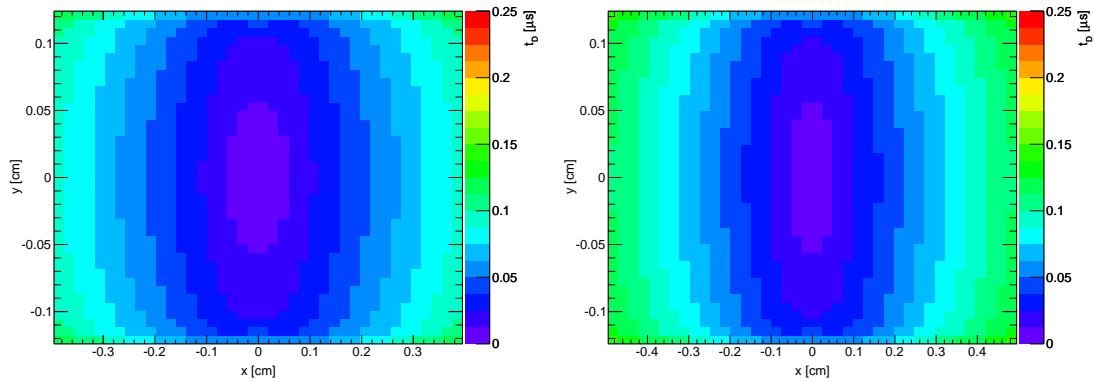


Figure 12.33: The electron arrival times in  $\mu\text{s}$  for a Xe/CO<sub>2</sub> (80/20) gas mixture. Shown are the drift times as a function of the position of the primary ionization relative to an anode wire for the 4+4 MWPC with  $U_A = 1940$  V (left) and the 5+5 version with  $U_A = 2220$  V (right).

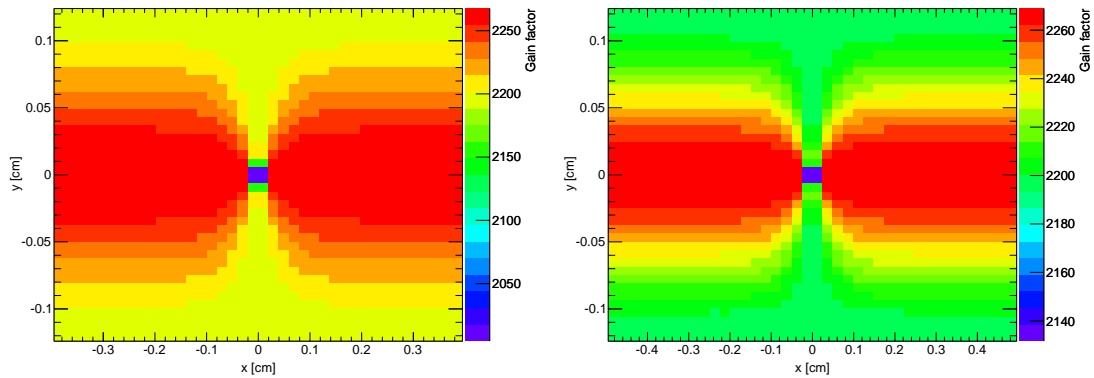


Figure 12.34: The spatial gas gain distribution for a Xe/CO<sub>2</sub> (80/20) gas mixture. Shown are the gain factors as a function of the position of the primary ionization relative to an anode wire for the 4+4 MWPC with  $U_A = 1940$  V (left) and the 5+5 version with  $U_A = 2220$  V (right).

since one would like to avoid glueing the entrance window foil to the radiation, as additional glue absorbs TR-photons, the mechanical support would only be provided in the case of an internal overpressure. Alternatively, the entrance window can be supported by a lattice grid, as foreseen for the baseline CBM-TRD. However, this configuration still does not prevent a bulging of the foil in the region between the ledges of the lattice which is larger in magnitude than required for the fast MWPC layout.

Another option, that has therefore been investigated, is the use of a special alternating high voltage configuration that reduces gain variations caused by mechanical deformations [VHK11]. GARFIELD simulations [Vee98, Hel13] show that this layout should be much less sensitive (see open symbols in the right panel of Fig. 12.35).

### 12.5.5 Fast prototype with alternating high voltage configuration

To study the effects of an alternating high voltage configuration on the gas gain stability, a small aluminum prototype with dimensions of  $21.8 \times 21.8 \text{ cm}^2$  has been built. Thin sense wires (Au-plated W,  $20 \mu\text{m}$  diameter) and thicker field wires (Cu-Be,  $79 \mu\text{m}$  diameter) are arranged on the anode plane with a pitch of  $2.5 \text{ mm}$ . A thin aluminized Mylar-foil ( $19 \mu\text{m}$  thickness) serves as front cathode and entrance window at the same time. A pad plane with readout pads of the size  $4.7 \times 49.7 \text{ mm}^2$  is used as rear cathode. Both, front and rear cathode, have a distance of  $4 \text{ mm}$  to

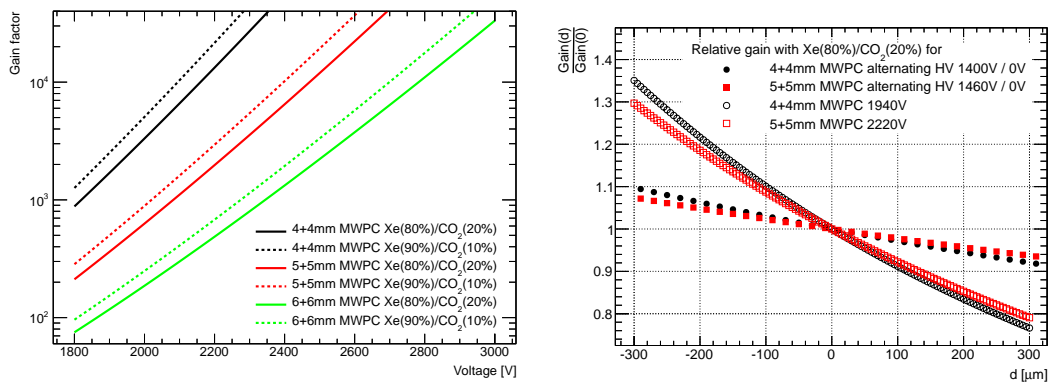


Figure 12.35: Left: the average gas gain factor as a function of the applied anode voltage. Shown are GARFIELD [Vee98] calculations for two different gas mixtures (Xe/CO<sub>2</sub> (80/20) and Xe/CO<sub>2</sub> (90/10)) and three different MWPC types (4+4, 5+5, 6+6) [Hel13]. Right: The relative gas gain factor as a function of the change of the anode-cathode distance  $d$  for a gas mixture Xe/CO<sub>2</sub> (80/20) for two MWPC types (4+4 and 5+5) [Are14]. Shown are the results with a regular wire and with an alternating wire plane.

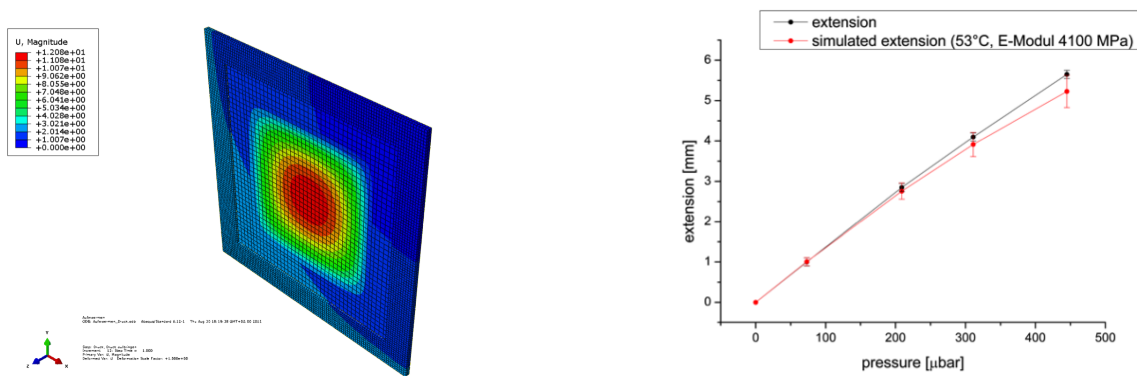


Figure 12.36: Left: calculated deformation of a stretched  $60 \times 60 \text{ cm}^2$  foil for a pressure difference of  $250 \mu\text{bar}$  [Reu13, Gmb13]. Right: comparison of the simulated deformation at the center of the foil to the measurement [Reu13].

the anode plane, leading to a total gas gap of 8 mm. Figure 12.37 shows the layout of the wire configuration and a sketch of the build prototype.

First measurements in a laboratory environment were performed with an  $^{55}\text{Fe}$  source [Glä01]. The sense wire current was measured for different positions at various differential pressures  $\Delta p$ . The field wires were for these tests set to ground potential, while the nominal anode voltages are 1400 V (4+4) and 1460 V (5+5). Standard prototypes without field wires and with similar dimensions were employed for reference measurements. The first tests give a clear indication for a superior performance in terms of gas gain stability for the new prototypes. The effect that the gas gain shows variations up to 60 % for an relative overpressure of  $\Delta p = 0.5 \text{ mbar}$ , as seen for the standard set up (left panel of Fig. 12.38), is drastically reduced for the setup with alternating wires (variations are below 10 %) as shown in the right panel of Fig. 12.38.

The differences in the electric field configurations between the standard prototype and the one with alternating wires cause also different electron drift times. These have also been calculated using the GARFIELD program [Vee98, Hel13, Glä01] and are compared in Fig. 12.39. The alternative configuration results in a distribution that is more peaked towards smaller times in

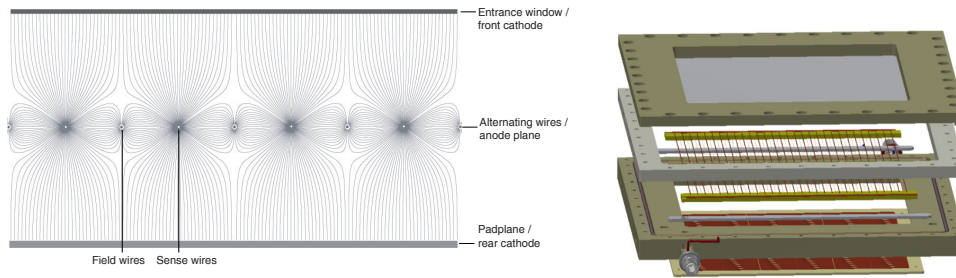


Figure 12.37: Prototype of a fast MWPC with alternating wire configuration. The left panel shows the wire layout together with the resulting electrical field lines. A sketch of the small size prototype is shown on the right.

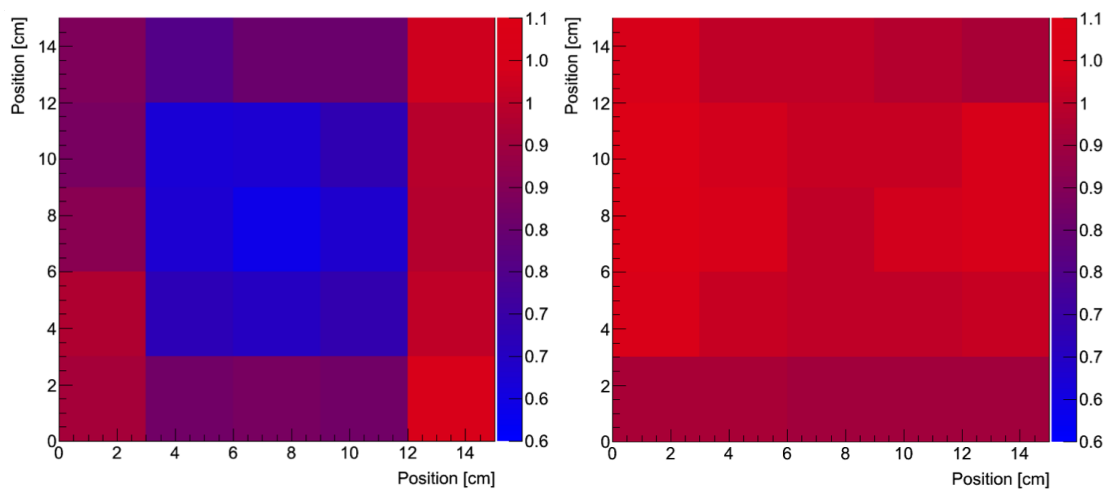


Figure 12.38: Comparison of the position dependent gas gain as measured in the laboratory with an  $^{55}\text{Fe}$  source on the anode wires for a relative overpressure of  $\Delta p = 0.5$  mbar (gas mixture: Ar/CO<sub>2</sub> (80/20)) [Glä01]. The left figure shows the result for the standard prototype, while on the right the measurement for the version with alternating wire configuration is shown.

comparison to the standard version, which exhibits a relatively flat time distribution. A potential disadvantage of the modified version is the slightly longer tail in the distribution for drift times above 150 ns. However, the fraction of the signal contained in the tail above times of 0.12  $\mu\text{s}$  is below 20 %.

### 12.5.6 Test beam performance

Due to the thinner gas volume of the fast MWPC in comparison to the baseline design with additional drift region, the absorption of transition radiation photons might be reduced, resulting thus in a lower performance in terms of electron identification. Therefore this was investigated with the full size (i.e.  $57 \times 57 \text{ cm}^2$ ) prototypes of the readout chambers with standard wire plane layout (without alternating HV) in combination with different radiator types at the CERN-PS test beam [Are14]. Figure 12.40 summarizes the results for the thinnest prototype (4+4 mm). Using a regular foil stack radiator (250 foils with 0.7 mm distance) a fraction of misidentified pions of  $\sim 0.1\%$  can be achieved. This radiator type provides a reference for a comparison to the baseline readout chamber type, where this radiator yielded a slightly better pion efficiency ( $\sim 0.05\%$ ). Still, the degradation is not dramatic and illustrates that also the thinner fast prototypes would provide a viable option for the inner readout chambers. Also with a foam type

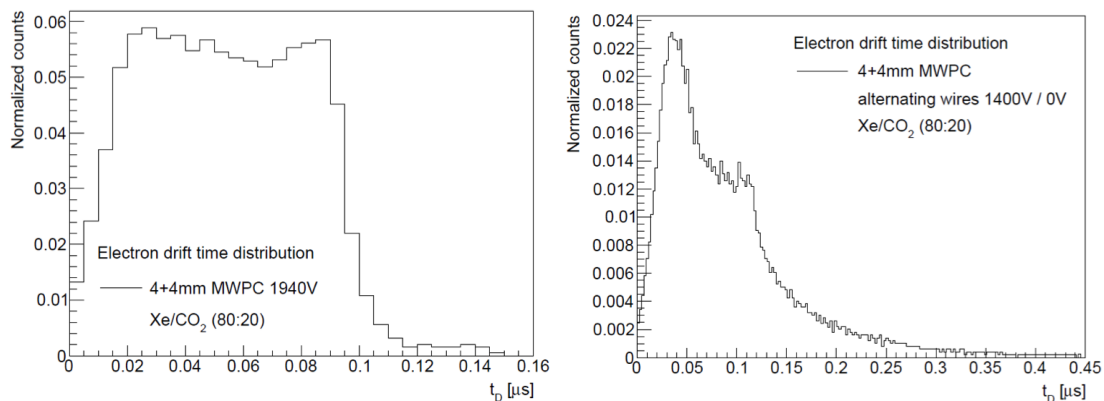


Figure 12.39: The signal collection times as simulated with GARFIELD. The distribution on the left has been calculated for the standard prototype, while the one on the right is for the one with alternating wire configuration.

radiator (labeled “R002” in Fig. 12.40) a sufficient performance exceeding the design goal for ten layers can be achieved. This radiator type is a relatively solid PE foam with a material thickness of  $\sim 12\ \mu\text{m}$  and an average bubble size of  $600\ \mu\text{m}$ .

Figure 12.41 shows the measured pad response functions for the fast MWPC prototypes. They are compared to the expectation from the Mathieson formula (Eq. 9.1) for the corresponding parameters for anode wire pitch, wire diameter and distances between wire and cathode plane. The curves are quite close to the measurements, although the agreement is not perfect. The discrepancies are on one side due to the fact that the used pad plane was not optimized for the dimensions of the MWPC layout, and on the other side due to deformations of the entrance window foil causing distortions in the electric field.

### 12.5.7 Conclusion on the fast MWPC prototype

In summary, the fast readout chamber concept provides a viable option in the case that the hit rates will turn out to be too high for the usage of chambers with drift region in the inner sectors, in particular for an operation at the SIS300. Its higher sensitivity to gain variations can to a large extent be reduced by a wire configuration with alternating high voltages, while the remaining variations will have to be adjusted by a time-dependent gain calibration procedure (see Sect. 9.4). The achievable performance of the fast MWPCs in terms of electron identification and position resolution are only slightly worse than the baseline solution. A detailed study with a full time based simulation, including all the known detector responses, for a high interaction rate heavy-ion scenario with continuous readout will have to be performed to assess whether a replacement of inner chambers needs to be done for future detector upgrades.

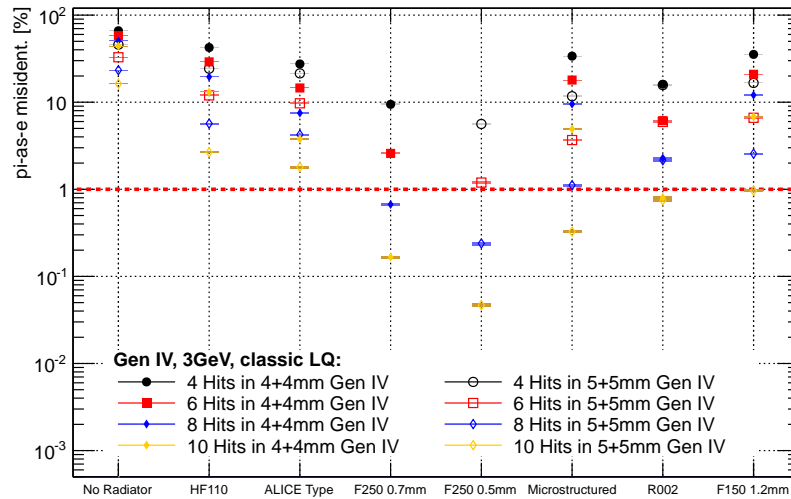


Figure 12.40: The fraction of pions misidentified as electrons measured in test beams at the CERN-PS at a beam momentum of  $3\text{ GeV}/c$ . The data are for prototypes with 4+4 mm and 5+5 mm thickness. Shown are results for different radiator types obtained with likelihood method (LQ), extrapolated to different number of layers [Are14].

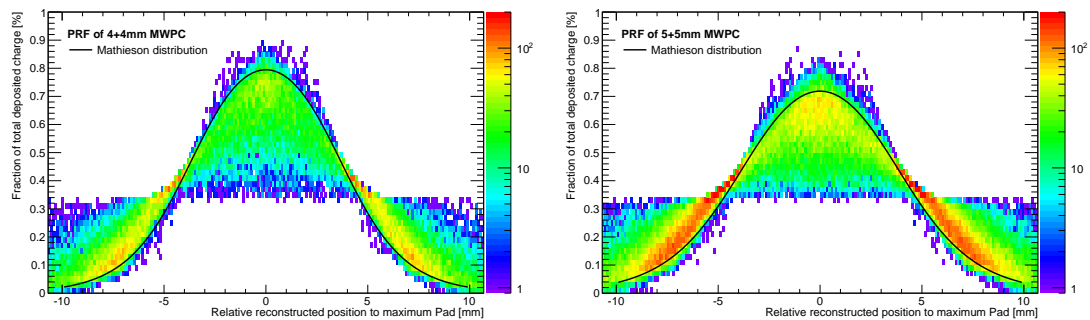


Figure 12.41: The pad response function as measured in test beams at the CERN-PS as a beam momentum of  $3\text{ GeV}/c$  [Are14]. Shown are results for the 4+4 (left) and 5+5 (right) prototype. The data are compared to calculations with the Mathieson formula (Eq. 9.1), shown as solid lines.

## Appendix A

# The CBM Collaboration

T. Ablyazimov<sup>1</sup>, A. Abuhoza<sup>2,61</sup>, R.P. Adak<sup>3</sup>, M. Adamczyk<sup>4</sup>, K. Agarwal<sup>5</sup>, M.M. Aggarwal<sup>6</sup>, F. Ahmad<sup>7</sup>, N. Ahmad<sup>8</sup>, S. Ahmad<sup>7</sup>, A. Akindinov<sup>9</sup>, P. Akishin<sup>1</sup>, E. Akishina<sup>1</sup>, T. Akishina<sup>1</sup>, V. Akishina<sup>10,1,2</sup>, A. Akram<sup>11</sup>, M. Al-Turany<sup>2</sup>, I. Alekseev<sup>9</sup>, E. Alexandrov<sup>1</sup>, I. Alexandrov<sup>1</sup>, S. Amar-Youcef<sup>12</sup>, M. Anđelić<sup>13</sup>, O. Andreeva<sup>14</sup>, C. Andrei<sup>15</sup>, A. Andronic<sup>2</sup>, Yu. Anisimov<sup>16</sup>, H. Appelshäuser<sup>12</sup>, D. Argintaru<sup>17</sup>, E. Atkin<sup>18</sup>, S. Avdeev<sup>16</sup>, R. Averbek<sup>2</sup>, M.D. Azmi<sup>8</sup>, V. Baban<sup>17</sup>, E. Badura<sup>2</sup>, S. Bähr<sup>19</sup>, T. Balog<sup>2</sup>, M. Balzer<sup>19</sup>, S. Bandyopadhyay<sup>20</sup>, E. Bao<sup>11</sup>, N. Baranova<sup>21</sup>, D. Bartos<sup>15</sup>, S. Bashir<sup>7</sup>, M. Baszczyk<sup>22</sup>, O. Batenkov<sup>23</sup>, V. Baublis<sup>24</sup>, M. Baznat<sup>16</sup>, J. Becker<sup>19</sup>, K.-H. Becker<sup>25</sup>, S. Belogurov<sup>1</sup>, A. Belousov<sup>10</sup>, D. Belyakov<sup>1</sup>, J. Bendarouach<sup>26</sup>, I. Berceanu<sup>15</sup>, A. Bercuci<sup>15</sup>, A. Berdnikov<sup>27</sup>, Y. Berdnikov<sup>27</sup>, R. Berendes<sup>28</sup>, G. Berezin<sup>16</sup>, C. Bergmann<sup>28</sup>, D. Bertini<sup>2</sup>, O. Bertini<sup>2</sup>, C. Beşliu<sup>17</sup>, O. Bezshyyko<sup>29</sup>, P.P. Bhaduri<sup>2,30</sup>, A. Bhasin<sup>31</sup>, A.K. Bhati<sup>6</sup>, B. Bhattacharjee<sup>32</sup>, A. Bhattacharyya<sup>20</sup>, T.K. Bhattacharyya<sup>33</sup>, S. Biswas<sup>3</sup>, T. Blank<sup>19</sup>, D. Blau<sup>34</sup>, V. Blinov<sup>2</sup>, C. Blume<sup>12</sup>, Yu. Bocharov<sup>18</sup>, J. Book<sup>12</sup>, J. Brzychczyk<sup>4</sup>, A. Bubak<sup>35</sup>, T. Bus<sup>12</sup>, V. Butuzov<sup>18</sup>, A. Bychkov<sup>16</sup>, A. Byszuk<sup>36</sup>, M. Călin<sup>17</sup>, Ping Cao<sup>37</sup>, G. Caragheorgheopol<sup>15</sup>, I. Carević<sup>13</sup>, V. Cătănescu<sup>15</sup>, A. Chakrabarti<sup>20</sup>, Sanatan Chattopadhyay<sup>20</sup>, Subhasis Chattopadhyay<sup>30,3</sup>, A. Chaus<sup>38</sup>, Jianping Cheng<sup>39</sup>, V. Chepurinov<sup>16</sup>, H. Cherif<sup>12,2</sup>, A. Chernogorov<sup>9</sup>, M.I. Ciobanu<sup>2,62</sup>, G. Claus<sup>40</sup>, F. Constantin<sup>15</sup>, M. Csanád<sup>41</sup>, Supriya Das<sup>3</sup>, Susovan Das<sup>5</sup>, J. de Cuveland<sup>10</sup>, B. Debnath<sup>32</sup>, D. Dementiev<sup>16</sup>, Wendi Deng<sup>42</sup>, Zhi Deng<sup>39</sup>, H. Deppe<sup>2</sup>, I. Deppner<sup>11</sup>, O. Derenovskaya<sup>1</sup>, C.A. Deveaux<sup>26</sup>, M. Deveaux<sup>12</sup>, K. Dey<sup>32</sup>, V. Dobyryn<sup>24</sup>, D. Doering<sup>12</sup>, Sheng Dong<sup>42</sup>, A. Dorokhov<sup>40</sup>, A. Drozd<sup>22</sup>, A.K. Dubey<sup>30</sup>, S. Dubnichka<sup>16</sup>, Z. Dubnichkova<sup>16</sup>, M. Dürr<sup>26</sup>, L. Dutka<sup>4</sup>, M. Dželalija<sup>13</sup>, V.V. Elsha<sup>16</sup>, D. Emschermann<sup>2</sup>, H. Engel<sup>43</sup>, V. Eremin<sup>44</sup>, T. Eşanu<sup>17</sup>, J. Eschke<sup>45,2</sup>, Xingming Fan<sup>46</sup>, O. Fateev<sup>16</sup>, Shengqin Feng<sup>47</sup>, S.P.D. Figuli<sup>19</sup>, I. Filozova<sup>1</sup>, D. Finogeev<sup>14</sup>, P. Fischer<sup>48</sup>, H. Flemming<sup>2</sup>, J. Förtsch<sup>25</sup>, U. Frankendorf<sup>2</sup>, V. Friese<sup>2</sup>, E. Friske<sup>5</sup>, I. Fröhlich<sup>12</sup>, J. Frühauf<sup>2</sup>, J. Gajda<sup>22</sup>, T. Galatyuk<sup>49,2</sup>, G. Gangopadhyay<sup>20</sup>, C. García Chávez<sup>43</sup>, J. Gebelein<sup>43</sup>, P. Ghosh<sup>12,2</sup>, S.K. Ghosh<sup>3</sup>, S. Gläsel<sup>12</sup>, M. Goffe<sup>40</sup>, L. Golinka-Bezshyyko<sup>29</sup>, V. Golovatyuk<sup>16</sup>, S. Golovnya<sup>50</sup>, V. Golovtsov<sup>24</sup>, M. Golubeva<sup>14</sup>, D. Golubkov<sup>9</sup>, A. Gómez Ramírez<sup>43</sup>, S. Gorbunov<sup>10</sup>, S. Gorokhov<sup>50</sup>, D. Gottschalk<sup>11</sup>, P. Gryboś<sup>22</sup>, F. Guber<sup>14</sup>, K. Gudima<sup>16</sup>, M. Gumiński<sup>36</sup>, A. Gupta<sup>31</sup>, Yu. Gusakov<sup>16</sup>, Dong Han<sup>39</sup>, H. Hartmann<sup>10</sup>, J. Hehner<sup>2</sup>, N. Heine<sup>28</sup>, A. Herghelegiu<sup>15</sup>, N. Herrmann<sup>11</sup>, B. Heß<sup>5</sup>, J.M. Heuser<sup>2</sup>, A. Himmi<sup>40</sup>, C. Höhne<sup>26</sup>, R. Holzmann<sup>2</sup>, Dongdong Hu<sup>37</sup>, Guangming Huang<sup>42</sup>, Xinjie Huang<sup>39</sup>, D. Hutter<sup>10</sup>, A. Ierusalimov<sup>16</sup>, M. Irfan<sup>8</sup>, D. Ivanishev<sup>24</sup>, M. Ivanov<sup>2</sup>, P. Ivanov<sup>18</sup>, Valery Ivanov<sup>1</sup>, Victor Ivanov<sup>1</sup>, Vladimir Ivanov<sup>24,18</sup>, A. Ivashkin<sup>14</sup>, K. Jaaskelainen<sup>40</sup>, H. Jahan<sup>8</sup>, V. Jain<sup>30</sup>, V. Jakovlev<sup>23</sup>, T. Janson<sup>43</sup>, Di Jiang<sup>37</sup>, A. Jipa<sup>17</sup>, I. Kadenko<sup>29</sup>, P. Kähler<sup>28</sup>, B. Kämpfer<sup>46,63</sup>, V. Kalinin<sup>23</sup>, J. Kallunkathariyil<sup>4</sup>, K.-H. Kampert<sup>25</sup>, E. Kaptur<sup>35</sup>, R. Karabowicz<sup>2</sup>, D. Karmanov<sup>21</sup>, V. Karnaukhov<sup>16</sup>, K. Kasiński<sup>22</sup>, G. Kasprowicz<sup>36</sup>, M. Kaur<sup>6</sup>, A. Kazantsev<sup>34</sup>, U. Keschull<sup>43</sup>, G. Kekelidze<sup>16</sup>, M.M. Khan<sup>8</sup>, A. Khanzadeev<sup>24,18</sup>, F. Khasanov<sup>9</sup>, A. Khvorostukhin<sup>16</sup>, V. Kirakosyan<sup>16</sup>,

A. Kiryakov<sup>50</sup>, M. Kiš<sup>2</sup>, I. Kisel<sup>10</sup>, P. Kisel<sup>12,2,1</sup>, S. Kiselev<sup>9</sup>, T. Kiss<sup>51</sup>, P. Klaus<sup>12</sup>, R. Kłeczek<sup>22</sup>,  
 Ch. Klein-Bösing<sup>28</sup>, V. Kleipa<sup>2</sup>, V. Klochkov<sup>2,12</sup>, P. Kmon<sup>22</sup>, K. Koch<sup>2</sup>, L. Kochenda<sup>24,18</sup>,  
 P. Koczoń<sup>2</sup>, M. Kohn<sup>28</sup>, B. Komkov<sup>24</sup>, M. Korolev<sup>21</sup>, I. Korolko<sup>9</sup>, R. Kotte<sup>46</sup>, A. Kovalchuk<sup>38</sup>,  
 S. Kowalski<sup>35</sup>, M. Koziel<sup>12</sup>, G. Kozlov<sup>10,1</sup>, V. Kozlov<sup>24</sup>, V. Kramarenko<sup>16</sup>, P. Kravtsov<sup>24,18</sup>,  
 E. Krebs<sup>12</sup>, I. Kres<sup>25</sup>, D. Kresan<sup>2</sup>, G. Kretschmar<sup>12</sup>, M. Krieger<sup>48</sup>, A.V. Kryanev<sup>1,18</sup>,  
 E. Kryshen<sup>24</sup>, M. Kuc<sup>52</sup>, W. Kucewicz<sup>22</sup>, V. Kucher<sup>10</sup>, L. Kudin<sup>24</sup>, A. Kugler<sup>53</sup>, A. Kumar<sup>30</sup>,  
 L. Kumar<sup>6</sup>, A. Kurepin<sup>14</sup>, N. Kurepin<sup>14</sup>, A. Kurilkin<sup>16</sup>, P. Kurilkin<sup>16</sup>, V. Kushpil<sup>53</sup>,  
 S. Kuznetsov<sup>16</sup>, V. Kyva<sup>38</sup>, V. Ladygin<sup>16</sup>, C. Lara<sup>43</sup>, P. Larionov<sup>12,2</sup>, A. Laso  
 García<sup>46,63</sup>, E. Lavrik<sup>5</sup>, I. Lazanu<sup>17</sup>, A. Lebedev<sup>2,1</sup>, S. Lebedev<sup>26,1</sup>, E. Lebedeva<sup>26</sup>, J. Lehnert<sup>2</sup>,  
 Y. Leifels<sup>2</sup>, Qiyang Li<sup>12,42</sup>, Xin Li<sup>37</sup>, Yuanjing Li<sup>39</sup>, V. Lindenstruth<sup>10,2</sup>, B. Linnik<sup>12</sup>, Feng Liu<sup>42</sup>,  
 I. Lobanov<sup>50</sup>, E. Lobanova<sup>50</sup>, S. Löchner<sup>2</sup>, P.-A. Loizeau<sup>2</sup>, S.A. Lone<sup>7</sup>, J.A. Lucio  
 Martínez<sup>43</sup>, Xiaofeng Luo<sup>42</sup>, A. Lymanets<sup>2,38</sup>, Pengfei Lyu<sup>39</sup>, A. Maevskaya<sup>14</sup>, S. Mahajan<sup>31</sup>,  
 T. Mahmoud<sup>26</sup>, P. Maj<sup>22</sup>, Z. Majka<sup>4</sup>, A. Malakhov<sup>16</sup>, E. Malankin<sup>18</sup>, D. Malkevich<sup>9</sup>,  
 O. Malyatina<sup>18</sup>, H. Malygina<sup>12,2,38</sup>, S. Mandal<sup>30</sup>, V. Manko<sup>34</sup>, A.M. Marin Garcia<sup>2</sup>, J. Markert<sup>2</sup>,  
 S. Masciocchi<sup>2</sup>, T. Matulewicz<sup>52</sup>, L. Meder<sup>19</sup>, M. Merkin<sup>21</sup>, V. Mialkovski<sup>16</sup>, J. Michel<sup>12</sup>,  
 N. Miftakhov<sup>24</sup>, L. Mik<sup>22</sup>, K. Mikhailov<sup>9</sup>, V. Mikhaylov<sup>53</sup>, V. Militsija<sup>38</sup>, M.F. Mir<sup>7</sup>,  
 D. Miskowicz<sup>2</sup>, I. Momot<sup>12,2,38</sup>, T. Morhardt<sup>2</sup>, S. Morozov<sup>14</sup>, W.F.J. Müller<sup>45,2</sup>, C. Müntz<sup>12</sup>,  
 S. Mukherjee<sup>3</sup>, C.E. Muñoz Castillo<sup>43</sup>, Yu. Murin<sup>16</sup>, C. Nandi<sup>30</sup>, E. Nandy<sup>30</sup>, L. Naumann<sup>46</sup>,  
 T. Nayak<sup>30</sup>, V.S. Negi<sup>30</sup>, W. Niebur<sup>2</sup>, V. Nikulin<sup>24</sup>, D. Normanov<sup>18</sup>, A. Oancea<sup>43</sup>, Kunsu Oh<sup>54</sup>,  
 Yu. Onishchuk<sup>29</sup>, G. Ososkov<sup>1</sup>, P. Otfinowski<sup>22</sup>, E. Ovcharenko<sup>1</sup>, S. Pal<sup>30</sup>, I. Panasenko<sup>5,38</sup>,  
 N.R. Panda<sup>55</sup>, S. Parzhitskiy<sup>16</sup>, V. Patel<sup>25</sup>, C. Pauly<sup>25</sup>, D. Peshekhonov<sup>16</sup>, V. Petráček<sup>56</sup>,  
 M. Petri<sup>12</sup>, M. Petriş<sup>15</sup>, A. Petrovici<sup>15</sup>, M. Petrovici<sup>15</sup>, A. Petrovskiy<sup>18</sup>, O. Petukhov<sup>14</sup>,  
 D. Pfeifer<sup>25</sup>, K. Piasecki<sup>52</sup>, J. Pietraszko<sup>2</sup>, R. Planeta<sup>4</sup>, V. Plotnikov<sup>9</sup>, V. Plujko<sup>29</sup>, J. Pluta<sup>36</sup>,  
 A. Pop<sup>15</sup>, B.V.K.S. Potukuchi<sup>31</sup>, K. Poźniak<sup>36,52</sup>, A. Prakash<sup>53</sup>, S.K. Prasad<sup>3</sup>, M. Prokudin<sup>9</sup>,  
 M. Pugach<sup>10,2,38</sup>, V. Pugatch<sup>38</sup>, S. Querchfeld<sup>25</sup>, L. Radulescu<sup>15</sup>, S. Raha<sup>3</sup>, W. Raja<sup>7</sup>, F. Rami<sup>40</sup>,  
 R. Raniwala<sup>57</sup>, S. Raniwala<sup>57</sup>, A. Raportirenko<sup>1</sup>, J. Rautenberg<sup>25</sup>, J. Rauza<sup>22</sup>, R. Ray<sup>3</sup>,  
 S. Razin<sup>16</sup>, S. Reinecke<sup>25</sup>, A. Reinefeld<sup>58</sup>, A. Reshetin<sup>14</sup>, C. Ristea<sup>17</sup>, O. Ristea<sup>17</sup>, A. Rodriguez  
 Rodriguez<sup>2</sup>, F. Roether<sup>12</sup>, R. Romaniuk<sup>36</sup>, A. Rost<sup>49</sup>, E. Rostchin<sup>24,18</sup>, I. Rostovtseva<sup>9</sup>,  
 J. Rożynek<sup>52</sup>, Yu. Ryabov<sup>24</sup>, R. Sahoo<sup>59</sup>, P.K. Sahu<sup>55</sup>, S.K. Sahu<sup>55</sup>, J. Saini<sup>30</sup>, S. Samanta<sup>3</sup>,  
 S.S. Sambyal<sup>31</sup>, V. Samsonov<sup>24,18,27</sup>, O. Sander<sup>19</sup>, S. Sarangi<sup>33</sup>, S. Sau<sup>20</sup>, C. Schiaua<sup>15</sup>,  
 F. Schintke<sup>58</sup>, C.J. Schmidt<sup>2</sup>, H.R. Schmidt<sup>5</sup>, J. Scholten<sup>12</sup>, K. Schweda<sup>2</sup>, F. Seck<sup>49</sup>, S. Seddiki<sup>2</sup>,  
 I. Selyuzhenkov<sup>2</sup>, A. Semennikov<sup>9</sup>, A. Senger<sup>2</sup>, P. Senger<sup>2,12</sup>, A. Shabanov<sup>14</sup>, A. Shabunov<sup>16</sup>,  
 Ming Shao<sup>37</sup>, A.D. Sheremetiev<sup>16</sup>, Shusu Shi<sup>42</sup>, N. Shumeiko<sup>16</sup>, V. Shumikhin<sup>18</sup>, I. Sibiryak<sup>34</sup>,  
 B. Sikora<sup>52</sup>, A. Simakov<sup>18</sup>, C. Simon<sup>11</sup>, C. Simons<sup>2</sup>, A.K. Singh<sup>33</sup>, B.K. Singh<sup>60</sup>, C.P. Singh<sup>60</sup>,  
 V. Singhal<sup>30</sup>, M. Singla<sup>2</sup>, P. Sitzmann<sup>12</sup>, K. Siwek-Wilczyńska<sup>52</sup>, L. Škoda<sup>56</sup>, I. Skwira-Chalot<sup>52</sup>,  
 I. Som<sup>33</sup>, Guofeng Song<sup>37</sup>, D. Soyk<sup>2</sup>, P. Staszal<sup>4</sup>, M. Strikhanov<sup>18</sup>, S. Strothauer<sup>12</sup>, J. Stroth<sup>12,2</sup>,  
 C. Sturm<sup>2</sup>, R. Sultanov<sup>9</sup>, Yongjie Sun<sup>37</sup>, D. Svirida<sup>9</sup>, O. Svoboda<sup>53</sup>, R. Szczygieł<sup>22</sup>, Zebo Tang<sup>37</sup>,  
 M. Tanha<sup>12</sup>, J. Tarasiuk<sup>52</sup>, O. Tarassenkova<sup>24</sup>, M.-G. Târzilă<sup>15</sup>, M. Teklishyn<sup>45,38</sup>, T. Tischler<sup>12</sup>,  
 P. Tlustý<sup>53</sup>, T. Tölyhi<sup>51</sup>, A. Toia<sup>2,12</sup>, N. Topil'skaya<sup>14</sup>, M. Träger<sup>2</sup>, I. Tsakov<sup>16</sup>, Yu. Tsyupa<sup>50</sup>,  
 N.G. Tutaras<sup>17</sup>, F. Uhlig<sup>2</sup>, E. Usenko<sup>14</sup>, I. Valin<sup>40</sup>, D. Varga<sup>51</sup>, I. Vassiliev<sup>2</sup>, O. Vasylyev<sup>2</sup>,  
 E. Verbitskaya<sup>44</sup>, A. Veshikov<sup>23</sup>, R. Visinka<sup>2</sup>, S. Volkov<sup>24</sup>, A. Volochniuk<sup>29</sup>, A. Vorobiev<sup>50</sup>,  
 Aleksey Voronin<sup>16</sup>, Alexander Voronin<sup>21</sup>, V. Vovchenko<sup>10</sup>, M. Vznuzdaev<sup>24</sup>, Dong Wang<sup>42</sup>,  
 Xi-Wei Wang<sup>47</sup>, Yi Wang<sup>39</sup>, M. Weber<sup>19</sup>, C. Wendisch<sup>2</sup>, J.P. Wessels<sup>28</sup>, M. Wiebusch<sup>12</sup>,  
 D. Wielanek<sup>36</sup>, A. Wieloch<sup>4</sup>, A. Wilms<sup>2</sup>, N. Winckler<sup>2</sup>, M. Winter<sup>40</sup>, K. Wiśniewski<sup>52</sup>,  
 Gy. Wolf<sup>51</sup>, Sanguk Won<sup>54</sup>, Ke-Jun Wu<sup>47</sup>, J. Wüstenfeld<sup>46</sup>, Changzhou Xiang<sup>42</sup>, Nu Xu<sup>42</sup>,  
 Junfeng Yang<sup>2,37</sup>, Rongxing Yang<sup>37</sup>, Zhongbao Yin<sup>42</sup>, In-Kwon Yoo<sup>54</sup>, B. Yuldashev<sup>16</sup>,  
 I. Yushmanov<sup>34</sup>, W. Zabolotny<sup>36,52</sup>, Yu. Zaitsev<sup>9</sup>, N.I. Zamiatin<sup>16</sup>, M. Zhalov<sup>24</sup>, Yifei Zhang<sup>37</sup>,  
 Lei Zhao<sup>37</sup>, Jiajun Zheng<sup>37</sup>, Sheng Zheng<sup>47</sup>, Daicui Zhou<sup>42</sup>, Jing Zhou<sup>47</sup>, Xianglei Zhu<sup>39</sup>,  
 A. Zinchenko<sup>16</sup>, M. Żoładź<sup>22</sup>, P. Zrelov<sup>1</sup>, V. Zryuev<sup>16</sup>, P. Zumbach<sup>2</sup>, M. Zyzak<sup>2</sup>

- <sup>1</sup>Laboratory of Information Technologies, Joint Institute for Nuclear Research (JINR-LIT),  
Dubna, Russia
- <sup>2</sup>GSI Helmholtzzentrum für Schwerionenforschung GmbH (GSI), Darmstadt, Germany
- <sup>3</sup>Department of Physics, Bose Institute, Kolkata, India
- <sup>4</sup>Marian Smoluchowski Institute of Physics, Jagiellonian University, Kraków, Poland
- <sup>5</sup>Physikalisches Institut, Eberhard Karls Universität Tübingen, Tübingen, Germany
- <sup>6</sup>Department of Physics, Panjab University, Chandigarh, India
- <sup>7</sup>Department of Physics, University of Kashmir, Srinagar, India
- <sup>8</sup>Department of Physics, Aligarh Muslim University, Aligarh, India
- <sup>9</sup>Institute for Theoretical and Experimental Physics (ITEP), Moscow, Russia
- <sup>10</sup>Frankfurt Institute for Advanced Studies, Goethe-Universität Frankfurt (FIAS), Frankfurt,  
Germany
- <sup>11</sup>Physikalisches Institut, Universität Heidelberg, Heidelberg, Germany
- <sup>12</sup>Institut für Kernphysik, Goethe-Universität Frankfurt, Frankfurt, Germany
- <sup>13</sup>University of Split, Split, Croatia
- <sup>14</sup>Institute for Nuclear Research (INR), Moscow, Russia
- <sup>15</sup>Horia Hulubei National Institute of Physics and Nuclear Engineering (IFIN-HH), Bucharest,  
Romania
- <sup>16</sup>Veksler and Baldin Laboratory of High Energy Physics, Joint Institute for Nuclear Research  
(JINR-VBLHEP), Dubna, Russia
- <sup>17</sup>Atomic and Nuclear Physics Department, University of Bucharest, Bucharest, Romania
- <sup>18</sup>National Research Nuclear University MEPhI, Moscow, Russia
- <sup>19</sup>Karlsruhe Institute of Technology (KIT), Karlsruhe, Germany
- <sup>20</sup>Department of Physics and Department of Electronic Science, University of Calcutta, Kolkata,  
India
- <sup>21</sup>Skobeltsyn Institute of Nuclear Physics, Lomonosov Moscow State University (SINP-MSU),  
Moscow, Russia
- <sup>22</sup>AGH University of Science and Technology (AGH), Kraków, Poland
- <sup>23</sup>V.G. Khlopin Radium Institute (KRI), St. Petersburg, Russia
- <sup>24</sup>National Research Center "Kurchatov Institute" B.P.Konstantinov, Petersburg Nuclear Physics  
Institute (PNPI), Gatchina, Russia
- <sup>25</sup>Fakultät für Mathematik und Naturwissenschaften, Bergische Universität Wuppertal,  
Wuppertal, Germany
- <sup>26</sup>Justus-Liebig-Universität Gießen, Gießen, Germany
- <sup>27</sup>St. Petersburg Polytechnic University (SPbPU), St. Petersburg, Russia
- <sup>28</sup>Institut für Kernphysik, Westfälische Wilhelms-Universität Münster, Münster, Germany
- <sup>29</sup>Department of Nuclear Physics, Taras Shevchenko National University of Kyiv, Kyiv, Ukraine
- <sup>30</sup>Variable Energy Cyclotron Centre (VECC), Kolkata, India
- <sup>31</sup>Department of Physics, University of Jammu, Jammu, India
- <sup>32</sup>Department of Physics, Gauhati University, Guwahati, India
- <sup>33</sup>Indian Institute of Technology Kharagpur, Kharagpur, India
- <sup>34</sup>National Research Centre "Kurchatov Institute", Moscow, Russia
- <sup>35</sup>Institute of Physics, University of Silesia, Katowice, Poland
- <sup>36</sup>Institute of Electronic Systems, Warsaw University of Technology, Warsaw, Poland
- <sup>37</sup>Department of Modern Physics, University of Science & Technology of China (USTC), Hefei,  
China
- <sup>38</sup>High Energy Physics Department, Kiev Institute for Nuclear Research (KINR), Kyiv, Ukraine
- <sup>39</sup>Department of Engineering Physics, Tsinghua University, Beijing, China
- <sup>40</sup>Institut Pluridisciplinaire Hubert Curien (IPHC), IN2P3-CNRS and Université de Strasbourg,  
Strasbourg, France

- <sup>41</sup>Eötvös Loránd University (ELTE), Budapest, Hungary
- <sup>42</sup>College of Physical Science and Technology, Central China Normal University (CCNU), Wuhan, China
- <sup>43</sup>Institute for Computer Science, Goethe-Universität Frankfurt, Frankfurt, Germany
- <sup>44</sup>Ioffe Institute, Russian Academy of Sciences, St. Petersburg, Russia
- <sup>45</sup>Facility for Antiproton and Ion Research in Europe GmbH (FAIR), Darmstadt, Germany
- <sup>46</sup>Institut für Strahlenphysik, Helmholtz-Zentrum Dresden-Rossendorf (HZDR), Dresden, Germany
- <sup>47</sup>College of Science, China Three Gorges University (CTGU), Yichang, China
- <sup>48</sup>Institut für Technische Informatik, Universität Heidelberg, Mannheim, Germany
- <sup>49</sup>Institut für Kernphysik, Technische Universität Darmstadt, Darmstadt, Germany
- <sup>50</sup>Institute for High Energy Physics (IHEP), Protvino, Russia
- <sup>51</sup>Institute for Particle and Nuclear Physics, Wigner Research Centre for Physics, Hungarian Academy of Sciences, Budapest, Hungary
- <sup>52</sup>Institute of Experimental Physics, University of Warsaw, Warsaw, Poland
- <sup>53</sup>Nuclear Physics Institute of the Czech Academy of Sciences, Řež, Czech Republic
- <sup>54</sup>Pusan National University (PNU), Pusan, Korea
- <sup>55</sup>Institute of Physics, Bhubaneswar, India
- <sup>56</sup>Czech Technical University (CTU), Prague, Czech Republic
- <sup>57</sup>Physics Department, University of Rajasthan, Jaipur, India
- <sup>58</sup>Konrad-Zuse-Zentrum für Informationstechnik Berlin (ZIB), Berlin, Germany
- <sup>59</sup>Indian Institute of Technology Indore, Indore, India
- <sup>60</sup>Department of Physics, Banaras Hindu University, Varanasi, India
- <sup>61</sup>also: King Abdulaziz City for Science and Technology (KACST), Riyadh, Saudi Arabia
- <sup>62</sup>also: Institute of Space Science, Bucharest, Romania
- <sup>63</sup>also: Technische Universität Dresden, Dresden, Germany

## Appendix B

### List of Acronyms

<b>A:</b>	ADC	Analog-to-Digital Converter
	AFCK	AMC FMC Carrier Kintex
	AGS	Alternating Gradient Synchrotron
	ALICE	A Large Ion Collider Experiment
	AMC	Advanced Mezzanine Card
	ANN	Artificial Neural Network
	ASIC	Application Specific Integrated Circuit
	AWRF	Anode Wire Response Function
<b>B:</b>	BDT	Boosted Decision Tree
	BNL	Brookhaven National Laboratory
	BR	Branching Ratio
<b>C:</b>	CBM	Compressed Baryonic Matter
	CERN	Conseil Européen pour la Recherche Nucléaire
	CF	Carbon Fibre
	CFRP	Carbon Fibre Reinforced Plastic
	CLK	CLock
	CPU	Central Processing Unit
	CRI	Common Readout Interface
	CSA	Charge Sensitive Amplifier
<b>D:</b>	DAQ	Data AcQuisition
	DCS	Detector Control System
	DPB	Data Processing Board
	DSP	Digital Signal Processor
	DSTRD	Double-Sided TRD
	DTW	Drift Time Window
<b>E:</b>	ECAL	Electromagnetic CALorimeter
	ECS	Experiment Control System

	ENC	Equivalent Noise Charge
	ENOB	Effective Number Of Bits
<b>F:</b>	FAIR	Facility of Antiproton and Ion Research
	FASP	Fast Analog Signal Processor
	FEB	Front-End Boards
	FEE	Front-End Electronic
	FIFO	First In First Out
	FLES	First Level Event Selector
	FLIB	FLES Interface Board
	FLIM	FLES Interface Module
	FMC	FPGA Mezzanine Card
	FNR	First Neighbor Readout
	FPGA	Field Programmable Gate Array
	FT	Flat Top
	FWHM	Full Width Half Maximum
<b>G:</b>	GBT	GigaBit Transceiver
	GEANT	GEometry ANd Tracking
	GEM	Gas Electron Multiplier
	GH	Glueing Hours
<b>H:</b>	HDMI	High-Definition Multimedia Interface
	HDL	Hardware Description Language
	HSD	Hadron String Dynamics
	HT	High Tension
	HV	High Voltage
<b>I:</b>	ID	IDentification
	IIR	Infinite Impulse Response
	IMR	Intermediate Mass Region
	ISO	International Organization for Standardization
<b>J:</b>	JINR	Joint Institute of Nuclear Research
<b>L:</b>	LFR	Likelihood Function Ratio
	LHC	Large Hadron Collider
	LQ	Likelihood derived from charge ( $Q$ ) measurement
	LS	Layer Support
	LV	Low Voltage
<b>M:</b>	MADC	Multiplexed Analog-to-Digital Converter
	MAPD	Multi-Avalanche Photo-Diodes
	MAPS	Monolithic Active Pixel Sensors

	MAPT	Multi-Anode Photomultiplier Tubes
	MBS	Multi Branch System
	MC	Monte Carlo
	MIP	Minimum Ionizing Particle
	MPO	Multi-fiber Push On connector
	MPV	Most Probable Value
	MRPC	Multi-gap Resistive Plate Chambers
	MSV	Modularized Start Version
	MUCH	MUon CHambers
	MVD	Micro Vertex Detector
	MWPC	Multi-Wire Proportional Chamber
<b>N:</b>	NICA	Nuclotron-based Ion Collider fAcility
	NIEL	Non-Ionizing Energy Loss
	NIST	National Institute of Standards and Technology
<b>P:</b>	PASA	Pre-Amplifier Shaping Amplifier
	PC	Power Consumption
	PCB	Printed Circuit Board
	PDF	Probability Density Function
	PE	PolyEthylene
	PID	Particle IDentification
	PMMA	PolyMethylMethAcrylate
	POB	POwer Boards
	PP	PolyPropylene
	PRF	Pad Response Function
	PS	Power Supply
		Proton Synchrotron
	PSD	Participant Spectator Detector
	PWR	PoWeR (USB socket)
<b>Q:</b>	QDC	Charge-to-Digital Converter
	QGP	Quark-Gluon Plasma
<b>R:</b>	RCT	Readout ConTroler
	REQ	REQuest signal
	RHIC	Relativistic Heavy-Ion Collider
	RICH	Ring Imaging CHerenkov
	RPC	Resistive Plate Chamber
	RST	ReSeT signal
	ROB	Read-Out Board
	ROC	Read-Out Chamber
<b>S:</b>	SIS	Schwer-Ionen Synchrotron

	SPADIC	Self-triggered Pulse Amplification and Digitization ASIC
	SPS	Super Proton Synchrotron
	SSTRD	Single-Sided TRD
	ST	Shaping Time
	STAR	Solenoidal Tracker At RHIC
	STS	Silicon Tracking System
<b>T:</b>	TFC	Timing and Flow Control system
	THR	THReshold
	TOF	Time-Of-Flight
	TR	Transition Radiation
	TRD	Transition Radiation Detector
	TTL	Transistor-Transistor Logic
<b>U:</b>	UDP	User Datagram Protocol
	UrQMD	Ultra-relativistic Quantum Molecular Dynamics
	UMC	United Microelectronics Corporation
	UV	Ultra-Violet
<b>V:</b>	VTR	Versatile TransReceiver
	VTT	Versatile Twin-Transmitter
<b>W:</b>	WH	Working Hours
	WHPD	Working Hour Per Day
	WHPW	Working Hour Per Week
	WLS	WaveLength Shifter
<b>X:</b>	XT	Cross-Talk
	XYTER	X-Y-Time-Energy Readout

## Appendix C

### Additional Figures

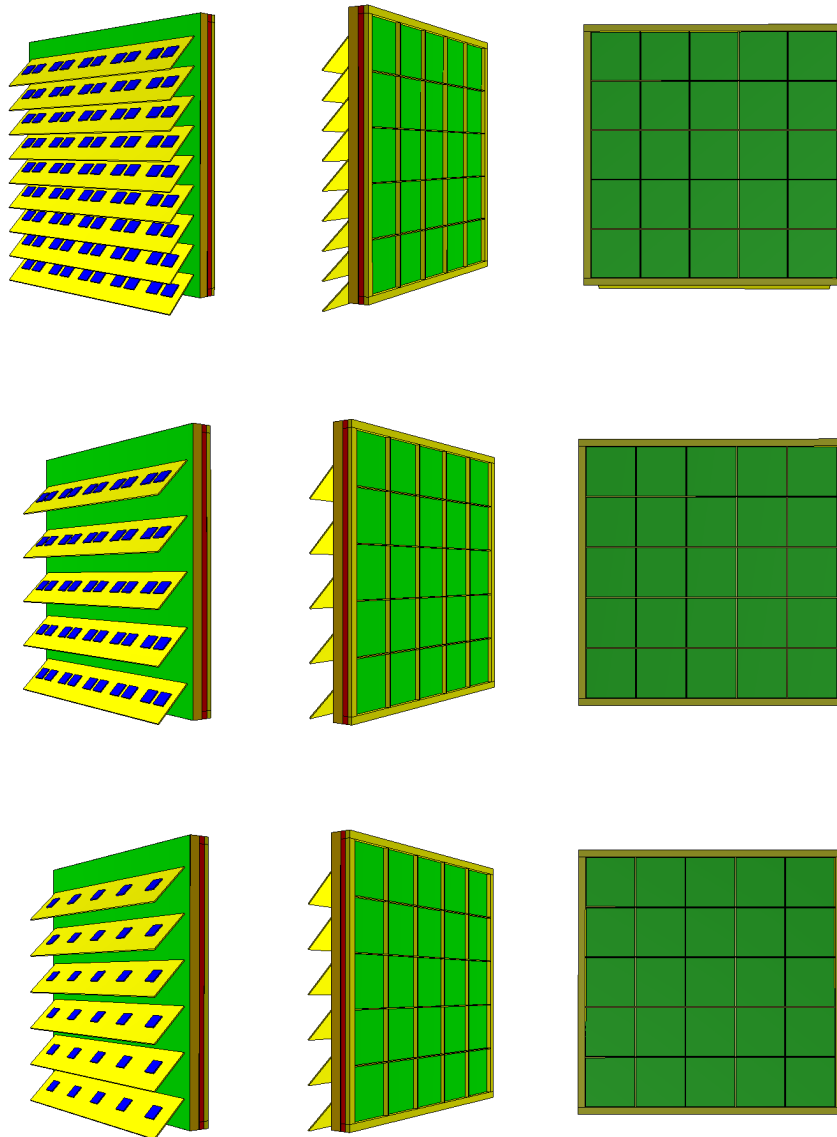


Figure C.1: The small TRD module types 1, 2, and 3 for the inner part of the detector.

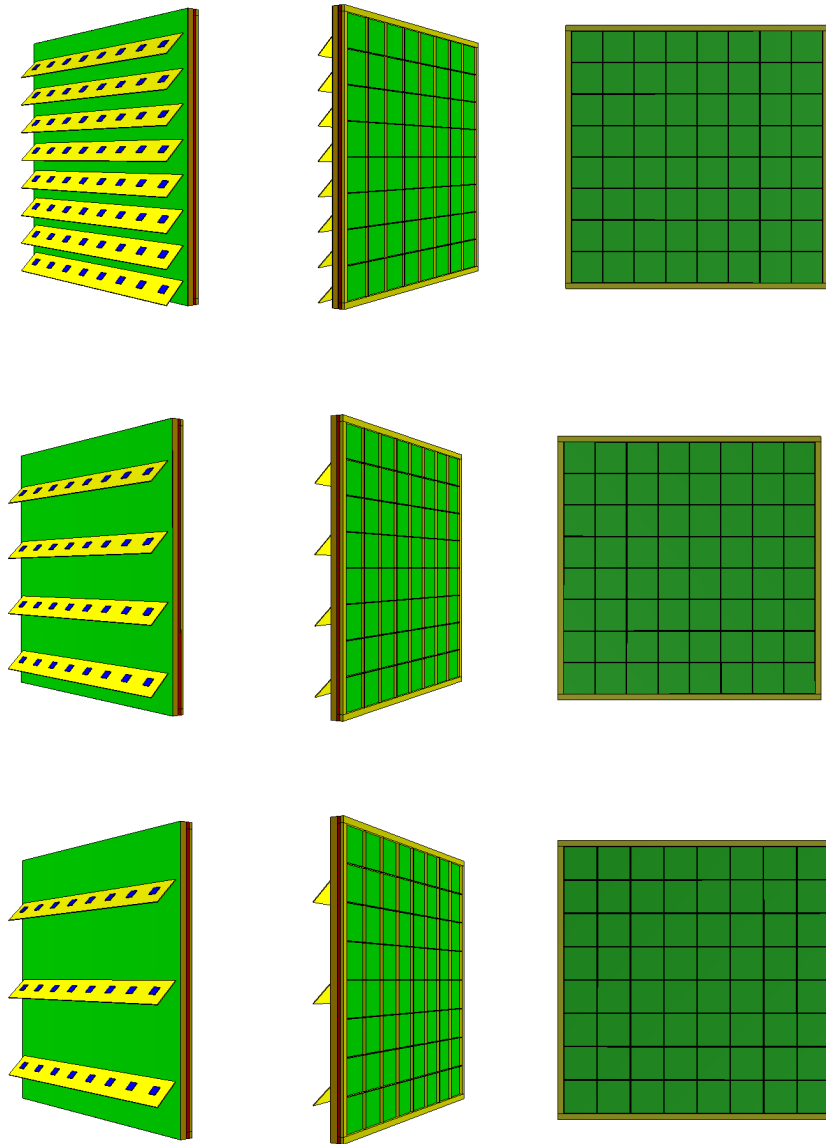


Figure C.2: The large TRD module types 6, 7, and 8 for the outer part of the detector.

# Bibliography

- [A<sup>+</sup>99] S. Afanasev et al. The NA49 large acceptance hadron detector. *Nucl. Instrum. Meth.*, A430:210–244, 1999.
- [A<sup>+</sup>03] S. Agostinelli et al. GEANT4: A Simulation toolkit. *Nucl. Instrum. Meth.*, A506:250–303, 2003.
- [A<sup>+</sup>04] A. Andronic et al. Energy loss of pions and electrons of 1-GeV/c to 6-GeV/c in drift chambers operated with Xe, CO(2)(15%). *Nucl. Instrum. Meth.*, A519:508–517, 2004.
- [A<sup>+</sup>05] B. Alessandro et al. A New measurement of  $J/\psi$  suppression in Pb-Pb collisions at 158-GeV per nucleon. *Eur. Phys. J.*, C39:335–345, 2005.
- [A<sup>+</sup>06] Y. Aoki et al. The Order of the quantum chromodynamics transition predicted by the standard model of particle physics. *Nature*, 443:675–678, 2006.
- [A<sup>+</sup>07] E. P. Akishina et al. Electron/pion identification in the CBM TRD applying a multilayer perceptron, 01 2007. <https://www-alt.gsi.de/documents/DOC-2008-Mar-156.html>.
- [A<sup>+</sup>09] R. Arnaldi et al. NA60 results on thermal dimuons. *Eur. Phys. J.*, C61:711–720, 2009.
- [A<sup>+</sup>10a] A. Adare et al. Detailed measurement of the  $e^+e^-$  pair continuum in  $p + p$  and Au+Au collisions at  $\sqrt{s_{NN}} = 200$  GeV and implications for direct photon production. *Phys. Rev.*, C81:034911, 2010.
- [A<sup>+</sup>10b] A. Andronic et al. Hadron Production in Ultra-relativistic Nuclear Collisions: Quarkyonic Matter and a Triple Point in the Phase Diagram of QCD. *Nucl. Phys.*, A837:65–86, 2010.
- [A<sup>+</sup>11] A. Adare et al.  $J/\psi$  suppression at forward rapidity in Au+Au collisions at  $\sqrt{s_{NN}} = 200$  GeV. *Phys. Rev.*, C84:054912, 2011.
- [A<sup>+</sup>12] A. Aduszkiewicz et al. NA61/SHINE at the CERN SPS: Plans, status and first results. *Acta Phys. Polon.*, B43:635, 2012.
- [A<sup>+</sup>14] B. Abelev et al. Centrality, rapidity and transverse momentum dependence of  $J/\psi$  suppression in Pb-Pb collisions at  $\sqrt{s_{NN}}=2.76$  TeV. *Phys. Lett.*, B734:314–327, 2014.
- [A<sup>+</sup>16] J. Adam et al. The ALICE Transition Radiation Detector, 2016. To be submitted to *Nucl. Instrum. Meth. A*.
- [ABMS06] A. Andronic, P. Braun-Munzinger, and J. Stachel. Hadron production in central nucleus-nucleus collisions at chemical freeze-out. *Nucl. Phys.*, A772:167–199, 2006.

- [ABMSS11] A. Andronic, P. Braun-Munzinger, J. Stachel, and H. Stocker. Production of light nuclei, hypernuclei and their antiparticles in relativistic nuclear collisions. *Phys. Lett.*, B697:203–207, 2011.
- [AC80] W. W. M. Allison and J. H. Cobb. Relativistic Charged Particle Identification by Energy Loss. *Ann. Rev. Nucl. Part. Sci.*, 30:253–298, 1980.
- [AFKP12] T. Armbruster, P. Fischer, M. Krieger, and I. Peric. Multi-channel charge pulse amplification, digitization and processing ASIC for detector applications. In *Nuclear Science Symposium and Medical Imaging Conference (NSS/MIC), 2012 IEEE*, pages 697–702, Oct 2012.
- [AFP10] T. Armbruster, P. Fischer, and I. Peric. SPADIC – A self-triggered pulse amplification and digitization ASIC. In *IEEE Nuclear Science Symposium Medical Imaging Conference*, pages 1358–1362, Oct 2010.
- [AH10] M. Al-Helwi. Gain Calibration of the ALICE Transition Radiation Detector with Krypton-83. Diploma thesis, Ruprecht-Karls Universität Heidelberg, 2010.
- [AK] T. Armbruster and M. Krieger. SPADIC project website. <http://spadic.uni-hd.de>.
- [Are14] A. Arend. *Optimization of a Transition Radiation Detector for the Compressed Baryonic Matter Experiment*. PhD thesis, Goethe-Universität Frankfurt, 2014.
- [Arm13] T. Armbruster. *SPADIC – A self-triggered detector readout ASIC with multi-channel amplification and digitization*. PhD thesis, University of Heidelberg, 2013.
- [AW12] A. Andronic and J. P. Wessels. Transition Radiation Detectors. *Nucl. Instrum. Meth.*, A666:130–147, 2012.
- [B<sup>+</sup>87] R. Brun et al. GEANT3. *CERN report*, 1987.
- [B<sup>+</sup>98] S. A. Bass et al. Microscopic models for ultrarelativistic heavy ion collisions. *Prog. Part. Nucl. Phys.*, 41:255–369, 1998. [Prog. Part. Nucl. Phys.41,225(1998)].
- [B<sup>+</sup>07] G. Battistoni et al. The FLUKA code: Description and benchmarking. *AIP Conf. Proc.*, 896:31–49, 2007.
- [B<sup>+</sup>10] S. Borsanyi et al. Is there still any  $T_c$  mystery in lattice QCD? Results with physical masses in the continuum limit III. *JHEP*, 09:073, 2010.
- [B<sup>+</sup>12] A. Bazavov et al. The chiral and deconfinement aspects of the QCD transition. *Phys. Rev.*, D85:054503, 2012.
- [B<sup>+</sup>16a] A. Bercuci et al. , 2016. To be submitted to Nucl. Instrum. Meth. A.
- [B<sup>+</sup>16b] A. Bercuci et al. , 2016. To be submitted to Nucl. Instrum. Meth. A.
- [B<sup>+</sup>16c] D. Blaschke et al. Topical issue on Exploring Strongly Interacting Matter at High Densities - NICA White Paper. *The European Physical Journal A*, 52(8):1–1, 2016.
- [Bal13] T. Ballé. Studien zum Einfluss der Ausdehnung des Eingangsfensters auf die Gasverstärkung des CBM-TRD. Bachelor’s thesis, Goethe-Universität Frankfurt, 2013.

- [Ber09] C. Bergmann. Development and Test of a Transition Radiation Detector Prototype for CBM @ FAIR. Diploma thesis, Institut für Kernphysik, Westfälische Wilhelms-Universität Münster, 2009.
- [Ber14] C. Bergmann. *Development, Simulation and Test of Transition Radiation Detector Prototypes for the Compressed Baryonic Matter Experiment at the Facility for Antiproton and Ion Research*. PhD thesis, Institut für Kernphysik, WWU Münster, 2014.
- [BK02] V. Blobel and C. Kleinwort. A New method for the high precision alignment of track detectors. In *Advanced statistical techniques in particle physics. Proceedings, Conference, Durham, UK, March 18-22, 2002*, pages URL-STR(9), 2002.
- [BO98] M. J. Berger and K. Olsen. XCOM: Photon Cross Sections Database. NIST Standard Reference Database 8, 3 1998.
- [Boo14] J. Book. *J/ψ production in Pb-Pb collisions with ALICE at the LHC*. PhD thesis, Goethe-Universität Frankfurt, 2014.
- [BR94] W. Blum and L. Rolandi. *Particle Detection with Drift Chambers*. Springer-Verlag, 1994.
- [BR97] B. Brun and F. Rademakers, editors. *ROOT - An Object Oriented Data Analysis Framework*, AIHENP'96 Workshop, Lausanne, Sep. 1997. Nucl. Inst. Meth. in Phys. Res. A 389 (1997) 81-86.
- [C<sup>+</sup>01] P. Cortese et al. *ALICE transition-radiation detector: Technical Design Report*. Technical Design Report ALICE. CERN, Geneva, 2001.
- [C<sup>+</sup>10] V. Cătănescu et al. Front End Electronics for High Counting Rate TRD Using a Prototype ASIC. *CBM Progress Report 2009*, page 47, 2010.
- [C<sup>+</sup>11] G. Caragheorgheopol et al. Front-end electronics for high counting rate TRD. *CBM Progress Report 2010*, page 46, 2011.
- [C<sup>+</sup>13a] M. W. Conroy et al. Liquid drainage from high-expansion (HiEx) aqueous foams during and after filling of a container. *Colloids and Surfaces A: Physicochemical and Engineering Aspects*, 426(0):70–97, 2013.
- [C<sup>+</sup>13b] F. Constantin et al. FPGA-based free running mode acquisition for a high counting rate TRD. *CBM Progress Report 2012*, page 56, 2013.
- [C<sup>+</sup>15] S. Chattopadhyay et al. *Technical Design Report for the CBM : Muon Chambers (MuCh)*. CBM Technical Design Reports. GSI, Darmstadt, 2015.
- [C<sup>+</sup>16] S. Chattopadhyay et al. Challenges in QCD matter physics - The Compressed Baryonic Matter experiment at FAIR. arXiv:1607.01487, 2016.
- [CB99] W. Cassing and E. L. Bratkovskaya. Hadronic and electromagnetic probes of hot and dense nuclear matter. *Phys. Rept.*, 308:65–233, 1999.
- [CBC09] V. Cătănescu, B. Bartos, and G. Caragheorgheopol. Analog FEE for High Counting Rate Transition Radiation Detector. EuNPC+DPG Conference, Bochum, March 2009.

- [CBS01] W. Cassing, E. L. Bratkovskaya, and A. Sibirtsev. Open charm production in relativistic nucleus-nucleus collisions. *Nucl. Phys.*, A691:753–778, 2001.
- [CC<sup>+</sup>01] M. Ciobanu, V. Catanescu, et al. Preamplifier/shaper for ALICE TRD. *IFIN-HH Scientific Report IFIN-HH 2000*, page 64, 2001.
- [CHMP74] M. L. Cherry, G. Hartmann, D. Mueller, and T. A. Prince. Transition radiation from relativistic electrons in periodic radiators. *Phys. Rev.*, D10:3594–3607, 1974.
- [CMP74] M. L. Cherry, D. Mueller, and T. A. Prince. The efficient identification of relativistic particles by transition radiation. *Nucl. Instrum. Meth.*, 115:141–150, 1974.
- [Col05] CBM Collaboration. CBM Progress Report 2005, January 2005.
- [Col11] CBM Collaboration. CBM Report 2012-01, Nuclear matter physics at SIS-100, 2011.
- [C07] V. Cătănescu. Specific requirements for analog electronics for a high counting rate TRD. 10th CBM Collaboration Meeting, September 2007.
- [E<sup>+</sup>17] D. Emschermann et al. *Technical Design Report for the CBM Online Systems*. CBM Technical Design Reports. GSI, Darmstadt, 2017.
- [EC96] W. Ehehalt and W. Cassing. Relativistic transport approach for nucleus nucleus collisions from SIS to SPS energies. *Nucl. Phys.*, A602:449–486, 1996.
- [Eur] Europractice. CADENCE. <http://www.europractice.stfc.ac.uk/software/cadence.html>.
- [EZ94] B. Elisabetta and W. Zbigniew. PHOTOS: A Universal Monte Carlo for QED radiative corrections. Version 2.0. *Comput. Phys. Commun.*, 79:291–308, 1994.
- [F<sup>+</sup>00] R. Fruhwirth et al. *Data analysis techniques for high-energy physics*. Cambridge University Press, 2000.
- [F<sup>+</sup>07] I. Frohlich et al. Pluto: A Monte Carlo Simulation Tool for Hadronic Physics. *PoS*, ACAT2007:076, 2007.
- [F<sup>+</sup>11] B. Friman et al. The CBM physics book: Compressed baryonic matter in laboratory experiments. *Lect. Notes Phys.*, 814:pp.1–980, 2011.
- [FH11] K. Fukushima and T. Hatsuda. The phase diagram of dense QCD. *Rept. Prog. Phys.*, 74:014001, 2011.
- [FK04] Z. Fodor and S. D. Katz. Critical point of QCD at finite T and mu, lattice results for physical quark masses. *JHEP*, 04:050, 2004.
- [Fru87] R. Fruhwirth. Application of Kalman filtering to track and vertex fitting. *Nucl. Instrum. Meth.*, A262:444–450, 1987.
- [FS75] C. W. Fabjan and W. Struczinski. Coherent Emission of Transition Radiation in Periodic Radiators. *Phys. Lett.*, B57:483, 1975.
- [G<sup>+</sup>06] H. Gutbrod et al. *FAIR baseline technical report*. GSI, Darmstadt, 2006.
- [G<sup>+</sup>16] T. Galatyuk et al. Thermal Dileptons from Coarse-Grained Transport as Fireball Probes at SIS Energies. *Eur. Phys. J.*, A52(5):131, 2016.

- [Gal14] T. Galatyuk. HADES overview. *Nucl. Phys.*, A931:41–51, 2014.
- [GGY75] G. M. Garibian, L. A. Gevorgian, and C. Yang. The calculation of X-ray transition radiation generated in regular- and irregular-layered media. *Nucl. Instrum. Meth.*, 125(1):133–137, 1975.
- [Glä01] S. Gläfel. Untersuchung von TRD-Prototypen mit alternierender Hochspannung für das CBM-Experiment. Bachelor’s thesis, Goethe-Universität Frankfurt, 201.
- [Gmb13] Dassault Systemes Deutschland GmbH. Abaqus edition 6.12, 2013.
- [H<sup>+</sup>13] C. Höhne et al. *Technical Design Report for the CBM Ring Imaging Cherenkov Detector*. CBM Technical Design Reports. GSI, Darmstadt, 2013.
- [Hel13] E. Hellbär. Elektrostatische Simulationsstudien zum Übergangsstrahlungsdetektor des CBM-Experiments. Bachelor’s thesis, Goethe-Universität Frankfurt, 2013.
- [INC16] XILINX INC. [www.xilinx.com/publications/prod\\_mktg/sp601\\_product\\_brief.pdf](http://www.xilinx.com/publications/prod_mktg/sp601_product_brief.pdf), 2016.
- [Int16] Maxim Integrated. [www.maximintegrated.com/en/datasheet/index.mvp/id/6419](http://www.maximintegrated.com/en/datasheet/index.mvp/id/6419), 2016.
- [Kal60] R. E. Kalman. A New Approach to Linear Filtering and Prediction Problems. *Transactions of the ASME—Journal of Basic Engineering*, 82(Series D):35–45, 1960.
- [Kis06] I. Kisel. Event reconstruction in the CBM experiment. *Nucl. Instrum. Meth.*, A566:85–88, 2006.
- [KKO<sup>+</sup>14] K. Kasinski, R. Kleczek, P. Otfinowski, R. Szczygiel, and P. Grybos. STS-XYTER, a high count-rate self-triggering silicon strip detector readout IC for high resolution time and energy measurements. In *2014 IEEE Nuclear Science Symposium and Medical Imaging Conference (NSS/MIC)*, pages 1–6, Nov 2014.
- [Kri11] M. Krieger. Entwurf und Simulation eines digitalen Tail-Cancellation-Filters. Diploma thesis, University of Heidelberg, 2011.
- [Lan01] D. J. Lange. The EvtGen particle decay simulation package. *Nucl. Instrum. Meth.*, A462:152–155, 2001.
- [LB13] F. Lemke and U. Bruening. A Hierarchical Synchronized Data Acquisition Network for CBM. *IEEE Transactions on Nuclear Science*, 60(5):3654–3660, Oct 2013.
- [LO08] A. Lebedev and G. Ososkov. LIT track propagation for CBM. *CBM note*, 2008.
- [LW98] B. Lasiuk and C. A. Whitten. Use of Krypton-83 as a calibration source for the STAR TPC. Technical report, BNL, 1998.
- [Mat88] E. Mathieson. Cathode Charge Distributions in Multiwire Chambers. 4: Empirical Formula for Small Anode - Cathode Separation. *Nucl. Instrum. Meth.*, A270:602–603, 1988.
- [Maz00] M. N. Mazziotta. A Monte Carlo code for full simulation of a transition radiation detector. *Comput. Phys. Commun.*, 132:110–123, 2000.
- [MS86] T. Matsui and H. Satz.  $J/\psi$  Suppression by Quark-Gluon Plasma Formation. *Phys. Lett.*, B178:416–422, 1986.

- [O<sup>+</sup>14] K. A. Olive et al. Review of Particle Physics. *Chin. Phys.*, C38:090001, 2014.
- [P<sup>+</sup>07a] M. Petriş et al. High counting rate transition radiation detector . *Nucl. Instr. Meth.*, A581:406–409, 2007.
- [P<sup>+</sup>07b] M. Petrovici et al. A high-efficiency Transition Radiation Detector for high-counting-rate environments. *Nucl. Instrum. Meth.*, A579:961–966, 2007.
- [P<sup>+</sup>11] M. Petrovici et al. A Two-Dimension Position Sensitive High Efficiency Transition Radiation Detector for High Counting Rate Environment. *Rom. Journ. Phys.*, 56:654–663, 2011.
- [P<sup>+</sup>13a] M. Petriş et al. TRD detector development for the CBM experiment. *Nucl. Instrum. Meth.*, A732:375–379, 2013.
- [P<sup>+</sup>13b] M. Petriş et al. Two-dimensional position sensitive transition radiation detector. *Nucl. Instrum. Meth.*, A714:17–23, 2013.
- [PAK<sup>+</sup>10] I. Peric, T. Armbruster, M. Koch, C. Kreidl, and P. Fischer. DCD – The Multi-Channel Current-Mode ADC Chip for the Readout of DEPFET Pixel Detectors. *IEEE Transactions on Nuclear Science*, 57(2):743–753, April 2010.
- [Pre07] W. Press. *Numerical Recipes: The Art of Scientific Computing*. Cambridge Univ. Press, 2007.
- [Reu13] K. Reuß. Studien zur Ausdehnung des Eingangsfensters des CBM-TRDs. Bachelor’s thesis, Goethe-Universität Frankfurt, 2013.
- [RvH16] R. Rapp and H. van Hees. Thermal Dileptons as Fireball Thermometer and Chronometer. *Phys. Lett.*, B753:586–590, 2016.
- [RWvH10] R. Rapp, J. Wambach, and H. van Hees. The Chiral Restoration Transition of QCD and Low Mass Dileptons. *Landolt-Bornstein*, 23:134, 2010.
- [S<sup>+</sup>05] H.K. Solveit et al. 16 channels ASIC preamplifier-shaper. *GSI Scientific Report 2005-1*, 2005.
- [S<sup>+</sup>11] M. Staib et al. RD51-Note-2011-004, 2011.
- [S<sup>+</sup>12] A. Schmah et al. Highlights of the Beam Energy Scan from STAR. *Central Eur. J. Phys.*, 10:1238–1241, 2012.
- [Sec15] F. Seck. Development of a Realistic Event Generator for In-Medium and QGP Dileptons. Master’s thesis, Technische Universität Darmstadt, 2015.
- [Sei14] M. Seidl. Studien zur Ausdehnung des Eingangsfensters des CBM-TRDs. Bachelor’s thesis, Goethe-Universität Frankfurt, 2014.
- [Spe10] H. J. Specht. Thermal Dileptons from Hot and Dense Strongly Interacting Matter. *AIP Conf. Proc.*, 1322:1–10, 2010.
- [Sti11] J. H. Stiller. Gain Calibration of the ALICE TRD using the Decay of <sup>83</sup>Kr and Alignment of the ALICE TRD. Diploma thesis, Ruprecht-Karls Universität Heidelberg, 2011.
- [Thi96] D. M. Thiessen. The Gas System for the HERMES Transition Radiation Detector. Master’s thesis, Simon Fraser University Vancouver, 1996.

- [Vee98] R. Veenhof. GARFIELD, recent developments. *Nucl. Instrum. Meth.*, A419:726–730, 1998.
- [VHK11] D. Varga, G. Hamar, and G. Kiss. Asymmetric multi-wire proportional chamber with reduced requirements to mechanical precision. *Nucl. Instrum. Meth.*, A648:163–167, 2011.